Searching for Light Scalar Dark Matter with Gravitational Waves Detectors

Francesco Cipriano

To cite this version:

Francesco Cipriano. Searching for Light Scalar Dark Matter with Gravitational Waves Detectors. Instrumentation and Methods for Astrophysic [astro-ph.IM]. Université Côte d'Azur, 2020. English. NNT : . tel-03180567

HAL Id: tel-03180567
https://theses.hal.science/tel-03180567

Submitted on 25 Mar 2021

UNIVERSITÉ
CÔTE D'AZUR

ÉCOLE DOCTORALE
SCIENCES
FONDAMENTALES
ET APPLIQUÉES

THÈSE DE DOCTORAT

Searching for Light Scalar Dark Matter with Gravitational Waves Detectors

Francesco CIPRIANO
Laboratoire ARTEMIS - Observatoire de la Côte d'Azur

Présentée en vue de l'obtention du grade de docteur en
Science de la Planéte et de l'Univers
d'Université Côte d'Azur

Thése dirigée par : Michel Boer DR CNRS
Et co-encadrée par : Olivier Minazzoli CR – Centre Scientifique de Monaco

Soutenue le : 10 Septembre 2020

Devant le jury, composé de :

Mairi Sakellariadou, Prof. King's College London, **Rapportrice**
Tania Regimbau (HDR), DR LAPP, **Rapportrice**
Christophe Le Poncin-Lafitte (HDR), Astronome, SYRTE, **Examinateur**
Aurélien Hees, CR, SYRTE, **Examinateur**

Abstract

The existence of the dark matter and the truth beyond its nature has been one of the greatest puzzle of the twentieth century and still it is nowadays. In the last decades several hypothesis, such as the WIMPs model, have been proposed to solve such puzzle but none of them has been able so far to succeed.
In this thesis work we will focus on an other very appealing model in which dark matter is successfully described by an ultra-light scalar field whose origin can be sought in the low-energy limit of one of the most promising unification theories: the String Theory.

In this work we show how such scalar field, if present, interacts with standard matter and in particular with the optical apparatus that is at the core of gravitational waves antennas. We derive and discuss the signal produced by this interaction through different approaches deriving both approximated and exact solutions. Special attention is paid to the second-order term of the signal approximate series expansion whose contribution ends up to be not negligible when one factors in the specific geometrical dimensions and frequency range of gravitational waves detectors like Advanced LIGO and Advanced Virgo.
As suggested by recent surveys, we assume the presence of a dark matter stream in the local neighborhood of the solar system and show its effect on the signal.

We then propose and discuss a hierarchical statistical analysis aimed to the signal detection. In case of no detection a limit curve for the coupling parameter d_g^* is derived. Such curve is then analyzed in detail showing the magnitude of the contribution of the first-order and second-order terms of the signal series expansion. We analyze the modification of the constraint curve due to the variation of the fraction of local dark matter belonging to the stream. We show finally how the constraint curve responds to variations of the search parameter and discuss the optimal choices.

Keywords:- *Alternative Theory of Gravitation* - *Scalar Tensor Theory* - *Dark Matter* - *Gravitational Waves* - *Signal Analysis*

Résumé

L'existence de la matière noire et la vérité sur sa nature a été l'une des plus grandes énigmes du XXe siècle et elle l'est encore aujourd'hui. Au cours des dernières décennies, plusieurs hypothèses, telles que le modèle WIMPs, ont été proposées pour résoudre une telle énigme. Aucune d'entre elles n'a pour l'instant réussi.

Dans ce travail de thèse, nous nous concentrerons sur un autre modèle très attrayant dans lequel la matière noire pourrait être décrite avec succès par un champ scalaire ultra-léger. L'origine de ce champ peut être recherchée dans la limite de basse énergie de l'une des théories d'unification les plus prometteuses : la théorie des cordes.

Dans ce travail, nous montrons comment un tel champ scalaire, s'il est présent, interagit avec la matière standard et en particulier avec l'appareil optique qui est au cœur des antennes d'ondes gravitationnelles. Nous évaluons et nous discutons le signal produit par cette interaction à travers différentes approches. Des solutions approximatives et exactes sont ensuite obtenues. Une attention particulière est accordée au terme du deuxième ordre de l'expansion en série approximative du signal. On trouve, en effet, que sa contribution finit par ne pas être négligeable lorsque l'on tient compte des dimensions géométriques spécifiques et de la gamme de fréquence des détecteurs d'ondes gravitationnelles comme Advanced LIGO et Advanced Virgo.

En tenant compte des travaux récents, nous supposons la présence d'un flux de matière noire voisin du système solaire et nous montrons son effet sur le signal.

Nous proposons et discutons une analyse statistique hiérarchique visant à la détection du signal. En cas de non-détection, une courbe limite pour le paramètre de couplage d_g^* est dérivée. Cette courbe est ensuite analysée en détail montrant l'ampleur de la contribution des termes de premier ordre et de deuxième ordre de l'expansion en série de signaux. Nous analysons la modification de la courbe de contrainte en raison de la variation de la fraction de matière noire locale appartenant au flux. Nous montrons enfin comment la courbe de contrainte répond aux variations du paramètre de recherche. Une discussion sur des choix optimaux est proposée.

Mots clés:- *Théorie Alternative de la Gravitation* - *Théorie Tenseur Scalaire* - *Matière Noire* - *Ondes Gravitationnelles* - *Analyse de Signal*

Contents

Introduction

Although the theory of General Relativity has passed numerous tests, it is nowadays challenged by theoretical considerations and by galactic and cosmological evidences [130]. From a theoretical point of view, because of its *classical* frame, General Relativity cannot be dealt with in the same way as for others fundamental interactions. Numerous theoretical developments of a quantum theory of gravitation, that would be able to unify the gravitational sector with the standard model of particles, also seem to demand for a modification of the Einstein's theory.

In addition to this, some of the current galactic and cosmological observations seem to require the introduction of new entities, such as the *dark energy* and the *dark matter*, in order to be explained. Recent analyses of the Cosmic Microwave Background suggest that only around 30% of the total energy density in our universe is accounted by matter, and the fraction becomes way smaller if one considers just the standard barionic matter [100]. On galactic scale, we see that the observed rotational curves of galaxies, as well as their total luminosity, do not fit the prediction based on General Relativity. This strongly suggest the presence of something, i.e. the dark matter, able to affect the gravitational behavior of the system it is a part of, without showing any kind of electromagnetic interaction [105, 124]. Such exotic and mysterious components of our universe can be interpreted as new types of matter, as a modification of the undergoing theory of gravitation, or as a combination of the two.

In the last decades, astronomers and physicists have come up with different ideas in order to address the aforementioned inconsistencies of General Relativity. One of the first hypothesis assumed *intergalactic gas* to be the responsible of the high galactic mass-to-luminosity ratio values. However, it was discarded when studies on the Coma and Pegasus I clusters showed that hydrogen abundance was less than the 2% of what would have been required for gravitational binding [97, 87]. An other hypothesis saw the galactic dark matter made up of massive astrophysical compact halo objects, MACHOs in short. In this group one would find black holes, neutron stars as well as white and red dwarf and planets. Nowadays the MACHOs hypothesis is quite strongly dismissed as gravitational microlensing surveys together with the determination of the primordial light element abundances favor a non-baryonic nature for the dark matter [100, 83, 120]. If dark matter is not made up of baryonic matter, then one must look elsewhere. WIMPs (Weakly Interacting Massive Particles) seemed to be able to accommodate this requirement becoming one of the most popular dark matter candidate of the last decade. Loosely speaking, a WIMP is any massive particle that possess a weak, but non negligible coupling to the ordinary matter. In the last years several experiments have been performed in order to detect this weakly interacting massive particles, both through direct detection methods (see for example [28, 1]) and through indirect detection method (see for example [101, 13, 63]). Unfortunately, nowadays the WIMP hypothesis has not been able yet to prove herself true despite the effort gone into it.

Motivated by this -to date- unsuccessful search, scientists have began to increase their attention on alternative viable candidates, among which we find ultralight scalar fields. Such dark matter candidate consist in a massive scalar field ϕ which oscillate in time when its mass is larger than $m_\phi \gg \hbar H/c^2 \sim 1.5 \times 10^{-33}\, eV/c^2$. Where, in the previous inequality, H denotes the Hubble constant and m_ϕ represent the scalar field mass that, in our study, takes values from $10^{-14}\, eV/c^2$ up to $10^{-11}\, eV/c^2$.

The oscillating behavior of ultralight scalar field generates various peculiar phenomena that one can exploit in order to probe its existence. For instance, the oscillation of the scalar field ϕ induces a similar behavior in the fine-structure constant α, the electron mass m_e or the quantum chromodynamic mass scale. In turn, these variations creates a modulation in the energy spacing ΔE between two electronic levels as well as in the hyperfine transition frequency ratio of different atoms. [20] and [68] show, for example, how one could look for these effects in order to validate the presence of the scalar field. In the same way, as proposed in [61], one can exploit the induced oscillation of the Bohr radius, and the resulting variation of the atoms size and length of chemical bonds, to detect the scalar field via the implementation of optical cavities.

In our work we investigate the possibility of detecting this ultralight scalar field dark matter with a gravitational wave antenna such as Advance LIGO and Advanced Virgo, which in the last five years have proven to be extremely sensible instrument and able to push their boundaries further and further [3, 4, 5]. The spatial variations of the scalar field is in fact able to exert position-dependent oscillatory force on gravitational waves detectors' optical equipment. As a result, the optical equipment undergoes position-dependent oscillatory motions, which ends up with non-vanishing signals in the gravitational wave detectors' outputs. In this work, we derive an expression for the signal, first approximately, with the geodesic deviation and then, exactly, through a rigorous geometrical derivation. We propose a two-step search strategy optimized to find sinusoidal-like signals. A detailed discussion addresses the assumptions and approximations on which such detection method is based on and how one could adapt it if those assumptions would reveal to be unmet. Finally we test the effectiveness of the search strategy proposed in this work by applying it to fake data. In particular, we bury in Gaussian noise a signal that reproduces the one that would be generated by the interaction of the ultra-light scalar field with the interferometer's optical apparatus. We then apply the proposed detection method to see whether or not it allows us to recover the signal. In case of no detection, we assess how strong are the constraints we are able to put on the parameter of the underling interaction theoretical model.

The organization of the document is as follows. The first chapter of this manuscript will be devoted to a recap of the basis of the theory of *general relativity.* In its final part we will introduce the so-called *scalar-tensor* theory as an extension of the Einstein's theory. In chapter 2 we will deal with the physic beyond the gravitational waves. We will explain the principles that allow gravitational waves interferometer to work and the basic approach to signal analysis used to look for a detection. Chapter 3 will focus on the dark matter paradigm addressing two main questions: why do we think dark matter exist? what is dark matter made of? We will analyze some of the most compelling hypothesis such as the WIMPs' and FDM hypothesis and discuss the state of the art as it is nowadays. Finally in the last chapter we will show how the dark matter can be described in the framework of the scalar-tensor theory through the consideration of a ultra-light scalar field coupled with the standard matter. We will show how this scalar field would interact with the optical apparatus of gravitational waves interferometers extrapolating the kind of output signal it would produce. A signal analysis approach will be presented subsequently to finally conclude with the possible constraint one would be able to put on one of the model most important parameter in case of no detection. A final section is then dedicated to data simulations and analysis.

Chapter 1

General Relativity and its extensions

1.1 General Relativity

A good point to start if one wants to understand how gravity can be described through the curvature of the space-time is to consider one of the most known physical principles: the **Principle of Equivalence**. In its weak formulation (Weak Equivalence Principle, or WEP) it states that the inertial mass of a body m_i is equals to its gravitational mass m_g. The inertial mass is the constant that multiplies the acceleration in the second law of the Newtonian mechanics

$$\vec{F} = m_i \vec{a} \tag{1.1}$$

and quantifies the resistance one feels when one tries to move an object. For a given object, this quantity assumes always the same value despite the nature of the force acting on it (mechanical, electromagnetic, etc.). On the other side, the gravitational mass relates the gravitational force exerted on an object with the variation of the gravitational potential Ψ,

$$\vec{F}_g = m_g \nabla \Psi. \tag{1.2}$$

Although a priori these two quantities have very little in common, it has been proved to extremely high precision that $m_i = m_g$. A direct consequence of this equality is the universal interaction between matter and gravity. Every object falls at the same rate when it is subject to the same gravitational field. Such behavior allows us to reformulate the weak equivalence principle as follows: *In a small enough region of the space-time, the motion of* *free-falling objects are the same in a gravitational field and a uniformly accelerated frame.* Let us imagine to be in a box, unable to observe the outside world, while doing experiments involving the motion of test objects. Let us imagine also that such a box is accelerating at a constant rate. The weak equivalence principle states that there is no way for us to disentangle the effect of the gravitational field from those of an uniformly accelerating frame by studying the behavior of freely-falling objects. Famous is the example of the lift accelerating in the vacuum with an acceleration $\vec{a}$ perpendicular to the floor, direct toward the roof, and equal in magnitude to the acceleration $\vec{g}$ we experience on the Earth's surface. There would be no way to distinguish between the trajectory of a freely-falling objects inside such lift and one inside a lift at rest on the Earth's surface. After the conclusion of his theory of the special relativity (SR), Einstein thought to generalize the weak equivalence principle to something more inclusive that could better account for the new theoretical frame given by the SR. This extension of the weak equivalence principle is known as the **Einstein Equivalence Principle**, or EEP and states that *in small region of the space-time, the laws of physics reduce to those of special relativity; thus it is impossible to detect the existence of a gravitational field by means of local experiments.* One of the major implication of the Einstein equivalence principle is that there is not such thing as a gravitational neutral object that can be used to measure the acceleration due to gravity. Because every objects respond to the presence of gravity in the same way, the gravitational acceleration is not something one can reliably define. The idea then is to get rid of it defining freely-falling objects as unaccelerated. But if gravity no longer generates an acceleration it means the it can no longer be regarded to as a force and its effects must be addressed to something else. As we will see this "something else" is indeed the curvature of the space-time.

1.1.1 Space-time manifold and metric

An other consequence of the Einstein equivalence principle is that the idea of an infinitely extended inertial frame is no more acceptable. If one start to build a structure out of rigid rods and clocks around a freely-falling object in order to define an inertial frame, he or she will soon discover that far away particles, initially at rest respect to this frame, will start to accelerate as a consequence of the in-homogeneity of the gravitational field. Therefore, the best one can do is to define locally inertial frames as those frames which follow the motion of individual freely-falling objects in a small region of the space-time. In order to capture and describe this new complexity of the space-time one needs to use mathematical structures known as **differential manifolds**. A differential manifold can be regarded as a set that looks locally like a flat space, but might have a very different global geometry. To have an example of such a mathematical structure, one has to look not further than the surface of the Earth. It looks essentially flat if we confine our observation to small enough region of it, and definitely round if we let us look at it as a whole. To be a little more rigorous one can say that a manifold describes a space with a possible complex topology and morphology that nevertheless behaves locally as the flat Euclidean space. The flat Euclidean space, also known as $\mathbf{R^n}$, is the set of n-tuples $\left(x^1, x^2, ..., x^n\right)$ equipped with a flat, positive-defined, metric $\eta_{\mu\nu} = diag\,(1, ..., 1)$, where "diag" means a diagonal matrix with the given elements. It is worth to remark that this local association between the manifold and the Euclidean space holds true only as far as one is considering the behavior of function and coordinate. By no means this wants to say that the metric would be the same. It is the metric, in fact, that encodes the information on the manifold morphology and curvature. The metric itself is described by the symmetric, non-degenerate (0, 2) tensor $g_{\mu\nu}$. This tensor covers countless roles and one can easily say that is one of the most important pillars of Einstein's theory. To enumerate few of these, we just need to consider that the metric determines causality; it provides a notion of local inertial frame; is fundamental in the definition of "future" and "past" events and replaces the Newtonian gravitational field Ψ in the description of the gravitational interaction. A way to characterize a given metric is through its *signature*. In order to do it, one needs first to put the metric in its canonical form

$$g_{\mu\nu} = diag\,(-1, -1, ..., +1, ...0, ..., 0)\,. \tag{1.3}$$

The metric signature is then defined as the number of both positive and negative eigenvalues. If the metric is continuous and all its eigenvalues are different from zero, its signature will be the same at every point of the manifold. In the literature a metric with all positive eigenvalues is called *Euclidean* or *Reimannian*. If there is instead a single negative eigenvalues one refers to it as a *Lorentzian* or *Pseudo-Riemannian* metric. Any other combination represent an *indefinite* metric. In the theory of the general relativity, for example, one considers a four-dimensional manifold whose metric is characterized by the signature (-1, +1, +1, +1). In particular, the negative eigenvalue is associated with the temporal dimension of the space-time whereas the three positive ones are associated with the remaining three spatial dimensions.

It is possible to show that, at any given point p of the manifold, there exist a coordinate system $x^{\hat{\mu}}$ that allows us to express the metric in its canonical form and to set equal to zero all its first derivatives

$$g_{\hat{\mu}\hat{\nu}}(p) = \eta_{\mu\nu}, \quad \partial_{\hat{\sigma}} g_{\hat{\mu}\hat{\nu}}(p) = 0. \tag{1.4}$$

Such coordinates are referred to as *local inertial coordinates*. Note that, if in the local inertial coordinates frame one has the ability to make the metric at the point p looks like that of flat space, it means that the information on the manifold curvature cannot be encoded either in $g_{\mu\nu}$ or in its first derivatives $\partial_\sigma g_{\mu\nu}$. The second derivatives of the metric are the one who play the most important role in describing the space curvature. It turns out true in fact that there are no way to set $\partial_\rho \partial_\sigma g_{\mu\nu} = 0$ for any manifold that is not the Euclidean flat space itself.

1.1.2 Parallel-transport and geodesic equation

But what is exactly the curvature of the space-time and how can we describe it from a more appropriate mathematical point of view? We are used to think about curvature as an extrinsic characteristic of the space. We are able to say that a surface is curve because of the way it bends in $\mathbf{R^3}$. However, as far as we know, our space-time is not naturally embedded in a higher dimensional space. That's the reason way one usually prefers to use an intrinsic definition of curvature that therefore can be applied for every manifold, in any situation. This notion of curvature can be defined in terms of parallel transport. It is very intuitive to understand that to parallel transport a vector, for example, means to move it along a path having it always pointing in the same direction. One can immediately grasp how this notion can help us characterizing the curvature of a manifold if he or she considers that on a plane, a parallel-transported vector always coincides with its initial value. However this is not true on a sphere, see Fig. 1.1.

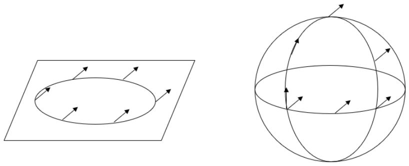

Figure 1.1: On the left we show the parallel transport of a vector around a closed curve on a plane. One can see that the vector "comes back" pointing in the same direction. On the right we show the parallel transport of a vector around a closed curve on a sphere. This time the vector comes back rotated by a certain angle.

In order to perform a parallel transport, we need to define some sort of derivative. In fact, given a notion of derivative, one can state that a vector is parallel transported along a curve if its derivative is zero along that given curve. Unfortunately, the common partial derivative will not do the work as it is a coordinate system dependent object and we need something that will not change when we change the coordinate system we are in (something said covariant). This is the reason why we introduce the covariant derivative ∇. The covariant derivative, or derivative operator, is a linear map that transforms (k, l) tensor into (k, l+1) tensor. One also requires it other proprieties such as to satisfy the Leibniz rule and to be commutative with tensor contraction. Such derivative operator can be defined through the way it acts upon vector, co-vector and by extension any (k, l) tensor as follows

$$\begin{aligned}\nabla_\mu t^\nu &= \partial_\mu t^\nu + \Gamma^\nu_{\mu\sigma} t^\sigma;\\ \nabla_\mu \omega_\nu &= \partial_\mu \omega_\nu - \Gamma^\sigma_{\mu\nu}\omega_\sigma;\end{aligned} \tag{1.5}$$

and for a generic (k, l) tensor

$$\begin{aligned}\nabla_\sigma T^{\mu_1 \dots \mu_k}_{\nu_1 \dots \nu_l} = \partial_\sigma T^{\mu_1 \dots \mu_k}_{\nu_1 \dots \nu_l} &+ \sum_i \Gamma^{\mu_i}_{\sigma\rho} T^{\mu_1 \dots \rho \dots \mu_k}_{\nu_1 \dots \nu_l}\\ &- \sum_j \Gamma^{\rho}_{\sigma\nu_j} T^{\mu_1 \dots \mu_k}_{\nu_1 \dots \rho \dots \nu_l}.\end{aligned} \tag{1.6}$$

Γs are known as *Christoffel symbols* and their purpose is to connect the partial derivative operator ∂ with a covariant derivative operator ∇. Provided with the tool of the covariant derivative, the notion of parallel transport along a curve C can be now defined as follows: given a vector v^μ, one can state that it is parallel transported along C if the equation

$$t^\nu \nabla_\nu v^\mu = 0 \tag{1.7}$$

is satisfied at each point as one moves along C, where t^ν represents, at any given point, the tangent of the curve. If one parameterizes C with the parameter t, then eq. (1.7) can be cast in the form

$$\frac{dv^\nu}{dt} + \sum_{\mu,\sigma} t^\mu \Gamma^\nu_{\mu\sigma} v^\sigma = 0. \tag{1.8}$$

Given a metric tensor $g_{\mu\nu}$ and two vectors v^μ and w^ν, it is possible to show that there exists only one derivative operator ∇ that leaves unchanged the inner product $g_{\mu\nu} t^\mu w^\nu$ when the two vectors are parallel transported along a generic curve. The Christoffel symbol that connects such operator with the partial derivative operator can be expressed in terms of the metric and its prime derivatives as follows

$$\Gamma^{\sigma}_{\mu\nu} = \frac{1}{2} g^{\sigma\rho} \left(\partial_{\mu} g_{\nu\rho} + \partial_{\nu} g_{\mu\rho} - \partial_{\rho} g_{\mu\nu} \right). \tag{1.9}$$

The importance of this choice is that in this way the sense of orthogonality, the vectors' norms and so on, are not spoiled by the act of parallel transporting.

The notion of parallel transport also allows us the characterize the geodesics of the manifold. A geodesic, as we will see, is the equivalent of a straight line in the Euclidean flat space. That is a line that goes "as straight as possible" given the intrinsic curvature of the manifold. One can translate this idea in term of parallel transport by demanding the tangent vector of the geodesic to be parallel propagated along the geodesic curve itself, i. e.

$$t^{\nu} \nabla_{\nu} t^{\mu} = 0. \tag{1.10}$$

In particular, the quantity $t^{\nu} \nabla_{\nu} t^{\mu}$ is equal to zero only for a particular parameterization of the curve called *affine parameterization.* For any other choice one would have the weaker condition

$$t^{\nu} \nabla_{\nu} t^{\mu} = \alpha t^{\mu}, \tag{1.11}$$

where α is an arbitrary function of the curve. However, since it is always possible to describe a curve in terms of its affine parameter, there is no loss of generality in considering only curves which satisfy eq. (1.10) rather then (1.11). Once again, one can write eq. (1.10) in a way that makes explicit the curve parameterization

$$\frac{d^2 x^{\mu}}{dt^2} + \Gamma^{\mu}_{\sigma\nu} \frac{dx^{\nu}}{dt} \frac{dx^{\sigma}}{dt} = 0, \tag{1.12}$$

where the repeated indexes are summed over. Immediately we see that in a flat space-time, where the Christoffel symbols Γ are equal to zero, the geodesic equation reduces to

$$\frac{d^2 x^{\mu}}{dt^2} = 0 \tag{1.13}$$

and thus describes a straight line. We know that the straight line in Euclidean space also represents the path of shortest distance between two points. It can be proved that such propriety can be is translated to geodesics in case of curved space. To show how this can be demonstrated let us consider a timelike path in the space-time, the result will then be applicable to any kind of path. For timelike path, we know that is more convenient to reason in terms of the proper time defined by the following functional

$$\tau = \int \left(-g_{\mu\nu} \frac{dx^\mu}{d\lambda} \frac{dx^\nu}{d\lambda} \right)^{1/2} d\lambda, \tag{1.14}$$

where the integral is over the path between two points of a given space-time that can be causally connected. One could find the stationary points of this functional through the usual calculus-of-variation method. However, because of the particular form of the functional, one can make things easier considering that

$$\begin{aligned} \delta\tau &= \int \delta\sqrt{-f} d\lambda \\ &= -\int \frac{1}{2} \left(-f\right)^{-1/2} \delta f d\lambda, \end{aligned} \tag{1.15}$$

where

$$f = g_{\mu\nu} \frac{dx^\mu}{d\lambda} \frac{dx^\nu}{d\lambda}. \tag{1.16}$$

If now one chooses the arbitrary parameter λ to be exactly the proper time τ, then the tangent vector becomes the four-velocity U^μ and

$$f = g_{\mu\nu} \frac{dx^\mu}{d\tau} \frac{dx^\nu}{d\tau} = g_{\mu\nu} U^\mu U^\nu = -1. \tag{1.17}$$

Injecting eq. (1.17) in eq. (1.15), one can see that

$$\delta\tau = -1/2 \int \delta f d\tau, \tag{1.18}$$

which simplifies the derivation. Hence one can search for the stationary point of the functional

$$I = \frac{1}{2} \int g_{\mu\nu} \frac{dx^\mu}{d\tau} \frac{dx^\nu}{d\tau} d\tau. \tag{1.19}$$

The variation δI can be recovered by considering the change in the integral under the infinitesimal variation of the path

$$\begin{aligned} x^\mu &\to x^\mu + \delta x^\mu \\ g_{\mu\nu} &\to g_{\mu\nu} + \left(\partial_\sigma g_{\mu\nu}\right) \delta x^\sigma. \end{aligned} \tag{1.20}$$

After some integration by part one obtains

$$\delta I = \int \left[g_{\mu\nu} \frac{d^2 x^\mu}{d\tau^2} + \frac{1}{2} \left(\partial_\mu g_{\nu\sigma} + \partial_\nu g_{\mu\sigma} - \partial_\sigma g_{\mu\nu} \right) \frac{dx^\mu}{d\tau} \frac{dx^\nu}{d\tau} \right] \delta x^\sigma d\tau. \tag{1.21}$$

In order to find a stationary point the integrated term must vanish for any variation δx^σ. This is true if and only if

$$g_{\mu\nu} \frac{d^2 x^\mu}{d\tau^2} + \frac{1}{2} \left(\partial_\mu g_{\nu\sigma} + \partial_\nu g_{\mu\sigma} - \partial_\sigma g_{\mu\nu} \right) \frac{dx^\mu}{d\tau} \frac{dx^\nu}{d\tau} = 0. \tag{1.22}$$

One can see that if we multiply eq. (1.22) by the inverse metric $g^{\sigma\rho}$ we end up exactly with the geodesic equation as described in eq. (1.12) where the Christoffel symbols defined in eq. (1.9) are the special ones defined from the space-time metric $g_{\mu\nu}$.

1.1.3 Curvature and Riemann tensor

Geodesic curves can be also used in order to characterize the curvature of the manifold. It is known that one of the postulate of the Euclidean flat geometry is that *initially parallel straight lines remain parallel forever*. We have seen how the notion of geodesic generalizes the straight line of the Euclidean flat space, so we can ask ourselves if this postulate stays true also when applied to geodesics. With very little surprise, the answer is negative if the space considered is anything else that the flat space. Let us consider the spherical representation of our planet. One can imagine two travelers that move toward the north pole starting from the equator at two nearby location (see Fig. 1.2).

Even if their paths are straight and parallel at the beginning, the two will eventually cross at the pole. This well known behavior is a direct consequence of the Earth curvature. Let us now try to describe this phenomenon in a more rigorous mathematical way. One can start by considering a one-parameter family of geodesics $\gamma_s(t)$. That is a collection of geodesics parameterized by the affine parameter t and labeled by $s \in \mathbf{R}$.

Provided that the members of such a family do not cross each other at any point, any point of the surface described by γ_s can be characterized by the coordinates $x^\mu(s,t)$. It is straightforward to define two natural vector fields associated with x^μ. The first is the vector field of the geodesics tangent vectors

$$T^\mu = \frac{\partial x^\mu}{\partial t}, \tag{1.23}$$

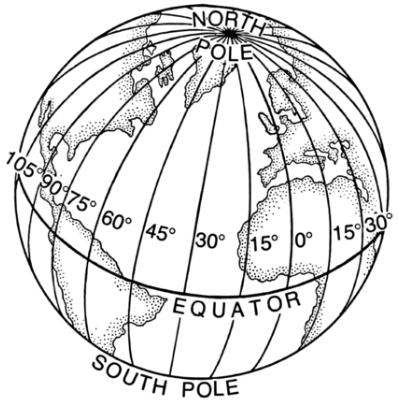

Figure 1.2: Even if the meridians are parallel to each other along the equator line, due to the Earth curvature they eventually meet of the North Pole.

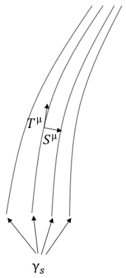

Figure 1.3: One-parameter family of geodesics γ_s with tangent $T\mu$ and deviation vector S^μ.

whereas the second

$$S^\mu = \frac{\partial x^\mu}{\partial s} \tag{1.24}$$

is usually referred to as the deviation vector field. The reason for this is that S^μ provides us with the intuitive notion of how far a geodesic is from its neighborhood. It make sense then to define the a vector field whose role is to describe how fast this “distance” between two adjacent geodesics varies as one moves along the geodesics themselves. To do this one considers the vector field

$$V^\mu = T^\sigma \nabla_\sigma S^\mu. \tag{1.25}$$

Similarly one also defines the "relative acceleration" vector field

$$A^\mu = T^\sigma \nabla_\sigma V^\mu . \tag{1.26}$$

Since S and T are basis vectors of the coordinate system $x^\mu(s,t)$ one can prove that the relation

$$S^\sigma \nabla_\sigma T^\mu = T^\sigma \nabla_\sigma S^\mu \tag{1.27}$$

holds true. With this in mind, one is ready to compute the acceleration

$$\begin{aligned} A^\mu &= T^\rho \nabla_\rho \left(T^\sigma \nabla_\sigma S^\mu\right) \\ &= T^\rho \nabla_\rho \left(S^\sigma \nabla_\sigma T^\mu\right) \\ &= \left(T^\rho \nabla_\rho S^\sigma\right)\left(\nabla_\rho T^\mu\right) + T^\rho S^\sigma \nabla_\rho \nabla_\sigma T^\mu , \end{aligned} \tag{1.28}$$

where in the second line one has utilized relation (1.27) and the third line results from the application of the Leibniz rule. Next step is to add and subtract the quantity $T^\rho S^\sigma \nabla_\sigma \nabla_\rho T^\mu$. Note that, because in curved space the covariant derivative operator does not commute, this $T^\rho S^\sigma \nabla_\sigma \nabla_\rho T^\mu$ is very much different from $T^\rho S^\sigma \nabla_\rho \nabla_\sigma T^\mu$. It follows that

$$\begin{aligned} A^\mu &= \left(T^\rho \nabla_\rho S^\sigma\right)\left(\nabla_\rho T^\mu\right) + T^\rho S^\sigma \nabla_\sigma \nabla_\rho T^\mu \\ &\quad + T^\rho S^\sigma \left(\nabla_\rho \nabla_\sigma - \nabla_\sigma \nabla_\rho\right) T^\mu \\ &= T^\rho S^\sigma \left(\nabla_\rho \nabla_\sigma - \nabla_\sigma \nabla_\rho\right) T^\mu . \end{aligned} \tag{1.29}$$

It is useful at this point to define the *Riemann tensor* $R^\mu_{\nu\sigma\rho}$ so that

$$\left(\nabla_\rho \nabla_\sigma - \nabla_\sigma \nabla_\rho\right) T^\mu = R^\mu_{\nu\sigma\rho} T^\nu . \tag{1.30}$$

Plugging this into the previous calculation, one finally obtains

$$A^\mu = R^\mu_{\nu\sigma\rho} T^\nu T^\rho S^\sigma . \tag{1.31}$$

The Riemann tensor turns out to be crucial in the description of curved manifold as it single handedly encodes all the information one needs to describe the curvature of the manifold. For this reason it is worth to look more into detail its property. In order to do this, it is useful to express the Riemann tensor in terms of Christoffel symbols and their derivatives

$$R^\sigma_{\mu\rho\nu} = \partial_\rho \Gamma^\sigma_{\mu\nu} - \partial_\nu \Gamma^\sigma_{\mu\rho} + \Gamma^\lambda_{\mu\nu}\Gamma^\sigma_{\lambda\rho} - \Gamma^\lambda_{\mu\rho}\Gamma^\sigma_{\lambda\nu} . \tag{1.32}$$

The Riemann tensor has a total of n^4 components where n is the dimension of the manifold one is considering. Because of numerous symmetry propriety this tensor satisfies, among the n^4 components the independent ones are just

$$\frac{1}{12} n^2 \left(n^2 - 1\right) . \tag{1.33}$$

In our case, we are interested in the number of independent components for $n = 4$. It turns out that in this case they are 20. These twenty components are strictly related with the twenty degrees of freedom in the second derivatives of the metric. Those are exactly the twenty degrees of freedom that cannot be set to zero no matter the choice of the coordinate system. Also important, for reasons that will be clear later, is the fact that the Riemann tensor satisfy the *Bianchi identity*

$$\nabla_\lambda R_{\rho\sigma\mu\nu} + \nabla_\rho R_{\sigma\lambda\mu\nu} + \nabla_\sigma R_{\lambda\rho\mu\nu} = 0 \tag{1.34}$$

where $R_{\rho\sigma\mu\nu} = g_{\rho\omega} R^{\omega}_{\sigma\mu\nu}$.
The Riemann tensor can be decomposed into its "trace part" and "trace free part". To obtain the first, we need to contract its first and third indexes

$$R^{\sigma}_{\mu\sigma\nu} = R_{\mu\nu}. \tag{1.35}$$

The result of this operation is called *Ricci tensor* and it can be proved that it is the only non-trivial (0,2) tensor one can built contracting the Riemann tensor. Its trace $R = R^{\mu}_{\mu}$ is known as the *Ricci scalar*. The trace free part takes the name of *Weyl tensor* and, for manifold of dimensions $n \geq 3$, is defined by the equation

$$\begin{aligned} C_{\rho\sigma\mu\nu} = R_{\rho\sigma\mu\nu} &- \frac{2}{(n-2)}\left(g_{\rho[\mu} R_{\nu]\sigma} - g_{\sigma[\mu} R_{\nu]\rho}\right) \\ &+ \frac{2}{(n-1)(n-2)} g_{\rho[\mu} g_{\nu]\rho} R, \end{aligned} \tag{1.36}$$

where the square brackets mean that one is taking the symmetric sum over the indexes, e.g.

$$A_{[\mu\nu]} = A_{\mu\nu} + A_{\nu\mu}. \tag{1.37}$$

Let us now focus our attention on the trace part of $R^{\rho}_{\sigma\mu\nu}$ and its contraction, namely the Ricci tensor and the Ricci scalar respectively. In particular, as a consequence of the fact that the Bianchi identity is respected by the Riemann tensor, $R_{\mu\nu}$ and R satisfy the following equation

$$\nabla^{\mu} R_{\rho\mu} = \frac{1}{2} \nabla_\rho R. \tag{1.38}$$

This expression is also known as the twice-contracted Bianchi identity and can be re-written in the form

$$\nabla^{\mu}\left(R_{\mu\nu} - \frac{1}{2} g_{\mu\nu} R\right) = 0. \tag{1.39}$$

The divergence-free tensor

$$G_{\mu\nu} = R_{\mu\nu} - \frac{1}{2} g_{\mu\nu} R \tag{1.40}$$

takes the name of *Einstein tensor* and is of great importance for the Einstein theory of general relativity.

1.1.4 Einstein's Equation

Let us now discuss the Einstein field equations of the space-time and see how to recover them. As for the geodesic equation, the field equations of general relativity can be found through the principle of least action. Given the action

$$S = \int \mathcal{L}\left(\vartheta^i, \nabla_\mu \vartheta^i\right) d^n x, \tag{1.41}$$

its critical points will be the classical solutions we are looking for. Here $\vartheta^i\left(x\right)$ represent a set of fields that are the dynamical variables of the theory. The quantities $d^n x$ and $\mathcal{L}$ are instead densities whose product is a well-defined tensor. An other way to see it, is to decompose the Lagrangian density $\mathcal{L}$ as follows

$$\begin{aligned} &\mathcal{L} = \sqrt{g}\hat{\mathcal{L}}, \\ &\rightarrow \int \sqrt{-g}\hat{\mathcal{L}}\left(\vartheta^i, \partial_\mu \vartheta^i\right) d^n x \end{aligned} \tag{1.42}$$

Here $\hat{\mathcal{L}}$ is the Lagrangian of the theory, thus a scalar quantity, while the product $\sqrt{-g} d^n x$ represents the invariant volume element. To see why it is soo, let us consider the the transformations

$$x^\mu = x^\mu\left(\hat{x}^\nu\right), \tag{1.43}$$

where the $\hat{x}^\nu$ are the coordinates associated with the local inertial system. Then one has

$$d^n x = J d^n \hat{x}, \quad J = det\left(\frac{\partial x^\mu}{\partial \hat{x}^\nu}\right). \tag{1.44}$$

The Jacobian of the transformation can be evaluated considering that

$$\begin{aligned} &g_{\hat{\sigma}\hat{\rho}} = diag\left(-1, 1, 1, 1\right), \\ &g_{\hat{\sigma}\hat{\rho}} = \frac{\partial x^\mu}{\partial \hat{x}^\sigma} \frac{\partial x^\nu}{\partial \hat{x}^\rho} g_{\mu\nu}, \\ &\rightarrow \hat{g} = -1 = J^2 g. \end{aligned} \tag{1.45}$$

It follows that the expression for the invariant volume element is

$$d^n\hat{x} = \frac{1}{J}d^n x = \sqrt{-g}d^n x. \tag{1.46}$$

The task we are left with is to chose our Lagrangian $\hat{\mathcal{L}}$. In our case the dynamical variable is the metric $g_{\mu\nu}$, so $\hat{\mathcal{L}}$ must be a scalar quantity made out of the space-time metric. Moreover, this scalar must somehow include at least the second derivatives of the metric as we have shown that the metric itself, as well as its first derivatives, can be set to zero at any one point. As we just saw, the Riemann tensor is made from the second second derivatives of the metric and we know at least one scalar quantity that can be constructed from it, the Ricci tensor R. It can be proved that any nontrivial tensor that involves the metric and its derivatives up to the second order, can be expressed in terms of the metric and the Riemann tensor. Therefore, the Ricci scalar is the only independent scalar made out of the metric and its first and second derivatives. The choice $\hat{\mathcal{L}} = R$ seems therefore to be the simplest one. The deriving action

$$S_H = \int \sqrt{-g}Rd^n x, \tag{1.47}$$

is usually referred to as the *Hilber action*, or *Einstein-Hilbert action*. As one can is, S_H is not expressed in the form (1.41). We know on the other hand that this would not be possible as the $\nabla_\sigma g_{\mu\nu} = 0$. This means that one cannot use the Euler-Lagrange equations and needs instead to consider how small variations of the metric affect the action S_H. In practices, is more convenient to study the behavior of S_H under variations of the inverse metric $g^{\mu\nu}$. It can be proved that the stationary points obtained in this way are the same one would have obtained varying the action with respect to $g_{\mu\nu}$. Therefore one has

$$\begin{aligned} \delta S_H &= \delta \int \sqrt{-g}Rd^n x = \delta \int \sqrt{-g}g^{\mu\nu}R_{\mu\nu}d^n x \\ &= \int d^n x R\delta\sqrt{-g} + \int d^n x\sqrt{-g}R_{\mu\nu}\delta g^{\mu\nu} + \int d^n x\sqrt{-g}g^{\mu\nu}\delta R_{\mu\nu}. \end{aligned} \tag{1.48}$$

The second term on the r.h.s. is already in the correct form $X \cdot \delta g^{\mu\nu}$, so all we need to do is to evaluate the other remaining two. As for the first of them, one can use the relation

$$\delta g = g^{\mu\nu}\delta g_{\mu\nu} = -g g_{\mu\nu}\delta g^{\mu\nu}, \tag{1.49}$$

that leads then to

$$\delta\sqrt{-g} = -\frac{1}{2\sqrt{-g}}\delta g = -\frac{1}{2\sqrt{-g}} g_{\mu\nu}\delta g^{\mu\nu}. \tag{1.50}$$

For the last term we consider that

$$\delta R_{\mu\nu} = \nabla_\rho \left(\delta\Gamma^\rho_{\mu\nu}\right) - \nabla_\nu \left(\delta\Gamma^\rho_{\rho\mu}\right). \tag{1.51}$$

Therefore the integral becomes

$$\begin{aligned} &\int d^n x \sqrt{-g} g^{\mu\nu} \delta R_{\mu\nu} \\ =& \int d^n x \sqrt{-g} g^{\mu\nu} \left[\nabla_\rho \left(\delta\Gamma^\rho_{\mu\nu}\right) - \nabla_\nu \left(\delta\Gamma^\rho_{\rho\mu}\right)\right] \\ =& \int d^n x \sqrt{-g} \nabla_\rho \left[g^{\mu\nu} \left(\delta\Gamma^\rho_{\mu\nu}\right) - g^{\mu\rho} \left(\delta\Gamma^\rho_{\rho\nu}\right)\right]. \end{aligned} \tag{1.52}$$

As one can see, the third term is an integral with respect to the invariant volume element of the covariant divergence of a vector. Therefore, it can be set to zero by making the variation vanish to the infinity. Wrapping up the last results, we have

$$\delta S_H = \int d^n x \sqrt{-g} \left[R_{\mu\nu} - \frac{1}{2} g_{\mu\nu} R\right] \delta g^{\mu\nu}. \tag{1.53}$$

Stationary points are the ones which satisfy the condition $\delta S_H / \delta g^{\mu\nu} = 0$ and therefore one has

$$\frac{1}{\sqrt{-g}} \frac{\delta S_H}{\delta g^{\mu\nu}} = R_{\mu\nu} - \frac{1}{2} g_{\mu\nu} R = 0. \tag{1.54}$$

These are the well-known *Einstein's field equations*, or to be more precise, the Einstein's field equations in vacuum, as we haven't considered any contribution related to the matter distribution. In order to get the general equations one has to consider the action

$$S = \frac{c^4}{16\pi G} S_H + S_M, \tag{1.55}$$

where S_M is the action for the matter and S_H has been normalized to obtain the correct dimension. The quantity $16\pi G/c^4$ represents in fact the coupling constant between matter and geometry. Following the same steps as before, one obtains

$$\frac{1}{\sqrt{-g}} \frac{\delta S}{\delta g^{\mu\nu}} = \frac{c^4}{16\pi G} \left(R_{\mu\nu} - \frac{1}{2} g_{\mu\nu} R\right) + \frac{1}{\sqrt{-g}} \frac{\delta S_M}{\delta g^{\mu\nu}} = 0. \tag{1.56}$$

If now we define the energy-momentum tensor to be

$$T_{\mu\nu} = -2\frac{1}{\sqrt{-g}}\frac{\delta S_M}{\delta g^{\mu\nu}}, \tag{1.57}$$

we recover the complete Einstein's equations

$$R_{\mu\nu} - \frac{1}{2}g_{\mu\nu}R = \frac{8\pi G}{c^4}T_{\mu\nu}. \tag{1.58}$$

It is worth to notice that the left hand side of the equation is exactly the Einstein tensor $G_{\mu\nu}$. therefore eq. (1.58) can be written as

$$G_{\mu\nu} = \frac{8\pi G}{c^4}T_{\mu\nu}. \tag{1.59}$$

The identification of the variation of S_M with the energy-momentum tensor $T_{\mu\nu}$ could seem a little bit boldly. We would like then to show that it is indeed a well motivated choice. Let start by considering the Poisson equation

$$\nabla^2\Psi = 4\pi G\rho, \tag{1.60}$$

with Ψ the gravitational potential and ρ the mass density. Of course one would like the Einstein's equations to reduce to them in the Newtonian limit. To see how our choice of $T^{\mu\nu}$ allows exactly that let consider the contraction of eq. (1.58)

$$R = -\frac{8\pi G}{c^4}T. \tag{1.61}$$

The Einstein's equation can be now re-written in the slightly different form

$$R_{\mu\nu} = \frac{8\pi G}{c^4}\left(T_{\mu\nu} - \frac{1}{2}g_{\mu\nu}T\right). \tag{1.62}$$

In the Newtonian limit, we can assume gravity to be weak and time-independent. We can also assume particle's velocity to be not relativistic. In this frame, the energy-momentum tensor for a perfect fluid is described by

$$T_{\mu\nu} = \left(c^2\rho + p\right)U_\mu U_\nu + pg_{\mu\nu}, \tag{1.63}$$

where p and $c^2\rho$ describe respectively the momentum density and rest energy and U^μ is the fluid four-velocity. In reality the pressure can be neglected in the Newtonian limit as the particles of the fluid have velocities well below the one of the light. Therefore the energy-momentum tensor reduces to

$$T_{\mu\nu} = c^2\rho U^\mu U^\nu. \tag{1.64}$$

The fluid we are describing represents then some massive body, e.g. the Earth, that can be thought as dust. In the fluid rest frame, one has

$$U^\mu = \left(U^0, 0, 0, 0\right), \tag{1.65}$$

where the time-like component U^0 of the four-velocity can be fixed through the normalization

$$g_{\mu\nu} U^\mu U^\nu = -1. \tag{1.66}$$

In the Newtonian limit g_{00} and g^{00} are equal to the Minkowski metric component η_{00}, η^{00} plus a correction proportional to the gravitational potential Ψ

$$\begin{aligned} g_{00} &= -1 - \frac{2}{c^2}\Psi \\ g^{00} &= -1 + \frac{2}{c^2}\Psi. \end{aligned} \tag{1.67}$$

Therefore, up to the first order in the correction Ψ one has

$$U^0 = 1 - \frac{1}{c^2}\Psi. \tag{1.68}$$

The T_{00} component of the energy-momentum tensor then assume the form

$$T_{00} = c^2\rho \left(1 - \frac{1}{c^2}\Psi\right)\left(1 - \frac{1}{c^2}\Psi\right). \tag{1.69}$$

However, since the energy density $c^2\rho$ is already assumed to be small, one can neglect all the correction terms and get

$$T_{00} = c^2\rho, \qquad T_{\mu\nu} = 0 \text{ for } \mu,\, \nu \neq 0. \tag{1.70}$$

In the same way, the trace of $T_{\mu\nu}$ can be approximated to

$$T = g^{00} T_{00} = -c^2\rho. \tag{1.71}$$

With these results to our disposal we can write the field equations as follows

$$R_{00} = \frac{4\pi G}{c^2}\rho. \tag{1.72}$$

We need now to evaluate the R_{00} component of the Ricci tensor in the Newtonian approximation. First we notice that $R_{00} = R^i_{0i0}$ as the component R^0_{000} of the Riemann tensor is zero. Therefore one has

$$R_{00} = R^i_{0i0} = \partial_i \Gamma^i_{00} - \partial_0 \Gamma^i_{i0} + \Gamma^i_{i\lambda}\Gamma^\lambda_{00} - \Gamma^i_{0\lambda}\Gamma^\lambda_{i0}. \tag{1.73}$$

The last two terms on the right-hand side can be neglected as Γ is first order in the correction Ψ and thus $(\Gamma)^2$ contributes only at the second order. The second term instead is straight up zero as it involve a time derivative that vanish under the assumption of static field made in the Newtonian approximation. One is therefore left with

$$\begin{aligned} R = R^i_{0i0} &= \partial_i \Gamma^i_{00} \\ &= \frac{1}{c^2}\nabla^2\Psi. \end{aligned} \tag{1.74}$$

Finally, putting all together, one can see how we recover exactly the Poisson equation

$$\nabla^2\Psi = 4\pi G\rho. \tag{1.75}$$

1.2 The Standard Cosmological Model

One of the best achievement of the theory or General Relativity is the fact that it provides us for the first time with the tools necessary to describe, in a rigorous scientific way, the universe we live in. In this section we will introduce and briefly discuss the so-called Standard Cosmological Model and its key features.

It is easy to regard at the universe as the most heterogeneous system one could think of. We know for example that a galaxy disk is very different from the cold and desolate interstellar space, or that the center of the Milky Way bears little resemblance to our solar system. On small scales, in fact, this heterogeneity is certainly true. However, things are not the same when the scales in play are as big as hundreds of mega-parsec, or even bigger. Different observational results suggest that the universe is indeed rather uniform at this macro-scales. The most known observation that encourages this hypothesis is the 3K cosmic background radiation, i.e. the cosmic leftover from the Big Bang. This radiation that permeates our entire observable universe, although not perfectly smooth, presents deviations from regularity that are on the order of 10^{-5}, or less.

The hypothesis of a uniform universe, also known as *Cosmological Principle*, is mathematically described by the notions of *homogeneity* and *isotropy*. An homogeneous space is characterized by the fact that its metric is the same throughout the manifold. Isotropy, instead, refers to some specific point in the manifolds and states that in that point the space looks the same no matter in what direction we look. One must notice that *a priori* there is no relationship between homogeneity and isotropy. That's to say that a

manifold can be homogeneous but nowhere isotropic, or it can be isotropic around one of its points without being homogeneous. Nevertheless, if the manifold is isotropic around one point and also homogeneous, then it must be isotropic around all of its points. In the same way, if the manifold is isotropic around all its points, then it must also be homogeneous. In our case, observations strongly suggest that the universe around the Earth is isotropic. On the other side, if we accept that we are not at the center of the universe, we have to assume also that at any other point in the space the universe would appear isotropic as it appears to us. The space would than be isotropic everywhere, and thus homogeneous. We remark however that this characteristics apply only to space, and not to spacetime as a whole.
The spacetime of a universe that is homogeneous and isotropic in space, but evolving in time, can be described through a manifold like $\mathbf{R}\times\Sigma$. $\mathbf{R}$ denotes here the time direction, while Σ describes a three-dimensional space-like slide into which the universe can be foliated. The metric of this spacetime is then described in the **comoving coordinates** by

$$\begin{aligned} ds^2 &= -dt^2 + R(t)\, d\sigma^2, \\ d\sigma^2 &= \gamma_{ij}(x)\, dx^i dx^j \end{aligned} \tag{1.76}$$

where t represents the cosmic time, $R(t)$ is the scale factor and $d\sigma^2$ is the three-dimensional metric defined on Σ. It is worth to notice that because of the particular coordinates we have chosen, the coefficient in front of dt^2 doesn't depend on the x^i and the metric doesn't present any cross terms $dtdx^i$.
It is useful to think of homogeneity and isotropy in terms of symmetries. One can in fact think of homogeneity as invariance of the space under translations, while isotropy represents the invariance under rotations. This means that $d\sigma^2$ cannot be any metric, but it needs to satisfies these symmetries. A metric that does so has the form

$$\begin{aligned} d\sigma^2 &= \frac{dr^2}{1-kr^2} + r^2 d\Omega^2, \\ d\Omega^2 &= d\theta^2 + \sin^2\theta d\phi^2, \end{aligned} \tag{1.77}$$

where k is related to the three-dimensional Ricci scalar by the equation

$$k = R_{(3)}/6, \tag{1.78}$$

end, therefore, encodes the information on the curvature of Σ. The overall metric on the spacetime becomes therefore

$$ds^2 = -dt^2 + R(t)\left[\frac{dr^2}{1-kr^2} + r^2 d\Omega^2\right], \tag{1.79}$$

also known as **Freidmann-Robertson-Walker metric**, or FRW metric. In the usual parameterization, it is common to absorb the physical size of the manifold into the scale factor $R(t)$ in order to normalize the parameter k which therefore can take the values

$$k \in \{-1, 0, +1\}. \tag{1.80}$$

Such parameterization is possible as the Freidmann-Robertson-Walker metric is invariant under the transformation

$$\begin{aligned} R &\to \lambda^{-1} R', \\ r &\to \lambda r', \\ k &\to \lambda^{-2} k'. \end{aligned} \tag{1.81}$$

As k encodes the curvature information, for different values of the parameter our three-dimensional manifold will assume different geometries. To better understand the nature and the shape assumed by the manifold, it is useful to introduce the new radial coordinate defined by

$$d\mu = \frac{dr}{\sqrt{1 - kr^2}}, \tag{1.82}$$

that can be integrated to obtain

$$r = F_k(\mu). \tag{1.83}$$

One can see now that if $k = -1$, the metric on Σ becomes

$$d\sigma^2 = d\mu^2 + (\sinh \mu)^2 \, d\Omega^2. \tag{1.84}$$

This metric describes a three-dimensional hyperboloide of constant negative curvature. It is also referred in the literature as **open** space, as globally the space described by this metric could extend forever.
For $k = 0$ one obtains

$$\begin{aligned} d\sigma^2 &= d\mu^2 + \mu^2 d\Omega^2 \\ &= dx^2 + dy^2 + dz^2. \end{aligned} \tag{1.85}$$

This metric denotes a three-dimensional **flat** manifold, i.e. the flat Euclidean space.
Finally, for $k = +1$, we have

$$d\sigma^2 = d\mu^2 + (\sin \mu)^2 \, d\Omega^2, \tag{1.86}$$

that is the metric of a three-sphere. In this case, the space one is considering is **closed** and characterized by a positive curvature.

Now that we know what kind of metric we need to describe our homogeneous and isotropic universe, we can use the Einstein's equations to determine how this metric will evolve. In order to do this, it is common in literature to redefine $R\left(t\right)$ in order to have the dimensionless scale factor

$$a\left(t\right)=\frac{R\left(t\right)}{R_0}. \tag{1.87}$$

According to transformation (1.81) the radial coordinate and the curvature parameter become

$$\begin{aligned} r &= R_0 r', \\ k &= \frac{k'}{R_0^2}. \end{aligned} \tag{1.88}$$

One can see how in this different parameterization the radial curvature acquire the dimension of a distance while the curvature parameter has the dimension of a distance^{-2}. The FRW metric then reads

$$ds^2=-dt^2+a\left(t\right)\left[\frac{dr^2}{1-kr^2}+r^2d\Omega^2\right] \tag{1.89}$$

The next step now is to derive the dynamic of the scale factor $a\left(t\right)$ through the Einstein's equations. In order to do so, we need to characterize the matter content of the universe. Following the literature, we choose to model the matter and energy content of our universe by a perfect fluid that is at rest in the comoving coordinates. We obtain therefore

$$T_{\mu\nu}=\left(c^2\rho+p\right)U_\mu U_\nu+pg_{\mu\nu}, \tag{1.90}$$

where $T_{\mu\nu}$ represents the energy-momentum tensor while $U^\mu=(1,0,0,0)$ denotes the fluid four-velocity. However, we are not done yet. As we will see, we also need to characterize the relationship between the fluid energy density ρ and its pressure p. It is the common in cosmology to consider the simple *equation of state*

$$p=\omega\rho, \tag{1.91}$$

where ω is a constant independent of time.

If now one plugs eq. (1.90) and eq. (1.91) into the zero component of the conservation of energy equation $\nabla_\mu T^\mu_0=0$, one gets

$$\frac{\dot{\rho}}{\rho}=-3\left(1+\omega\right)\frac{\dot{a}}{a}, \tag{1.92}$$

that one can then integrate to obtain

$$\rho \propto a^{-3(1+\omega)}. \tag{1.93}$$

A priori, the cosmological fluid is made up of different contributions and therefore studying its dynamic is not trivial. Nevertheless, is educational to analyze its asymptotic behavior when one of its components dominates all the others.

Ordinary stars and galaxies, and in general any set of collisionless nonrelativistic particles, represent the **matter** component of the cosmological fluid. The peculiarity of this component is that its pressure is negligible in comparison with its energy density and thus, it can be considered equal to zero

$$p_M = 0. \tag{1.94}$$

This is the reason why it is often referred to as *dust*. As we will see, the dark matter model considered in this work possesses this property. In a universe where the *matter* component is the dominating one, the energy density evolves as the inverse of the cube of the scale factor

$$\rho_M \propto a^{-3}. \tag{1.95}$$

In this scenario, in fact, the most important contribution to the energy density comes from the rest energy, that in turns is proportional to the number density. As the universe gets bigger (smaller) the number density will of course decrease (increase) at a rate that is proportional to the cube of the scale factor a. The overall energy density of the fluid will therefore do the same.

The second key component is the **radiation**, which is characterized by the equation of state

$$p_R = \frac{1}{3}c^2\rho_R. \tag{1.96}$$

With radiation we intend not just the actual electromagnetic radiation, but also massive particles which moves at speeds very close to the speed of light. Those particles, as far as their equation of states is concerned, becomes in fact indistinguishable from photons. When the evolution of the cosmological fluid is driven by this *radiation*, the dynamics of its energy density is given by

$$\rho_R \propto a^{-4}. \tag{1.97}$$

If on one side, in fact, the number density of photons and relativistic particles decreases at the same rate of the number density of the nonrelativistic

particles, on the other side the former also lose energy because of redshift at a rate of a^{-1}. We think that today the matter energy density is around three orders of magnitude bigger that the radiation energy density. However, as the two densities evolves differently, this means that in the past, when the universe was much smaller, the radiation energy density was the dominant one.
Finally, one can think of the vacuum energy also as a perfect fluid characterize by the equation of state

$$p_\Lambda = -c^2 \rho_\Lambda. \tag{1.98}$$

It would therefore represent a third component for the cosmological fluid whose energy density would be unaffected by the expansion(contraction) of our universe

$$\rho_\Lambda \propto a^0. \tag{1.99}$$

Therefore, in an expanding universe such it is the one we are living in, if there is a nonzero vacuum energy, it will eventually dominate the other two components in the long run.

In general however, the evolution of the cosmological energy density, as well as the dynamic of the scale factor $a\left(t\right)$, is derived through the Einstein's equations

$$R_{\mu\nu} - \Lambda g_{\mu\nu} = \frac{8\pi G}{c^4}\left(T_{\mu\nu} - \frac{1}{2}g_{\mu\nu}T\right), \tag{1.100}$$

where Λ is the so-called *Cosmological constant.*
From the Friedmann-Robertson-Walker metric (1.89) the nonzero components of the Ricci tensor can be evaluated obtaining

$$\begin{aligned}
R_{00} &= -3\frac{\ddot{a}}{a}, \\
R_{11} &= \frac{a\ddot{a} + 2\dot{a}^2 + 2k}{1 - kr^2}, \\
R_{22} &= r^2\left(a\ddot{a} + 2\dot{a}^2 + 2k\right), \\
R_{33} &= r^2\left(a\ddot{a} + 2\dot{a}^2 + 2k\right)\sin^2\theta.
\end{aligned} \tag{1.101}$$

Plugging eq. (1.101) and eq. (1.90) into the Einstein's equations, one gets

$$\left(\frac{\dot{a}}{a}\right)^2 = \frac{8\pi G}{3}\rho - \frac{kc^2}{a^2} + \frac{1}{3}\Lambda c^2, \tag{1.102}$$

and

$$\frac{\ddot{a}}{a} = -\frac{4\pi G}{3}\left(\rho + \frac{3p}{c^2}\right) + \frac{1}{3}\Lambda c^2. \tag{1.103}$$

These are known as the **Friedmann equations** and define the evolution of the Friedmann-Robertson-Walker metric once the content of our universe and its geometrical features are given.

The factor

$$H \equiv \frac{\dot{a}}{a} \tag{1.104}$$

is referred to as the *Hubble parameter* and is usually used to describe the rate of the expansion of the universe. Observations suggest that its current value - often referred to as the *Hubble constant* H_0 - should be around $70 \pm 10 km/sec/Mpc$. Since there is still some uncertainty on its exact value, it is often parametrized as follows

$$H_0 = 100h\ km/sec/Mpc, \tag{1.105}$$

where all the uncertainties are condensed into the parameter h. The Hubble constant, among other things, allow us to set a "standard" cosmological time given by

$$\begin{aligned} t_H &= H_0^{-1} \\ &= 3.09 \times 10^{17} h^{-1} sec, \end{aligned} \tag{1.106}$$

as well as a standard cosmological length

$$\begin{aligned} d_H &= H_0^{-1} c \\ &= 9.25 \times 10^{25} h^{-1} m. \end{aligned} \tag{1.107}$$

This is extremely useful to evaluate which phenomena are important at cosmological scales, and which instead can be neglected.

Current observations suggest that Hubble parameter is actually increasing. That is to say that, not only our universe is expanding, but that the rate at which it is growing is getting bigger and bigger. Such acceleration can be explained by the cosmological constant that would represent an intrinsic curvature of the space-time geometry of our universe. An other option could be to assume instead the presence of a vacuum energy component in the cosmological fluid. Such component, in the literature, is referred to as **dark energy**. In a universe where this component has the same order of magnitude of the matter component, the second Friedmann equation (1.103) reads

$$\frac{\ddot{a}}{a} = -\frac{4\pi G}{3}\left(\rho_M - \frac{2p_\Lambda}{c^2}\right), \tag{1.108}$$

where we have defined

$$\rho_\Lambda = \frac{\Lambda c^2}{8\pi G}, \qquad p_\Lambda = -\frac{\Lambda c^4}{8\pi G}. \tag{1.109}$$

We see then that, if p_Λ is big enough, the r.h.s. of the equation will assume positive values leading to an accelerated expansion. It proves useful at this point to introduce the concepts of **critical density** and **density parameter**. The former is defined as follows

$$\rho_{crit} = \frac{3H^2}{8\pi G}, \tag{1.110}$$

whereas the latter is simply given by the ratio

$$\Omega = \frac{\rho}{\rho_{crit}}. \tag{1.111}$$

Equation (1.102) can be recast in the form

$$\Omega - 1 = \frac{kc^2}{H^2 a^2}, \tag{1.112}$$

where the density parameter encodes all type of contribution, i.e. $\Omega = \Omega_M + \Omega_R + \Omega_\Lambda$. We see that the sign of k, and thus the spacial geometry of the universe, is determined by whether Ω is greater than, equal to, or less than one. The critical density defines therefore the value of energy density one needs to have a flat space. If $\rho > \rho_{crit}$, we will have a closed space, while if $\rho < \rho_{crit}$ we will have an open one. Recent observations seems to imply that the universe we live in is spatially flat, i.e. $\Omega \sim 1$. Moreover, the biggest contributions to the density parameter Ω, nowadays, seems to come from its matter and vacuum components. One has, respectively

$$(\Omega_M)_0 \sim 0.3 \qquad (\Omega_\Lambda)_0 \sim 0.7 \tag{1.113}$$

It seems likely in fact that the radiation density, although dominant in the very early stages of our universe, is significantly lower than the other two in the present epoch.

It is worth to look more into the matter contribution to the density parameter. We said that it represents roughly the 30% of the total energy density present in our universe, but we still haven't specified what its constituents are. As we know, it must be made up of nonrelativistic particles. However we have no guarantees that those particles are the same one that we find in the so-called **ordinary matter**, i.e. everything that is made from atoms and their constituents. Generally speaking, the rest mass - and thus the energy density - associated with ordinary matter comes mostly from baryons. Electrons in fact are characterized by masses around thousand times lighter than the one ascribed to protons and neutrons. It turns out, however, that the standard baryonic mass isn't enough to account by itself for the observed density. As we briefly discuss in chapter 3, recently estimations based on the cosmic microwave background seem to favor a remarkably small value for the baryon density

$$\begin{aligned} & \omega_b = \Omega_b h^2 \simeq 0.02 \\ \Longrightarrow \; & \Omega_b \simeq 0.04. \end{aligned} \tag{1.114}$$

There must be therefore some kind of nonbaryonic matter able to account for this significant discrepancy. To distinguish nonbaryonic matter from ordinary matter, the former is usually referred to as **dark matter**. In chapter 3 we discuss the evidences that support the existence of such exotic matter, as well as some of the most known dark matter candidates.

As we have seen, even if the the Cosmological Standard Model seems to be well in accordance with most of the observational data, it does also rise a lot of open questions.

The nature of dark matter and dark energy are for example one of those. Although it is possible that the latter is connected with the so-called cosmological constant Λ, one still needs to justify its presence in the Einstein's equations and why its contribution to the total energy density of the cosmological fluid is, in our epoch, precisely of the same order of magnitude of the energy density derived from the matter contribution. If we go back to eq. (1.99) and eq. (1.95) we see how the ratio between the two energy densities evolves as

$$\frac{\rho_\Lambda}{\rho_M} \propto a^3. \tag{1.115}$$

This means that in a universe that expands, or contracts, it is extremely unlikely for this ratio to be of the order of unity as it seems to be nowadays. Although the *anthropic principle* could answer this paradox, it isn't seen by the scientific community as a satisfying solution.

Beside this, the Cosmological Standard Model seems to present also some fine-tuning issues. They are usually referred to as the *flatness problem* and the *horizon problem.* Without going to much into details, *flatness problem* is related to the fact that $\Omega = 1$ is an “unstable point”, i.e. any deviation from this values - even the smallest one - will grow with time. Therefore, the only way for our universe to be flat in the current epoch is to assume that at its early stages it was even “flatter”. That’s to say that one has to fine tone the initial value of Ω so that

$$\Omega_I - 1 \ll 1. \tag{1.116}$$

Such strong assumption would require a well motivated theoretical support that is lacking in the standard gravitational theory.

On the other side, the *horizon problem* derives from the fact that there is only a finite distance that photons can have traveled within the age of the universe. One of the implications that derives from this is that points of the universe that are far away enough from each other cannot be in casual contact. That means that whatever happens in one of the two points, it cannot affect (or be affected by) what happens in the other point. It becomes therefore extremely difficult to justify the degree of homogeneity that we measure in the Cosmic Microwave Background.

The common paradigm, accepted by scientists in order to address this problems, hypothesizes an era in the very early universe of extremely fast expansion. This era is also referred to as the **Inflation** era. One way to obtain this inflationary phase is to consider the presence of a scalar filed whose energy density would be the engine powering this exponential-like expansion. We will not discuss this subject in this document, as it is out of the scope of our work. Nevertheless we wanted to point out how, even at cosmological level, the theory of general relativity seems to require some tweaks to fit the observational data we now have at our disposal.

1.3 Extended theories of General Relativity

While the success of the General Relativity is undisputed, this theory also exhibits a series of inconsistencies and shortcomings that have led physicists to wonder if the gravitational theory developed by Einstein is indeed the definitive theory one must use to explain the gravitational interaction and the phenomena that derive from it.

From a theoretical point of view, one of the key issue with the General Relativity is represented by its *classical* frame which isn’t suited to be easily quantized. This prevent us from deal with gravitation in the same way we deal with other fundamental interactions creating a serious obstacle to a general unification. One of the reason why General Relativity is so hard to quantized is that the gravitational field one would like to quantized is coupled to itself. The non-linearity that derives from this feature seems to be in direct contradiction with the superposition principle that is one of the main tenet of quantum theory. Beside this, one also needs to take into account that General Relativity assumes a classical description of matter that we know cannot be valid at the atomic and subatomic scales that dominates the primordial universe.

From an observational point of view, on the other side, Einstein's theory of gravity is affected by several shortcomings both at cosmological and galactic scale. One just needs to think about the Standard Cosmological Model paradoxes such as the *flatness problem* and the *horizon problem*, or the *missing mass problem* that mostly concerns galactic scales and will be discussed more in detail later in this manuscript.

One way to address these problems is to assume that the interaction between the geometry of the spacetime with the quantum fields generates some back-reaction that modify the gravitational Lagrangian. With *Extended theories of gravitation* one usually referrers to all those theories in which the effective Lagrangian presents higher-order terms of the curvature invariants, e.g. R^2 or $R^{\mu\nu}R_{\mu\nu}$, or terms with *nonminimal* coupled scalar fields, e.g $\phi^2 R$.

1.3.1 Scalar-Tensor Theories

The theory of General Relativity is also referred to as a tensor theory as its main actor is the metric tensor $g_{\mu\nu}$. By analogy, one can guess that in the scalar-tensor theories there will be two main actors: the metric tensor and a scalar field. It must be stressed that the additional scalar field is not simply added on top of the general relativity, instead it enters into the structure of the theory in a nontrivial manner through a *nonminimal* coupling term.

One of the strongest theoretical motivation behind the development of scalar tensor theories lies in the wish to recover the Mach's Principle. George Berkeley followed by Ernst Mach - from which the principle takes the name - reinterpreted the Newton's rotating bucket argument arguing that the empty space of the Newtonian mechanics is not empty at all. It is in fact filled with enormous quantities of matter. The Mach's principle states therefore that the inertial forces experienced by a body in nonuniform motion are determined by the quantity and distribution of matter in the universe. Historically, Einstein himself was inspired by this idea that was suggestive of a connection between geometry and matter. The way in which scalar-tensor theories recover the Mach's principle is by "promoting" the gravitational constant G to a function of a scalar field φ. It turns out, as we will see, that the source of the scalar field is the matter distribution in the considered system (e.g. the universe) [32]. It follows therefore that the gravitational parameter G, and thus the inertial forces as well, depends now on the geometrical distribution of the matter present in the system. Moreover, the fact that G is no more a constant, but rather a function able to vary in time and space following the variation of the scalar field itself, also plays well into the Dirac's large numbers hypothesis [52]. This hypothesis tries to address a set of large number "coincidences" that gained the attentions of others theorists in his time. According to Dirac's hypothesis, what would appears as a coincidence could be explained, at physical level, if one assumes that the physical constants are actually not constants and that their values depend on the age of the Universe. We conclude remarking that, from a cosmological and galactic observational point of view, scalar-tensor theories are also very interesting. On one side, in fact, they can give rise to the inflationary scenarios often invoked to address several problems of the Cosmological Standard Model. On the other side, they are also able to provide very appealing dark matter models as we will see in the following chapters of this document.

1.3.2 The prototype Brans-Dicke model

One of the first pioneers of the scalar-tensor theories was P. Jordan, who started to embed a four-dimensional curved manifold in a five-dimensional flat spacetime. He demonstrated that a constraint in formulating projective geometry can be a four-dimensional scalar field which in turns allows us to describe a spacetime-dependent gravitational constant in accordance with the Mach' principle and the Dirac's hypothesis.

In the last decades, numerous scalar-tensor theories have been developed. Discussing all of them would be lengthy and out of the scope of this study. Nevertheless, we find that could be useful to briefly review at least the one among them that is considered in the literature as the prototype of a scalar-tensor theory: the Brans-Dicke model.

We start with the fundamental Lagrangian

$$\mathcal{L}_{BD} = \frac{1}{\chi}\sqrt{-g}\left(\varphi R - \omega\frac{1}{\varphi}g^{\mu\nu}\partial_\mu\varphi\partial_\nu\varphi\right) + L_{matter}\left(\Psi\right), \tag{1.117}$$

where φ is the Brans-Dicke (BD) scalar field, ω is a constant, Ψ represents the matter fields and $\chi = 8\pi G/c^4$. Here, as we will see below, G is a constant which is not the constant of Newton that is measured with Cavendish type experiments. It is worth to remark that, in this prototype model, the matter Lagrangian L_{matter} is assumed to be independent from the scalar field φ such that the theory satisfies the weak equivalence principle [131]. As we

will see, this assumption will be relaxed in the main part of the manuscript. Moreover, the scalar field itself doesn't have a mass term as usually happens in more sophisticated scalar-tensor models as the one we will consider.
Let us now focus our attention on the two terms the scalar field figures in. The second one

$$-\omega\frac{1}{\varphi}g^{\mu\nu}\partial_\mu\varphi\partial_\nu\varphi, \tag{1.118}$$

is the minimal coupling term as it can be obtained via the "comma-to-semicolon rule" from

$$-\omega\frac{1}{\varphi}\eta^{\mu\nu}\partial_\mu\varphi\partial_\nu\varphi. \tag{1.119}$$

The "comma-to-semicolon rule" is the substitution rule[1]

$$\eta_{\mu\nu}\to g_{\mu\nu}, \qquad \partial_\mu\to\nabla_\mu. \tag{1.120}$$

On the other hand, there is no way to recover the first term applying the "comma-to-semicolon rule". It is this term indeed that encodes the nonminimal coupling. The reason why this is important is because the two terms behaves in two totally different ways in the local inertial frame: one reduces to a simplified version of itself, the other vanish completely. It is also worth to notice that the nonminimal coupling term replaces the standard term of the Hilbert-Einstein action

$$\frac{1}{\chi}\sqrt{-g}R. \tag{1.121}$$

One could think of it as if we replaced the standard constant by an effective one that depends on the scalar field background's value.

$$\frac{1}{\chi_{eff}}=\frac{c^4\varphi}{8\pi G}=\frac{c^4}{8\pi G_{eff}}. \tag{1.122}$$

This also plays along the assumption suggested by Dirac that the gravitational constant should not be an invariable quantity, but rather something determined by the status of the gravitational system. Nevertheless, it must be pointed out that also G_{eff} is still not the Newton constant one would measure from Cavendish type experiments, as it doesn't take into account the contribution to the Newton constant coming from the scalar field kinetic term. See below.
As one has done for the Einstein's theory, the Brans-Dicke field equations

---

[1] in eq. (1.118) we took advantage of the fact that the standard derivative and the covariant derivative of a scalar field coincide

can be recovered via the variation of the action

$$S_{BD} = \int \sqrt{-g}\mathcal{L}_{BD} d^n x. \tag{1.123}$$

However, since this time the independent fields are two, the metric tensor field $g_{\mu\nu}$ and the scalar field φ, we shall consider two variations of the action. The first one, is the one we take with respect of the metric tensor and can be calculated in a similar fashion to what done in the previous section. For this reason we will give here directly the result

$$\varphi G_{\mu\nu} + g_{\mu\nu}\Box\varphi - \nabla_\mu\nabla_\nu\varphi = \chi T_{\mu\nu} + \frac{\omega}{\varphi}\left(\nabla_\mu\varphi\nabla_\nu\varphi - \frac{1}{2}g_{\mu\nu}\nabla_\sigma\varphi\nabla^\sigma\varphi\right), \tag{1.124}$$

where $\Box$ is a covariant d'Alembert operator defined by

$$\Box\varphi = \frac{1}{\sqrt{-g}}\partial_\mu\left(\sqrt{-g}g^{\mu\nu}\partial_\nu\varphi\right). \tag{1.125}$$

Let us now consider the variation with respect to the scalar field φ

$$\delta\mathcal{L}_{BD} = R\delta\varphi + \frac{\omega}{\varphi^2}\nabla_\sigma\varphi\nabla^\sigma\varphi\delta\varphi - \frac{2\omega}{\varphi}\nabla^\sigma\delta\nabla_\sigma\varphi. \tag{1.126}$$

After integrating by parts, it can be set equal to the Klein-Gordon equation

$$\varphi R - \omega\frac{\nabla^\sigma\varphi\nabla_\sigma\varphi}{\varphi} + 2\omega\Box\varphi = 0 \tag{1.127}$$

plus a pure divergence term that vanishes when integrated over the invariant volume. If now one confronts the Klein-Gordon equation with the trace of eq. (1.124)

$$-R\varphi + 3\Box\varphi = \chi T - \omega\frac{\nabla_\sigma\varphi\nabla^\sigma\varphi}{\varphi}, \tag{1.128}$$

we finally obtain

$$\Box\varphi = \frac{\chi}{2\omega + 3}T. \tag{1.129}$$

Equation (1.129) shows that the source of the scalar field is indeed the matter distribution. Although such result could seem counterintuitive at first as $\mathcal{L}_{matter}$ does not depend on φ, the reason why it is possible lies exactly in the presence of the nonminimal coupling term. Moreover from eq. (1.129) one can also see that in the limit $\omega \to \infty$ the coupling between matter and scalar field vanishes and the theory tends to the standard General Relativity. The absence of a direct coupling between matter and scalar field at the Lagrangian level does has also another important consequence, that is to preserve the covariant conservation law of matter

$$\nabla_\mu T^{\mu\nu} = 0. \tag{1.130}$$

This can be shown by evaluating the covariant derivative ∇_μ of the controvariant form of eq. (1.124). The preservation of eq. (1.130) implies that the world lines of point mass particles are geodesic of the space-time. The weak equivalence principle therefore isn't violated.

If one makes a post-Newtonian development of the theory [131], the effective gravitational constant that appears in the time-time component of the metric is

$$G_N = \frac{2\omega + 4}{2\omega + 3}\frac{G}{\phi_0}, \tag{1.131}$$

where ϕ_0 is the background value of the scalar field in the solar system (see eq. (38) in [131]). This G_N is the actual value of the measured constant of Newton in Cavendish-like experiments. As one can see, it is indeed inversely proportional to the value of the background ϕ, which may evolve with time on a cosmological time scale. However, it also depends on the parameter ω that appears in the kinetic term of the scalar filed.

In the last decades, several experiments have been performed to constraint the values of the free parameter ω. One of the most stringent one comes from measuring the shift in frequency of a radio signal sent from, and to, the Cassini spacecraft while close to conjunction with the Sun [30]. The results of this test suggest that $\omega > 4 \times 10^4$ at the 2σ-level. Although such an high values could seem to be difficult to justify from a theoretical point of view, is not impossible. In they work [45], T. Damour and K. Nordtvedt show that scalar-tensor theories generically contain a natural attractor mechanism which drives them toward the standard theory of General Relativity. The fact that, nowadays, the parameter ω is so high could therefore be justified by this mechanism. In any case it is worth to remind that, as a prototype, one does not expect the Brans-Dicke model to represent the definitive theory of gravitation. To conclude this subsection, we want to underline that when the scalar-field actually possesses a mass term - as we assume in our study - the observational constraints are weakened with respect to the massless case. See for example [134] and the discussion therein.

1.3.3 Connection with String Theory

Now that we have seen the very basic mechanisms of scalar-tensor theories through the example of the Brans-Dicke model, we would like to conclude this section, and chapter, briefly discussing another of the reason why this branch of gravitational theories is so appealing. That is the fact that scalar fields seem to natural appear in the context of unification theories such as the *string theory*. This is also the case for theories with additional[2], compactified, dimensions. Not by chance the Kaluza-Klein theory was of great inspiration for Jordan as we have already mentioned. Let us take for example the string theory. It has been proved that in the low-energy limit, a closed string has a zero mode that can be described by a symmetric tensor behaving the same way as the metric tensor. In this context, the graviton has as companion a scalar field Φ. Without going to much into the details, it can be shown that the field equations at tree level of these zero-mode fields are described by

$$\begin{aligned}
&R_{\bar{\mu}\bar{\nu}} = -2\nabla_{\bar{\mu}}\nabla_{\bar{\nu}}\Phi + \frac{1}{4}H_{\bar{\mu}\bar{\rho}\bar{\sigma}}H_{\bar{\nu}}^{\bar{\rho}\bar{\sigma}} \\
&\nabla_{\bar{\lambda}}H^{\bar{\lambda}\bar{\mu}\bar{\nu}} - 2\left(\partial_{\bar{\lambda}}\Phi\right)H^{\bar{\lambda}\bar{\mu}\bar{\nu}} = 0 \\
&R = 4\left(\Box\Phi + (\partial\Phi)^2\right) + \frac{1}{12}\left(HH\right),
\end{aligned} \tag{1.132}$$

where the totally antisymmetric field strength is defined through

$$H_{\bar{\mu}\bar{\nu}\bar{\lambda}} = \partial_{\bar{\mu}}B_{\bar{\nu}\bar{\lambda}} + \textsf{cyclic permutations}, \tag{1.133}$$

and $B_{\bar{\mu}\bar{\nu}}$ is itself an antisymmetric second-rank tensor field. It turns out that the same field equations can be obtained from the following Lagrangian [58]

$$\mathcal{L}_{str} = \sqrt{-g}e^{-2\Phi}\left(\frac{1}{2}R + 2g^{\bar{\mu}\bar{\nu}}\partial_{\bar{\mu}}\Phi\partial_{\bar{\nu}}\Phi - \frac{1}{2}H_{\bar{\mu}\bar{\nu}\bar{\lambda}}H^{\bar{\mu}\bar{\nu}\bar{\lambda}}\right). \tag{1.134}$$

The non-perturbative version of the field equations (1.132) are not known in either string or superstring theories, and so is not the corresponding effective Lagrangian. However, Damour and Polyakov [43] argued that it should take the following generic form (here directly written in 4 dimensions)

$$\begin{aligned}
S = \int d^4x\sqrt{\hat{g}}\Bigg\{&\frac{B_g\left(\Phi\right)}{\alpha'}\hat{R} + \frac{B_\Phi\left(\Phi\right)}{\alpha'}\left[4\hat{\Box}\Phi - 4\left(\hat{\nabla}\Phi\right)^2\right] \\
&-B_F\left(\Phi\right)\frac{k}{4}\hat{F}^2 - B_\psi\left(\Phi\right)\bar{\hat{\psi}}\hat{D}\hat{\psi} + ...\Bigg\},
\end{aligned} \tag{1.135}$$

where $\hat{g}_{\mu\nu}$ represents the metric appearing in the σ-model formulation of string theory and is employed to define all the covariant constructs present

---

[2] here with "additional" we mean any dimension beyond the fourth

in the previous equation ($\hat{\nabla}$, $\hat{R}$, $\hat{D}$, ...). The dilaton is denoted here by Φ whereas $\hat{F}$ and $\bar{\hat{\psi}}\hat{D}\hat{\psi}$ describe the electromagnetic and the fermionic sectors. The functions $B_i\left(\Phi\right)$ with $i = g, \Phi, F, \psi$ describe how the dilaton couples with each sector.

One could now think to perform a conformal transformation of the metric with a rescaling of the scalar field in order to recast the action into a the more standard form where the coefficient in front of the gravity factor $\hat{R}$ is equals to one and the second term of eq. (1.135) reduces to the standard scalar field kinetic term. In technical terms, one has sent the action from the string frame to the Einstein frame [121].

In this frame, if one assumes that the dilaton field Φ does not vary too much, we can expand the coupling functions $B_i\left(\Phi\right)$ around some background values B_{i_0} as follows

$$B_i\left(\Phi\right) \simeq B_{i_0} + d_i\Phi, \tag{1.136}$$

where $d_i = \partial B_i/\partial\Phi$. As mentioned in [43], it is generally expected that a non-perturbative effect should also lead to give an effective potential to the dilaton (or moduli) field(s). Hence, the more general low energy effective action expected from superstring theory is something like eq. (1.135), but with an additional potential. In this way one would recover something extremely similar to the scalar-tensor action we consider in our study, see equations (3.32-3.34).

The fact that scalar fields naturally appear in unification theories like the string theory has certainly contributed to the growth of interest in scalar-tensor theories. However, if they reached the success they had, it is also because of they ability to tackle some of the well-known limit of the general relativity. In the last chapter of this manuscript we will see, in fact, how dark matter can be modeled by an ultra-light scalar field coupled with the Lagrangian matter and how the presence of such scalar field could be detected thanks to gravitational waves antenna. As we still don't know what dark matter is, such model is relevant in its own right and doesn't necessarily needs to be motivated by some unification theory. Nevertheless, we found worth to at least point out that it could indeed be the case, as massless or light scalar fields with a coupling to matter are generically expected from string and superstring theories.

Chapter 2

Gravitational Waves

2.1 Linearized Gravity and Gravitational Waves

Linearized gravity is an approximation of the general theory in which the gravitational field is assumed to be weak, but not static. This ability to vary with time, together with the absence of any restriction on the motion of the test particles, in turn allows to discuss phenomena such as gravitational radiation and light deflection that are out of the domain of some more restrictive approximation, such as the well-known Newtonian approximation. The weakness of the gravitational field can be expressed in mathematical terms by stating that it exists at least one coordinate frame in which the total metric $g_{\mu\nu}$ can be decomposed into the the Minkowski metric plus a small perturbation

$$g_{\mu\nu} = \eta_{\mu\nu} + h_{\mu\nu}, \qquad |h_{\mu\nu}| \ll 1. \tag{2.1}$$

We will assume that in such a frame the flat Minkowski metric takes its canonical form

$$\eta_{\mu\nu} = diag\,(-1, +1, +1, +1)\,. \tag{2.2}$$

As a consequence of the condition we required for the perturbation, one is allowed to neglect anything that is higher than the first order in $h_{\mu\nu}$. It follows then that the inverse metric $g^{\mu\nu}$ has the form

$$g^{\mu\nu} = \eta^{\mu\nu} - h^{\mu\nu}. \tag{2.3}$$

One can actually think of the linearized gravity as a theory which is described by the symmetric tensor $h_{\mu\nu}$ and its evolution in the flat spacetime. In order to recover the field equations for the perturbation we first start writing down the Christoffel symbols

$$\begin{aligned}\Gamma^{\sigma}_{\mu\nu} &= \frac{1}{2}g^{\sigma\rho}\left(\partial_\mu g_{\nu\rho} + \partial_\nu g_{\mu\rho} - \partial_\rho g_{\mu\nu}\right) \\ &= \frac{1}{2}\eta^{\sigma\rho}\left(\partial_\mu h_{\nu\rho} + \partial_\nu h_{\mu\rho} - \partial_\rho h_{\mu\nu}\right).\end{aligned} \tag{2.4}$$

We can now pass to the Riemann tensor. Here one can notice that since the Christoffel symbols are already of the same order of magnitude of the perturbation, the terms in the Riemann tensor in which they multiply each others can be ignored.

$$\begin{aligned}R_{\mu\nu\rho\sigma} &= \eta_{\mu\nu}\partial_\rho\Gamma^{\lambda}_{\nu\rho} - \eta_{\mu\lambda}\Gamma^{\lambda}_{\nu\rho} \\ &= \frac{1}{2}\left(\partial_\rho\partial_\nu h_{\mu\sigma} + \partial_\sigma\partial_\mu h_{\nu\rho} - \partial_\sigma\partial_\nu h_{\mu\rho} - \partial_\rho\partial_\mu h_{\nu\sigma}\right).\end{aligned} \tag{2.5}$$

The Ricci tensor is obtained by contracting over the indexes μ and ρ

$$R_{\mu\nu} = \frac{1}{2}\left(\partial_\sigma\partial_\nu h^{\sigma}_{\mu} + \partial_\sigma\partial_\mu h^{\sigma}_{\nu} - \partial_\mu\partial_\nu h - \Box h_{\mu\nu}\right), \tag{2.6}$$

where $\Box$ is the D'Alembertian in the flat space

$$\Box = -\partial_t^2 + \partial_x^2 + \partial_y^2 + \partial_z^2, \tag{2.7}$$

and the trace of the perturbation h is defined as follows

$$h = \eta^{\mu\nu}h_{\mu\nu} = h^{\mu}_{\mu}. \tag{2.8}$$

Contracting the two indexes we are left with gives the Ricci scalar

$$R = \partial_\mu\partial_\nu h^{\mu\nu} - \Box h. \tag{2.9}$$

Finally combining eq. (2.6) and eq. (2.9) one obtains the Einstein tensor

$$\begin{aligned}G_{\mu\nu} &= R_{\mu\nu} - \frac{1}{2}R = \\ &= \frac{1}{2}\left(\partial_\sigma\partial_\nu h^{\sigma}_{\mu} + \partial_\sigma\partial_\mu h^{\sigma}_{\nu} - \partial_\mu\partial_\nu h - \Box h_{\mu\nu} - \eta_{\mu\nu}\partial_\rho\partial_\sigma h^{\rho\sigma} + \eta_{\mu\nu}\Box h\right).\end{aligned} \tag{2.10}$$

The field equations describing the dynamic of the perturbation field $h_{\mu\nu}$ are then

$$G_{\mu\nu} = \frac{8\pi G}{c^4}T_{\mu\nu}, \tag{2.11}$$

where $T_{\mu\nu}$ is the energy-momentum tensor. It is worth to notice that one needs to evaluate the former tensor only to the zeroth order in $h_{\mu\nu}$. In fact, for the weak-field limit assumption to apply, $T_{\mu\nu}$ must itself be small.

Before going further, it is useful to examine the degrees of freedom associated with these equations and their gauge invariance. At the beginning of this section we assumed the existence of at least one coordinate frame in which the metric could be decomposed into a flat component $\eta_{\mu\nu}$, plus a small perturbation $h_{\mu\nu}$. However, such demand is not able to completely specify the coordinate frame we are going to work into. It could very much be possible to find an other frame in which our metric would be described by

$$g_{\mu\nu} = \eta_{\mu\nu} + \tilde{h}_{\mu\nu}, \tag{2.12}$$

where

$$|\tilde{h}_{\mu\nu}| \ll 1 \quad and \quad \tilde{h}_{\mu\nu} \neq h_{\mu\nu}. \tag{2.13}$$

To makes things more clear let us imagine two diffeomorphic manifolds, M_b and M_p. The former represent the background spacetime on which one has defined the flat Minkowski metric $\eta_{\mu\nu}$. The latter is instead the physical spacetime where one has the metric $g_{\mu\nu}$ obeying the Einstein field equations. Finally let us call ϕ the diffeomorphism that connects the two manifold - $\phi : M_b \to M_p$ - and that allows us to move tensors from the background spacetime to the physical spacetime, and vice versa. The perturbation $h_{\mu\nu}$ can be now regarded as the difference between the pulled-back metric of the physical spacetime and the flat one of the background

$$h_{\mu\nu} = \left(\phi^* g\right)_{\mu\nu} - \eta_{\mu\nu}. \tag{2.14}$$

In order to be consistent with what assumed above, we will consider among all the possible diffeomorphisms only the ones for which the condition $|h_{\mu\nu}| \ll 1$ holds true. However even if one limit his or her choice in this way, the number of permissible diffeomorphisms is still large. To see how we can group together all of them, let us consider the one-parameter family of diffeomorphisms $\varphi_\epsilon : M_b \to M_p$ generated by the vector field $\xi^\mu\left(x\right)$. One can now define the family of perturbations

$$h^{(\epsilon)}_{\mu\nu} = \left[\varphi^*_\epsilon\left(\phi^* g\right)\right]_{\mu\nu} - \eta_{\mu\nu}, \tag{2.15}$$

where the condition $|h^{(\epsilon)}_{\mu\nu}| \ll 1$ will still hold for ϵ small enough. Making use of the perturbation definition we gave just above, we then obtain

$$\begin{aligned} h^{(\epsilon)}_{\mu\nu} &= \varphi^*_\epsilon \left(h + \eta\right)_{\mu\nu} - \eta_{\mu\nu} \\ &= \varphi^*_\epsilon \left(h_{\mu\nu}\right) + \varphi^*_\epsilon \left(\eta_{\mu\nu}\right) - \eta_{\mu\nu} \\ &= \varphi^*_\epsilon \left(h_{\mu\nu}\right) + \epsilon \left[\frac{\varphi^*_\epsilon \left(\eta_{\mu\nu}\right) - \eta_{\mu\nu}}{\epsilon}\right]. \end{aligned} \tag{2.16}$$

If ϵ is small as we assumed it to be, than at the lowest order the first therm on the r.h.s. of eq. (2.16) will be equal to $h_{\mu\nu}$ whereas the remaining other two will give the Lie derivative of the metric along the vector field ξ^μ. Since in our case we are considering the Minkowski metric, one has

$$h^{(\epsilon)}_{\mu\nu} = h_{\mu\nu} + \epsilon \left(\partial_\mu \xi_\nu + \partial_\nu \xi_\mu\right). \tag{2.17}$$

This equation shows that perturbations related to each other through the quantity $\epsilon \left(\partial_\mu \xi_\nu + \partial_\nu \xi_\mu\right)$ represent physically equivalent spacetimes. The diffeomorphism φ_ϵ allow us to change the representation without modifying the physical situation or spoiling the requirement for the perturbation to be small. In this sense the linearized theory is said to be gauge invariant and eq. (2.17) denotes the permitted gauge transformation. It is interesting to notice that, as for the electromagnetism, the invariance is the result of the conservation of some tensor under the gauge transformation. For the electromagnetism this tensor is $F_{\mu\nu}$, that is invariant under the electromagnetic gauge transformation $A_\mu \to A_\mu + \partial_\mu \lambda$. On the other hand, in our case is the variation of the Riemann tensor to be zero for the transformation described by eq. (2.17) as one can easily see

$$\begin{aligned} \delta R_{\mu\nu\rho\sigma} = \frac{1}{2} &\left(\partial_{\rho\nu\mu}\epsilon_\sigma + \partial_{\rho\nu\sigma}\epsilon_\mu + \partial_{\sigma\mu\nu}\epsilon_\rho + \partial_{\sigma\mu\rho}\epsilon_\nu \right. \\ &\left. -\partial_{\sigma\mu\rho}\epsilon_\nu - \partial_{\sigma\mu\nu}\epsilon_\rho - \partial_{\rho\nu\mu}\epsilon_\sigma - \partial_{\rho\nu\sigma}\epsilon_\mu\right) = 0. \end{aligned} \tag{2.18}$$

Making use of this gauge freedom allows us to greatly simplify the field equations of the perturbation. We start introducing the so called trace-reversed perturbation

$$\bar{h}_{\mu\nu} = h_{\mu\nu} - \frac{1}{2}\eta_{\mu\nu} h, \tag{2.19}$$

where one can see that the reason why this quantity is named trace-reversed perturbation is because

$$\bar{h} = \eta^{\mu\nu}\bar{h}_{\mu\nu} = -h. \tag{2.20}$$

The Einstein equations (2.11) in terms of $\bar{h}_{\mu\nu}$ read as follows

$$\Box\bar{h}_{\mu\nu} - \eta_{\mu\nu}\partial^\rho\partial^\sigma\bar{h}_{\rho\sigma} - \partial^\rho\partial_\nu\bar{h}_{\mu\rho} - \partial^\rho\partial_\mu\bar{h}_{\nu\rho} = -\frac{16\pi G}{c^4}T_{\mu\nu}. \tag{2.21}$$

At the same time, the gauge transformation equation becomes

$$\bar{h}^{(\epsilon)}_{\mu\nu} = \bar{h}_{\mu\nu} - \epsilon\left(\partial_\mu\xi_\nu + \partial_\nu\xi_\mu - \eta_{\mu\nu}\partial^\sigma\xi_\sigma\right). \tag{2.22}$$

If one chooses the vector field ξ_μ such that it satisfies the condition

$$\Box\xi_\mu = -\partial^\nu\bar{h}_{\mu\nu}, \tag{2.23}$$

the relation

$$\partial^\nu\bar{h}^{(\epsilon)}_{\mu\nu} = 0 \tag{2.24}$$

will hold true for the gauged transformed perturbation. The field equations then reduce themselves to the simple wave equations

$$\Box\bar{h}_{\mu\nu} = -\frac{16\pi G}{c^4}T_{\mu\nu}. \tag{2.25}$$

Equation (2.24) is often referred to as the Lorentz gauge[1] and reduces the independent components of the symmetric tensor $\bar{h}_{\mu\nu}$ from ten to six. Furthermore, it must be observed that the Lorentz gauge does not fix the gauge completely and indeed it leaves us with still some degrees of freedom to play with in order to further simplify the field equations.

Let start by studying the free-propagation case. Outside the source one has

$$\Box\bar{h}_{\mu\nu} = 0, \tag{2.26}$$

as the energy-momentum tensor is null. One can now use the residual gauge freedom to require the perturbation to meet the following conditions

$$\begin{aligned} &\bar{h}_{0\mu} = 0 \\ &\bar{h}^i_i = 0 \\ &\partial^i\bar{h}_{ij} = 0, \end{aligned} \tag{2.27}$$

where the index i runs only on the spatial dimensions. The gauge results to be totally fixed by these additional conditions and goes under the name of transverse-traceless gauge, or simply TT gauge. The remaining degrees of freedom of the perturbation are now only two. It must be remarked however,

---

[1] it can also be referred to as the Hillbert gauge or the harmonic gauge.

that this gauge choice can be done only outside the source. Moreover it is very clear from the definition (2.19) that in the TT gauge $\bar{h}_{\mu\nu} = h_{\mu\nu}$.
A particular well-known set of solutions for the wave equation (2.26) are the plane waves

$$h^{TT}_{\mu\nu} = C_{\mu\nu} e^{ik_\sigma x^\sigma} \tag{2.28}$$

with $C_{\mu\nu}$ describing a two time covariant tensor, constant and symmetric. In order to satisfy the transverse-traceless conditions (2.27), $C_{\mu\nu}$ must be itself traceless and purely spatial

$$\begin{aligned} &C_{0\nu} = 0 \\ &\eta^{\mu\nu} C_{\mu\nu} = 0. \end{aligned} \tag{2.29}$$

In order for (2.28) to represent a solution of the wave equation (2.26), the constant wave vector k_σ must be a null vector

$$k_\sigma k^\sigma = 0. \tag{2.30}$$

If one writes $k^\sigma = \left(\omega, k^1, k^2, k^3\right)$ where ω is the frequency of the wave, this condition translates to

$$\omega^2 = \delta_{ij} k^i k^j. \tag{2.31}$$

Moreover, if one wants the perturbation to be transverse, the wave vector also has to be orthogonal to the tensor $C_{\mu\nu}$. This is mathematically encoded in the relation

$$k^\mu C_{\mu\nu} = 0. \tag{2.32}$$

To help visualizing the form and the effect of a gravitational wave let us assume our wave is traveling along the x^3 direction, that is

$$k^\mu = \left(\omega, 0, 0, k^3\right) = \left(\omega, 0, 0, \omega\right). \tag{2.33}$$

From the conditions $C_{0\nu} = 0$ and $k^\mu C_{\mu\nu}$ it follows that $C_{3\nu} = 0$ as well. Our tensor $C_{\mu\nu}$ has then the form

$$C_{\mu\nu} = \begin{pmatrix} 0 & 0 & 0 & 0 \\ 0 & C_{11} & C_{12} & 0 \\ 0 & C_{21} & C_{22} & 0 \\ 0 & 0 & 0 & 0 \end{pmatrix}. \tag{2.34}$$

Finally we can further simplify its form by taking in consideration that it must be symmetric and traceless.

$$C_{\mu\nu} = \begin{pmatrix} 0 & 0 & 0 & 0 \\ 0 & C_{11} & C_{12} & 0 \\ 0 & C_{12} & -C_{11} & 0 \\ 0 & 0 & 0 & 0 \end{pmatrix}. \tag{2.35}$$

As one can see, the two tensor components C_{11} and C_{12} together with the frequency ω are all one needs to completely characterized the wave. The independent tensor components are related with the two possible polarization of the gravitational perturbation and are usually represented with the symbols h_+ and $h_\times$, respectively. The reason for such a choice will be soon be clear. Adding all together our perturbation can be described through the following formula

$$h^{TT}_{\mu\nu} = \begin{pmatrix} 0 & 0 & 0 & 0 \\ 0 & h_+ & h_\times & 0 \\ 0 & h_\times & -h_+ & 0 \\ 0 & 0 & 0 & 0 \end{pmatrix} e^{i\omega k_\sigma x^\sigma}. \tag{2.36}$$

Let see now how the passage of a gravitational wave would effect a simple "detector" composed by a ring of test masses. See Fig. 2.1

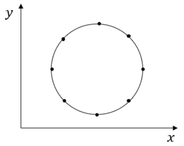

Figure 2.1: Ring of equidistant test particles.

We have seen how advantageous is to describe the gravitational perturbation in the TT frame, however it is not the frame normally used to describe what happen in a ground based detector. Let us assume for the moment that our laboratory, as well as the detector within it, are inside a drag-free satellite. Then all the apparatus would be in free fall in the total gravitational field generated by the Earth - and by the gravitational waves that could be present. If we restrict our attention to a region of space small enough, then in the Fermi normal coordinate system the metric ds^2 is flat whether or not gravitational waves are present

$$ds^2 \simeq -c^2dt^2 + \delta_{ij}dx^i dx^j. \tag{2.37}$$

As we are considering a free falling frame, we know that the derivatives of $g_{\mu\nu}$ are null at the point P around which we expand. Therefore no correction to the metric appear at the fist order in $|x^i|$. If we push the expansion at the second order, we get

$$\begin{aligned} ds^2 \simeq & - c^2dt^2 \left[1 + R_{0i0j}x^i x^j\right] \\ & - \frac{4}{3}cdtdx^i R_{0ijk}x^j x^k + dx^i dx^j \left[\delta_{ij} - \frac{1}{3}R_{ikjl}x^k x^l\right], \end{aligned} \tag{2.38}$$

where the second order derivatives of the metric have been expressed in terms of the Riemann tensor that, in turn, is evaluated at the expansion point P. For ground-based detectors things are a little bit more complex as, of course, they are not in free fall with respect of the Earth gravity and they also rotates respect to the local gyroscopes defined by the Fermi normal coordinate system. As a result, the metric in the laboratory frame up to $O\left(|x|^2\right)$ is

$$\begin{aligned} ds^2 \simeq & -c^2dt^2\left[1+\frac{2}{c^2}\vec{a}\cdot\vec{x}+\frac{1}{c^4}\left(\vec{a}\cdot\vec{x}\right)^2-\frac{1}{c^2}\left(\vec{\Omega}\times\vec{x}\right)^2+R_{0i0j}x^ix^j\right] \\ & + 2cdtdx^i\left[\frac{1}{c}\epsilon_{ijk}\Omega^jx^k-\frac{2}{3}R_{0jik}x^jx^k\right] \\ & + dx^idx^j\left[\delta_{ij}-\frac{1}{3}R_{ikjl}x^kx^l\right]. \end{aligned} \tag{2.39}$$

Here $\vec{a}$ represents the acceleration of the detector with respect to the local free-falling frame whereas $\vec{\Omega}$ describes its angular velocity relative to the local gyroscopes. Such coordinate system takes the name of *proper detector frame* and it is the one often implicitly used to describe phenomena that take place in a laboratory. The effects of the gravitational waves are coded in the quadratic order term proportional to the Riemann tensor which also accounts for the slowly varying gravitational field of the Earth. In principle, in order to detect the effect of gravitational wave one should first get rid off all the other contributions to the metric perturbation due to the inertial acceleration $2\vec{a}\cdot\vec{x}/c^2$, the gravitational redshift $\left(\vec{a}\cdot\vec{x}/c^2\right)^2$, etc. (see [92]), that often are many order of magnitude stronger. However, this problem can be circumvented by focusing the response of the detector in a frequency window high enough that all those static and slowly-varying terms are negligible, whereas the contribution coming from the gravitational waves is still effective[2]. This means that in order to deduce the dynamic of the test masses one can use the free-falling frame metric described in eq. (2.38). To do this one can make use of the geodesic deviation equation

$$\frac{d^2\xi^i}{d\tau^2}+\xi^\sigma\partial_\sigma\Gamma^i_{00}\left(\frac{dx^0}{d\tau}\right)^2=0, \tag{2.40}$$

where we exploited the fact that the Christoffel symbols vanishe at the expansion point P and that the $dx^i/d\tau$ term is negligible compared to the

---

[2] The effect of the acceleration a^i is directly counterbalanced by the suspension mechanism and thus can be neglected as well.

$dx^0/d\tau$ since, as far as we describe the detectors component, we are in a non-relativistic regime. It is easy to show that because $g_{\mu\nu} = \eta_{\mu\nu} + O\left(x^i x^j\right)$, the only non-zero terms in $\partial_\sigma \Gamma^i_{00}$ are the one in which the two metric's derivatives present are spatial derivatives acting on $x^i x^j$. As a result of this, overall, at P the quantities $\Gamma^\rho_{\mu\nu}$, $\partial_0 \Gamma^i_{00}$ and $\partial_0 \Gamma^i_{0j}$ are equal to zero. One finds therefore that

$$\xi^\sigma \partial_\sigma \Gamma^i_{00} = \xi^j \partial_j \Gamma^i_{00} = \xi^j R^i_{0j0}. \tag{2.41}$$

We can now re-write eq. (2.40) in the from

$$\frac{d^2\xi^i}{d\tau^2} + \xi^j R^i_{0j0} \left(\frac{dx^0}{d\tau}\right)^2 = 0. \tag{2.42}$$

If we limit ourselves to linear order in the perturbation h, this equation can be further simplified. We know in fact that dt^2 differs from $d\tau^2$ for a correction term $\simeq O\left(h^2\right)$. On the other side, the Riemann tensor R^i_{0j0} is by itself $= (h)$. This allows us to replace the proper time τ with the coordinate time t obtaining

$$\ddot{\xi}^i = -c^2 R^i_{0j0} \xi^j. \tag{2.43}$$

The only thing we have left is to evaluate the Riemann tensor component R^i_{0j0} in the proper detector frame. However since the Riemann tensor is *invariant* in the linearized version of the general relativity, one can evaluate it in any other frame and the result will not change. We can thus evaluate it in the TT frame where it has the simple form

$$R^i_{0j0} = -\frac{1}{2c^2} \ddot{h}^{TT}_{ij}. \tag{2.44}$$

Finally the geodesic deviation equation is obtained by plugging eq. (2.44) into eq. (2.43)

$$\ddot{\xi}^i = \frac{1}{2} \ddot{h}^{TT}_{ij} \xi^j. \tag{2.45}$$

If we consider our ring of test masses to be initially at rest in the proper detector frame and the ring's center to coincide with its origin, then the quantity ξ^i describes the distance of a test mass with respect to the origin. As before, we consider a gravitational waves propagating along the x^3 direction whereas the ring is completely contained in the orthogonal plane $\left(x^1, x^2\right)$. If one considers just the + polarization and chooses the origin of time so that $h^{TT}_{ij} = 0$ at $t = 0$, then in the $\left(x^1, x^2\right)$ plane the perturbation is described by

$$h_{ij}^{TT} = h_+ \begin{pmatrix} 1 & 0 & 0 \\ 0 & -1 & 0 \\ 0 & 0 & 0 \end{pmatrix} \sin \omega t. \tag{2.46}$$

We can write the vector ξ_i as follows

$$\xi_i \left(t\right) = \left(x_0 + \delta x\left(t\right), y_0 + \delta y\left(t\right), z_0 + \delta z\left(t\right)\right), \tag{2.47}$$

where (x_0, y_0, z_0) are the unperturbed positions while δx, δy and δz are the displacements induced by the gravitational perturbation. We now apply eq. (2.45) obtaining

$$\begin{aligned} \delta\ddot{x} &= -\frac{h_+}{2}\left(x_0 + \delta x\right)\omega^2 \sin\omega t, \\ \delta\ddot{y} &= +\frac{h_+}{2}\left(y_0 + \delta y\right)\omega^2 \sin\omega t \\ \delta\ddot{z} &= 0. \end{aligned} \tag{2.48}$$

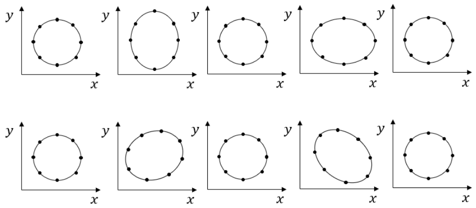

Figure 2.2: *Top*: the distortion induced on the test particles ring by the passage of a gravitational wave with + polarization. *Bottom*: the distortion induced on the test particles ring by the passage of a gravitational wave with × polarization.

The fist thing one can notice is that the test masses are confined in the (x, y) plane. Moreover since both δx and δy are $O\left(h_+\right)$, they end up to be negligible with respect to the constant counterparts x_0, y_0 at the linear order in the perturbation h. Then equations (2.48) are easily integrated to give

$$\begin{aligned} \delta x\left(t\right) &= \frac{h_+}{2} x_0 \sin\omega t \\ \delta y\left(t\right) &= -\frac{h_+}{2} y_0 \sin\omega t. \end{aligned} \tag{2.49}$$

The same process can be repeated with a × polarized gravitational wave obtaining

$$\begin{aligned}\delta x\left(t\right) &= \frac{h_\times}{2} y_0 \sin \omega t \\ \delta y\left(t\right) &= \frac{h_\times}{2} x_0 \sin \omega t.\end{aligned} \tag{2.50}$$

The resulting effect on the test masses composing our ring-shaped detector is shown in Fig. 2.2 and makes clear the reason why the two polarization are named the way they are.

2.2 Detection of Gravitational Waves

2.2.1 Interferometers

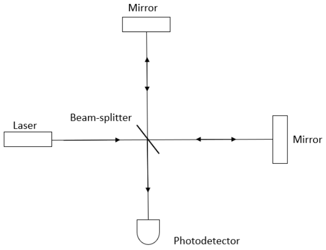

Figure 2.3: Schematic representation of a Michelson interferometer.

Now that we have seen how gravitational waves interact with a simple configuration of test masses, let us make a step forward and see how they interact with actual detectors. The idea to detect gravitational waves through the use of interferometers was first proposed by M. Gertsenshtein and V. I. Pustovoit in the 1962. A large gravitational waves interferometer is an extremely complex apparatus that at its core shares very much in common with a Michelson interferometer. See Fig. 2.3. At the detector's base one has a laser which plays the role of a monochromatic light source whose light is sent on a beam-splitter. The beam splitter separates the laser beam in two beam of equal amplitude, each of which then travels in one of the two perpendicular arms the detector is made of. At the end of these arms, totally reflecting mirrors allow the beams to travel back to the beam-splitter where they recombine together. Finally a photodetector collect part of the recombined beam - while the other part goes back toward the laser - and measure its intensity whose variations can be used to spot the passage of

gravitational waves.
Let us consider the position of the beam-splitter as the origin of our coordinate frame, and let us also identify the arms directions as the $\hat{x}$ and $\hat{y}$ directions so that the positions of the mirrors are identified by the coordinates (ξ_x, ξ_y). Let us assume now a gravitational wave coming from the z direction with only the plus polarization

$$h_+ (t) = h_0 \cos (\omega_{gw} t) . \tag{2.51}$$

The dynamic of the mirror on the x arm in the presence of such a wave is then described by

$$\ddot{\xi}_x = \frac{1}{2} \ddot{h}_+ \xi_x , \tag{2.52}$$

where we used eq. (2.45) and consider that the mirror cannot move in the y direction, $\xi_y (0) = \dot{\xi}_y (0) = 0$. One can solve equation (2.52) perturbatively in h_0 by substituting $\xi_x = L_x$. The solution of the resulting equation is then

$$\xi_x (t) = L_x + \frac{h_0 L_x}{2} \cos (\omega_{gw} t) . \tag{2.53}$$

A photon that starts at the beam-splitter at time t_0, moving along the positive x axis, will reach the mirror at the time t_1 given by the relation $c (t_1 - t_0) = \xi_x (t_1)$. Once again one can solve this equation perturbatively in h_0. The result reads

$$c (t_1 - t_0)^{(x)} = L_x + \frac{h_0 L_x}{2} \cos [\omega_{gw} (t_0 + L_x/c)] . \tag{2.54}$$

After a round-trip, the photon gets back at the beam-splitter at a time t_2 defined by

$$\Delta T^{(x)} (t) = t_2^{(x)} - t_0^{(x)} = 2 \frac{L_x}{c} + \frac{h_0 L_x}{c} \cos [\omega_{gw} (t_0 + L_x/c)] . \tag{2.55}$$

As in general we are interested in the light coming out of the beam-splitter it is useful to rename $t_2 = t$ and express the time t_0 as a function of it

$$t_0^{(x)} = t - 2 \frac{L_x}{c} + \frac{h_0 L_x}{c} \cos [\omega_{gw} (t - L_x/c)] , \tag{2.56}$$

where, at the first order in h_0, the relation $t_0 = t - 2L/c$ holds true. As one can see, the time-of-flight of the photons in the interferometer arms is directly affected by the presence of the gravitational wave.

To understand how the detector capitalized on this making possible to detect the gravitational wave let us consider the electric field of the input laser light

$$E_x = E_0 e^{-i\omega_L t + i\vec{k}_L\cdot\vec{x}}, \tag{2.57}$$

where we denoted by ω_L and k_L the frequency of the laser and its wavenumber, respectively. Then at time $t_0^{(x)}$ the electric field at the beam-splitter is described by

$$\begin{aligned} E^{(x)}(t) &= -\frac{1}{2}E_0 e^{-i\omega_L t_0^{(x)}} \\ &= -\frac{1}{2}E_0 e^{-i\omega_L(t-2L_x/c)+ih_0\frac{\omega_L L_x}{c}\cos[\omega_{gw}(t-L_x/c)]}. \end{aligned} \tag{2.58}$$

where the overall factor 1/2 comes from the reflection and transmission at the mirror. In the same way, one can describe the field that went through the y arm as follows

$$\begin{aligned} E^{(y)}(t) &= \frac{1}{2}E_0 e^{-i\omega_L t_0^{(y)}} \\ &= \frac{1}{2}E_0 e^{-i\omega_L(t-2L_y/c)-ih_0\frac{\omega_L L_y}{c}\cos[\omega_{gw}(t-L_y/c)]}. \end{aligned} \tag{2.59}$$

In order to simplify the notation we define the quantities

$$\begin{aligned} \Delta\phi_x(t) &= h_0\frac{\omega_L L_x}{c}\cos\left[\omega_{gw}\left(t-L_x/c\right)\right] \\ \Delta\phi_y(t) &= -h_0\frac{\omega_L L_y}{c}\cos\left[\omega_{gw}\left(t-L_y/c\right)\right]. \end{aligned} \tag{2.60}$$

As these two quantities are already of order h_0 we can replace the arms lengths L_x and L_y inside the cosines with

$$L = \frac{L_x + L_y}{2} \tag{2.61}$$

considering that in general they are very close to be exactly equal. The electric field in the two arms can be then written as follow

$$\begin{aligned} E^{(x)}(t) &= -\frac{1}{2}E_0 e^{-i\omega_L(t-2L/c)+ik_L(L_x-L_y)+i\Delta\phi_x(t)}, \\ E^{(y)}(t) &= +\frac{1}{2}E_0 e^{-i\omega_L(t-2L/c)-ik_L(L_x-L_y)+i\Delta\phi_y(t)}, \end{aligned} \tag{2.62}$$

with $\Delta\phi_x = -\Delta\phi_y$. The term $k_L(L_x - L_y)$ produces a constant phase ϕ_0 that can be adjusted to choose the best working point for the apparatus. The total electric field at the output is then

$$\begin{aligned} E_{out}(t) &= E^{(x)}(t) + E^{(y)}(t) \\ &= -\frac{1}{2}E_0 e^{-i\omega_L}(t - 2L/c)\left[e^{i(\phi_0+\Delta\phi_x)} + e^{-i(\phi_0+\Delta\phi_x)}\right] \\ &= -iE_0 e^{-i\omega_L(t-2L/c)}\sin\left[\phi_0 + \Delta\phi_x\right]. \end{aligned} \tag{2.63}$$

One can now see how the presence of a gravitational wave affects the total power $P \sim |E_{out}|^2$ measured at the photodetector

$$\begin{aligned} P &= P_0\sin^2\left[\phi_0 + \Delta\phi_x(t)\right] \\ &= \frac{1}{2}P_{=}\left\{1 - \cos\left[2\phi_0 + \Delta\phi_{gw}(t)\right]\right\}, \end{aligned} \tag{2.64}$$

where the effect of the gravitational wave is encoded in the factor $\Delta\phi_{gw} = \Delta\phi_x - \Delta\phi_y = 2\Delta\phi_x$.
Before going further, let us confront the phase modification generated by the gravitational wave $\Delta\phi_{gw}$ with the offset phase ϕ_0

$$\begin{aligned} \Delta\phi_{gw} &= 2Lk_L h_0\cos(t - L/c) \\ \phi_0 &= k_L(L_x - L_y). \end{aligned} \tag{2.65}$$

One can notice that in the limit $\omega_{gw}L/c \ll 1$ the effect of the gravitational waves on the phase shift is formally equivalent to a modification of the arms length asymmetry $L_x - L_y$ equals to

$$\Delta(L_x - L_y) = 2Lh(t - L/c), \tag{2.66}$$

or, in terms of photons time-of-flight ΔT inside the arms as

$$\Delta T^{(x)} - \Delta T^{(y)} = \frac{2L}{c}h(t - L/c). \tag{2.67}$$

Now that we have seen how gravitational waves modify the power measured at the photodetector, what is left to do is to decide how to extract the information on the phase from the interfetometer output. Unfortunately this proves to be less trivial that one could initially think. Let us consider eq. (2.64). A priori we could think that the best choice is to select $\phi_0 = \pi/4$ as working point since it is the maximum of the derivative $\partial P/\partial\phi_0$ and therefore the sensibility to a variation of the kind $\phi_0 \to \phi_0 + \Delta\phi_{gw}$, due to the effect of a gravitational wave, would be at its maximum as well. However one will soon notice that there is indeed a problem with such a choice. The issue is that we would then be extremely sensible also to the laser power variations $P_0 \to P_0 + \Delta P_0$ and, unfortunately, these variations are expected to be much stronger than the signal one would expect from gravitational waves. An other strategy could be to set the working point on a dark fringe $\phi_0 = 0$. The advantage of such a choice is that the output, when gravitational waves are not present, is zero and measurement are no more affected by the laser power fluctuations. However this come with a huge drawback. At the working point $\phi_0 = 0$ both the power output P and its derivative $\partial P / \partial \phi_0$ are null. As a consequence the variation ΔP induced by the passage of a gravitational wave would be of the order $O\left(h^2\right)$ making it impossible to be detected. In order to overcome this issue one modulates the input laser light thanks to a Pockels cell. In this way the input laser beam acquires a time-varying phase and, once expanded in Fourier modes, it reads

$$E_{in} = E_0 \left[J_0\left(\Gamma\right) e^{-i\omega_L t} + J_1\left(\Gamma\right) e^{-i(\omega_L + \Omega_{mod})t} - J_1\left(\Gamma\right) e^{-i(\omega_L - \Omega_{mod})t} + ...\right], \tag{2.68}$$

where the dots encode the terms with frequencies $\omega_L \pm n\Omega_{mod}$ for $n = 2, 3, ...$ $\Omega_{mod} = 2\pi f_{mod}$ is a parameter directly proportional to the modulation frequency, Γ is the modulation index and J_n are the Bessel functions. The net effect of the modulation is then to create sidebands in the input signal. Although these sidebands are a priori infinite, for small Γ all of them but the first two can be neglected. If we define the sidebands frequency $\omega_\pm$ and wavenumber $k_\pm$ as follows

$$\omega_\pm = \omega_L \pm \Omega_{mod}, \qquad k_\pm = \frac{\omega_\pm}{c}, \tag{2.69}$$

then the electric fields at the output for the carrier and the sidebands are respectively

$$\begin{aligned} \left(E_{out}\right)_c &= -iE_0 J_0\left(\Gamma\right) e^{-i\omega_L t + 2ik_L L} \sin\left(2\pi \frac{\Delta L}{\lambda_L}\right), \\ \left(E_{out}\right)_\pm &= \mp E_0 J_1\left(\Gamma\right) e^{-i\omega_\pm t + 2ik_\pm L} \sin\left[2\pi\left(\frac{\Delta L}{\lambda_L} \pm \frac{\Delta L}{\lambda_{mod}}\right)\right], \end{aligned} \tag{2.70}$$

where we defined

$$L = \frac{L_x + L_y}{2}, \qquad \Delta L = L_x - L_y. \tag{2.71}$$

It easy to see that if one chooses $L_x = L_y \rightarrow \Delta L = 0$, then both the carrier and the two sidebands are on the dark fringe and $(E_{out})_c = (E_{out})_\pm = 0$. However, the situation is very much different if one chooses instead to have two arms of different length and in particular in such a way that their difference is equal to an integer number of laser wavelengths. Such a choice is also known as *Schnupp asymmetry.* If we plug $\Delta L = n\lambda_L$ into the equations (2.70) we obtain

$$\begin{aligned} &(E_{out})_c = 0, \\ &(E_{out})_\pm = \mp E_0 J_1(\Gamma)\, e^{-i\omega_\pm t + 2ik_\pm L} \sin(2\pi\Delta L/\lambda_{mod})\,. \end{aligned} \tag{2.72}$$

The carrier remains on a dark fringe whereas the sidebands do not. Let us consider now a gravitational wave with a plus polarization passing through the detector along its orthogonal axis such that one has

$$\Delta L \rightarrow \Delta L + Lh(t)\,. \tag{2.73}$$

The total electric field at the output of the interferometer would then be

$$\begin{aligned} (E_{out})_{tot} = (E_{out})_c + (E_{out})_+ + (E_{out})_- &= -iE_0 e^{-i\omega_L t + 2ik_L L} \\ &\times \left[J_0(\Gamma)\, k_L L h(t) + 2J_1(\Gamma)\sin(2\pi\Delta L/\lambda_{mod})\cos(\Omega_{mod}t - \alpha)\right], \end{aligned} \tag{2.74}$$

where to simplify the notation we have defined the phase $\alpha = 4\pi L/\lambda_{mod}$. It is important to mention that in the term accounting for the sidebands, the second, the correction term $O(h)$ to the quantity ΔL has been neglected as it would have led to an undetectable term $\sim O(h^2)$ in the power output. The total power output $|(E_{out})_{tot}|^2$ is composed by three terms. The first one derives from the modulus contribution and, as expected, is proportional to $O(h^2)$. The second term is proportional to $\cos^2(\Omega_{mod}t - \alpha)$ and it is the squared modulus of the sidebands contribution. This term is not affected by the presence of the gravitational wave and, once one recast it in the form

$$\cos^2(\Omega_{mod}t - \alpha) = \frac{1}{2}\left[1 + \cos(2\Omega_{mod}t - 2\alpha)\right], \tag{2.75}$$

we can see that it is made up of a direct current term plus an oscillating term characterized by the frequency $2\Omega_{mod}$. Finally the third therm represents the beatings between the carrier and the sidebands

$$4E_0^2 J_0(\Gamma)\, J_1(\Gamma)\, k_L L h(t) \sin(2\pi\Delta L/\lambda_{mod})\cos(\Omega_{mod} - \alpha)\,. \tag{2.76}$$

It oscillates with a frequency Ω_{mod} and, more important, it is linear in the perturbation $h\left(t\right)$. Thanks to the modulation of the input laser light and the asymmetric arms one is able to use the interferometer as a null instrument that in presence of gravitational waves is still able to produce an output linear in the perturbation amplitude h. Finally, it is worth to notice that since the sidebands are not on the dark fringe, fluctuation of the laser power can still affect the final output. However the great advantage is that now the signal is encoded in a term characterized by the modulation frequency f_{mod} rather than the perturbation frequency f_{gw}. This means that the signal has now to compete with variation of the laser power at modulation frequency that are way smaller as f_{mod} is typically several order of magnitude greater than f_{gw}.

2.3 Introduction to signal analysis with GW detectors

We have seen how the modulation of the input laser light allows us to collect more easily the information about the gravitational perturbation that are carried by the detector output. Unfortunately, fluctuations of the input laser are not the only responsible for overall apparatus noise. In this section we will address the issue of how to extract the meaningful part of the signal from the typically much larger detector noise. This section also represents a theoretical introduction to the analysis tools we will use in the subsection **Search Strategy** (4.3.3) of chapter 4.

As first step, let us characterize the noise in a way that will make it easier to deal with it. One can think of a gravitational waves detector as a linear system whose input is the gravitational wave signal that one wants to detect and whose output is a combination of the same signal with some noise. Usually the input is described by the scalar quantity

$$h\left(t\right) = D^{ij} h_{ij}\left(t\right). \tag{2.77}$$

Here D^{ij} represents the *detector tensor*, a constant tensor which depends only on the detector geometry. For a gravitational wave interferometer it takes the form

$$D^{ij} = \hat{x}^i \hat{x}^j - \hat{y}^i \hat{y}^j. \tag{2.78}$$

On the other hand, the output signal is the juxtaposition of $h_{out}\left(t\right)$, a linear function in the frequency space of the input $h\left(t\right)$, and the noise contribution

$$s_{out}\left(t\right) = h_{out}\left(t\right) + n_{out}\left(t\right). \tag{2.79}$$

The relation between $h_{out}\left(t\right)$ and the input signal is described by

$$\tilde{h}_{out}\left(f\right) = T\left(f\right)\tilde{h}\left(f\right), \tag{2.80}$$

where $T\left(f\right)$ is the *transfer function* of the system. More precisely one can think of a detector as a sequence on linear systems whose output is the input of the next stage down on the line. A priori, one should consider the noise contribution at each of these steps and propagate it up to the final output. An easier way to characterize the detector noise is instead to introduce the effective quantity $n\left(t\right)$ defined as follows

$$\tilde{n}\left(f\right) = T^{-1}\left(f\right)\tilde{n}_{out}\left(f\right), \tag{2.81}$$

where $n_{out}\left(t\right)$ is the total noise measured at the fictitious output. Therefore, $n\left(t\right)$ should be interpreted as the noise that, if injected at the apparatus input, would produce the measured noise $n_{out}\left(t\right)$ at the output. The advantage of this definition is that $n\left(t\right)$ can be compared directly with the effect of the gravitational wave $h\left(t\right)$. One can then introduce the sum

$$s\left(t\right) = h\left(t\right) + n\left(t\right) \tag{2.82}$$

and consider this quantity to be the output of the detector. The advantage of referring everything to the input quantities $h\left(t\right)$, $n\left(t\right)$ is that one can use the latter to estimate the minimum magnitude of the gravitational perturbation needed in order for the signal to be detectable[3]. Let us now define the spectral noise density. We start considering the noise auto-correlation function

$$R\left(\tau\right) = \left\langle n\left(t+\tau\right)n\left(t\right)\right\rangle. \tag{2.83}$$

Together with the average value $\left\langle n\left(t\right)\right\rangle$ this is all one needs to characterize $n\left(t\right)$ assuming that it is a Gaussian stochastic process. Furthermore, if the noise is stationary, $\left\langle n\left(t\right)\right\rangle$ can be set to zero with a constant shift. Usually one can assume that $R\left(\tau\right)$ goes to zero quite fast for $|\tau| \to \infty$ as any information about the noise at a time t provides very little insight on the noise value at the subsequent time $t+\tau$. This means that one can take the Fourier transform of the auto-correlation function and define the one-sided noise spectral density $S_n\left(f\right)$ as follows

$$\frac{1}{2}S_n\left(f\right) = \int_{-\infty}^{\infty} d\tau R\left(\tau\right)e^{i2\pi f\tau}. \tag{2.84}$$

---

[3] The other advantage is that it makes more straightforward to compare the performance of different detectors

We can invert this relation to get

$$R(\tau) = \frac{1}{2}\int_{-\infty}^{\infty} df S_n(f)\, e^{-i2\pi f\tau}, \tag{2.85}$$

where one has taken advantage of the reality of the auto-correlation function $R(\tau)$ and its invariance under time translations. Finally we consider the case

$$\begin{aligned} R(0) &= \langle n^2(t) \rangle \\ &= \int_0^{\infty} df S_n(f)\,. \end{aligned} \tag{2.86}$$

One can use this result to show that, if $\tilde{n}(f)$ does exist, definition (2.84) is equivalent to

$$\langle \tilde{n}^*(f)\, \tilde{n}(f') \rangle = \delta(f - f')\, \frac{1}{2} S_n(f)\,, \tag{2.87}$$

One can notice here that for $f = f'$ the right-hand side of the latter equation diverges. Fortunately this is true only if the Fourier transform is performed on a time domain of infinite length. In a real experiment, one is able to collect data only for a finite time T. Therefore, once one takes into consideration this restriction on the time interval, one has

$$\delta(f = 0) = \left[\int_{-T/2}^{T/2} dt e^{-i2\pi f t}\right]\Bigg|_{f=0} = T, \tag{2.88}$$

and thus

$$\langle |\tilde{n}(f)|^2 \rangle = \frac{1}{2} T S_n(f)\,. \tag{2.89}$$

Having at our disposal the quantity $S_n(f)$ to describe the detector noise, the next goal now is to understand how to get valuable information from the data despite the noise contribution. In particular, there are two questions that one would like to answer. First, whether or not a gravitational wave signal is present in the data. Second, in case the signal is present, what are the physical characteristics of the source. Such questions can be addressed using the technique of classical inference. Classical statistic is a branch of statistical inference in which probability is defined as the "long-run relative occurrence of an event in a set of identical experiments". For this reason is also referred to as frequentist statistic. Following this interpretation, the measured data are the result of random draws based on an underlying probability distribution $p(d|H)$. Here d denotes the set of data while H represents the hypothesis, or model, we assume the distribution is based on. A *statistics* are defined as a random variables constructed from the data. Their purpose is usually to estimate parameters related to the signal or indicate how well a particular hypothesis is represented by the collected data. They are typically constructed from likelihood function, although this is not an a priori requirement. The probability distribution of these statistics takes the name of *sampling distribution.* If the statistic is simple enough, it can be evaluated analytically, otherwise Monte Carlo simulations are usually used. In either cases they are needed in order to able to calculate *confidence intervals* for parameters estimation or p-values for hypothesis testing. So how one can use these tools to look for a gravitational wave signal? Let assume that one wants to confirm the hypothesis that a gravitational wave signal with some fixed but unknown amplitude $a > 0$ is present in the data. Let us define such hypothesis as H_1. Let us now introduce the other hypothesis H_0 that there is no gravitational wave signal in the data, i.e. $a = 0$. The latter is also known in the literature as *null hypothesis.* The common strategy is to argue for H_1 by arguing against H_0. We need then something that can tell us how likely it is for the parameter a to be equals to zero according to the data we measured. In order to do that one defines a particular statistic Λ, known as *detection statistic*, that will be the core of the statistical test. In particular, if the observed value Λ_{obs} obtained through the data lies far out in the tails of the statistic sampling distribution, then the data themselves are most likely not consistent with the hypothesis we assumed and thus such hypothesis can be rejected. The confidence level with which one rejects H_0 is quantified thought the *significance* of the test, also called as p-value. Such quantity is defined as follows

$$p = Prob\left(\Lambda > \Lambda_{obs}|H_0\right) = \int_{\Lambda_{obs}}^{\infty} p\left(\Lambda|H_0\right) d\Lambda, \tag{2.90}$$

where $p\left(\Lambda|H_0\right)$ is the statistic sampling distribution under the assumption that the *null hypothesis* is correct. Usually, the confidence level of the rejection is set *a priori.* A threshold value Λ_* is then evaluated from it according to the *false alarm probability* α (see Fig. 2.4) that, in turn, is defined by

$$\alpha = Prob\left(\Lambda > \Lambda_*|H_0\right) = \int_{\Lambda_*}^{\infty} p\left(\Lambda|H_0\right) d\Lambda. \tag{2.91}$$

The *false alarm probability* function measures the probability to obtain $\Lambda_{obs} > \Lambda_*$ by pure chance. That is to say that α tells how likely it is for one to reject the *null hypothesis* when it is actually true. On the other side, the *false dismissal error* β tells us how likely it is for one to accept

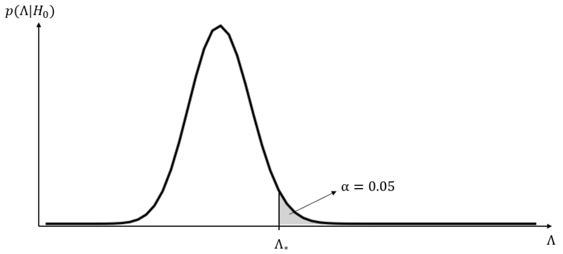

Figure 2.4: A binomial distribution with parameter $n = 60$ and $p = 0.35$. The value of α equals the area under the probability distribution for $\Lambda \geq \Lambda_* = 28$.

the *null hypothesis*, i.e. $\Lambda_{obs} < \Lambda_*$, when it is actually false. It is defined as follows

$$\beta = Prob\,(\Lambda < \Lambda_*|H_a) = \int_{-\infty}^{\Lambda_*} p\,(\Lambda|H_a)\,d\Lambda, \tag{2.92}$$

where $p\,(\Lambda|H_a)$ describes the sampling distribution of the detection statistic assuming the presence in the data of a signal characterized by the amplitude a. It is easy to see how these two quantities are intrinsically related together. In fact, if we set an high threshold value Λ_* in order to minimize the false alarm probability, the false dismissal probability will in turn increase. To check this, one just needs to consider that β is defined as the probability for the detection statistic to assume a value Λ_{obs} smaller than the detection threshold Λ_*. Hence, higher is the threshold we set, higher is the false dismissal probability we will obtain. By the same token, a small threshold value, although able to reduce the false dismissal probability, will also increase the probability of a false alarm as a consequence of the less strict requirement one assumes to establish the presence of a signal in the data. In general it is up to the analysts to decide how to balance these two properties choosing the most suitable value for the detection threshold. In particular, in the context of gravitational waves data analysis, it is common to set the false alarm probability to some low value, i.e. 5%, and chose as detection statistic the one that minimizes the false dismissal probability. Such approach is also known as the *Neyman-Pearson criterion.* In order to check how efficient are the choices one has made in terms of signal detection, one defines the *test power* or *detection probability*

$$\gamma\,(a) = 1 - \beta\,(a)\,. \tag{2.93}$$

The detection probability is used to quantify the fraction of times that the test statistic is able to correctly spot the presence of a signal in the data, given the false alarm rate α as well as the amplitude of the signal itself a. See Fig. 2.5.

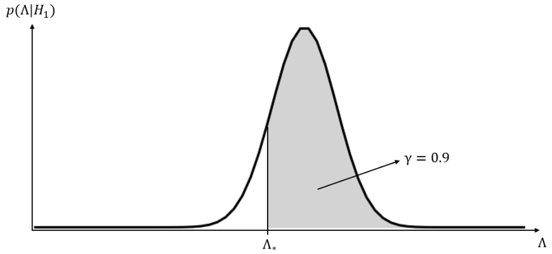

Figure 2.5: A binomial distribution with parameter $n = 60$ and $p = 0.54$. The value of p has been chosen so that the area under the probability distribution for $\Lambda \geq \Lambda_* = 28$ is equal to 0.9.

One of the great advantage of the detection probability is that it is data-independent and, as such, it can be used as a *figure-of-merit* for proposed search method. In fact, because it also depends on the signal amplitude, it can be used to get valuable information about the signal even in absence of a detection. This is particularly useful when one deals with unknown parameter characterizing the source model or the theory behind it, as we will see in the last part of Chapter 4.

Chapter 3

Introduction to the Dark Matter paradigm

3.1 Introduction

The study of the dark matter paradigm is nowadays one of the most puzzling and at the same time compelling task for many cosmologists and astronomers. The phrase ”dark matter” itself has gone under an important development in the last decades. While at first the word ”dark” was just a mere adjective representing the impossibility to detect this astrophysical material because of their supposed faint electromagnetic emission, nowadays the phrase ”dark matter” is often used as a name, a proper noun to account for whatever makes up the bulk of our Universe's matter density. In this chapter, we aim to throw some light on its history focusing on the theoretical arguments and observations that led to the establishment of the dark matter as the standard explanation for a wide variety of astrophysical observations. Some of the most known dark matter candidates will be presented and discussed, exploring their pros and cons.

Before going further it would be reasonable to address the elephant in the room: ”what is dark matter?”. Unfortunately physicists and astronomers are still far from being able to provide an exact and exhaustive answer to this question. Nevertheless we can give an “operative” definition of dark matter by qualitative describing the features one wants to ascribe to it. One can describe dark matter as some form of material that either emits, reflects nor absorbs electromagnetic radiation (radio waves, light, gamma rays, etc..). Let's imagine to have a cloud of dark matter interposing between a source of light and an observer. What happens is that the light goes straight through

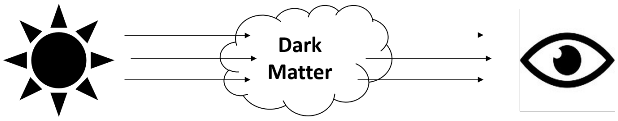

Figure 3.1: The light rays that pass through the *dark matter* do not interact with it eventually reaching unperturbed the observer.

the cloud eventually reaching the observer. It doesn't bounce off, it doesn't get absorbed, it doesn't interact in any way with the dark matter could.

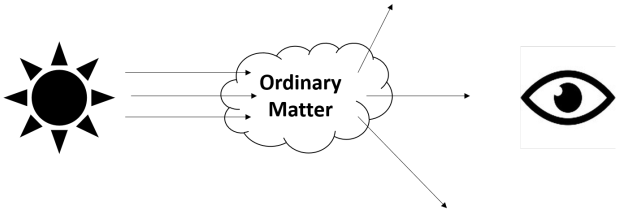

Figure 3.2: The light rays that pass through the *ordinary matter* can be reflected, absorbed, etc.. before reaching the observer.

On the other hand normal matter, which is everything that makes us up and everything we know about, would indeed appear dark to the same observer. That is of course because it does something different: it interacts with light. Standard matter may looks dark because it can absorb light, or reflect it, so that the light will not reach the observer whereas dark matter is just invisible. Now that we have addressed this first question, we can move on the next one:" Why do we believe dark matter exists?"

3.2 Dark Matter evidences

3.2.1 Galaxy Clusters

From a chronological point of view, the study of the mass of galaxy clusters gave one of the first hints of dark matter existence. Galaxy clusters are the most extended gravitationally bound systems and, as such, they provide an ideal tool for cosmologists to study the formation and evolution of the structures of the Universe. In the first half of the 20th century the astronomer Fritz Zwicky published two works on galaxies cluster, in 1933 and in 1937 respectively [137, 138], in which he proposed different methods to determine their mass. Motivated by the large scatter in the apparent velocities of several galaxies within it, he focused his attention to the particular case of

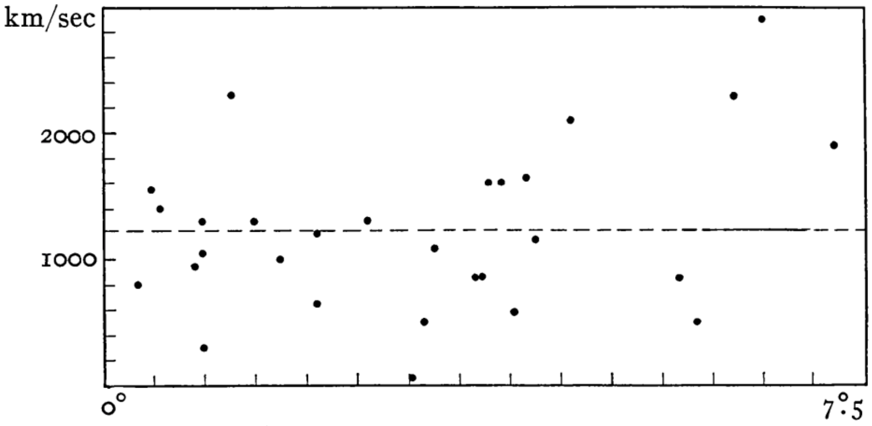

Figure 3.3: Distribution of the Virgo Cluster galaxies member velocities as a function of their distances from the cluster center [115].

the Coma cluster. From the observed velocity dispersion Zwicky obtained a conservative lower limit on the mass of the cluster of $4.5 \times 10^{13} M_{\odot}$. If one considers that the Coma cluster contains about one thousand galaxies within a radius of 2×10^6 light-years, such a value corresponds to an average mass-per-galaxy of about $4.5 \times 10^{11} M_{\odot}$. Assuming that the average absolute luminosity for cluster galaxies is around 8.5×10^7 times that of the Sun, we are led to a remarkable high mass-to-light ration of 500. Although we know nowadays that this is quite an overestimation due to the incorrect value he used for the Hubble constant[1], this result clearly suggests the presence of some sort of non emitting mass component in the cluster. The pioneering study of Fritz Zwicky is followed in the successive decades by numerous other works. Sinclair Smith publishes his study on the Virgo Cluster in the 1936 [115] in which, analyzing thirty-two members of the cluster, he concludes that "high line-of-sight velocities are just as likely to be found in one part of the cluster as others". Assuming that the outer members of the cluster are moving in a circular orbit, he estimates the total mass of the Virgo cluster to be $2 \times 10^{47} g \simeq 10^{14} M_{\odot}$. Neglecting the intergalactic material this leads to an average mass of $2 \times 10^{11} M_{\odot}$ for the 500 galaxies members. This estimate, as the one obtained by Zwicky, is indeed incompatible with the one previously derived by Hubbles.

In the 1951 Thornton Page approaches the problem on a different angle

---

[1] Zwicky used the value estimated by Hubble and Humason $H_0 = 558 kmMpc/s$ with an estimated uncertainty of 10-20%[76].

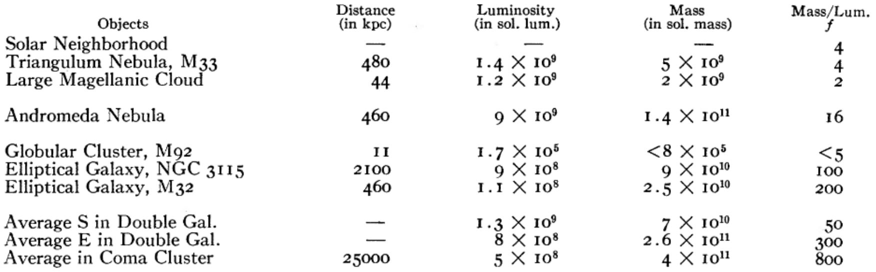

Objects	Distance (in kpc)	Luminosity (in sol. lum.)	Mass (in sol. mass)	Mass/Lum. f
Solar Neighborhood	—	—	—	4
Triangulum Nebula, M33	480	1.4×10^9	5×10^9	4
Large Magellanic Cloud	44	1.2×10^9	2×10^9	2
Andromeda Nebula	460	9×10^9	1.4×10^{11}	16
Globular Cluster, M92	11	1.7×10^5	$<8 \times 10^5$	<5
Elliptical Galaxy, NGC 3115	2100	9×10^8	9×10^{10}	100
Elliptical Galaxy, M32	460	1.1×10^8	2.5×10^{10}	200
Average S in Double Gal.	—	1.3×10^9	7×10^{10}	50
Average E in Double Gal.	—	8×10^8	2.6×10^{11}	300
Average in Coma Cluster	25000	5×10^8	4×10^{11}	800

Figure 3.4: A table showing the distance, luminosity, mass and mass-to-light ratio of different galaxies and galactic cluster as compiled by M. Schwarzschild in his paper [113].

studying several systems of double galaxies [95]. The analysis of the angular separation and the radial velocities of twenty pairs of galaxies suggests an average individual mass of $8 \times 10^{10} M_\odot$, with an uncertainty much less than ±40%. It is worth to mention that in his work Thornton Page also identifies a group of remarkably heavy galaxies, characterized by a mean individual mass of $1.5 \times 10^{11} M_\odot$, thus further whetting what is also referred to as "missing mass problem".

Three years later in the 1954 Martin Schwarzchild, son of the famous Karl Schwarzchild, contributes to shed some light on the missing mass issue by extending the analysis to several astrophysical objects of great interest among which one finds the Coma cluster itself [113]. Martin Schwarzchild updates the distance scale of the celestial bodies and, in the case of the Coma cluster, he also gets rid of the tales values for the radial velocities assuming they could belong to some non-members. Of the twenty-two observed galaxies, five are rejected bringing the root mean square radial velocity relative to the mean of the cluster from $1080 km/s$ down to $630 km/s$. He obtains a final total mass of $3 \times 10^{14} M_\odot$ that, divided among the eight hundred member galaxies, results in an average individual mass of $4 \times 10^{11} M_\odot$ in accordance with Zwicky previous investigation. Martin Schwarzschild summarizes all his results in the table here showed as Fig. 3.4 in which one can see different objects showing a mass-to-light ratio of the same order as the one of the Coma cluster. At this point in time the dark matter hypothesis is not yet commonly accepted, nor is it disregarded. Nevertheless, it is very clear to the astronomers community that the discrepancy between the masses of galaxies inferred from cluster dynamics and those from the rotation of galaxies, or their luminosity, is a problem that needs more information to be finally solved.

As we have seen, the determination of the galaxies cluster masses has historically played a key role supporting the dark matter assumption. In the following part we will briefly touch on three different methods of measuring a galaxies cluster mass.

The Virial theorem: early estimates of cluster masses were based on the application of the Virial theorem. Even if this theorem had already been used in astronomy, the merit to first apply it to galaxies clusters in order to infer their masses goes to Fritz Zwicky, whose work we already cited in the beginning of this chapter. If one assumes that clusters of galaxies are bound and self-gravitating systems, than the virial theorem provides us with a relation between the kinetic and potential energies of the system

$$\bar{T} = -\frac{1}{2}\bar{U}, \tag{3.1}$$

where the bar represents the time average

$$\bar{A} = \frac{1}{\tau}\int_{t=0}^{\tau} dt A\left(t\right) dt. \tag{3.2}$$

One can estimate U assuming at first approximation that the galaxies are, on the average, uniformly distributed inside a sphere of radius R. This is a fair approximation to use if we limit ourselves to just a qualitative order of magnitude estimation. The masses of a generic cluster shell and the sphere delimited by it are

$$m_{\text{ shell }} = 4\pi r^2 \rho dr \quad \text{and} \quad m_{\text{ sphere }} = \frac{4}{3}\pi r^3 \rho. \tag{3.3}$$

Where ρ is considered to be the constant density

$$\rho = \frac{3M}{4\pi R^3}. \tag{3.4}$$

Therefore, the energy required in order to strip away the outermost shell is

$$dU = -G\frac{m_{\text{ shell }}\, m_{\text{ sphere }}}{r}. \tag{3.5}$$

We can then find the total binding energy by integrating over all the shells obtaining

$$\begin{aligned} U &= -G\int_0^R \frac{\left(4\pi r^2\rho\right)\left(\frac{4}{3}\pi r^3\rho\right)}{r} dr \\ &= -\frac{3GM^2}{5R}. \end{aligned} \tag{3.6}$$

Finally, one can express the total kinetic energy $\bar{T}$ in terms of the total mass M by defining the average velocity

$$\bar{v}_{av} : \bar{T} = \sum_{i=1}^{N} m_i \bar{v}_i^2 = \sum_{i=1}^{N} m_i \bar{v}_{av}^2 = M \bar{v}_{av}^2. \tag{3.7}$$

Combining eq. (3.1), eq. (3.6) and eq. (3.7) one obtains

$$M = \frac{5R\bar{v}_{av}^2}{3G}. \tag{3.8}$$

It is worth to underline that, as Zwicky states himself, this method provides just an order of magnitude estimate. Projection effects, contamination by foreground galaxies and anisotropy of the velocity distribution may introduce uncertainties into the determination of the galactic cluster mass. Nevertheless it remains true that these uncertainties by themselves are too small to explain the virial masses Zwicky and other found.

X-Ray: the hot ionized gas present in the galaxies clusters emits in the X-rays band. The gas has a temperature of order $10^8 K$ and contains around $10^{-3} atoms/cm^3$. The fully ionized hydrogen and helium in the clusters produce most of the electrons present in the gas. One defines $\rho_g(r)$ as the mass density of the cluster gas at the distance r. If we assume that the gas is in hydro-static equilibrium, so that the pressure gradient balances the gravitational acceleration, one has

$$\frac{dP}{dr} = -\rho_g(r) g(r). \tag{3.9}$$

The gas pressure P can be related to the density via the ideal gas law

$$\frac{P}{k_B T} = \frac{\rho_g}{\mu_p m_p}, \tag{3.10}$$

where m_p is the mass of the proton and μ_p is the mean atomic mass of the plasma, approximately equal to 0.6 amu. It follows that, for a spherically symmetric system in hydro-static equilibrium, the total dynamical mass under the premise of Newtonian gravity is given by

$$M(r) = -\frac{k_b T r}{G \mu_p m_p} \left(\frac{d\, ln \rho_g(r)}{d\, ln\, r} + \frac{d\, ln\, T(r)}{d\, ln\, r} \right). \tag{3.11}$$

If the gas is isothermal, we can describe its distribution through the formula

$$\rho_g = \rho_g(0)[1 + (R/R_c)^2]^{-3\beta/2}. \tag{3.12}$$

Here R_c represents the core radius and the parameter β is define as follow

$$\beta = \frac{\mu_p m_p \sigma^2}{k_b T}, \tag{3.13}$$

where σ is the line-of-sight velocity dispersion. In the literature this is also referred to as the hydro-static isothermal β-model.

The upside of this method respect to the previous one is the absence of contamination effects together with the fact that the mass distribution is derived directly without any assumption about the dark matter distribution as in the case with the virial theorem. The accuracy of this model has been examined though several hydrodynamical numerical simulations in the past years with sometimes contradictory results. From his study in the 1996, Evrard found that the hydro-static isothermal β-model was able to reproduce remarkably accurate estimates when utilized at radii where the cluster mean density is between 500 and 2500 times the critical density [53]. However, in the same years other authors such as Balland and Blanchard argued for the opposite conclusion stating that the hydro-static equilibrium equation is unstable and so the resulting accuracy of the mass estimates is rather poor [26]. If one jumps ten years ahead, one can find an other study investigating the bias on the X-ray mass estimates with mock long Chandra exposures of five cluster of galaxies obtained from high-resolution hydrodynamic simulation. The authors found that the mass profile obtained via direct application of the hydro-static equilibrium equation was more robust than the one based on the β-model which underestimated the cluster mass up to a 40% [102] [2]. Nowadays application of machine learning techniques to this problem seems to provide very promising updates by identifying the morphological parameters which encode the dynamical state of the cluster. Focusing the attention on the surface brightness concentration, smoothness and asymmetry, parameters whose feature importance reveals to be the highest among the others will allow to improve the accuracy of the future cluster masses predictions as discussed by Sheridan B. Green et al. in their recent paper [66].

---

[2] It is important to remark that the data analysis performed in this work has been made assuming ideal conditions as for example the perfect knowledge on both the background and the instrument response.

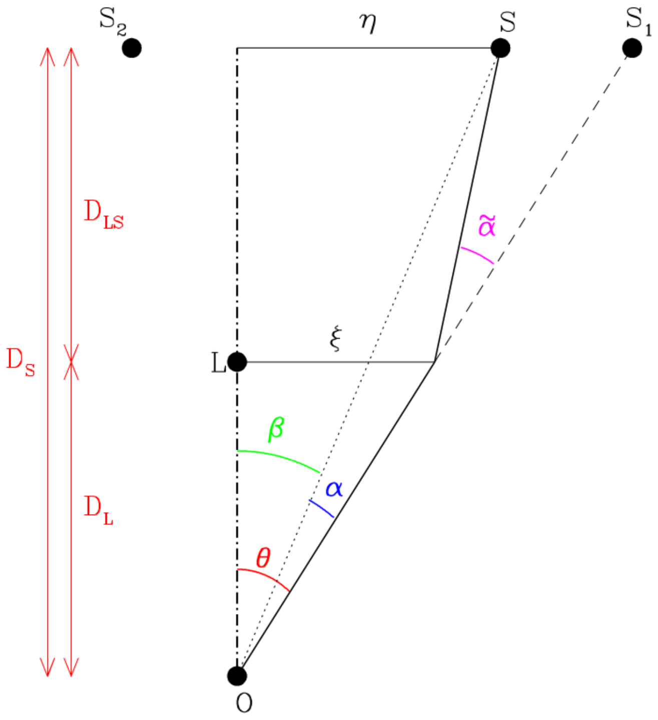

Figure 3.5: The effect of the lens L is to distort the angles β that would be observed in a flat Minkowski background into the angles θ [127].

Gravitational lensing: the last approach we will speak about is the one based on the gravitational lensing mechanism. The fact that light should be affected by the mass distribution of the environment is a quite an old idea. Newton himself was one of its greater supporter. However it was only later that physicists, tanks to the theory of the general relativity, were able to fully describe this phenomenon. Let us assume to have a source S, an observer O and a lens L between them as shown in Fig. 3.5. Light rays emitted from S are deflected by the lens. As a result of this, the observer sees the images in direction corresponding to the tangents to the real incoming light ray paths. If we define $M(\xi)$ as the mass inside the radius ξ, one can evaluate the deflection angle $\tilde{\alpha}(\xi)$ as follows[3]

$$\tilde{\alpha}(\xi) = \frac{4GM(\xi)}{c^2\xi}. \tag{3.14}$$

One can differentiate between three different kinds of gravitational lensing: strong lensing, weak lensing and microlensing. In particular, we are interested in the second one, the weak gravitational lensing. Weak lensing occurs when a non-uniform matter distribution laying between the observing point and distant light sources affects the measurable properties of the sources. Position, shape and brightness of the source can be modified due to the lensing effect. In general, modifications of the position are very difficult to deal with due to the lack of knowledge about the unaffected original position. As for the shape deformation, it can be measured by averaging over a whole ensemble of images. This is possible because the weak lensing acts as the coherent deformation of the shapes of extended backgrounds sources. For this reason large sky surveys such as SDSS [135], COSMOS survey [81], CFHTLS [71], etc. play a key role in the study of this phenomenon.
The first detection of a coherent weak lensing signal is due to Tyson, Valdes and Wenk [123]. They found a systematic alignment of 20-60 faint background galaxy images centered on foreground galaxy cluster. Three years later, N. Kaiser and G. Squires proposed a powerful method to reconstruct the surface mass distribution of the galaxies cluster taking advantage of the relations between the external shear, the convergence and the effective lensing potential. More details can be found in [78]. This method was largely employed and expanded in the following years. In the 1996 G. Wilson, S. Cole and C.S. Frenk proposed a method for estimating a multiplicative factor in order to compensate for the diminished magnitude of the reconstructed density surface in this simulations. They proved that, thanks to this adjustment, weak lensing observations can, not only reproduce accurate maps of the cluster morphology, but also provide a quantitative measurement of the cluster mass distribution [132]. One year earlier, in the 1995, P. Schnelder and C. Seitz proposed the theoretical basis to extend the Kaiser & Squires method to the nonlinear regime, where the liner approximation could not be considered valid anymore as it happens close to the center region of the cluster [112]. More recent works also show how one can take advantage of the weak lensing phenomenon to determine the cluster center [114]. Such an improvement of the cluster center localization, in turn, allows a better

---

[3] It is worth to specify that the previous equation holds true only for the circular-symmetric case in the thin-lens approximation.

estimate of the cluster mass further showing how the gravitational lensing tool plays a key role in the galactic cluster analysis.

3.2.2 Galactic Rotation Curves

The so-called "missing-mass" problem that we have briefly mentioned previously has historically been one of the most important pieces of evidence for dark matter existence. Its origin dates back to beginning of the 20th century when astronomers started to investigate Andromeda (M31) rotation curve, i.e. the circular velocity profile of the stars and gas as a function of their distance from the galactic center [24]. It is actually fairy easy to grasp a qualitatively idea of what this curve should looks like simply using the Kepler's laws. For this purpose let's consider a generic spiral galaxy in which the majority of the stars are located in the galactic disc surrounding its center. Applying the Kepler's third laws one can deduce its rotation curve. If one focuses on the stars populating the outer region of the disc, we can approximate the gravitational force that acts upon them to be the force that would be generated by a mass $M(r)$ located at the center of the galaxy. Then it follows

$$T^2 = \frac{4\pi^2}{G\left(M\left(r\right) + m_{star}\right)} r^3, \tag{3.15}$$

where T is the star's orbital period, m_{star} is its mass and $M\left(r\right)$ represents the total mass inside the orbit of the star. Assuming that $M\left(r\right) \gg m_{star}$[4] one finally gets

$$v\left(r\right) = \sqrt{\frac{GM\left(r\right)}{r}}. \tag{3.16}$$

For $r \to \infty$ we can assume the amount of mass inside the orbit to be the total mass M of the galaxy. We then finally recover the expression

$$v\left(r\right) = \sqrt{\frac{GM}{r}}. \tag{3.17}$$

One would expect the rotational curve to exhibits a power law asymptotic behavior $v\left(r\right) \propto r^{-1/2}$ for large galactocentric radii. However, this expectation turns out to not be in agreement with the experimental measurements as shown in Fig.3.6. In the 1957 a work presenting the first radio rotation curve of M31 was published by van de Hulst, Jean Jacques Raimond, and Hugo van Woerden. Thanks to the new 25 meter radio telescope, the

---

[4] reasonable for outer region's stars

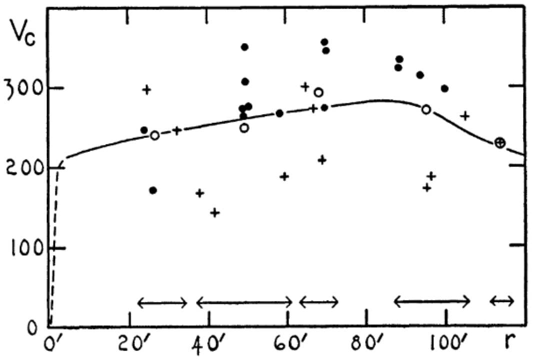

Figure 3.6: The plot shows the circular velocities in the Andromeda Nebula as a function of the distance from the galactic center. The velocities a reported in km/s. In particular the dots mark the observations on the north following side of the nebula whereas the crosses represent the observations on the south preceding side. The circles, finally, identify the normal points [113].

observation could be extended up to 2 degrees away from the galactic center. Remarkably, the rotation curve appeared to remain "flat" even at that greater distances [124].

"At first glance we see from the position of the maxima that [the rotation curve] is of the order of 200 to 250 km/sec throughout this region and that it does not strongly decrease with increasing distance from the center"

The 21 cm emission originates from the "hyperfine structure" of the hydrogen atom. This is a corrections to the hydrogen atom model that takes in account the weak interaction between the spins of the proton and of the electron in the atom. One can think of the quantum spin as the angular momentum of particles spinning on their own axis. In the particular case of an hydrogen atom these particles would be the proton and the electron. Keeping this simple picture in mind, one can think the electron and the proton as magnetic dipoles generating slights magnetic fields due to their rotating motion. The 21 cm transition is a direct result of the interaction of these two "magnetic" fields. There is in fact an energy difference between when the dipole moments of the two particles are aligned or anti-aligned. In particular, the state where the two magnetic moments are anti-aligned is

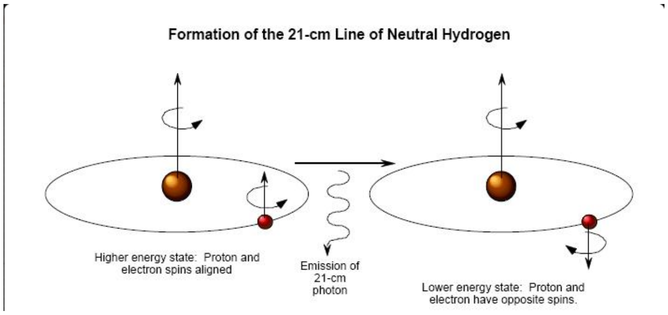

Figure 3.7: Schematisation of the hydrogen atomic transition.

a lower energy state. When the two magnetic moments are aligned, in fact, the energy increases making the system less stable. When the electron in the atom goes under a transition from aligned to anti-aligned a photon is produced (for reference see Fig. 3.7). The wavelength of the released photon happens to be of 21 cm from which one gets this line name. The reasons why this emission is so important in astronomy and for the evolution of the missing-mass problem are multiple. First it allows to expand the survey frequency pull out from the optical and near infrared range. Galaxies can now be identified on the bases of their gas content rather than of theirs stellar one. This come very handy when trying to detect low surface brightness galaxies which usually lack in stars quantity. This advantage of course holds true also for galaxies' outer regions where the local stellar density drops down. The other advantage is that one can get spectral data in a natural way along with all the information that they carry with them, e.g. the redshift, or recession velocity and the rotational velocity of the galaxy. The 21 cm emission, therefore, allows also to extend the rotational curve to larger radii.

In the 1970 good quality spectroscopic observations are extended out to 110 arcminutes away from the galactic center thanks to the image tube spectrograph developed by Kent Ford ten years earlier, thus establishing an other milestone in the context of the galactic rotation curves. In the same year Vera Rubin and Kent Ford publish their work [108] showing that the data they obtained are indeed compatibles with radio measurements obtained in the 1966 by M. Roberts [104]. It is also worth to mention the study done by K. Freeman on the rotation curves pick for the M33 and NGC 300 [56] and the work published by D. Rogstad and G. Shostak on the rotation curves of five different galaxies - M33, NGC 2403, IC 342, M101 and NGC 6946 [105]. Freeman noticed that the rotation curves exhibited pick at

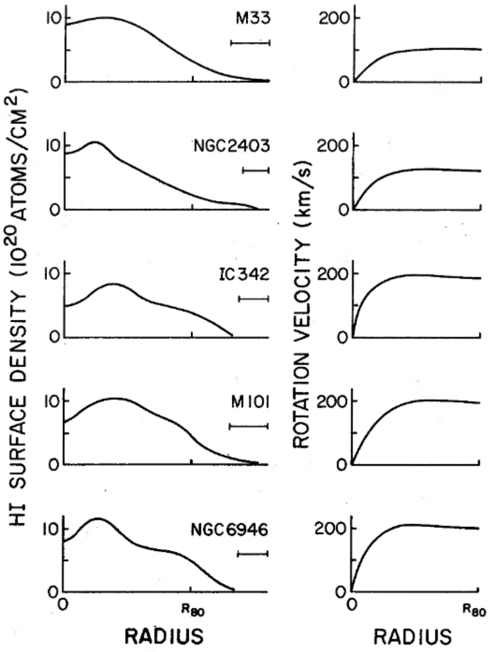

Figure 3.8: The plot shows the azimuthally averaged hydrogen surface densities (on the left) and the rotation velocities (on the right) for the galaxies M33, NGC2403, IC342, M101 and NGC 6946. R_{80} marks the radius within which the 80% of the observed hydrogen is found [105].

larger radii than predicted whereas D. Rogstad and G. Shostak found that the rotation curve for all the five galaxies they studied remained flat out to the largest radii observed. See Fig.3.8. In the next years, several other works follow. The galaxies pull and the maximum observed radius grow to a point where it seems fair to assume that the rotation curves of these objects stay flat well beyond the optical size of the galaxies. Such result strongly suggests that the galaxies mass continues to grow beyond the region occupied by the stars and gas [109]. By the end of the eighties, the flat rotation curves observed by radio astronomers has done much to establish the existence of some kind of invisible mass filling the outer parts of galaxies as we read in the review on the status of the "missing mass problem" authored by Sandra Faber and John Gallagher [54].

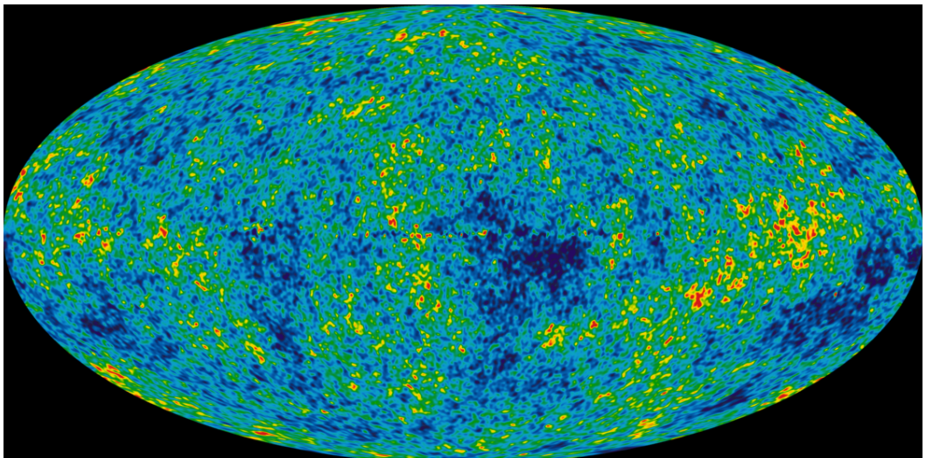

Figure 3.9: The full-sky image of the temperature fluctuations in the cosmic microwaves background as a result of nine years of WMAP data collection.

3.2.3 Cosmic Microwave Background

The cosmic microwave background (CMB) radiation first discovered by Penzias and Wilson [96] represents an other extremely powerful tool to constrain different key characteristics of our Universe such as its geometry and its matter content. This radiation is thought to be the leftover from the Big Bang. Right after the Big Bang, the Universe is an hot and dense plasma of photons, leptons and quarks. Protons appear some time later when the Universe had expanded and cooled enough. At this stage, the mean free path a photon can travel before encountering a free electron is still very short and thus the early Universe results to be effectively opaque to electromagnetic radiation. Eventually, the temperature goes down enough that the formation of neutral hydrogen becomes energetically favored and the fraction of free electrons and protons drops substantially. The hydrogen atoms created after this recombination present electrons in a high energy state. The transition of these electrons to lower energy states is associated with photons emission. Such a phenomenon goes under the name of *photon decoupling*. The cosmic microwave background radiation that we observe today is made up exactly by these photons that decoupled from matter and traveled freely through the universe. Today, the CMB shows a thermal spectrum almost indistinguishable from the one of a black body at a temperature of 2.72548 ± 0.00057 K. Such a spectrum, characterized by small anisotropies, seems to be otherwise homogeneous to an extremely high degree. These anisotropies can be modeled as small fluctuation about the Friedmann-Robertson-Walker metric whose dynamics is led by the laws of general relativity. The extensive data obtained by space missions like COBE [27], WMAPS [119] and PLANK [101] allowed the use of the Monte Carlo Markov Chain method to reproduce the evolution of the Universe and finally constrain the primary parameters of the model. As an example in Fig. 3.10 we show the list of parameters utilized by the Plank collaboration in one of their recent analysis [100]. As one can see, although the baryon density $\omega_b = \Omega_b h^2$ and dark matter density $\omega_c = \Omega_c h^2$ are allowed to variate in the range [0.005, 0.1] and [0.001, 0.99] respectively, the current determination for these two parameters are according to the Plank collaboration around the values $\omega_b = 0.02230 \pm 0.00014$ and $\omega_c = 0.1188 \pm 0.0010$ [5]. We see it more explicitly in Fig. 3.11. The estimations of the barion and dark matter densities can vary slightly depending on the data sets one decides to use in conjunction with the one deriving from the CMB observation. The use of external data sets as a complement to the CMB anisotropies power spectrum is done not only to improve the final estimations themselves, but mainly to remove - or at least mitigate - the degeneracy in the parameter space. To conclude, the analysis of the anisotropies of the cosmic microwave background radiation not only seems to prove the auto consistency of the ΛCDM model, but also represent a strong hint to the existence of dark matter from a large scale (high redshift) point of view.

3.3 Dark Matter candidates

3.3.1 Intergalactic gas and MACHOs

We saw how the idea that some form of hidden mass is present in both galaxies and galactic cluster strengthened during the twentieth century. Astronomers came up with different ideas in order to address and hopefully shade light on the mass discrepancy problem. One of the first hypothesis assumed *intergalactic gas* to be the responsible of such high mass-to-luminosity ratio values. However, it was put aside when studies on the Coma and Pegasus I clusters showed that hydrogen abundance was less than the 2% of what would have been required for gravitational binding [97, 87]. With the intergalactic gas ruled out, the next hypothesis pointed to what were probably the second most likely candidates: compact objects qualitatively similar to ordinary stars but otherwise much less luminous. In this group

---

[5] the error intervals here represent the 68% confidence limit.

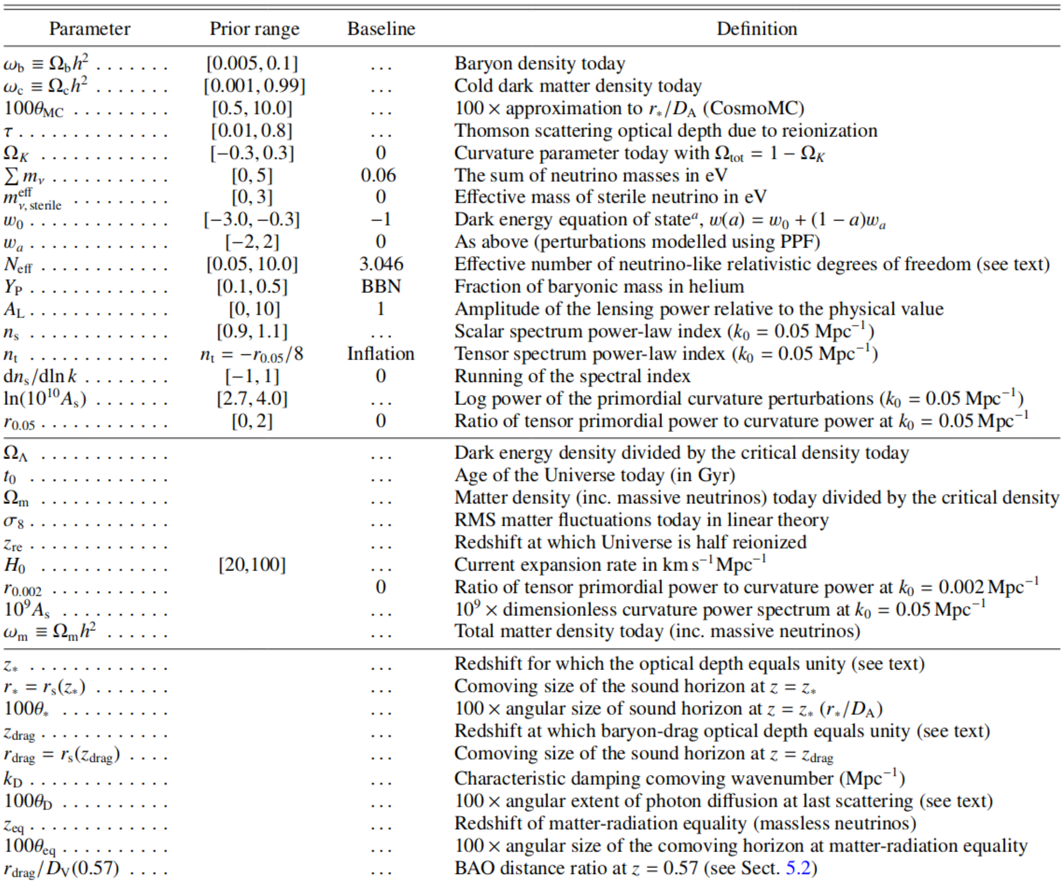

Parameter	Prior range	Baseline	Definition
$\omega_b \equiv \Omega_b h^2$	$[0.005, 0.1]$	...	Baryon density today
$\omega_c \equiv \Omega_c h^2$	$[0.001, 0.99]$	...	Cold dark matter density today
$100\theta_{MC}$	$[0.5, 10.0]$	...	$100 \times$ approximation to r_*/D_A (CosmoMC)
τ	$[0.01, 0.8]$	...	Thomson scattering optical depth due to reionization
Ω_K	$[-0.3, 0.3]$	0	Curvature parameter today with $\Omega_{tot} = 1 - \Omega_K$
$\sum m_\nu$	$[0, 5]$	0.06	The sum of neutrino masses in eV
$m^{eff}_{\nu,\,sterile}$	$[0, 3]$	0	Effective mass of sterile neutrino in eV
w_0	$[-3.0, -0.3]$	-1	Dark energy equation of state^a, $w(a) = w_0 + (1-a)w_a$
w_a	$[-2, 2]$	0	As above (perturbations modelled using PPF)
N_{eff}	$[0.05, 10.0]$	3.046	Effective number of neutrino-like relativistic degrees of freedom (see text)
Y_P	$[0.1, 0.5]$	BBN	Fraction of baryonic mass in helium
A_L	$[0, 10]$	1	Amplitude of the lensing power relative to the physical value
n_s	$[0.9, 1.1]$	...	Scalar spectrum power-law index ($k_0 = 0.05\,\mathrm{Mpc}^{-1}$)
n_t	$n_t = -r_{0.05}/8$	Inflation	Tensor spectrum power-law index ($k_0 = 0.05\,\mathrm{Mpc}^{-1}$)
$dn_s/d\ln k$	$[-1, 1]$	0	Running of the spectral index
$\ln(10^{10}A_s)$	$[2.7, 4.0]$	...	Log power of the primordial curvature perturbations ($k_0 = 0.05\,\mathrm{Mpc}^{-1}$)
$r_{0.05}$	$[0, 2]$	0	Ratio of tensor primordial power to curvature power at $k_0 = 0.05\,\mathrm{Mpc}^{-1}$
Ω_Λ		...	Dark energy density divided by the critical density today
t_0		...	Age of the Universe today (in Gyr)
Ω_m		...	Matter density (inc. massive neutrinos) today divided by the critical density
σ_8		...	RMS matter fluctuations today in linear theory
z_{re}		...	Redshift at which Universe is half reionized
H_0	$[20, 100]$	...	Current expansion rate in $\mathrm{km\,s^{-1}Mpc^{-1}}$
$r_{0.002}$		0	Ratio of tensor primordial power to curvature power at $k_0 = 0.002\,\mathrm{Mpc}^{-1}$
$10^9 A_s$		...	$10^9 \times$ dimensionless curvature power spectrum at $k_0 = 0.05\,\mathrm{Mpc}^{-1}$
$\omega_m \equiv \Omega_m h^2$		...	Total matter density today (inc. massive neutrinos)
z_*		...	Redshift for which the optical depth equals unity (see text)
$r_* = r_s(z_*)$		...	Comoving size of the sound horizon at $z = z_*$
$100\theta_*$		...	$100 \times$ angular size of sound horizon at $z = z_*$ (r_*/D_A)
z_{drag}		...	Redshift at which baryon-drag optical depth equals unity (see text)
$r_{drag} = r_s(z_{drag})$		...	Comoving size of the sound horizon at $z = z_{drag}$
k_D		...	Characteristic damping comoving wavenumber (Mpc^{-1})
$100\theta_D$		...	$100 \times$ angular extent of photon diffusion at last scattering (see text)
z_{eq}		...	Redshift of matter-radiation equality (massless neutrinos)
$100\theta_{eq}$		...	$100 \times$ angular size of the comoving horizon at matter-radiation equality
$r_{drag}/D_V(0.57)$		...	BAO distance ratio at $z = 0.57$ (see Sect. 5.2)

Figure 3.10: List of the cosmological parameters used. For each of them a summary definition as well as the value taken in the base ΛCDM model (where appropriate) is given. The top block groups the primary parameters that are varied in the Monte Carlo Markov Chain with uniform priors. The range of these priors are listed in square brackets.
Note In addition to the other priors, a hard prior of [20, 100] km/(s Mpc) has been imposed on the Hubble constant H_0.

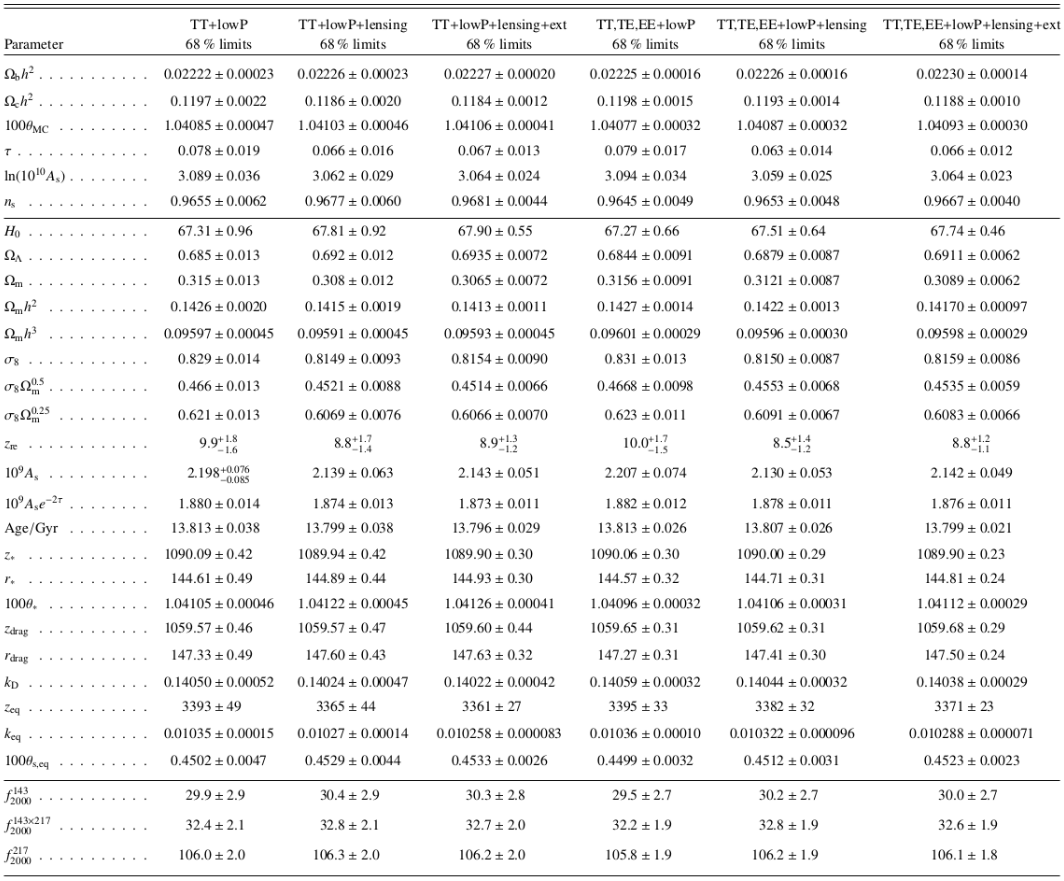

Parameter	TT+lowP 68 % limits	TT+lowP+lensing 68 % limits	TT+lowP+lensing+ext 68 % limits	TT,TE,EE+lowP 68 % limits	TT,TE,EE+lowP+lensing 68 % limits	TT,TE,EE+lowP+lensing+ext 68 % limits
$\Omega_b h^2$	0.02222 ± 0.00023	0.02226 ± 0.00023	0.02227 ± 0.00020	0.02225 ± 0.00016	0.02226 ± 0.00016	0.02230 ± 0.00014
$\Omega_c h^2$	0.1197 ± 0.0022	0.1186 ± 0.0020	0.1184 ± 0.0012	0.1198 ± 0.0015	0.1193 ± 0.0014	0.1188 ± 0.0010
$100\theta_{MC}$	1.04085 ± 0.00047	1.04103 ± 0.00046	1.04106 ± 0.00041	1.04077 ± 0.00032	1.04087 ± 0.00032	1.04093 ± 0.00030
τ	0.078 ± 0.019	0.066 ± 0.016	0.067 ± 0.013	0.079 ± 0.017	0.063 ± 0.014	0.066 ± 0.012
$\ln(10^{10} A_s)$	3.089 ± 0.036	3.062 ± 0.029	3.064 ± 0.024	3.094 ± 0.034	3.059 ± 0.025	3.064 ± 0.023
n_s	0.9655 ± 0.0062	0.9677 ± 0.0060	0.9681 ± 0.0044	0.9645 ± 0.0049	0.9653 ± 0.0048	0.9667 ± 0.0040
H_0	67.31 ± 0.96	67.81 ± 0.92	67.90 ± 0.55	67.27 ± 0.66	67.51 ± 0.64	67.74 ± 0.46
Ω_Λ	0.685 ± 0.013	0.692 ± 0.012	0.6935 ± 0.0072	0.6844 ± 0.0091	0.6879 ± 0.0087	0.6911 ± 0.0062
Ω_m	0.315 ± 0.013	0.308 ± 0.012	0.3065 ± 0.0072	0.3156 ± 0.0091	0.3121 ± 0.0087	0.3089 ± 0.0062
$\Omega_m h^2$	0.1426 ± 0.0020	0.1415 ± 0.0019	0.1413 ± 0.0011	0.1427 ± 0.0014	0.1422 ± 0.0013	0.14170 ± 0.00097
$\Omega_m h^3$	0.09597 ± 0.00045	0.09591 ± 0.00045	0.09593 ± 0.00045	0.09601 ± 0.00029	0.09596 ± 0.00030	0.09598 ± 0.00029
σ_8	0.829 ± 0.014	0.8149 ± 0.0093	0.8154 ± 0.0090	0.831 ± 0.013	0.8150 ± 0.0087	0.8159 ± 0.0086
$\sigma_8 \Omega_m^{0.5}$	0.466 ± 0.013	0.4521 ± 0.0088	0.4514 ± 0.0066	0.4668 ± 0.0098	0.4553 ± 0.0068	0.4535 ± 0.0059
$\sigma_8 \Omega_m^{0.25}$	0.621 ± 0.013	0.6069 ± 0.0076	0.6066 ± 0.0070	0.623 ± 0.011	0.6091 ± 0.0067	0.6083 ± 0.0066
z_{re}	$9.9^{+1.8}_{-1.6}$	$8.8^{+1.7}_{-1.4}$	$8.9^{+1.3}_{-1.2}$	$10.0^{+1.7}_{-1.5}$	$8.5^{+1.4}_{-1.2}$	$8.8^{+1.2}_{-1.1}$
$10^9 A_s$	$2.198^{+0.076}_{-0.085}$	2.139 ± 0.063	2.143 ± 0.051	2.207 ± 0.074	2.130 ± 0.053	2.142 ± 0.049
$10^9 A_s e^{-2\tau}$	1.880 ± 0.014	1.874 ± 0.013	1.873 ± 0.011	1.882 ± 0.012	1.878 ± 0.011	1.876 ± 0.011
Age/Gyr	13.813 ± 0.038	13.799 ± 0.038	13.796 ± 0.029	13.813 ± 0.026	13.807 ± 0.026	13.799 ± 0.021
z_*	1090.09 ± 0.42	1089.94 ± 0.42	1089.90 ± 0.30	1090.06 ± 0.30	1090.00 ± 0.29	1089.90 ± 0.23
r_*	144.61 ± 0.49	144.89 ± 0.44	144.93 ± 0.30	144.57 ± 0.32	144.71 ± 0.31	144.81 ± 0.24
$100\theta_*$	1.04105 ± 0.00046	1.04122 ± 0.00045	1.04126 ± 0.00041	1.04096 ± 0.00032	1.04106 ± 0.00031	1.04112 ± 0.00029
z_{drag}	1059.57 ± 0.46	1059.57 ± 0.47	1059.60 ± 0.44	1059.65 ± 0.31	1059.62 ± 0.31	1059.68 ± 0.29
r_{drag}	147.33 ± 0.49	147.60 ± 0.43	147.63 ± 0.32	147.27 ± 0.31	147.41 ± 0.30	147.50 ± 0.24
k_D	0.14050 ± 0.00052	0.14024 ± 0.00047	0.14022 ± 0.00042	0.14059 ± 0.00032	0.14044 ± 0.00032	0.14038 ± 0.00029
z_{eq}	3393 ± 49	3365 ± 44	3361 ± 27	3395 ± 33	3382 ± 32	3371 ± 23
k_{eq}	0.01035 ± 0.00015	0.01027 ± 0.00014	0.010258 ± 0.000083	0.01036 ± 0.00010	0.010322 ± 0.000096	0.010288 ± 0.000071
$100\theta_{s,eq}$	0.4502 ± 0.0047	0.4529 ± 0.0044	0.4533 ± 0.0026	0.4499 ± 0.0032	0.4512 ± 0.0031	0.4523 ± 0.0023
f_{2000}^{143}	29.9 ± 2.9	30.4 ± 2.9	30.3 ± 2.8	29.5 ± 2.7	30.2 ± 2.7	30.0 ± 2.7
$f_{2000}^{143\times217}$	32.4 ± 2.1	32.8 ± 2.1	32.7 ± 2.0	32.2 ± 1.9	32.8 ± 1.9	32.6 ± 1.9
f_{2000}^{217}	106.0 ± 2.0	106.3 ± 2.0	106.2 ± 2.0	105.8 ± 1.9	106.2 ± 1.9	106.1 ± 1.8

Figure 3.11: List of the parameters 68% confidence limits for the base ΛCDM model. The confidence limits are obtained from the Plank CMB power spectra in conjunction with lensing reconstruction ("lensing") and external data ("ext") such as barionic acoustic oscillation (BAO) and joint light-curve Analysis (JLA) [101].

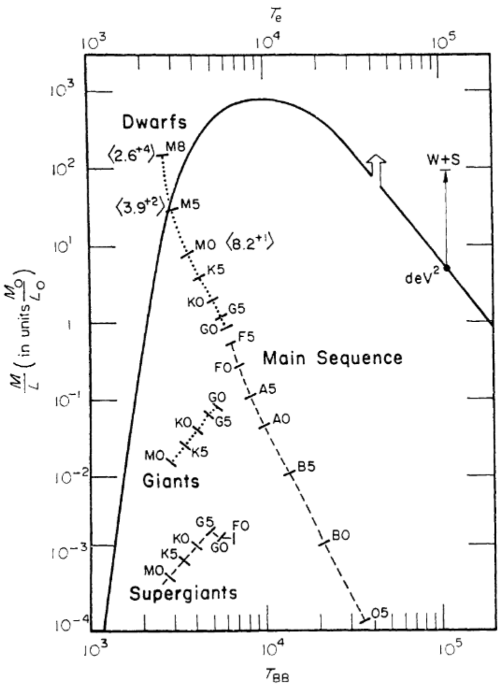

Figure 3.12: The plot shows the limit on the mass-luminosity-ratio of a population of stars whose total mass is sufficient to bind the Coma cluster. M8 dwarf stars, obtained continuing the stellar mass function are proposed as viable explanation to the mass-luminosity-ration discrepancy in the Coma cluster [118].

one finds black holes, neutron stars as well as white and red dwarf and planets. These objects, disseminated either in the galactic halos or in the intra-cluster space, all have at fist glance the quality needed to fit the role of "dark matter". As an example one can look at the J. Tarter and J. Silk paper in which they show that M8 dwarf stars cloud be able to account for the unseen mass present in the Coma cluster [118]. These objects were later grouped under the label MACHOs -massive astrophysical compact halo objects - by Kim Griest in contrast with the rising conjecture according to which dark matter would be made up of weakly interacting massive particles - WIMPs. Nowadays the MACHOs hypothesis is quite strongly dismissed as gravitational microlensing surveys, together with the determination of the primordial light element abundances, favor a non-baryonic nature for the dark matter. In fact, even if the MACHOs electromagnetic emission is very faint or totally absent by itself, these objects can still be detected by looking for the effect that their presence exerts on the light emitted by surrounding stars and galaxies. In particular, in any nearby galaxy, a star has a probability of 10^{-6} to be strongly microlensed by a compact object located in the Milky Way halo. The maximum amplification is obtained when the source, the observer and the lensing point mass are all perfectly aligned. The duration of the lensing phenomenon is expected to last between 2 hours and 2 years for object masses that range from $10^{-6}M_\odot$ to $10^{2}M_\odot$ [35]. In the 2000 a 5.7 years long detection campaign of the Large Magellanic Cloud reveals 13-17 possible candidates, way more than the 2-4 expected from the known stellar population. As a result the MACHO collaboration concluded that the macho halo fraction for the Large Magellanic Cloud was around 20% with a 95% confidence interval of 8% to 50% [14]. However, an other extensive campaign lead by the EROS (Experience pour la Recherche d'Objets Sombres) collaboration revealed that the previous result were quite too optimistic. Covering a larger solid angle than MACHO (43 deg^2 instead of 11 deg^2), thus reducing the contamination due to self-lensing, and having an higher sampling frequency, they were able to find just one candidate. As a result, the macho halo fraction value was updated to 8% with a 95% confidence level and machos in the mass range $0.6 \times 10^{-7}M_\odot < M < 15M_\odot$ were ruled out as primary dark matter candidates [83, 120]. As we already mentioned, the determination of the primordial light element abundances is of great importance in reinforcing the idea that machos can not be part of the dark matter paradigm. In the beginning of the second half of the twentieth century people started to realize that stellar nucleosynthesis could not account for total observed helium abundance [33]. Deuterium abundance also revealed to be an hot point. Despite the fact that it is not generated in stars, it appears to be very present in the interstellar medium. In the 1973, H. Reeves et al. argued that pregalactic nucleosynthetis offered the most plausible solution for this puzzling dilemma [103]. More important, the study of the abundance of the primordial light elements allowed to derive upper limits on the cosmological baryon density. In their paper published in May 2001, S. Burles et al. infer a baryonic fraction $\Omega_B h^2 = 0.020 \pm 0.002$ at 95% confidence level [34]. These value proves to be in good agreement with the one we just mentioned in the previous section obtained by WMAP and Plank through the analysis of the cosmic microwave background (see Fig. 3.13). In light of this results, it is rather clear that the answer to the missing mass problem cannot come from machos or baryonic matter.

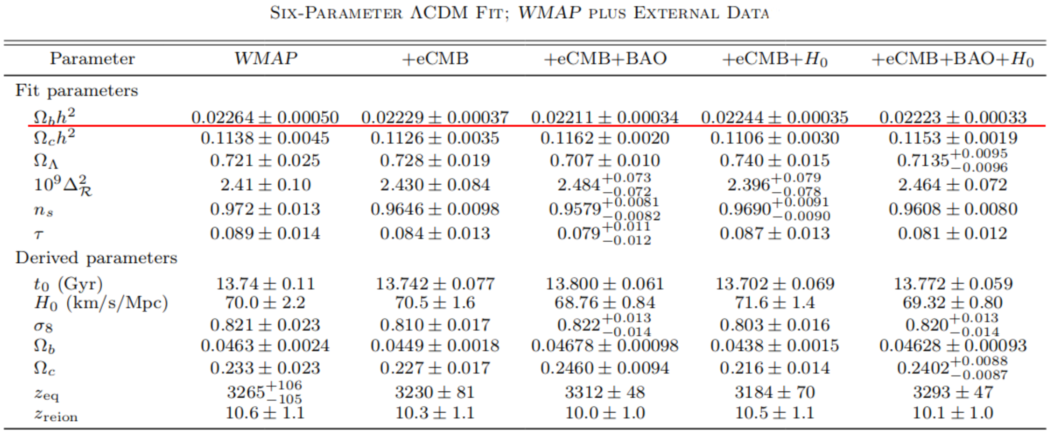

Six-Parameter ΛCDM Fit; *WMAP* plus External Data

Parameter	*WMAP*	+eCMB	+eCMB+BAO	+eCMB+H_0	+eCMB+BAO+H_0
Fit parameters					
$\Omega_b h^2$	0.02264 ± 0.00050	0.02229 ± 0.00037	0.02211 ± 0.00034	0.02244 ± 0.00035	0.02223 ± 0.00033
$\Omega_c h^2$	0.1138 ± 0.0045	0.1126 ± 0.0035	0.1162 ± 0.0020	0.1106 ± 0.0030	0.1153 ± 0.0019
Ω_Λ	0.721 ± 0.025	0.728 ± 0.019	0.707 ± 0.010	0.740 ± 0.015	$0.7135^{+0.0095}_{-0.0096}$
$10^9 \Delta^2_{\mathcal{R}}$	2.41 ± 0.10	2.430 ± 0.084	$2.484^{+0.073}_{-0.072}$	$2.396^{+0.079}_{-0.078}$	2.464 ± 0.072
n_s	0.972 ± 0.013	0.9646 ± 0.0098	$0.9579^{+0.0081}_{-0.0082}$	$0.9690^{+0.0091}_{-0.0090}$	0.9608 ± 0.0080
τ	0.089 ± 0.014	0.084 ± 0.013	$0.079^{+0.011}_{-0.012}$	0.087 ± 0.013	0.081 ± 0.012
Derived parameters					
t_0 (Gyr)	13.74 ± 0.11	13.742 ± 0.077	13.800 ± 0.061	13.702 ± 0.069	13.772 ± 0.059
H_0 (km/s/Mpc)	70.0 ± 2.2	70.5 ± 1.6	68.76 ± 0.84	71.6 ± 1.4	69.32 ± 0.80
σ_8	0.821 ± 0.023	0.810 ± 0.017	$0.822^{+0.013}_{-0.014}$	0.803 ± 0.016	$0.820^{+0.013}_{-0.014}$
Ω_b	0.0463 ± 0.0024	0.0449 ± 0.0018	0.04678 ± 0.00098	0.0438 ± 0.0015	0.04628 ± 0.00093
Ω_c	0.233 ± 0.023	0.227 ± 0.017	0.2460 ± 0.0094	0.216 ± 0.014	$0.2402^{+0.0088}_{-0.0087}$
$z_{\rm eq}$	3265^{+106}_{-105}	3230 ± 81	3312 ± 48	3184 ± 70	3293 ± 47
$z_{\rm reion}$	10.6 ± 1.1	10.3 ± 1.1	10.0 ± 1.0	10.5 ± 1.1	10.1 ± 1.0

Figure 3.13: ΛCDM model fit to $WMAP$ nine-year data combined with a progression of external data sets. For a complete list of parameter values for this model look at http://lambda.gsfc.nasa.gov/ [72]. The value for $\Omega_b h^2$ reported in the table shows why even if baryonic matter can contribute to account for the missing mass in galaxies and galactic clusters, it can not be the only reason behind this discrepancy.

3.3.2 WIMPs

If the constituents of dark matter cannot be found in baryonic matter, then one must look elsewhere. The weakly interacting massive particles (WIMPs) hypothesis responds exactly to this need. Strictly speaking only those particles whose mass is between 2 GeV and hundreds of TeV and that interact through the weak interaction coupling of the Standard Model fall into the wimps category. However, from a more loose point of view, any massive particle that possess a weak, but non negligible coupling to the ordinary matter could be referred as a wimp. Claiming for the existence of a new particle is not something someone does without second thoughts. To assume the existence of new kind of matter one would like to have more than just the need to solve an incongruity of its cosmological model. One of the reasons why wimps are so appealing is indeed because the scientific community already has different other motivation to extend the Standard Model in the weak sector. Most of these motivations arise from the need to explain experimental data that otherwise one would be able to justify only for seemingly “unnatural” choices of parameters. To give an example of this “fine-tuning” problem we can look at the Higgs boson mass m_h and its value. The physical mass of the Higgs boson is obtained by adding the quantum correction due to loop-level diagrams Δm_h^2 to the its standard tree-level mass m_{h0}^2

$$m_h^2 = m_{h0}^2 + \Delta m_h^2 \sim m_{h0}^2 + \frac{\lambda^2}{16\pi^2}\Lambda^2. \tag{3.18}$$

Here λ is an $\mathcal{O}(1)$ dimensionless coupling parameter whereas Λ represents the energy scale at which the standard model is no longer a valid description of the nature. Because Δm_h^2 is proportional to Λ one would expect m_h to be roughly of the same order of magnitude too. However, this does not seem to be the case as $m_h \sim 100\,GeV$ whereas $\Lambda \sim M_{Pl} \simeq 1.2 \times 10^{19}\,GeV$. This in turn implies that m_{h0}^2 and Δm_h^2 must cancel to 1 part in 10^{36} in order to obtain the expected physical Higgs mass, which is hardly reasonable. Such a paradox may be circumvented if $\Lambda \leq 1\,TeV$, that would imply the existence of new physics at the weak scale. One could also suggest that maybe the Higgs boson is not a fundamental scalar. However, even in this scenario, some new particle at the weak scale would be required in order to describe the Higgs boson structure. Either way the solution of the *hierarchy problem* - as it is called - seems to imply the existence of new particles with mass around $m_{weak} \sim 10\,GeV - TeV$.

An other reason why physicists has been attracted by the WIMP hypothesis has to do with the natural ability they have to match the expected abundance determined by the analysis of the cosmic microwave background. Such a feature is often referred to as the "WIMPs miracle". Let us assume that in the early hot and dense universe the (generic) dark matter (DM) particles χ, as well as the standard matter (SM), were in thermal equilibrium with the primordial thermal bath. Particles production from annihilation balanced each other out. The dark matter number density is defined as follows

$$n_\chi(T) = \int \frac{d^3p}{(2\pi)^3} f_\chi(p,T), \tag{3.19}$$

where f_χ represents the dark matter distribution function. One can then describe the cosmological evolution of the dark matter particle through the Boltzmann equation

$$\frac{dn_\chi}{dt} + 3H(T)\,n_\chi = -\langle\sigma v\rangle\left(n_\chi^2 - n_{\chi,eq}^2\right). \tag{3.20}$$

$H(T)$ is the Hubble rate whereas the quantity σv on the left hand side of the equation is the pair annihilation cross-section associated to the process

$$\chi + \chi \rightarrow SM + SM. \tag{3.21}$$

Being the cross-section temperature depended, its thermal averaged is taken. Finally $n_{\chi,eq}$ represents the equilibrium number density. One can estimate $n_{\chi,eq}$ by replacing f_χ with the equilibrium distribution function (conventionally taken to be the Maxwell-Boltzmann distribution) in the eq. (3.19). As the Universe expands it also starts to cool down and eventually its temperature drops below the dark matter mass. Under the hypothesis that the χ particle remains in a state of thermal equilibrium, its annihilation rate will enter the so-called "Boltzmann-tail" where

$$n_{\chi,eq} \propto e^{-m_\chi/T}. \tag{3.22}$$

In this state the number of dark matter particles would drop to zero, except that the Universe expansion prevents such a thing to happen. Once the Hubble rate $H(T)$ overcome the annihilation rate one gets what is called a thermal freeze-out. The Universe had become so large that the dark matter particles are no longer able to find each other to annihilate. Their number therefore asymptotically approaches to a constant called "thermal relic density"

$$\Omega_{DM} = \frac{m_\chi s_0 Y_0}{\rho_c}. \tag{3.23}$$

Here s_0 is the present time entropy density, Y_0 is the comoving dark matter number density evaluated at today's temperature and ρ_c is the critical density of the Universe

$$\rho_c(T) = \frac{3H(T)^2 M_{PL}^2}{8\pi}. \tag{3.24}$$

The comoving density Y_0 can be semi-analytically estimated through the equation

$$Y_0 \simeq \frac{\pi}{45} M_{PL} \left[\int_{T_0}^{T_f} g_*^{1/2} \langle\sigma v\rangle dT\right]^{-1}, \tag{3.25}$$

where T_f is the freeze-out temperature and $g_*^{1/2}$ is a function of the temperature T related to the degrees of freedom of the primordial thermal bath (see more in [64]).

The dark matter relic density can be then numerically evaluated making use of the expressions above

$$\Omega_{DM} h^2 \approx 8.76 \times 10^{-11} GeV^{-2} \left[\int_{T_0}^{T_f} g_*^{1/2} \langle\sigma v\rangle \frac{dT}{m_\chi}\right]^{-1}. \tag{3.26}$$

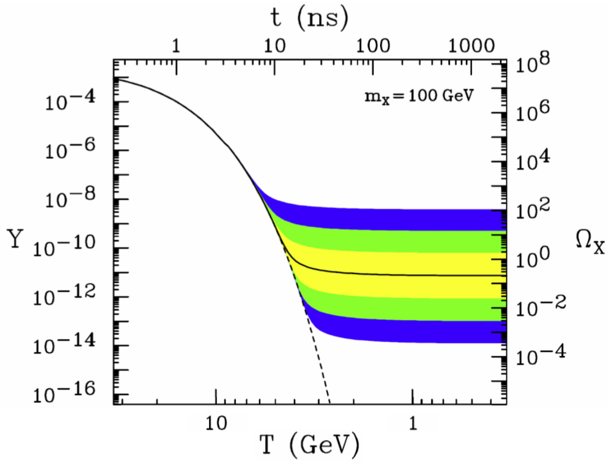

Figure 3.14: The panel shows the time (top) and temperature (bottom) dependence of the comoving number density Y and the thermal relic density $\Omega_\chi$of a 100 GeV, P-wave annihilating dark matter particle. The dashed line pictures the number density of a particle that remain in thermal equilibrium whereas the solid one is associated with an annihilation cross-section that yields to the relic density suggested by CMB analysis [55].

The reason why the WIMP hypothesis is such an attractive solution of the dark matter issue is that, for typical weak-scale pair annihilation cross-sections[6] $\sigma \sim G_F^2 T^2$, typical freeze-out temperature $T \sim m_\chi/20$ and for electroweak mass-scale $m_\chi \sim 200GeV$, the thermal relic density obtained through eq. (3.26) matches the experimental cosmological density determination $\Omega_{DM}h^2 \approx 0.12$. It must be realized that the occurrence of this match between theoretical and the experimental one relies specifically on the cross-section and partially on the particle's mass. Therefore, one must not regard at it as something unique to the weak scale and the weak interaction. By the same token, not all the wimp candidates are able to reproduce this result (see the neutralino relic density n the SUSY model [25]). Nevertheless, it is remarkable that particles whose existence has been hypothesized for theoretical reasons would also be able to solve the dark matter issue so elegantly.

An other characteristic usually ascribed to wimps is to not be relativistic around the time when they fall out of thermal equilibrium in the early Universe. The reason behind this are easy to understand. Let us assume dark matter particles to be relativist at the time of decoupling from thermal

---

[6] G_F represents the Fermi constant.

plasma. A candidate for this so-called hot dark matter (HDM) could be for example the light ($m_n \sim 10\, eV$) neutrinos. The limitations of this model have been known since the 1980s [129]. Because of the large primordial coherence length of the neutrino distribution, the resulting clustering scale cannot be consistent with what we observe, at least without exotic assumptions on the other cosmological parameters. As analyzed by C. S. Frenk and D. M. White, in such a universe supercluster formation would precede the formation of the galaxies themselves leading to a galaxy distribution characterized by a large and well-defined scale which is clearly in contrast with the pictures provided by the CfA redshift survey [57]. Because of this severe discrepancy, the community agree that hot dark matter contribution to the total dark matter density can only be negligible, if not completely null.

On the other hand non relativistic dark matter, also called cold dark matter (CDM), seems to behave in a very different way. Once decoupled from the thermal plasma, its density perturbations begin to grow linearly. This provides early potential wells that act as seeds to trigger and/or to enhance the development of standard matter density perturbations. Such a feature is in fact one of the main reason why the cold dark matter model is able to successful reproduce the observations provided by large scale structure numerical simulations Fig. 3.15. It must be said that the cold dark matter conjecture exhibits some weak points as well. Dissipationless ΛCDM simulations produce massive subhaloes whose density is too high to host any of the observed bright satellite [31] and fail to recover the correct number of substructure at the galactic scale [88]. In particular, the latter goes by the name of the "missing satellite problem" (MSP) and the scientific community seems to have taken a big step forward in solving it the last year. In their work published in November 2018, Stacy Y. Kim et al. show how the discrepancy underlying the missing satellite problem can be reduced, or even extinguished, thanks to the discovery of many new dwarfs below the luminosity limit thus strengthening the cold dark matter hypothesis [79].

Warm dark matter in the form of a sterile neutrino with a mass of a few KeV also has been considered as a possible candidate for a while. However recent studies based of high resolution hydrodynamical simulation seems to disfavor masses as low as $1 \sim 4$ keV with a confidence level between 2σ and 9σ [126].

In the last decades numerous efforts have been made to detect the presence of these particles. Bounds on WIMP interaction have been strongly improved and, in some cases, new phenomena have been discovered that could be addressed to the dark matter paradigm. This has been the result of different strategies whose principles we are going to touch in the next lines.

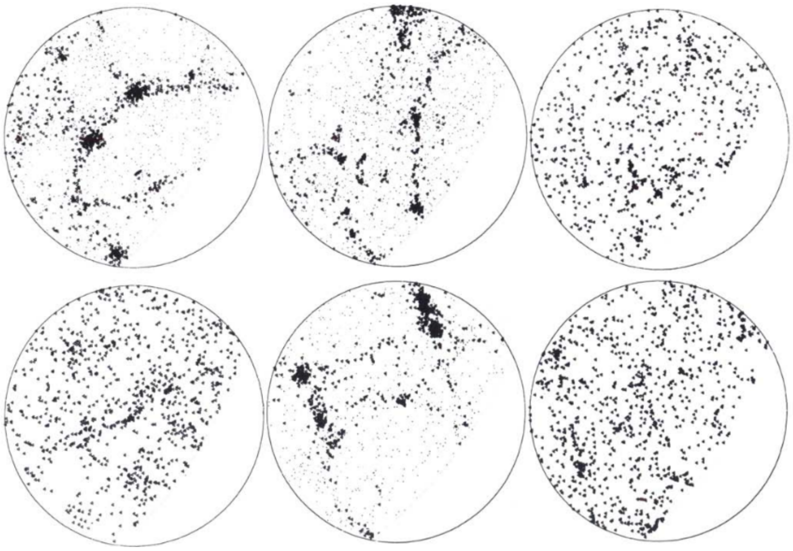

Figure 3.15: The figure shows the result of five N-body simulations together with the galaxy distribution in the CfA redshift survey. The middle-top, middle-bottom and the right-bottom panels utilize HDM models and assume $\Omega_m = 1$. The left-top and the left-bottom instead are based on CDM model and assume $\Omega_m = 0.2$[57].

Direct detection: one of the implication of the WIMP miracle is that in order to obtain the observed relic density, wimps must annihilate to other particles through the channel eq. (3.21). Assuming that those other particles are made of ordinary matter, the necessity of this interaction suggests that dark matter is also able to scatter off standard matter through interaction of the kind

$$\chi + SM \to \chi + SM, \tag{3.27}$$

whose energy footprint could be detected by measuring the nuclear recoil of the target [59, 98, 85]. It is worth to underline that the WIMP miracle not only suggests that such an interaction should exist, but also implies that DM-SM must be efficient. One can see then how cosmology provides us with bounds on this interaction rate. The WIMP-nuclei differential scattering event rate R as a function of the recoil energy E is described by the following equation

$$\frac{dR}{dE}\left(E\right) = \frac{\rho_\chi \sigma_0 F^2\left(E\right)}{2\mu^2 m_\chi} \int_{v_{min}}^{v^{esc}} d^3v \frac{f\left(\vec{v},t\right)}{v}. \tag{3.28}$$

As one can see, it depends directly on the local dark matter density ρ_χ and the DM-nucleus scattering cross-section in the zero momentum transfer limit σ_0 and it is inversely dependent on the dark matter mass m_χ and the square of the reduced mass of the WIMP-target system $\mu = m_\chi M / \left(m_\chi + M\right)$, for nucleus of mass M. Here $F\left(E\right)$ is the nuclear form factor of the target while v and $f\left(\vec{v},t\right)$ represent, respectively, the relative velocity of the WIMP χ with respect to the target and the distribution of the dark matter particle velocity with a cut-off at the galaxy escape velocity v_{esc}. Finally, v_{min} denotes the minimum velocity required for an event with energy E to occur

$$v_{min} = \frac{\delta + ME/\mu}{\sqrt{2ME}}, \tag{3.29}$$

with $\delta = 0$ in the case of elastic scattering. Since one is mostly interest in cold dark matter model, the limit $v \to 0$ is usually applied. One can then decompose the cross-section in two contributions:

$$\sigma_0 F^2\left(E\right) \simeq \sigma^{SD} F^2_{SD}\left(E\right) + \sigma^{SI} F^2_{SI}\left(E\right), \tag{3.30}$$

where the labels SD and SI identify the spin-dependent and the spin-independent contributions at zero momentum transfer respectively. The spin-independent component of the cross-section grows quadratically with respect of the atomic mass of the target nucleus when in absence of isospin violation. For this reason, the differential recoil event rate increases substantially for heavy target nuclei providing therefore stronger exclusion limits compared to the one obtained for the spin-dependent counterpart[7].

Although nuclear scattering is at the core of all the direct detection experiments, they differentiate from one to another based on the different choices of signal detection techniques utilized. In the case of the DAMA/LIBRA experiment [28] scintillating crystals are used in order to collect light signals from the WIMP-nucleus scattering. The DAMA/LIBRA experiment looks for evidence of the existence of dark matter particles in the galactic halo by analyzing the annual modulation signature of the single-hit events. The clear advantage of this strategy is to be dark matter model-independent. In the last years they have been reporting to detect a cosine-like modulated signal with measured period of 0.998 ± 0.002 yr that could be interpreted as originated by dark matter particles [29]. Other positive results have been obtained also by the Coherent Germanium Neutrino Technology (CoGeNT) collaboration. The CoGeNT experiment exploits the p-type point-contact germanium detectors to search for a dark matter signal. These detectors really shine in testing low-mass ($m_\chi \sim 10GeV$) dark matter candidates thanks to their low-energy threshold and ability to reject surface backgrounds. In the 2011 the analysis of a almost fifteen months of data showed a monthly modulation of the event rate in the low-energy region. The excess of events above the background was compatible with the one expected from dark matter despite the low significance of $\sim 2.8\sigma$ [1]. In the same year another promising development come from the Cryogenic Rare Event Search with Superconducting Thermometers project, in short CRESST-II. This experiment employs cryogenic detectors with $CaWO_4$ as scintillating target material to discriminate the type of interacting particle and detect a dark matter signature from the background signal. The total likelihood function in the parameter space exhibits two maxima corresponding to the WIMPS particle masses of $m_{\chi_1} = 25.3\,GeV$ and $m_{\chi_2} = 11.6\,GeV$ with a corresponding significance level of 4.2σ and 4.7σ respectively [19]. In the same region one also find the 3 WIMP candidate events observed by the CDMS-Si detector (Cryogenic Dark Matter Search). The maximum in the likelihood function suggests a WIMP mass of $m_\chi \sim 8.6GeV$ with an overall probability that these events could have been generated by background fluctuation estimated to be around 0.19%[37]. However, as one can see, the subsequent experiments SuperCDMS [8] and CDMS-II [9] are in the disagreement with this result

---

[7] It also important to mention that spin-zero isotopes do not give any signal in dark matter searches based on SD.

and imply that the signal is not caused by potential WIMPs candidates, but rather is a consequence of the fallacy of the background model utilized. The same can be told about the CRESST-II and CoGeNT results. Once a realistic model of surface roughness is employed in the calculation, a significant contribution to the number of events in the acceptance region in CRESST-II data arises from cascades of secondary recoils caused by recoiling 103 keV ^{206}Pb nucleus from decays of ^{210}Pb present on - and under - the surface of support used to hold the target in place [82]. Experiments like CDEX and MALBEK reject at 90% confidence level the parameter space region within 6 and 20 GeV thus strongly questioning the interpretation of the results obtained by the CoGeNT collaboration [136, 62]. On the other hand, independent analysis of the CoGeNT data concluded that a dark matter based interpretation of the excess events is preferred with a confidence not higher than 1.7σ once the event rise-time is properly fitted[8] thus allowing to better describe the background contribution [2, 46]. The signature detected by DAMA/LIBRA hasn't found confirmation in any follow up campaign and, even worst, other experiments seems to be in conflict with its result. Despite the annual modulation being able to reproduce several features expected for a dark matter signal, its interpretation as dark matter evidence would be in tension with null results obtained by other collaborations. XMASS [133], for example, reports exclusion upper limit of the DM-nucleus cross-section of $10^{-40} cm^2$ for dark matter particle masses between $6\,GeV$ up to $16\,GeV$ looking for annual modulation with a single phase liquid xenon detector. This takes away most of the region allowed by DAMA/LIBRA. Also the recent result from XENON1T seems to disfavor the interpretation of the annual modulation found by DAMA/LIBRA as due to dark matter particles by excluding new parameter space for the WIMP-nucleus cross-section for WIMP masses above 6 GeV in the case of spin-independent elastic scatter [21]. This still keep open the window for model dominated by inelastic and spin-dependent WIMP-proton coupling, with the caveat of assuming a different quenching factor in both experiments. However, also this option seems to produce strong tension with null results from other direct detection experiments [50]. As matter of fact the direct detection campaigns for WIMP have not been yet able to provide solid evidences of the existence of a WIMP candidate able to solve the dark matter paradigm. Nowadays the most stringent current limit on the spin-independent cross-section σ^{SI} are set by dual phase xenon detectors like the already mentioned XENON1T, as well as by other experiments like LUX [12] and PandaX-II [117] that set

---

[8] with a log-normal or a Pareto distribution.

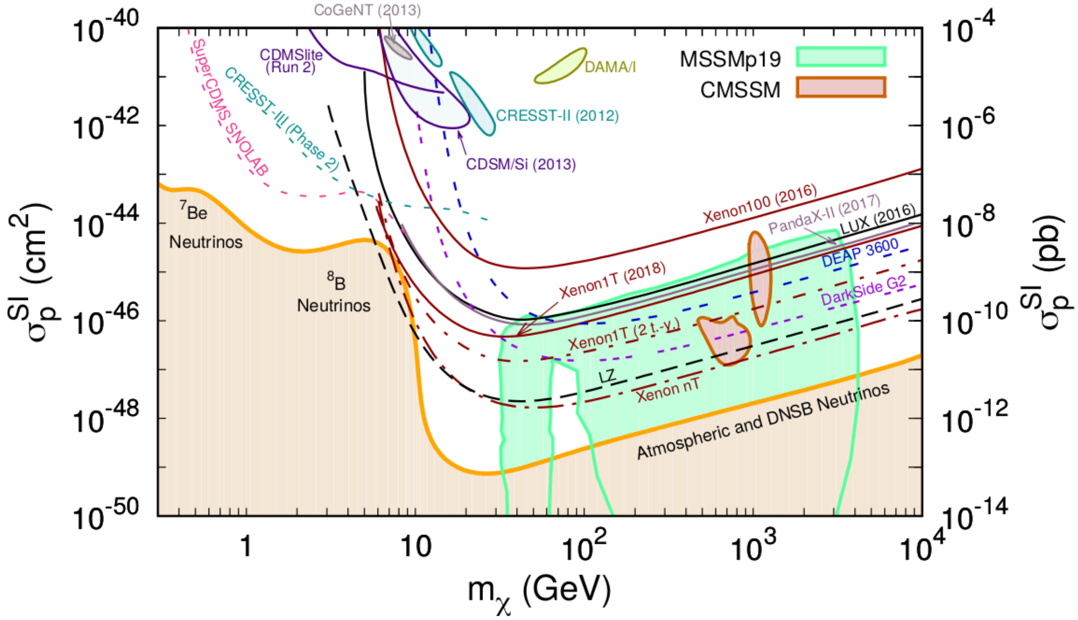

Figure 3.16: In the plot above current and expected future limits of the spin-independent cross-section σ^{SI} are shown as a function of the wimp candidate mass m_χ. More details in [107]. In is important to stress that the presented boundaries are a direct product of the underlying assumptions about the pertinent astrophysical quantities such as the local dark matter density or its velocity distribution. The latter being particularly important for those experiments sensitive only to the tails of the distribution.

important boundaries on σ^{SI} for masses between 40 and 50 GeV (see Fig. 3.16). Form the spin-dependent side new constrain lines have recently been published by the PICO collaboration [18, 17].

Indirect detection: if wimps particles do exist they are expected to annihilate. Indirect detection methods aim to find the byproducts of such annihilation over the galactic and/or extragalactic background. Gamma-ray emission constitute a main target for indirect detection as their propagation is mostly unaffected by the interstellar medium and Galactic magnetic fields. The direct advantage of such a feature is that data collected retain valuable information on the morphology and location of the emission region where the gamma-rays were produced [41, 60]. The gamma-ray flux from WIMP annihilation can be described by the following equation

$$\frac{d\Phi}{d\Omega dE} = \frac{\sigma v}{8\pi m_\chi^2}\frac{dN}{dE}\int_{l.o.s.} \rho^2 \left(\vec{r}\,(s,\Omega)\right) ds. \tag{3.31}$$

Here ρ represents the dark matter density that is integrated along the line of sight whereas Ω is the solid angle underlying the observed volume of the sky. The WIMP annihilation cross-section is encoded in the parameter σ while the candidate mass and its mean velocity are, respectively, m_χ and v. Finally one can see that the annihilation differential flux is also proportional to the energy spectrum dN/dE which expresses the number of gamma-rays produced per annihilation at the given energy E. As the differential flux is proportional to the dark matter density, some regions are more promising to look at compared to others. Those that stand out the most are the galactic center (GC) and the dwarf spheroidal galaxies (dSphs) of the Local Group. As for the Galactic center, there seems to be a reasonable suspicion that dark matter density could peak in the innermost region of our galaxy thus providing what would be probably the largest signal from WIMP annihilation. Unfortunately on the other hand, the inability to relay on a precise dark matter density model profile for the galactic center, together with the complexity of the potential conventional gamma-ray sources that also populate the same galactic region, strongly enhances the uncertainties on the inferred WIMP properties. These issues are alleviated in the case of dSphs which one theorizes to be dark matter dominated and whose gamma-ray budget one expects to be less effected by the astrophysical background. The trade off for the enhancement of the constraint obtained through dwarf spheroidal galaxies comes in the form of a much lower expected signal if compared to the Galactic Center. Worth to mention is also the possibility to perform a full sky search to have an overall constraint on dark matter annihilation. The idea is to look for spectral features and/or angular correlations produced by dark matter annihilation in the - approximately - isotropic background made up of the unresolved dark matter halos. Fig. 3.17 provides an easy-to-read summary of the pros and cons for the targets candidates we just mentioned, plus someone else. The Galactic Center seems indeed to exhibit an excess of gamma-ray above the expected background as shown by different analysis based on the Fermi-LAT[9] data [74]. For more details see also the analysis performed by the Fermi-LAT Collaboration itself using different specialized

---

[9] The Fermi Large Area Telescope (Fermi-LAT) is a pair-conversion spatial telescope with a precision tracker and calorimeter able to cover an energy range from below 20 MeV to more than 300 GeV [23].

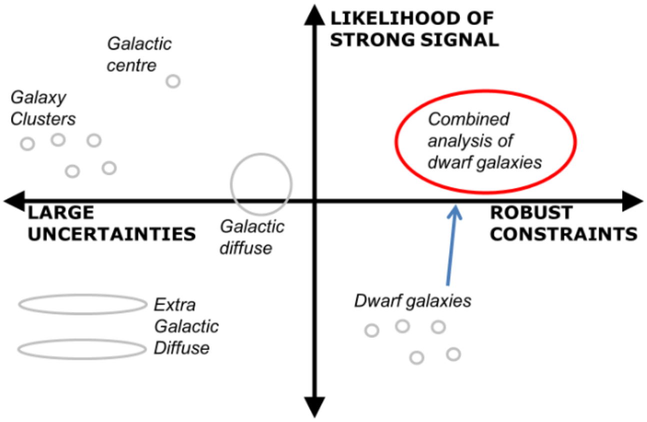

Figure 3.17: As one can see from this plot from [42], GC is the target that most likely would be able to produce a "detection" due to the high strength of the signal associated with it. Nevertheless, in term of robustness of the exclusion limits obtained, the combined analysis of dwarf galaxies represent by far a better option.

interstellar emission models in order to isolate the gamma-rays coming from the inner region (within ~ 1 kpc) from the one coming from the rest of the galaxy [11]. Although the presence of an excess in the gamma-ray flux seems to be quite established, whether or not its origin is related with WIMPs is still unclear. The difficulty comes mostly from intrinsic dependence between the spectral proprieties of the signal and the model assumed to describe the interstellar emission. Moreover as L. Roszkowski et al. point out in their paper [40], even if the morphological properties of the Galactic Center Excess (GCE) can be explained in the framework of small-scale dark matter substructures this would require that more than the 80% of the galactic halo must be made up of substructures. Such a hypothesis unfortunately is in strong contradiction with the results of numerical simulations. An other issue with this dark matter interpretation of the GCE raises from the fact that similar excess in the gamma-ray flux seems to be present also in other region along the galactic plane where the dark matter signal is expected to be zero [7]. On the other hand, the galactic center excess could also be explained by the presence of a population of unresolved millisecond pulsars. The advantage of this option is that the signature produced by the millisecond pulsar would match with the galactic center excess spectrum below the 10 GeV while the excess emission above this threshold can be related to the inverse Compton IC scattering of high energy electrons potentially produced as a secondary component [75]. Another possible way to explain the galactic center excess would involve a leptonic cosmic-rays outburst. Models with a single outburst underestimate the excess emission observed in the Galactic Center. However, models that consider the possibility of a second outburst seems to fit much better the data. Nevertheless, a little bit of fine-tuning is required in order for the gamma-ray emissions to exhibit roughly the same spectral shape at all relevant latitudes as observed by the Fermi-LAT [39]. Finally, an other option is to explain the galactic center excess with a stellar over-density in the Galactic bulge and in the nuclear stellar bulge as shown by the analysis carried on by O. Macias et al. employing an hydrodinamical model to register the position of interstellar gas associated with diffuse Galactic gamma-ray emissions [84]. To summarize, although the Galactic Center Excess is something established with a more than reasonable confidence, we are still far from clearly understand whether or not it is based on DM/WIMP annihilation or something totally different. Space based telescope as Fermi-LAT are not the only one working on dark matter indirect detection. A ground-based observational campaign is carried on by several other telescopes among which the Imaging Air Cherenkov Telescopes (IACTs) are for sure one of the most promising. Currently running IACTs include the VERITAS array on four 12m diameter telescopes in Arizona [73], the two MAGIC 17m diameter telescopes located in Canary Island of La Palma [15] and the four HESS telescopes placed in the Khomas highlands of Namibia [10]. Since gamma-rays interact with the atmosphere, ground-based detectors can not work the same way as the space-based one. What they do is instead to observe the Cherenkov light produced by the showers of charged particles created by the interaction between the atmosphere and the gamma-rays. One of the main challenge of this method is to recognize and map the background sources in order to distinguish them from the actual signal. Some of these sources, like the isotropic cosmic-ray background, turn out to be much stronger than the gamma-ray signal. For this reason the energy threshold are higher compared to those of the space telescopes like Fermi-LAT. However the large volume of atmosphere observed is usually able to mitigate this issue leading to effective observed area bigger than the spatial counterpart. In Fig. 3.18 the limit for the dark matter particles annihilation $\chi\chi \to b\bar{b}$ are summarized. As one can see, in the low dark matter mass sector the strongest limit comes from the constraints on σv around the time of recombination obtained by the Plank collaboration through the analysis of the CMB [101]. All the middle section, up to $m_\chi = 10^3 GeV$, is mostly constrained by the Fermi-LAT analysis of dwarf galaxies [13] and galactic center [63]. The latter being less competitive

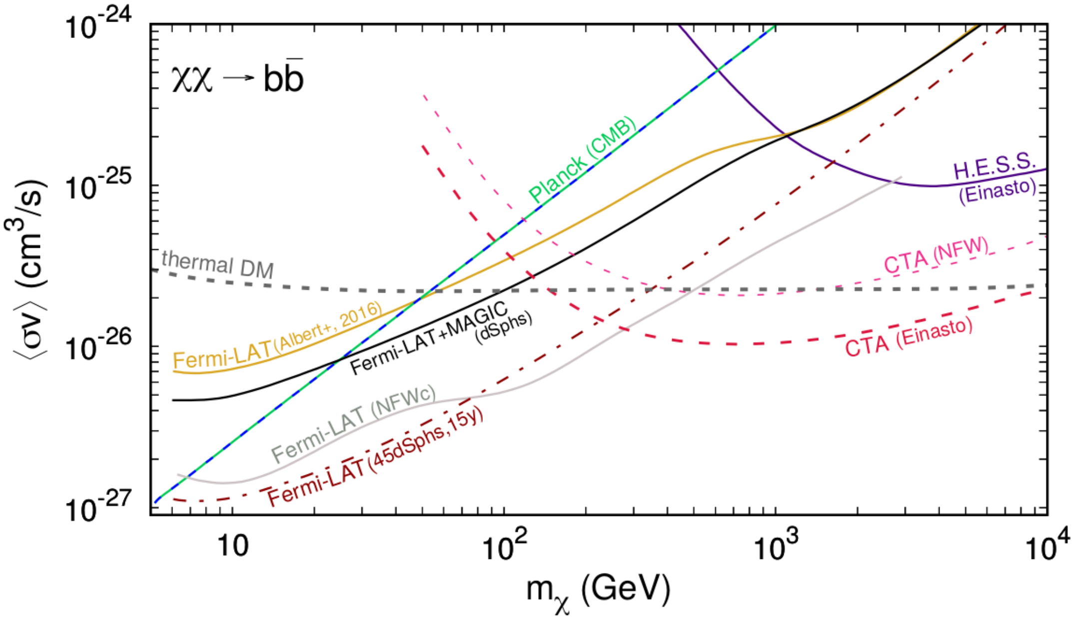

Figure 3.18: The plot from [107] shows the current and future limits on the DM annihilation cross-section compared to the one we have nowadays. As one can see the Fermi-LAT stacked analysis of 45 dwarf galaxies and 15 years of data [38] (dashed brown line) will improve the constraint in the low mass region providing limits on the same order of the one obtained from the GCE analysis. On the other hand of the spectrum, for masses up to $10^4 GeV$, thanks to the CTA collaboration one will be able to strengthen the constraint on the annihilation cross-section gaining almost one order of magnitude respect current one [36] (dashed pink and red lines).

due to the uncertainties in the halo profile. Finally in the high mass range $10^3 GeV < m_\chi < 10^4 GeV$ the HESS analysis of the galactic center improves the Fermi-LAT limits for the dark matter annihilation cross-section setting them to $\langle\sigma v\rangle(cm^3/s) \simeq 10^{-25}$ [6].

To wrap it up, the WIMP hypothesis although very promising has not been able to prove herself true. Despite the numerous experiments employed and the large range of approaches based on different detection methods and phenomena, we do not have yet any conclusive detection. For a more detailed description of WIMPs see [107, 22].

3.4 Fuzzy Dark Matter

Motivated by the -to date- unsuccessful search for wimp particles, in the last decades scientists have began to increase their focus on alternative viable dark matter candidates. Among these the Fuzzy Dark Matter (FDM) appears to be one of the most promising.

In the theory of General Relativity (GR) the metric tensor $g_{\mu\nu}$ is the only mediator of the gravitational interaction. Nevertheless, several extensions of the theory assume the presence of additional fields which contribute to determine the dynamics of the spacetime. The scalar-tensor theories develop from the pioneering work of Jordan, Brans and Dicke and are nowadays one of the most studied alternative theories of gravity. As the name suggests, in these theories the metric tensor is joined by a scalar field ϕ which in the FDM scenario plays also the role of dark matter candidate. Mathematically, this model can be described through the action

$$S = \frac{1}{c}\int d^4x \frac{\sqrt{-g}}{2k}\left[R - 2\partial_\gamma\phi\partial^\gamma\phi - V\left(\phi\right)\right] + S_{matter}\left(g_{\mu\nu}, \mathbf{\Psi}_i, \phi\right), \qquad (3.32)$$

with $k = 8\pi G/c^4$, R the Ricci scalar related to the space-time metric $g_{\mu\nu}$, $V\left(\phi\right)$ being the scalar field's potential, and S_{matter} the matter action

$$S_{matter} = \frac{1}{c}\int d^4x\sqrt{-g}\left[\mathcal{L}_{SM}\left(g_{\mu\nu}, \mathbf{\Psi}_i\right) + \mathcal{L}_{int}\left(g_{\mu\nu}, \mathbf{\Psi}_i, \phi\right)\right], \qquad (3.33)$$

where $\mathcal{L}_{SM}$ is the Lagrangian density of the Standard Model of particles depending on the standard model fields $\mathbf{\Psi}_i$ whereas $\mathcal{L}_{int}$ characterizes the interaction between the matter and the scalar field ϕ. The presence of the nonminimal coupling, here introduced by the term $\mathcal{L}_{int}$, as well as the existence of the scalar field ϕ is motivated by numerous extended theories such as the low energy action of string theories [65], extended $F(R)$ gravity [49] or Kaluza-Klein theories with additional compactified dimensions [93]. If we assume the coupling between the scalar field and the standard matter to be weak, then one can describe the interaction with its linear approximation which reads as follow

$$\mathcal{L}_{int} = \phi \left[\frac{d_e}{4e^2} F^2 - \frac{d_g \beta_g}{2g_3} \left(F^A \right)^2 - \sum_{i=e,u,d} \left(d_{m_i} + \gamma_{m_i} d_g \right) m_i \bar{\Psi}_i \Psi_i \right], \quad (3.34)$$

with $F_{\mu\nu}$ the standard electromagnetic Faraday tensor, e the electric charge of the electron, $F^A_{\mu\nu}$ the gluon strength tensor, g_3 the *Quantum Chromodynamics* (QCD) gauge coupling, β_3 the β function for the running of g_3, m_i the mass of the fermions, γ_{m_i} the anomalous dimension giving the energy running of the masses of the quantum chromodynamics coupled fermions and ψ_i fermion spinors. The interaction between the scalar field ϕ and the different matter sectors is parameterized by the constants d_{m_i} and d_g.

3.4.1 Motivation

It is common knowledge that the ΛCDM model is able to produce extremely accurate predictions at large scales. As an example, one has to look no further that the precision with which this model determines the power spectrum of mass fluctuations at the present time - redshift $z \simeq 0$ - from the observations of the cosmic microwave background - redshift $z \simeq 10^3$ - to within few percent. This becomes even more remarkable if one considers that the amplitude of these fluctuations has increased by five orders of magnitude in this span of time. On the other side, at smaller scales as those of the stellar distribution in normal galaxies - around 10kpc - the ΛCDM model predictions starts to be more sporadic, less accurate and sometimes even inconsistent with observations [128]. Even if complex and yet unknown baryonic dynamics may prove able to account for such inconsistencies, it is worth to explore those other well-motivated models, as the FDM model, that seems to be able to replicate the success of the CDM model at large scale as well as to solve some of its shortcoming at small scales.

Cusp-core problem: one of the discrepancies we mentioned before is the so-called "cups-core problem". A well established prediction of the CDM model is that the density in halos and subhalos should be inversely proportional to radius $\rho(r) \simeq r^{-1}$ of the system. One would then expect to measure singular density cusps in the center of these structures. On the other side FDM halos are characterized by a central core, sometimes called soliton, that rises as stationary, minimum-energy solution of the Schrodinger-Poisson equation. Although the degeneraicies intercurrent the velocity anisotropy profile and the observational signature of the mass profile make harder to chose for a final claim, the majority of studies seems to favor the core behavior over cusps [48].

The missing-satellite problem: the discrepancy between the expected distribution of CDM subhalos in massive galaxies and the number of small satellite galaxies observed to orbit luminous galaxies is often referred to as the missing-satellite problem [80]. Common solutions for this problem usually tap into the baryonic physics suggesting that gas accretion onto subhalos could be suppressed because of the heat generated by ultraviolet background radiation, or that the gas could be driven out by stellar winds and supernovae. The FDM model on the other hand predicts a number of low-mass subhalos much smaller, if compared to the CDM, making it able to address this problem in a very natural way. FDM suhalos, in fact, result to be more affected by tidal disruption. This is directly related with the capability of FDM to tunnel through the potential barrier centered on the tidal radius. One can actually constrain the minimum mass of FDM needed for a system to survive for a determined number of orbits at a given radius. See more in [77] and its appendix.

$$M > 6.7 \times 10^8 M_\odot \left(\frac{\mathcal{M}}{10^{11} M_\odot} \right)^{1/4} \left(\frac{10kpc}{a} \right)^{3/4} \left(\frac{10^{-22} eV}{m} \right)^{3/2}, \quad (3.35)$$

where M and $\mathcal{M}$ represent the mass of the subhalo and the host respectively, a is the radius, m is the FDM characteristic mass and it has been considered a number of orbits equal to 10. Numerical simulations seem to produce a similar cutoff as they find halo substructure suppression below $\simeq 10^8 M_\odot$ [110].

To-big-to-fail problem: dissipationless ΛCDM simulations predict the existence of massive subhaloes of the Milky Way characterized by high concentration and circular velocities. These halos are actually so dense that they can not host any of the Milky Way's bright satellites. Such haloes however are yet to be observed [31]. If one allows a fraction f of dark matter to be described by FDM then, for subhaloes masses smaller than $f M_m$, the concentration of the halos for the Milky Way would drop compared to the one predicted by the ΛCDM model. Here M_m is the characteristic mass associate to the modes k which entered the horizon when the sound speed was large [86]. One can also regard at the to-big-to-fail problem as the non-observation of large numbers of satellites with maximum circular velocity $v_{max} \geq 40kms^{-1}$. In this case one can easily see how FDM solve or at list alleviate this issue as the maximum circular velocity predicted by this dark matter model is 25% lower $v_{max} \sim 30kms^{-1}$.

3.4.2 Detection methods

It is already been mentioned that fuzzy dark matter is supposed to oscillate at its Compton frequency when $m_\phi \gg \hbar H/c^2 \sim 1.5 \times 10^{-33} eV/c^2$. Because of the fuzzy dark matter coupling with standard matter, these oscillation gives rise to a number of different phenomena that can be exploited as a way to probe the fuzzy dark matter existence.

Atomic spectroscopy: atomic spectroscopy in cesium vapor has been proved to be useful to test masses range between $8\times10^{-11}eV$ and $4\times10^{-7}eV$. The oscillation of the scalar field ϕ induces a similar behavior in the fine-structure constant α and the electron mass m_e. In turn, the variation of α and m_e creates a modulation in the energy spacing ΔE between two electronic levels in the ^{133}Cs atom. As shown by D. Antypas et al., one can look for this modulation by exciting the cesium vapor with a continuous-wave laser light of frequency $f_L \sim \Delta E/2\pi$ [20]. See Fig. 3.19 for the results. Likewise, A. Hees et al. use the dual $^{133}Cs/^{87}Rb$ atomic fountain clock FO2 at LNE-SYRTE as a tool to search for a sinusoidal signature in the atomic frequency ratio generated by the ultra-light scalar field [68]. The scalar field in fact produces an harmonic signature in the ratio of the Rb/Cs hyperfine frequencies as described by the following equation

$$y_{Rb}/y_{Cs} - 1 \approx \mathcal{O} + \left[k_\alpha d_e + k_q \left(d_{\hat{m}} - d_g\right)\right] \frac{1}{\omega} \left(\frac{8\pi G}{c^2}\rho_{DM}\right)^{1/2}, \tag{3.36}$$

where $d_{\hat{m}}$, d_e and d_g are dimensionless coefficients characterizing the coupling between the scalar and the standard model fields. $\mathcal{O}$ is a constant offset, k_α and k_q are sensitivity coefficients and ρ_{DM} is the dark matter local energy density. Even if any evidence has been found yet, the rapid progression of atomic clocks will open the way to similar searches with other types of transitions allowing to further probe the parameter space describing the coupling between this dark matter candidate and the standard matter.

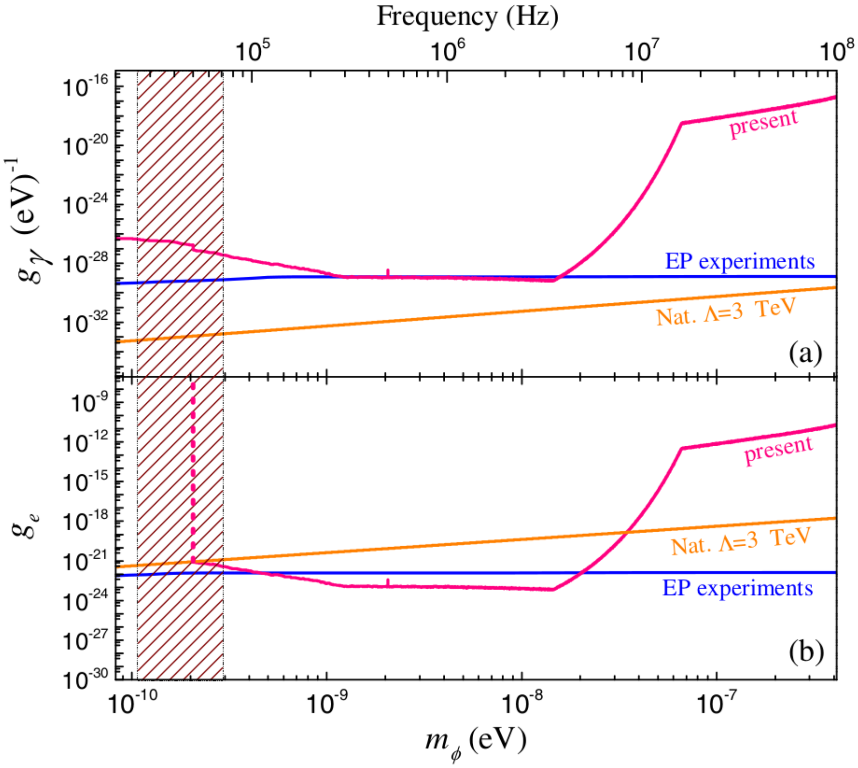

Figure 3.19: The panel shows the bounds on the coupling constants of DM to the photon and the electron, respectively g_γ and g_e [20].

Black Holes Superradiance: although some models assume dark matter to be able to have non gravitational interaction, most of the present observations and estimations one has on dark matter are a product of its gravitational effects in astrophysics and cosmology. That's why purely gravitational objects like black holes (BH) can be effectively used to probe the nature of dark matter. We know that under specific circumstances, black holes lose their angular momentum in a very efficient way when they interact with bosons present in their surroundings. This effect is known as superradiance [116]. In order for the superradiance mechanism to be effective, two conditions must be met. The first is that the boson population energy ω_b divided by the boson magnetic quantum number m associated with its angular momentum, must be smaller than the angular velocity of the balk hole event horizon Ω_H,

$$\frac{\omega_b}{m} < \Omega_H. \tag{3.37}$$

The second one is that

$$\Gamma_b \tau_{BH} \geq ln N_m, \tag{3.38}$$

where Γ_b is the growth rate of the field, τ_{BH} is the black hole characteristic timescale and N_m is the final occupation number of the cloud. What is important here is that the leading contribution to the growth rate Γ is dependent on the mass of the field. Thus monitoring the mass and the spin of a black hole one is able to constrain the boson field mass parameter. A paper has been published in the 2019 where Hooman Davoudiasl and Peter B. Denton take advantages of the initial data from the Event Horizon Telescope on M87* to limit the field mass parameter μ_b [47]. Fig. 3.20 shows the boundaries they obtained for μ_b as a function of the dimensionless spin parameter

$$a* = \frac{J_{BH}}{G_N M_{BH}^2}, \tag{3.39}$$

which is defined by the black hole angular momentum J_{BH}, its mass M_{BH} and the Newton's constant G_N.

Optical cavities: an other possibility is to exploit the DM-induced oscillation of the Bohr radius $a_0 = \hbar / (\alpha m_e c)$ that consequently gives rise to a variation of the atoms size as well as to the length of chemical bonds. Andrew A. Geraci et al. [61] propose the use of two co-located high-finesse Fabry-Perot optical cavities the first of which should consist of mirrors connected by a rigid cavity spacer while in the second optical cavity the two mirrors are suspended by pendulums. The goal of such arrangement is to

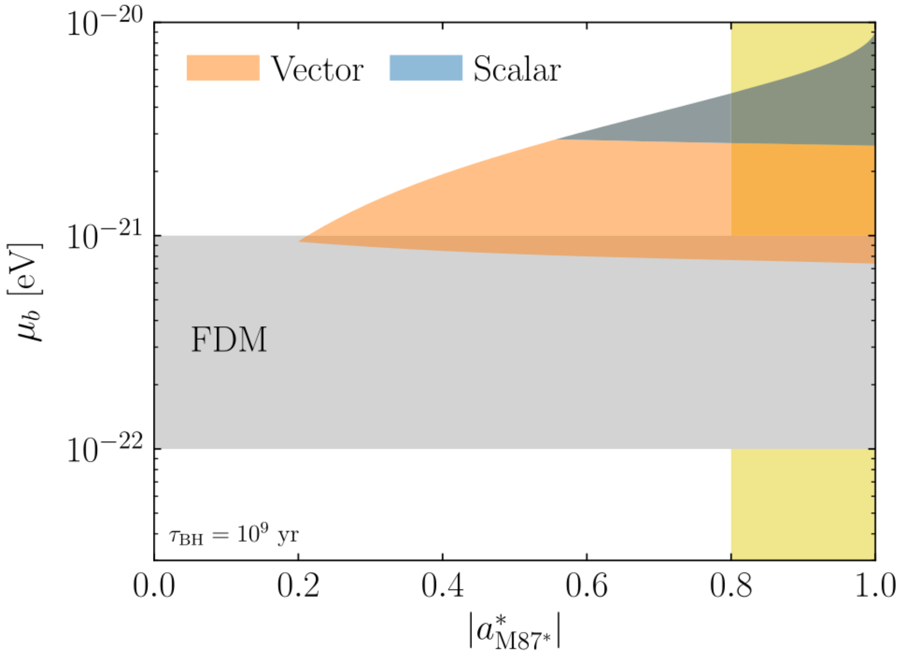

Figure 3.20: The panel shows the limit on light bosons as a function of the observed M87* dimensionless spin $a*$. The blue shaded area represent the constrain on the scalar model whereas the orange one shows the constrain on the vector model. The grey area is the range usually attributed to FDM and finally the 1σ inference region of the spin is colored in khaki [47].

create a discrepancy in the cavities' sensitivity to high-frequency variation in the length of the supporting spacer. As a result, the presence of an ultralight scalar field would create a spike in the power spectral density of the measured differential strain related with the two different optical cavities.

Chapter 4

Testing FDM in the solar system

In this chapter we will show how it is possible to detect the presence of fuzzy dark matter in the solar system through the use of gravitational waves antennas. The spatial variations of the scalar field is in fact able to exert a position-dependent oscillatory force on the gravitational waves detectors' optical equipment. As a result, the optical equipment undergoes position-dependent oscillatory motions, which ends up with non-vanishing signals in the outputs of the gravitational waves detectors. In the following sections of this chapter we will analyze this detection opportunity in more detail.

4.1 FDM Model

From action (3.32) the following field equations can be derived [70]:

$$R_{\mu\nu} = k\left[T_{\mu\nu} - \frac{1}{2}g_{\mu\nu}T\right] + 2\partial_\mu\phi\partial_\nu\phi + \frac{1}{2}g_{\mu\nu}V\left(\phi\right), \tag{4.1}$$

$$\Box\phi = -\frac{k}{2}\sigma + \frac{V'\left(\phi\right)}{4}, \tag{4.2}$$

with

$$T_{\mu\nu} = -\frac{2}{\sqrt{-g}}\frac{\delta\sqrt{-g}\mathcal{L}_{matter}}{\delta g^{\mu\nu}}, \tag{4.3}$$

$$\sigma = \frac{1}{\sqrt{-g}}\frac{\delta\sqrt{-g}\mathcal{L}_{matter}}{\delta\phi} = \frac{\delta\mathcal{L}_{int}}{\delta\phi}. \tag{4.4}$$

As it has been shown by Damour and Donoghue in their work [44], the action used to model the matter at the microscopic level, including the scalar field interaction (3.34), can phenomenologically be replaced at the macroscopic level by the standard point mass action

$$\mathcal{S}_{matter}\left(g_{\mu\nu}, \mathbf{\Psi}_i, \phi\right) = -c^2 \sum_A \int_A d\tau m_A\left(\phi\right), \tag{4.5}$$

where $d\tau$ is the proper time interval defined by $c^2 d\tau^2 = -g_{\mu\nu} dx^\mu dx^\nu$ and A is a label to differentiate the different bodies. The coupling strength between the scalar field and the matter is parameterized by the coupling factor

$$\alpha_A\left(\phi\right) = \frac{\partial \ln m_A\left(\phi\right)}{\partial \phi} = d_g + \bar{\alpha}_A, \tag{4.6}$$

where m_A is the mass of the body one is considering, $d_g = \frac{1}{\sqrt{4\pi G}} \frac{\partial ln \Lambda_3}{\partial \phi}$ is a universal contribution to α_A, while $\bar{\alpha}_A$ is the Equivalence Principle-violating part and depends on the body composition. Here Λ_3 is the quantum chromodynamics energy scale. In order to better understand where this decomposition comes from, one can think the mass m_A to be made up of two terms

$$m_A = m_A^{rest\, mass} + E_A^{binding}, \tag{4.7}$$

where the first term is the rest-mass contribution to the mass of an atom - such as the contribution from the fermions mass terms - while the second accounts for the binding energy. In particular, $E_A^{binding}$ is itself made up of two contributions: one from the strong interaction and another from the electromagnetic interaction. At the energy scale considered ($\mu \sim 1$ GeV) most of the mass of nucleons comes from the gluonic binding energy as the mass of the u and d quarks are $\sim$ MeV, whereas the mass of a proton is $\sim$ 1 GeV. At this scale, in fact, one has integrated out the effect of the weak interaction as well as the effect of the heavy quarks (c, b, and t).

When the dilaton field couples differently to different terms of the matter sector, the theory no longer satisfy the universality of free fall, as different contributions to the mass respond differently to this additional gravitational field. The precise way atoms are responsive to the non-minimal coupling depend on nuclear and atomic physics. For instance, nuclear processes that bind the nucleons together are sensitive to a change of the dilaton field, because a change of the dilaton field corresponds in effect to a change of the coupling constant of the standard model of particles (such as g_3 and α).

The decomposition of m_A translates to the parameter $\bar{\alpha}$ of eq. (4.6) which, therefore, can be decomposed as fallows

$$\bar{\alpha}_A = \bar{\alpha}_A^{r\,m\,wo.\,EM} + \bar{\alpha}_A^{bind} + \bar{\alpha}_A^{(de)}. \tag{4.8}$$

In particular, the first term on the r.h.s. encodes the contribution to $\bar{\alpha}_A$ coming from the terms linear in the quark and electron masses in the rest-mass contribution to the total mass m_A. It is worth to notice that $\bar{\alpha}_A^{r\,m\,wo.\,EM}$ doesn't contain any electromagnetic contribution. The effect of the electromagnetic contribution to the masses of the nucleons, together with the nuclear Coulomb energy term, are in fact encoded in the term $\bar{\alpha}_A^{(de)}$. Finally $\bar{\alpha}_A^{bind}$ denotes the contribution to $\bar{\alpha}_A$ coming from the strong interaction term present in the nuclear binding energy.
Through nuclear physic considerations, T. Damour and John F. Donoghue [44] evaluated these terms to be equal to

$$\begin{aligned}
\bar{\alpha}_A^{r\,m\,wo.\,EM} &\simeq F_A \left[0.040 \left(d_{\hat{m}} - d_g \right) + 0.0017 \left(d_{\delta_m} - d_g \right) \frac{A - 2Z}{A} \right. \\
&\quad \left. + 5.5 \times 10^{-4} \left(d_{m_e} - d_g \right) \frac{Z}{A} \right], \\
\bar{\alpha}_A^{bind} &= \left(d_{\hat{m}} - d_g \right) F_A \\
&\quad \times \left[0.045 - \frac{0.036}{A^{1/3}} - 0.020 \frac{\left(A - 2Z \right)^2}{A^2} - 1.42 \times 10^{-4} \frac{Z \left(Z - 1 \right)}{A^{4/3}} \right], \\
\bar{\alpha}_A^{(de)} &= d_e F_A \left[-1.4 + 8.2 \frac{Z}{A} + 7.7 \frac{Z \left(Z - 1 \right)}{A^{4/3}} \right] \times 10^{-4}.
\end{aligned} \tag{4.9}$$

Here Z denotes the atom's atomic number, A is its number mass and F_A is defined by

$$F_A = \frac{A \cdot m_{amu}}{m_A}, \tag{4.10}$$

where $m_{amu} = 931 MeV$ is the atomic mass unit. The parameter d_g, d_e and d_{m_e} are three of the five coupling parameters introduced in eq. (3.34), while $d_{\hat{m}}$ and d_{δ_m} denote the following linear combination of the remaining two

$$d_{\hat{m}} = \frac{d_{m_d} m_d + d_{m_u} m_u}{m_d + m_u}, \qquad d_{\delta m} = \frac{d_{m_d} m_d - d_{m_u} m_u}{m_d - m_u}, \tag{4.11}$$

where m_d, m_u are the mass of the up and down quarks. If we plug eq. (4.9) into eq. (4.8), we obtain

$$\bar{\alpha}_A = \left[\left(d_{\hat{m}} - d_g \right) Q_{\hat{m}} + \left(d_{\delta m} - d_g \right) Q_{\delta m} + \left(d_{m_e} - d_g \right) Q_{m_e} + d_e Q_e \right]_A, \tag{4.12}$$

where the coefficient Q_{k_a} plays the role of the "dilaton charge" coupled to the parameter k_a and are expressed through the following equations

$$Q_{\hat{m}} = F_A \left[0.093 - \frac{0.036}{A^{1/3}} - 0.020 \frac{(A-2Z)^2}{A^2} - 1.4 \times 10^{-4} \frac{Z\,(Z-1)}{A^{4/3}} \right], \tag{4.13}$$

$$Q_{\delta m} = F_A \left[0.0017 \frac{A-2Z}{A} \right], \tag{4.14}$$

$$Q_{m_e} = F_A \left[5.5 \times 10^{-4} \frac{Z}{A} \right], \tag{4.15}$$

$$Q_e = F_A \left[-1.4 + 8.2 \frac{Z}{A} + 7.7 \frac{Z\,(Z-1)}{A^{4/3}} \right] \times 10^{-4}. \tag{4.16}$$

Several charges have components that are not or weakly dependent on the atomic numbers A and Z. Hence, one can factor these contributions out in order to define a novel “universal” parameter d_g^*. This is what we will show now.

Following [44], one can assume

$$F_A \simeq 1, \tag{4.17}$$

and

$$Z \simeq \frac{1}{2} \frac{A}{1 + 0.015 A^{2/3}}. \tag{4.18}$$

The first simplification is motivated by the fact that the leading terms in the dilaton charges vary by factor of a few over different values of Z and A, while F_A differs from one only at 10^{-3} level. As for the second approximation, it is justified by the fact that the “valley” of stable nuclei is located, *a priori*, along the specific line where one has an equal number of protons and neutrons and therefore $A = 2Z$. Then, the presence of the Coulomb repulsion between protons modifies the stability conditions, favoring a relative small excess of neutrons over protons. This is why we obtain eq. (4.18).

We notice that, at this approximation level, the terms $0.020\,(A-2Z)^2\,/A^2$ in $Q_{\hat{m}}$ and $0.0017A - 2Z/A$ in $Q_{\delta m}$ are subdominant and can therefore be neglected. On the other side, one also finds that it is possible, at the leading order, to consider $A = 2Z$ in Q_{m_e} and Q_e.

Taking into consideration all of this, we simplify the dilaton charges obtaining

$$Q_{\hat{m}} \simeq \left[0.093 - \frac{0.036}{A^{1/3}} - 1.4 \times 10^{-4} \frac{Z\,(Z-1)}{A^{4/3}} \right], \tag{4.19}$$

$$Q_{m_e} \simeq 2.75 \times 10^{-4}, \tag{4.20}$$

and

$$Q_e \simeq \left[2.7 + 7.7\frac{Z\left(Z-1\right)}{A^{4/3}}\right] \times 10^{-4}. \tag{4.21}$$

We see now how terms that don't depend on the body composition appear in the approximated form of the dilaton charges. Those terms can be then taken out and incorporated into a new definition of d_g that encompasses all the composition independent terms, obtaining

$$d_g^* = d_g + 0.093\left(d_{\hat{m}} - d_g\right) + 2.75 \times 10^{-4}\left(d_{m_e} - d_g\right) + 2.7 \times 10^{-4} d_e. \tag{4.22}$$

Summing up what we have discussed, the coupling factor α_A can be decomposed into a universal parameter d_g^* plus the composition dependent factor

$$\bar{\alpha}_A = \left[Q'_{\hat{m}}\right]_A\left(d_{\hat{m}} - d_g\right) + \left[Q'_{m_e}\right]_A\left(d_{m_e} - d_g\right) + \left[Q'_e\right]_A d_e + \left[Q'_{\delta m}\right]_A\left(d_{\delta m} - d_g\right), \tag{4.23}$$

where the coefficients $\left[Q'_j\right]_A$ denote the parts of the dilaton charges that depend on the body composition.

4.1.1 Scalar field solution

If one considers a quadratic self-interacting potential of the kind

$$V\left(\phi\right) = 2\frac{c^2 m_\phi^2}{\hbar^2}\phi^2, \tag{4.24}$$

then m_ϕ has the dimension of a mass. This represents, in fact, a quite common choice for $V\left(\phi\right)$. However, the reason why we decided to consider this potential in our study is that it makes the scalar field behave as a pressureless fluid characterized only by its energy density, as we will see later in this subsection. Those are exactly the characteristics we ascribe to cold dark matter.

At the Minkowskian order the field equation for ϕ becomes

$$\frac{1}{c^2}\ddot{\phi}\left(\vec{x},t\right) - \Delta\phi\left(\vec{x},t\right) = -\frac{4\pi G}{c^2}\alpha_A\left(\phi\right)\rho_A\left(\vec{x}\right) - \frac{c^2 m_\phi^2}{\hbar^2}\phi\left(\vec{x},t\right), \tag{4.25}$$

where ρ_A is the standard matter density and $\alpha_A\left(\phi\right)$ is given by eq. (4.6). It is worth to remark that, in general, one would also have a term proportional to the Hubble parameter $H = \dot{a}/a$. However, because the timescale of the phenomena we are interested in is way smaller than $1/H$, it can be discarded.

Because of the linear nature of eq. (4.25), its most general solution can be derived by adding together its particular solutions, here referred to as ϕ_1 and ϕ_2. The latter can be obtained by solving respectively

$$\Box\phi_1 = -\frac{c^2 m_\phi^2}{\hbar^2}\phi_1, \tag{4.26}$$

$$\Box\phi_2 = \nabla^2\phi_2 = \frac{c^2 m_\phi^2}{\hbar^2}\phi_2 + \frac{4\pi G}{c^2}\alpha_A\left(\phi\right)\rho_A\left(\vec{x}\right). \tag{4.27}$$

It is worth to mention that $\phi_1\left(\vec{x},t\right)$ is a dynamic solution whereas $\phi_2\left(\vec{x}\right)$ is a static one as it does not evolve over time. Adding ϕ_1 and ϕ_2 together one gets

$$\begin{aligned}\phi\left(\vec{x},t\right) &= \phi_1\left(\vec{x},t\right) + \phi_2\left(\vec{x}\right), \\ &= \phi_0\cos\left(\vec{k}_{DM}\cdot\vec{x} - \omega_0 t + \delta\right) + Const\cdot\frac{e^{-m_\phi x}}{x}.\end{aligned} \tag{4.28}$$

where δ is an unknown phase, $|\mathbf{k}|^2 + \omega_\phi^2/c^2 = \omega_0^2/c^2$ and

$$\vec{k}_{DM} = \frac{\omega_\phi\vec{v}_{DM}}{c^2} \qquad and \qquad \omega_\phi = \frac{m_\phi c^2}{\hbar}. \tag{4.29}$$

(4.28) represents the most general solution to eq. (4.25).
Our goal will be to study the oscillating motion of the optical equipment induced by the presence of the scalar field ϕ and its interaction with the equipment itself. For this reason we can neglect the static part $\phi_2\left(\vec{x}\right)$ of the solution (4.28) and focus just on the dynamical one

$$\phi_1\left(\vec{x},t\right) = \phi_0\cos\left(\vec{k}_{DM}\cdot\vec{x} - \omega_0 t + \delta\right). \tag{4.30}$$

In order to show that the scalar field ϕ does represent a good dark matter candidate, we first consider its asymptotically behavior. At cosmological scales, the scalar field gives rise to an energy density [70]

$$\rho = \frac{c^2}{8\pi G}\left[\dot{\phi}^2 + \frac{c^2 V\left(\phi\right)}{2}\right], \tag{4.31}$$

and a pressure

$$p = \frac{c^2}{8\pi G}\left[\dot{\phi}^2 - \frac{c^2 V\left(\phi\right)}{2}\right]. \tag{4.32}$$

If one averages over one oscillating period, the pressure term vanishes whereas the energy density becomes [125]

$$\rho_\phi = \frac{c^6}{4\pi G\hbar^2}\frac{m_\phi^2\phi_0^2}{2}. \tag{4.33}$$

At large scale then, the scalar field ϕ can be regarded at as a pressureless fluid characterized by its energy density ρ_ϕ. Such characteristics are the same ascribed to the dark matter in the ΛCDM model. The fact that ϕ shares the same behavior of the dark matter is indeed one of the main reason why the community thinks it could be a very promising candidate.
If one assumes that the scalar field accounts for all the dark matter in the galaxy, then it is possible to estimate the magnitude ϕ_0 of the oscillation for any given value of the mass m_ϕ [68]. Using a value of the local galactic dark matter energy density of $\rho_{DM} = 0.5Gev/cm^3$ [94], the amplitude ϕ_0 at infinity is given by

$$\phi_0 \sim \frac{8\cdot 10^{-31}eV}{m_\phi}. \tag{4.34}$$

Since one wants to describe the dark matter present in our galaxy, we want the de Broglie wavelength associated with the oscillating scalar field to be smaller that the galactic size. As discussed in [51] one can identify the de Broglie wavelength of the scalar field with its coherent length $\lambda_c = \hbar/\left(m_\phi v_0\right)$. Here $v_0 \simeq 10^{-3}c$ is the dark matter dispersion virial velocity while m_ϕ is the mass of the scalar field. If one considers that the Milky Way size is around 10^{21}m, than one gets the condition

$$m_\phi \geq 10^{-24}eV \tag{4.35}$$

On the other side, in order for the scalar field to behave like a wave rather than a collection of particles, one needs the average mode occupation number $\bar{n}_{\mathbf{k}}$ to be much greater than one. Following [51] one defines the average mode occupation number as follows

$$\bar{n}_{\mathbf{k}} = (2\pi)^3\,\rho_{DM} f_{DM,k}\left(\mathbf{k}\right)/m_\phi, \tag{4.36}$$

where ρ_{DM} is the local dark matter energy density and $f_{DM,k}\left(\mathbf{k}\right)$ denotes the dark matter momentum distribution normalized with respect to k. Therefore, in order to have $\bar{n}_{\mathbf{k}} \gg 1$, one needs the number density ρ_{DM}/m_ϕ to be also much greater than one which leads to

$$m_\phi \leq 10eV. \tag{4.37}$$

Using this constrains in eq. (4.34), one gets $\phi_0 \leq 7\cdot 10^{-7}$ that justifies the Minkowskian approximation used in this work and proves that the model is self-consistent. Furthermore, we can combine the two boundaries given by eq. (4.35) and eq. (4.37) and translate them to f_ϕ through the eq. (4.29). One then obtains the following constrains on the oscillation frequency of the scalar field

$$10^{-10}Hz \leq f_\phi = \frac{\omega_\phi}{2\pi} \leq 10^{15}Hz. \tag{4.38}$$

As we know the Advanced LIGO and Virgo interferometers sensitivity range goes from $\sim 10Hz$ up to $\sim 10^4 Hz$. Such frequency range translates to a mass range that goes from $10^{-14}eV$ up to $10^{-11}eV$ and thus this will be the range we will be able to probe with the method discussed in this work.

4.2 GW detectors response to FDM

As discussed in the previous subsection the atomic mass, and thus the mass of the optical equipment in the interferometers, depends on the value of the scalar field ϕ. At the Minkowskian order one has:

$$S = -c^2 \int \frac{m_A(\phi)}{\gamma} dt, \tag{4.39}$$

where

$$\gamma = \frac{1}{\sqrt{1 - \left(\dot{x}^i_A/c\right)^2}}. \tag{4.40}$$

The Euler-Lagrange equations are then:

$$\frac{d}{dt}\left(\frac{\partial \mathcal{L}}{\partial \dot{x}^i_A}\right) = \frac{\partial \mathcal{L}}{\partial x^i_A}, \tag{4.41}$$

$$\frac{\partial \mathcal{L}}{\partial x^i_A} = -\frac{c^2}{\gamma}\partial_i m_A = -\frac{c^2}{\gamma}\frac{\partial m_A}{\partial \phi}\partial_i \phi, \tag{4.42}$$

$$\frac{\partial \mathcal{L}}{\partial \dot{x}^i_A} = m_A(\phi)\gamma \dot{x}^i_A \Rightarrow \frac{d}{dt}\left(\frac{\partial \mathcal{L}}{\partial \dot{x}^i_A}\right) = m_A(\phi)\gamma \ddot{x}^i_A + \dot{m}_A \gamma \dot{x}^i_A + m_A \dot{\gamma} \dot{x}^i_A. \tag{4.43}$$

Under the limit

$$\dot{x}^i_A \ll v^i_{DM} \quad and \quad \dot{x}^i_A \ll c \tag{4.44}$$

the test particle (the mirrors) is subject to the acceleration

$$\ddot{x}^i_A = a^i_A = -c^2 \frac{\partial \ln m_A(\phi)}{\partial \phi}\partial^i \phi = -c^2 \alpha(\phi)_A \partial^i \phi. \tag{4.45}$$

Injecting eq. (4.6) and the solution from the previous section, one finally gets

$$\begin{aligned} a^i_A &\simeq -c^2 d^*_g \phi_0 k^i_{DM} \sin\left(\vec{k}_{DM}\cdot\vec{x}-\omega_0 t+\delta\right) \\ &= -d^*_g \phi_0 \omega v^i_{DM} \sin\left(\vec{k}_{DM}\cdot\vec{x}-\omega_0 t+\delta\right). \end{aligned} \tag{4.46}$$

4.2.1 Effect on the phase shift $\Delta\varphi$

In this subsection we will derive the signal generated by the interaction between the scalar field ϕ and the optical equipment of the interferometer. In order to do this, two different methods are presented and discussed. The first one is based on the *geodesic deviation* and as such is in general valid only in the limit

$$f_0 \ll \frac{c}{2\pi L}, \tag{4.47}$$

where f_0 is the scalar field oscillation frequency, L is the length of the interferometers arms and c is the speed of the light. The second method is instead based on a rigorous *geometrical* derivation and will generalize the first for any values of f_0 and L. The method based on the geodesic deviation turns out to be the most common used in the literature and, as consequence of that, people have been missing in the model of the signal an additional term that comes from the non-approximative derivation. In this regard, an example will be discussed in the subsection (4.2.2).

Geodesic equation determination The interaction between the matter fields and the scalar filed generates through the acceleration (4.46) an additional phase shift $\Delta\varphi$ in the carrier. Therefore in a certain sense, the presence of the scalar field ϕ mimics the effects of the passage of a gravitational wave in the detector.
Let us consider the standard geodesic deviation equation

$$\ddot{\xi}^a + \xi^b u^c R^a_{cbd} u^d = 0, \tag{4.48}$$

where the term proportional to the Riemann tensor accounts for the effects of the gravitational waves. Because of the interaction of the scalar field with the standard matter at the Lagrangian level, a new term appears in eq. (4.48). The geodesic deviation is then described by the following equation

$$\ddot{\xi}^a + \xi^b u^c R^a_{cbd} u^d + d^*_g \xi^c \nabla_c \nabla^a \phi + d^*_g \xi^c \nabla_c \left(u^b u^a \nabla_b \phi\right) = 0. \tag{4.49}$$

See appendix A for a detailed derivation. Let us assume now that no gravitation wave is present - the Riemann tensor is null - and that the contribution to the acceleration $\ddot{\xi}^a$ comes from the interaction between the testing mass and the dark matter scalar field. Using the same assumption as the in the previous chapter, the geodesic deviation equation in the proper detector frame reads

$$\begin{aligned}\ddot{\xi}^a &= -\xi^c d_g^* \nabla_c \nabla^a \phi \\ &= \xi^j d_g^* \phi_0 \omega_0^2 \frac{v_i^{DM} v_j^{DM}}{c^2} \cos\left(\vec{k}_{DM} \cdot \vec{x} - \omega_0 t + \delta\right) .\end{aligned} \tag{4.50}$$

It is worth to notice that, since in the detector rest frame $u^a = (1, 0, 0, 0)$ for both the beam-splitter and the mirrors, the fourth term on the left hand side of eq. (4.49) doesn't play any role in the optical equipment dynamic described by eq. (4.50). Comparing the right hand term of eq. (4.50) with eq. (2.45) one can see that it is possible to identify the term multiplying the displacement ξ^j in the former equation as the second time derivative of some effective perturbation tensor produced by the presence of a fictitious gravitational wave

$$\ddot{h}_{ij}^{eff} = d_g^* \phi_0 \omega_0^2 \frac{v_i^{DM} v_j^{DM}}{c^2} \cos\left(\vec{k}_{DM} \cdot \vec{x} - \omega_0 t + \delta\right) . \tag{4.51}$$

In this sense one can say that the interaction between the scalar field ϕ and the test mass of the interferometer produces the same effect of a gravitational wave defined by

$$h_{ij}^{eff} \equiv d_g^* \phi_0 \frac{v_i^{DM} v_j^{DM}}{c^2} \cos\left(\vec{k}_{DM} \cdot \vec{x} - \omega_0 t + \delta\right) . \tag{4.52}$$

In order to obtain the effective signal one only needs to contract the effective tensor h_{ij}^{eff} with the *detector tensor* $D^{ij} = \hat{n}\hat{n} - \hat{m}\hat{m}$. The result is

$$h^{eff}(\vec{x}, t) = d_g^* \phi_0 \left[\frac{(\vec{v}_{DM} \cdot \hat{n})^2 - (\vec{v}_{DM} \cdot \hat{m})^2}{c^2} \right] \cos\left(\vec{k}_{DM} \cdot \vec{x} - \omega_0 t + \delta\right) . \tag{4.53}$$

As in the standard case, however, this is just an approximation whose validity holds true when

$$L \ll \frac{c}{\omega_0} \tag{4.54}$$

where L is the detector characteristic linear size and ω_0 is the scalar field frequency. This indeed assures that the displacement $|\xi^i|$ is much smaller

than the typical scale over which the scalar field changes substantially.
For a more rigorous derivation one has to derive the time-of-flight of the photons that travel in the arms of the detector ad evaluate how the presence of the scalar field modifies it. This is exactly what we will do in what follows.

Geometrical determination If one assumes that no gravitational wave is passing through the interferometer then the motion of the optical equipment is due exclusively to its interaction with the scalar field. Therefore its dynamic can be determined by intregrating eq. (4.46). For the mirror and the beam-splitter one gets respectively[1]

$$\begin{aligned} \vec{a}^B &\simeq -d_g^* \omega_0 \vec{v}_{DM} \phi_0 \sin\left(\vec{k}_{DM} \cdot \vec{r}_0^B - \omega_0 t + \delta\right) \\ \Rightarrow \vec{r}^B &= \frac{d_g^*}{\omega_0} \vec{v}_{DM} \phi_0 \sin\left(\vec{k}_{DM} \cdot \vec{r}_0^B - \omega_0 t + \delta\right) + \vec{r}_0^B, \end{aligned} \tag{4.55}$$

where terms of order $\left[d_g^* \omega_0 \left(\vec{v} \cdot \hat{n}\right) \phi_0\right]^2$ have been neglected. In the same way one also obtains

$$\begin{aligned} \vec{a}^M &\simeq -d_g^* \omega_0 \vec{v}_{DM} \phi_0 \sin\left(\vec{k}_{DM} \cdot \vec{r}_0^M - \omega_0 t + \delta\right) \\ \Rightarrow \vec{r}^M &= \frac{d_g^*}{\omega_0} \vec{v}_{DM} \phi_0 \sin\left(\vec{k}_{DM} \cdot \vec{r}_0^M - \omega_0 t + \delta\right) + \vec{r}_0^M, \end{aligned} \tag{4.56}$$

where the integration constants have been chosen so that

$$\left\langle \vec{r}^A \right\rangle = \vec{r}_0^A; \qquad \left\langle \dot{\vec{r}}^A \right\rangle = 0 \quad with \quad A = B, M. \tag{4.57}$$

If one defines the $\vec{x}$ axis as the one connecting the beam-splitter to the mirror, Then $\vec{r}_0^M - \vec{r}_0^B = \vec{L} \equiv \left(\vec{L} \cdot \hat{x}, 0, 0\right)$. In the proper detector frame, the space-time is assumed to be flat in absence of gravitational waves or any other perturbation. Then a photon that starts at the beam-splitter at time t_0, moving along the positive x axis, will reach the mirror at time t_1 given by

$$c\left(t_1 - t_0\right)^{(x)} = \vec{r}_M\left(t_1\right) \cdot \hat{x} - \vec{r}_B\left(t_0\right) \cdot \hat{x}, \tag{4.58}$$

whereas for the other way around one has

$$-c\left(t_2 - t_1\right)^{(x)} = \vec{r}_B\left(t_2\right) \cdot \hat{x} - \vec{r}_M\left(t_1\right) \cdot \hat{x}. \tag{4.59}$$

---

[1] the label B identifies the beam-splitter whereas the label M identifies the mirror

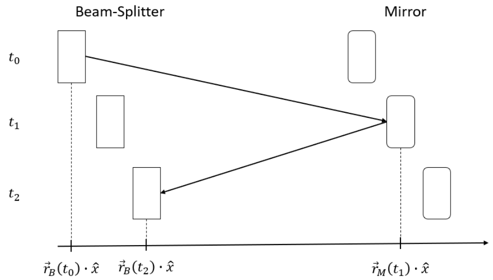

Figure 4.1: Schematic representation of the photon traveling path.

The expression for the round trip shown in Fig. 4.1 is finally obtained by combining the previous two equations

$$c\Delta T^{(x)} = c\left(t_2 - t_0\right) = 2\vec{r}_M\left(t_1\right)\cdot\hat{x} - \vec{r}_B\left(t_0\right)\cdot\hat{x} - \vec{r}_B\left(t_2\right)\cdot\hat{x}. \tag{4.60}$$

Let us now explicit the three terms on the right hand side one by one. The first one represents the position of the mirror at the time t_1

$$\begin{aligned}\vec{r}_M\left(t_1\right)\cdot\hat{x} &= \vec{x}_0^M\cdot\hat{x} + d_g^*\frac{\left(\vec{v}_{DM}\cdot\hat{x}\right)}{\omega_0}\phi_0\sin\left(\vec{k}_{DM}\cdot\vec{x}_0^M - \omega_0 t_1 + \delta\right) = \\ &= \vec{x}_0^B\cdot\hat{x} + L_x + d_g^*\frac{\left(\vec{v}_{DM}\cdot\hat{x}\right)}{\omega_0}\phi_0\sin\left(\vec{k}_{DM}\cdot\vec{x}_0^B - \omega_0 t_1 + \delta + \frac{\vec{v}_{DM}\cdot\hat{x}}{c}\cdot\frac{\omega_0 L}{c}\right),\end{aligned} \tag{4.61}$$

whereas the second and the third one describe respectively the position of the beam-splitter at the times t_0 and t_2

$$\begin{aligned}\vec{r}_B\left(t_0\right)\cdot\hat{x} &= \vec{x}_0^B\cdot\hat{x} + d_g^*\frac{\left(\vec{v}_{DM}\cdot\hat{x}\right)}{\omega_0}\phi_0\sin\left(\vec{k}_{DM}\cdot\vec{x}_0^B - \omega_0 t_0 + \delta\right) = \\ &= \vec{x}_0^B\cdot\hat{x} + d_g^*\frac{\left(\vec{v}_{DM}\cdot\hat{x}\right)}{\omega_0}\phi_0\sin\left(\vec{k}_{DM}\cdot\vec{x}_0^B - \omega_0 t_1 + \delta + \frac{\omega_0 L}{c}\right), \\ \vec{r}_B\left(t_2\right)\cdot\hat{x} &= \vec{x}_0^B\cdot\hat{x} + d_g^*\frac{\left(\vec{v}_{DM}\cdot\hat{x}\right)}{\omega_0}\phi_0\sin\left(\vec{k}_{DM}\cdot\vec{x}_0^B - \omega_0 t_1 + \delta - \frac{\omega_0 L}{c}\right).\end{aligned} \tag{4.62}$$

The total distance traveled by the photon is obtained by plugging eq. (4.61) and eq. (4.62) in to eq. (4.60)

$$\begin{aligned}
c\Delta T^{(x)} &= 2\cdot\vec{x}_0^B\cdot\hat{x}+2L_x+2d_g^*\frac{(\vec{v}_{DM}\cdot\hat{x})}{\omega_0}\phi_0\sin\left(\vec{k}_{DM}\cdot\vec{x}_0^B-\omega_0t_1+\delta+\frac{\vec{v}_{DM}\cdot\hat{x}}{c}\cdot\frac{\omega_0L}{c}\right)\\
&-\vec{x}_0^B\cdot\hat{x}-d_g^*\frac{(\vec{v}_{DM}\cdot\hat{x})}{\omega_0}\phi_0\sin\left(\vec{k}_{DM}\cdot\vec{x}_0^B-\omega_0t_1+\delta+\frac{\omega_0L}{c}\right)\\
&-\vec{x}_0^B\cdot\hat{x}-d_g^*\frac{(\vec{v}_{DM}\cdot\hat{x})}{\omega_0}\phi_0\sin\left(\vec{k}_{DM}\cdot\vec{x}_0^B-\omega_0t_1+\delta-\frac{\omega_0L}{c}\right)\\
&=2L_x+2d_g^*\frac{(\vec{v}_{DM}\cdot\hat{x})}{\omega_0}\phi_0\left[\cos\left(\frac{\vec{v}_{DM}\cdot\hat{x}}{c}\cdot\frac{\omega_0L}{c}\right)-\cos\left(\frac{\omega_0L}{c}\right)\right]\sin\left(\vec{k}_{DM}\cdot\vec{x}_0^B-\omega_0t_1+\delta\right)\\
&+2d_g^*\frac{(\vec{v}_{DM}\cdot\hat{x})}{\omega_0}\phi_0\sin\left(\frac{\vec{v}_{DM}\cdot\hat{x}}{c}\cdot\frac{\omega_0L}{c}\right)\cos\left(\vec{k}_{DM}\cdot\vec{x}_0^B-\omega_0t_1+\delta\right).
\end{aligned} \tag{4.63}$$

Before proceeding further we can re-write the last expression by considering that local dark matter velocity is not relativistic, in fact $|v_{DM}|/c\simeq10^{-3}\ll1$. Then eq. (4.63) can simplified to

$$\begin{aligned}
c\Delta T^{(x)} &\simeq 2L_x+2d_g^*\frac{(\vec{v}_{DM}\cdot\hat{x})}{\omega_0}\phi_0\left[1-\cos\left(\frac{\omega_0L}{c}\right)\right]\sin\left(\vec{k}_{DM}\cdot\vec{x}_0^B-\omega_0t_1+\delta\right)\\
&+2Ld_g^*\frac{(\vec{v}_{DM}\cdot\hat{x})^2}{c^2}\phi_0\cos\left(\vec{k}_{DM}\cdot\vec{x}_0^B-\omega_0t_1+\delta\right).
\end{aligned} \tag{4.64}$$

The same evaluation can now be repeated for the other arm of the interferometer

$$\begin{aligned}
c\Delta T^{(y)} &\simeq 2L_y+2d_g^*\frac{(\vec{v}_{DM}\cdot\hat{y})}{\omega_0}\phi_0\left[1-\cos\left(\frac{\omega_0L}{c}\right)\right]\sin\left(\vec{k}_{DM}\cdot\vec{x}_0^B-\omega_0t_1+\delta\right)\\
&+2Ld_g^*\frac{(\vec{v}_{DM}\cdot\hat{y})^2}{c^2}\phi_0\cos\left(\vec{k}_{DM}\cdot\vec{x}_0^B-\omega_0t_1+\delta\right).
\end{aligned} \tag{4.65}$$

The signal $h(\vec{x},t)$ is then determined thorough the equation

$$h(\vec{x},t)=\frac{c\left(\Delta T^{(x)}-\Delta T^{(y)}\right)}{2L}, \tag{4.66}$$

which leads to[2]

$$\begin{aligned}h\left(\vec{x},t\right) = {} & d_g^* \frac{\left(\vec{v}_{DM}\cdot\hat{n}\right)-\left(\vec{v}_{DM}\cdot\hat{m}\right)}{\omega_0 L}\phi_0\left[1-\cos\left(\frac{\omega_0 L}{c}\right)\right]\sin\left(\vec{k}_{DM}\cdot\vec{x}-\omega_0 t+\delta\right) \\ & + d_g^* \frac{\left(\vec{v}_{DM}\cdot\hat{n}\right)^2-\left(\vec{v}_{DM}\cdot\hat{m}\right)^2}{c^2}\phi_0\cos\left(\vec{k}_{DM}\cdot\vec{x}-\omega_0 t+\delta\right).\end{aligned} \tag{4.67}$$

Where one has replaced the notation $\hat{x}$, $\hat{y}$, $\vec{x}_0^B$ and t_1 with $\hat{n}$, $\hat{m}$, $\vec{x}$ and t in order to simplify the comparison with the previous result.
One has to remark two things about eq. (4.67). The first is that if we take its first order expansion in $\omega_0 L/c$

$$h_{first}\left(\vec{x},t\right) = d_g^* \frac{\left(\vec{v}_{DM}\cdot\hat{n}\right)^2-\left(\vec{v}_{DM}\cdot\hat{m}\right)^2}{c^2}\phi_0\cos\left(\vec{k}_{DM}\cdot\vec{x}-\omega_0 t+\delta\right), \tag{4.68}$$

one recovers exactly the same result we derived through the use of the geodesic deviation, see eq. (4.53). If one then pursuits the expansion up to the second order we obtain h_{first} plus a new term.

$$\begin{aligned}h\left(\vec{x},t\right) = {} & +d_g^* \frac{\left(\vec{v}_{DM}\cdot\hat{n}\right)^2-\left(\vec{v}_{DM}\cdot\hat{m}\right)^2}{c^2}\phi_0\cos\left(\vec{k}_{DM}\cdot\vec{x}-\omega_0 t+\delta\right) \\ & + \frac{1}{2}d_g^* \frac{\left(\vec{v}_{DM}\cdot\hat{n}\right)-\left(\vec{v}_{DM}\cdot\hat{m}\right)}{c}\frac{\omega_0 L}{c}\phi_0\sin\left(\vec{k}_{DM}\cdot\vec{x}-\omega_0 t+\delta\right).\end{aligned} \tag{4.69}$$

What is remarkable here is that if one considers the characteristic length and frequency band of the LIGO and Virgo detectors, this second order term contributes at the total signal as strongly as h_{first}. Therefore it can not be neglected. To show this, we first recall that ϕ_0 is actually a $\phi_0\left(\omega\right)$. In particular

$$\phi_0 \simeq \sqrt{\frac{8\pi G\rho_\phi}{c^2\omega_0^2}}. \tag{4.70}$$

Let us assume now for simplicity that the dark matter velocity is aligned with one of the interferometer arms. Then the amplitudes of the two oscillating terms are

$$\begin{aligned}A_1 &= d_g^* \frac{v_{DM}^2}{c^2}\frac{\sqrt{8\pi G\rho_\phi}}{c\omega_0}, \\ A_2 &= \frac{1}{2}d_g^* \frac{v_{DM}}{c}\frac{\omega_0 L}{c}\frac{\sqrt{8\pi G\rho_\phi}}{c\omega_0}.\end{aligned} \tag{4.71}$$

---

[2] we assumed $L = L_x = L_y$

It is now easy to see that if one considers $v_{DM}/c \simeq 10^{-3}$, $L \simeq 10^3$ and $\omega_0 \simeq 10^2$ the ration between the two amplitudes becomes

$$\frac{A_1}{A_2} = \frac{v_{DM}}{c}\frac{2c}{\omega_0 L} \simeq 1. \tag{4.72}$$

It is worth to note that the amplitude of A_2 doesn't depend on the oscillation frequency ω_0. The purpose of the simplified situation described here is just to make the reader aware that the amplitude of the two terms are comparable. Said in an other way, it is an example to show that there is at least one direction for which the second order term cannot be neglected. In any case, in the following and in particular in section 4.3, the appropriate dark matter velocity direction is taken in consideration, as it is its modulation due to the diurnal earth rotation. In Fig. 4.7 for example, it is shown that even in this case the two amplitudes remain comparable (depending of course also on the oscillating frequency of the signal).

We conclude this subsection by underling that, in the same way, one can check that the next order term is negligible as one would expect.

The amplitudes of the two oscillating terms, up to the third order, are in fact

$$\begin{aligned} A_1 &= d_g^* \frac{v_{DM}^2}{c^2}\frac{\sqrt{8\pi G\rho_\phi}}{c\omega_0}, \\ A_2 &= d_g^* \frac{v_{DM}}{\omega_0 L}\frac{\sqrt{8\pi G\rho_\phi}}{c\omega_0}\left[\frac{1}{2}\frac{\omega_0^2 L^2}{c^2} - \frac{1}{24}\frac{\omega_0^4 L^4}{c^4}\right]. \end{aligned} \tag{4.73}$$

Then, the ratio between the amplitudes A_2 and A_1 is

$$\frac{A_2}{A_1} = \frac{1}{2}\frac{\omega_0 L}{v_{DM}} - \frac{1}{24}\frac{\omega_0 L}{v_{DM}}\frac{\omega_0^2 L^2}{c^2}, \tag{4.74}$$

where one can see that for $L \simeq 10^3$ and $\omega_0 \simeq 10^2$ the third-order term is $\simeq 10^6$ times smaller than the others two, and thus negligible.

4.2.2 Relevance of the additional term for other similar DM searches

This kind of effect does play a role also in other experiment whose aim is to detect dark matter via the use of gravitational waves antennas. In their work [99], A. Pierce et al. propose to use gravitational waves interferometers to detect dark matter in the form of dark photons. As a result of the interaction with the dark matter, the test masses in the interferometer undergo the acceleration

$$\begin{aligned}\vec{a}_i\left(t,\vec{x}_i\right) &= \frac{\vec{F}_i\left(t,\vec{x}_i\right)}{M_i} \simeq \epsilon e\frac{q_{D,i}}{M_i}\partial_i\vec{A}\left(t,\vec{x}_i\right)\\ &= \epsilon e\frac{q_{D,i}}{M_i}m_A\vec{A}_0\cos\left(m_At-\vec{k}\cdot\vec{x}_i\right).\end{aligned} \tag{4.75}$$

Here ϵ gives the ratio of the dark photon coupling strength to the electromagnetic coupling strength, e is the electromagnetic coupling constant, M_i and $q_{D,i}$ are respectively the total mass and dark charge of the ith test object. The dark photon mass is described by m_a while $\vec{A}$ is the dark gauge field. In order to simplify the derivation that will follow, we introduce the quantity

$$\tilde{\epsilon} = -\epsilon e\frac{q_D}{M}m_A, \tag{4.76}$$

where one has taken in consideration that the test masses are composed of the same elements. Following the same steps that we have shown in the previous subsection, one can see that an additional non-negligible term pops up in the formula describing the amplitude of the oscillating differential displacement of the two interferometer arms (see appendix B for more details)

$$\Delta L = \sqrt{\left[a_x\cos\theta - a_y\sin\theta\right]^2\left(\frac{|k|L\sin\alpha}{m_A^2}\right)^2 + \frac{\left(a_x-a_y\right)^2L^4}{4c^4}}, \tag{4.77}$$

where the quantities a_x and a_y are defined as follows

$$a_x = -\tilde{\epsilon}A_x, \qquad a_y = -\tilde{\epsilon}A_y. \tag{4.78}$$

As we are interested in the quantity $\sqrt{\langle\Delta L^2\rangle}_{LIGO}$ defined in eq. (A3) of [99], we begin by squaring eq. (4.77) obtaining

$$\begin{aligned}\Delta L^2 = &\left[\cos\tilde{\theta}\cos\theta - \sin\tilde{\theta}\sin\theta\right]^2\left(\frac{|a||k|\hbar^2L\sin\alpha\sin\tilde{\alpha}}{c^4m_A^2}\right)^2\\ &+\frac{\left(\cos\tilde{\theta}-\sin\tilde{\theta}\right)^2|a|^2L^4\sin^2\tilde{\alpha}}{4c^4},\end{aligned} \tag{4.79}$$

where, in order to make the next step clearer, a_x and a_y have been expressed in spherical coordinates

$$a_x = |a|\cos\tilde{\theta}\sin\tilde{\alpha}, \qquad a_y = |a|\sin\tilde{\theta}\sin\tilde{\alpha}. \tag{4.80}$$

One can now take the average over all possible direction for $\vec{k}$ and $\vec{a}$

$$\begin{aligned}\langle \Delta L^2 \rangle &= \frac{1}{(4\pi)^2}\int_0^{2\pi} d\theta \int_0^{\pi} \sin\alpha d\alpha \int_0^{2\pi} d\tilde{\theta} \int_0^{\pi} \sin\tilde{\alpha} d\tilde{\alpha}\ \Delta L^2 \\ &= \frac{2}{9}\frac{|a|^2|k|^2\hbar^4 L^2}{c^8 m_A^4} + \frac{1}{6}\frac{|a|^2 L^4}{c^4}.\end{aligned} \tag{4.81}$$

Finally, we obtain $\sqrt{\langle \Delta L^2 \rangle}_{LIGO}$ by taking the square-root of the last expression

$$\sqrt{\langle \Delta L^2 \rangle}_{LIGO} = \sqrt{\frac{2}{9}\frac{|a|^2|k|^2 L^2}{m_A^4} + \frac{1}{6}|a|^2 L^4}. \tag{4.82}$$

A detailed derivation of the additional term

$$\frac{(a_x - a_y)^2 L^4}{4c^4} \tag{4.83}$$

that appears in eq. (4.77) is presented in appendix B of this manuscript.

Let us discuss this result. In particular, let us see how, with some manipulation, one could fairly easily get an hint of the effects produced by the second-order term.

In [99], the authors obtain

$$\sqrt{\langle \Delta L^2 \rangle}_{LIGO} \propto \frac{|a||k|\hbar^2 L}{c^4 m_A^2}, \tag{4.84}$$

where the proportional constant between the two previous quantity is what they define as C_{LIGO} and, in their case, its value happens to be equal to $\sqrt{2}/3$.

First of all, one can see how the introduction of the second-order correction makes the definition of C_{LIGO} unclear as, now, $\sqrt{\langle \Delta L^2 \rangle}_{LIGO}$ is no more proportional to $\frac{|a||k|\hbar^2 L}{c^4 m_A^2}$.

However, one could still stick with the proportional constant C_{LIGO} just to get an idea of what would be the effect introduced by the second-order correction on the study presented in [99]. In some sense, one introduces a novel proportional constant that must also depend on the specific mass of the dark matter field. In order to do that, it is useful to define a mass $\bar{m}_A$ such that the two contributions have the same amplitude:

$$\frac{2}{9}\frac{|a|^2|k|^2\hbar^4 L^2}{c^8 \bar{m}_A^4} = \frac{1}{6}\frac{|a|^2 L^4}{c^4}. \tag{4.85}$$

In particular, one finds that $\bar{m}_A = 4.43 \cdot 10^{-14}$eV which correspond to a scalar field oscillating frequency of $\simeq 10$ Hz. For $m_A = \bar{m}_A$ one has therefore

$$\begin{aligned}\sqrt{\langle \Delta L^2 \rangle}_{LIGO} &= \sqrt{\frac{2}{9}\frac{|a|^2|k|^2\hbar^4 L^2}{c^8 \bar{m}_A^4} + \frac{1}{6}\frac{|a|^2 L^4}{c^4}} \\ &= \sqrt{\frac{4}{9}\frac{|a|^2|k|^2\hbar^4 L^2}{c^8 \bar{m}_A^4}} \\ &= \frac{2}{3}\frac{|a||k|\hbar^2 L}{c^4 \bar{m}_A^2}.\end{aligned} \tag{4.86}$$

One can see that, thanks to this manipulation, the relation (4.84) is once again valid. Therefore, for what said before, it make sense now to define a constant of proportionality. One defines the new constant of proportionality $\bar{C}_{LIGO}(m_A)$, such that one has $\bar{C}_{LIGO}(\bar{m}_A) = \sqrt{2} C_{LIGO}$. The $\sqrt{2}$ comes from the fact that at $\bar{m}_A$, the first and second order exactly have the same amplitude. In this sense one cloud say that the *effective* result one obtains from the addition of the second-order correction term is to modify the value of the proportional constant C_{LIGO} in a way that depends on m_A. For masses $m_A \neq \bar{m}_A$, one would get

$$\bar{C}_{LIGO}(\lambda) = \sqrt{(1+\lambda^2)} C_{LIGO}, \tag{4.87}$$

where the parameter λ is defined by $m_A = \lambda \bar{m}_A$. It is worth to notice that in order to get the correct dependence from λ, one needs to make explicit the dependency of k on the scalar filed mass m_A: $k = v_0 m_A/\hbar$.

One can have a quick hint of what would be the effect of the introduction of this second-order term by simply replacing the constant C_{LIGO} with $\bar{C}_{LIGO}$, that is instead a function of the dilaton mass (and therefore of its oscillating frequency). To say it in other words, instead of considering the first order term plus the second-order one, we consider just the first-order term but we multiply it by a function of the dilaton mass rather than by a constant. This function, $\bar{C}_{LIGO}$, is what will encode the effect of the second-order term. As shown in Fig. 4.2, for a generic mass m_A much smaller than $\bar{m}_A$ ($\lambda \ll 1$), the magnitude of the second-order term is negligible compared to the one of the first-order term. As a result we obtain $\bar{C}_{LIGO} \simeq C_{LIGO}$. On the other side, for a generic mass m_A much bigger than $\bar{m}_A$ ($\lambda \gg 1$), the second term is the dominant one and thus the value of $\bar{C}_{LIGO}$ deviates from the constant value C_{LIGO} more and more.

This little excursus is meant just to give a rough idea about how the second

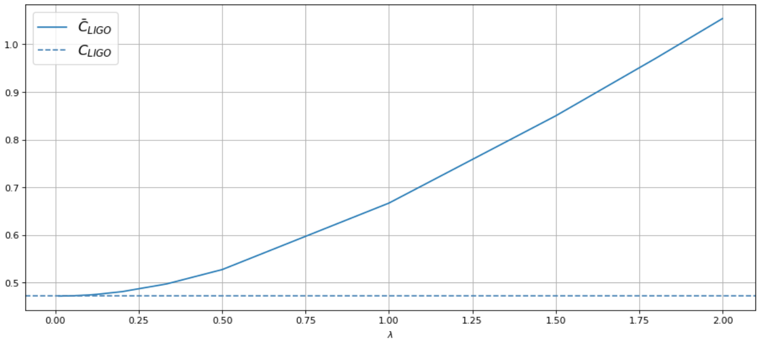

Figure 4.2: $\bar{C}_{LIGO}$ as function of the parameter λ.

order becomes dominant for oscillating scalar dark matter with a mass bigger than a specific value. In practice though, the most appropriate procedure is to follow is the one in which the second-order term and its effect on the quantity $\sqrt{\langle \Delta L^2 \rangle}_{LIGO}$ are explicitly considered.

4.3 Foreseen constraints on the parameters space

4.3.1 Dark Matter repartition model

In order to determine whether or not gravitational wave antennas are able to detect the signals produced by the dark matter, first one needs to characterize the local dark matter distribution. Following the work of Ciaran A. J. O'Hare et al. [94] we assume a total dark matter energy density $\rho_\phi \simeq 5 \cdot 10^{14} eV m^{-3}$. This total energy density is divided into two different contributions. The first of these is associated with the dark matter halo that envelops the Milky Way while the second represents the dark matter stream (S1) discussed in the paper. Streams are often present in halos simulations and, as other substructure, are generated by the tidal disruption of satellite galaxies and dark subhalos. Data from the Sloan Digital Sky Survey (SDSS) and the Gaia satellite [90, 91] strongly suggest for the presence of a counter-rotating stellar stream, together with its dark matter appendage, in the Solar neighborhood whose progenitor appears to be a massive dwarf spheroidal comparable to the present-day Fornax dwarf galaxy. The stream contains 34 confirmed stellar members and it is ~ 2 kpc wide. The mean position of its components in galactic coordinates is $(8.9, 0.6, 2.5)$ kpc with a dispersion of $(1.6, 1.4, 1.9)$ kpc and its mean velocity is given by $\vec{v}_{str} = (8.6, -286.7, -67.9)$ km/s. To have a direct comparison, the Solar po-

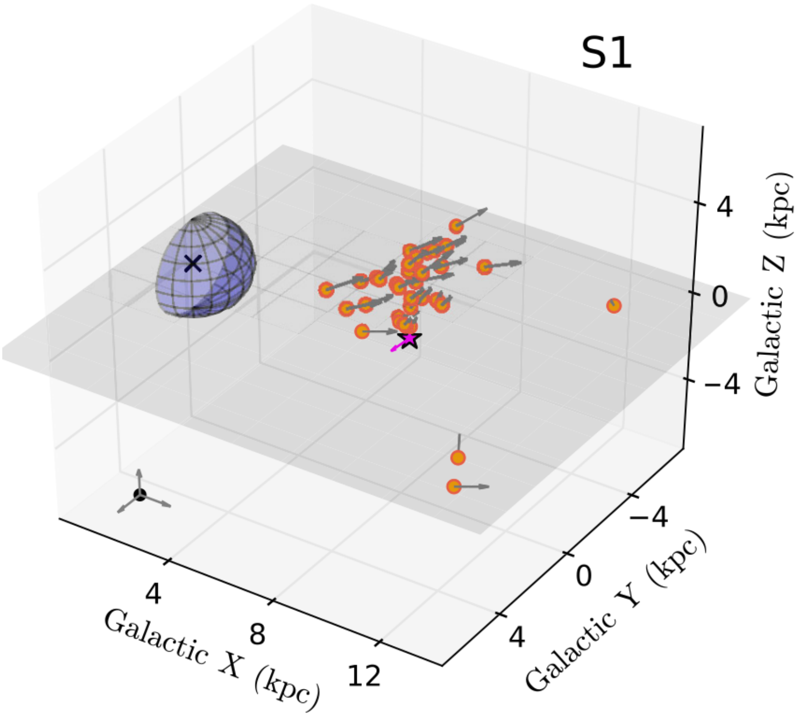

Figure 4.3: The figure shows the 34 confirmed members of the S1 stream (orange dots) together with their velocity (grey arrows). The sun and its velocity are represented instead by the magenta star and arrow. One can see how the sun moves clock-wise with respect to the galactic bulge (purple sphere) whereas the stream proceeds almost in the opposite direction.[94].

sition and velocity are $(8.2, 0, 0.014)$ kpc and $\vec{v}_\odot = (11.1, 245.04, 7.25)$ km/s respectively. It is easy to see then that not only the S1 stream is passing directly through the Solar neighborhood but also that it does it with a very high relative velocity due to its counter-rotating nature. Fig. 4.3 provides a visual representation of the stream morphology showing the portion of S1 that is interjected by the Gaia and SDSS data sets.

Following the suggestion of Ciaran A. J. O'Hare et al. [94] we model both components of the local dark matter through a Maxwellian distribution boosted by some velocity. For the halo we used as boost the laboratory velocity obtaining

$$f_h\left(\vec{v}\right) \simeq \frac{1}{\left(2\pi\sigma_h^2\right)^{3/2}} \exp\left(-\frac{|\vec{v}-\vec{v}_{lab}|^2}{2\sigma_h^2}\right). \tag{4.88}$$

Here $\sqrt{2}\sigma_h = v_0 = 232.8km/s$ [94] and $\vec{v}_{lab} = \vec{v}_{\odot}$. One can model the stream component in the same way by replacing σ_h with σ_s and $\vec{v}_{lab}$ with $\vec{v}_{lab} - \vec{v}_{str}$.

$$f_s\left(\vec{v}\right) \simeq \frac{1}{\left(2\pi\sigma_s^2\right)^{3/2}} \exp\left(-\frac{\left|\vec{v} - \vec{v}_{lab} + \vec{v}_{str}\right|^2}{2\sigma_s^2}\right), \tag{4.89}$$

with $\sigma_s \simeq 46km/s$ [94]. Next thing one needs to do is to determine how much of the local dark matter energy density is included in the halo and how much is in the stream. Unfortunately, measuring the dark matter component attached to S1 is a rather difficult task. For this reason following [94] we will consider the stream to be responsible for the 10% of the total amount of the local dark matter while the halo will account for the remaining 90%. This seems a rather reasonable assumption considering the massive nature of the stream progenitor. Fig. 4.4 shows how the presence S1 modify the dark matter speed distribution in the laboratory frame.

In light of what have been said, one can re-write equation (4.69) as follows

$$\begin{aligned} h\left(\vec{x}, t\right) &= h_1 \cos\left(\omega_0 t - \vec{k}_{DM} \cdot \vec{x} - \delta\right) - h_2 \sin\left(\omega_0 t - \vec{k}_{DM} \cdot \vec{x} - \delta\right) \\ &= \frac{\sqrt{8\pi G}}{c^3 \omega_0} d_g^* \left[\sqrt{\rho_s}\left(\vec{v}_s \cdot \vec{d}\right)\left(\vec{v}_s \cdot \vec{a}\right) + \sqrt{\rho_h}\left(\vec{v}_h \cdot \vec{d}\right)\left(\vec{v}_h \cdot \vec{a}\right)\right] \\ &\times \cos\left(\omega_0 t - \vec{k}_{DM} \cdot \vec{x} - \delta\right) \\ &- \frac{\sqrt{8\pi G}}{c^3} \frac{L}{2} d_g^* \left[\sqrt{\rho_s}\left(\vec{v}_s \cdot \vec{d}\right) + \sqrt{\rho_h}\left(\vec{v}_h \cdot \vec{d}\right)\right] \sin\left(\omega_0 t - \vec{k}_{DM} \cdot \vec{x} - \delta\right), \end{aligned} \tag{4.90}$$

where $\vec{d} = \hat{n} - \hat{m}$, $\vec{a} = \hat{n} + \hat{m}$ and one has defined the quantities

$$\rho_h = 0.9\rho_\phi, \qquad \rho_s = 0.1\rho_\phi, \tag{4.91}$$

and

$$\begin{aligned} \vec{v}_h &= \langle f_h\left(\vec{v}\right)\rangle = \left(-11.1, -245.04, -7.25\right) km/s, \\ \vec{v}_s &= \langle f_s\left(\vec{v}\right)\rangle = \left(-2.5, -531.74, -75.15\right) km/s. \end{aligned} \tag{4.92}$$

Before concluding this section, it is useful to re-write $\vec{v}_h$ and $\vec{v}_s$ in the equatorial coordinate system as this is the system we will use from now on. In order to do this one can simply write $\vec{v}_h$ and $\vec{v}_s$ in galactic spherical coordinate and then convert them into equatorial spherical coordinate through the following equations

$$\begin{aligned} \sin\delta &= \sin\delta_G \sin b + \cos\delta_G \cos b \cos\left(122^\circ.9 - l\right) \\ \cos\delta \sin\left(\alpha - \alpha_G\right) &= \cos b \sin\left(122^\circ.9 - l\right) \\ \cos\delta \cos\left(\alpha - \alpha_G\right) &= \cos\delta_G \sin b - \sin\delta_G \cos b \cos\left(122^\circ.9 - l\right). \end{aligned} \tag{4.93}$$

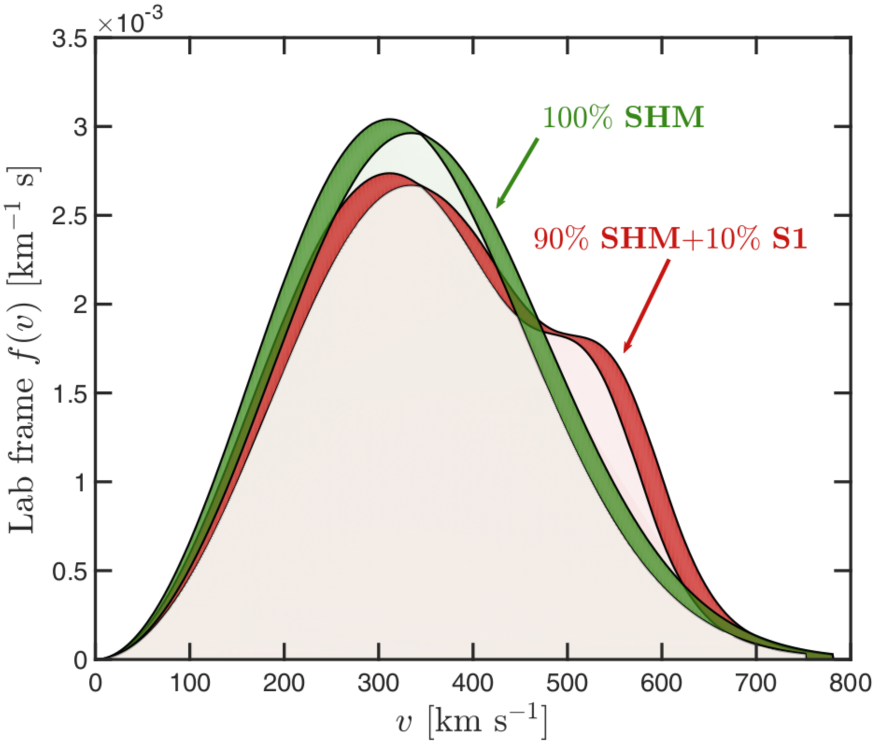

Figure 4.4: The plot shows the dark matter speed distribution for a model assuming the standard halo model(green) and the halo-plus-stream model (red). The colored region for each of the two models takes in account the modulation of the velocity distribution produced by the annual variation of $\vec{v}_{lab}$ due to the Earth rotation around the Sun [94]. Due to its negligible impact, this effect has not been considered in what follows.

Here $\alpha_G = 192^\circ.85$ and $\delta_G = 27^\circ.13$ represent respectively the right ascension and the declination of the Galactic Pole in the equatorial coordinate system. The right ascension and the declination of the vector one is transforming are given by α and δ whereas l and b are the vector's galactic longitude and latitude. In the equatorial coordinate system one then obtains

$$\begin{aligned}\vec{v}_h &= (-114.17, 120.03, -181.04)\, km/s \\ \vec{v}_s &= (-197.38, 253.37, -430.4)\, km/s.\end{aligned} \tag{4.94}$$

4.3.2 Diurnal response of the interferometers

Before discussing how the detector output signal can be analyzed in order to extract the signal we have to study how the angular efficiency of the gravitational antennas effects the strength of the signal as a result of the diurnal rotation of the Earth. This effect is encoded in the time evolution of the vector $\vec{a} = \hat{n} + \hat{m}$ and $\vec{d} = \hat{n} - \hat{m}$. Therefore, one needs to evaluate these vectors in the equatorial coordinate system. Let us consider the standard equatorial coordinate system. Its origin coincides with the center of the Earth, its z axis corresponds to the Earth's rotation axis and points toward the North pole. The x axis and y axis lie in the Earth's equatorial plane and the first points towards the vernal point. In this frame the vector characterizing the detector's arms directions can be described through the use of Euler's rotation matrix as follows

$$\hat{n} = R_z\left(\theta_1\right) R_y\left(\theta_2\right) R_z\left(\theta_3\right) \hat{n}_0, \qquad \hat{m} = R_z\left(\theta_1\right) R_y\left(\theta_2\right) R_z\left(\theta_3\right) \hat{m}_0, \tag{4.95}$$

with

$$\hat{n}_0 = (1,0,0)\,, \qquad \hat{m}_0 = (\cos\gamma, \sin\gamma, 0)\,. \tag{4.96}$$

The three quantities θ_1, θ_2 and θ_3 are instead function of the geodesic latitude of the detector site δ, the angle between the interferometer arms γ, the angle measured counter-clockwise from East to the bisector of the interferometer arms ξ. In particular

$$\begin{aligned}\theta_1 &= \delta_0 + \omega_E t \\ \theta_2 &= \frac{\pi}{2} - \delta \\ \theta_3 &= \xi - \frac{\gamma}{2} + \frac{\pi}{2},\end{aligned} \tag{4.97}$$

where ω_E and δ_0 are the Earth diurnal angular velocity and the phase defining the position of the Earth in its diurnal motion at $t = 0$. For the purpose

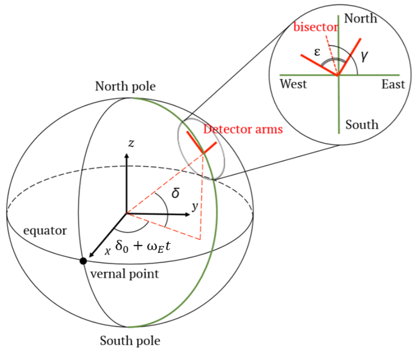

Figure 4.5: Ground-based detector configuration [89].

of what follows it is simpler to focus just on the time-dependent part of $\hat{n}$ and $\hat{m}$ that can be therefore put in the form

$$\hat{n}\,(t) = \begin{pmatrix} n_x \cos\left(\omega_E t\right) - n_y \sin\left(\omega_E t\right) \\ n_x \sin\left(\omega_E t\right) + n_y \cos\left(\omega_E t\right) \\ n_z \end{pmatrix}, \tag{4.98}$$

$$\hat{m}\,(t) = \begin{pmatrix} m_x \cos\left(\omega_E t\right) - m_y \sin\left(\omega_E t\right) \\ m_x \sin\left(\omega_E t\right) + m_y \cos\left(\omega_E t\right) \\ m_z \end{pmatrix}, \tag{4.99}$$

where the components n_x, n_y, n_z, m_x, m_y and m_z are constant defined by the aforementioned geometrical parameter

$$\begin{cases} n_x = \cos\theta_3 \cos\theta_2 \cos\delta_0 - \sin\theta_3 \sin\delta_0 \\ n_y = \cos\theta_3 \cos\theta_2 \sin\delta_0 + \sin\theta_3 \cos\delta_0 \\ n_z = -\cos\theta_3 \sin\theta_2, \end{cases} \tag{4.100}$$

and

$$\begin{cases} m_x = -\sin\theta_3 \cos\theta_2 \cos\delta_0 - \cos\theta_3 \sin\delta_0 \\ m_y = -\sin\theta_3 \cos\theta_2 \sin\delta_0 + \cos\theta_3 \cos\delta_0 \\ m_z = \sin\theta_3 \sin\theta_2. \end{cases} \tag{4.101}$$

We are now ready to discuss our strategy to detect the signal $h\left(\vec{x}, t\right)$. To

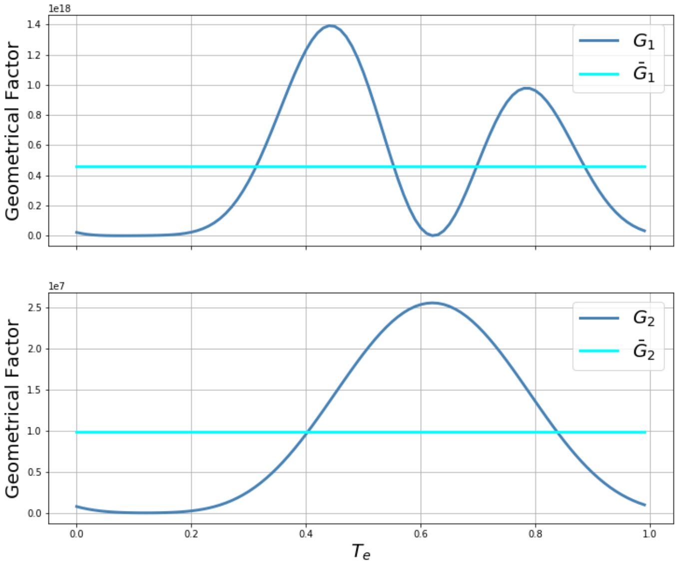

Figure 4.6: The top panel shows the evolution of the geometrical factor G_1 during the Earth's daily rotation together with its mean value $\bar{G}_1$. In the bottom panel one sees instead the evolution of G_2 and is mean value.

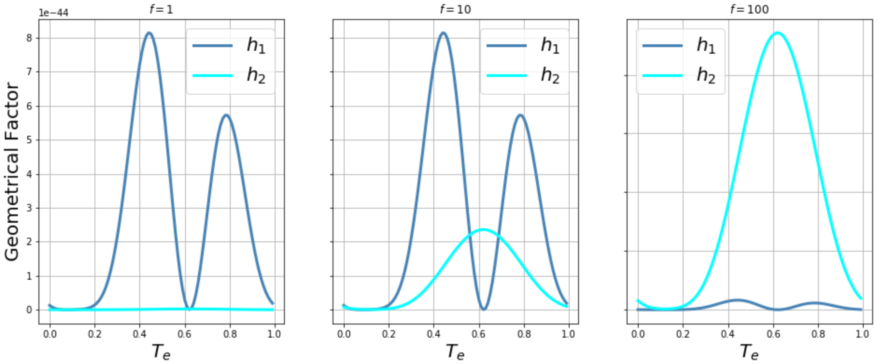

Figure 4.7: The plot compares the two amplitudes h_1 and h_2 for different choices of the signal characteristic frequency. In the left panel $f = 1$Hz and the term h_1 is dominant. In the middle panel one considers $f = 10$Hz for which the two amplitudes are of the same order. Finally, in the right panel we compare h_1 and h_2 for $f = 100$Hz where the first term becomes almost negligible. It is worth to remark that h_2 is independent of the signal frequency f.

start, it proves useful to express the signal as a single oscillating component

$$\begin{aligned} h\left(\vec{x},t\right) &= h\cos\left(\omega_0 t - \vec{k}_{DM}\cdot\vec{x} - \delta + \varphi\right), \\ h &= \frac{\sqrt{8\pi G}}{c^3}\left[\frac{G_1}{\omega_0^2} + \frac{L^2 G_2}{4}\right]^{1/2} d_g^*, \\ \varphi &= atan2\left(-\frac{\sqrt{8\pi G}}{c^3} d_g^* \frac{L}{2}\sqrt{G_2}, \frac{\sqrt{8\pi G}}{c^3\omega_0} d_g^*\sqrt{G_1}\right), \end{aligned} \tag{4.102}$$

where $G_1 = G_1\left(\omega_E t\right)$ and $G_2 = G_2\left(\omega_E t\right)$ are the geometrical factors

$$\begin{aligned} G_1 &= \left[\sqrt{\rho_s}\left(\vec{v}_s\cdot\vec{d}\right)\left(\vec{v}_s\cdot\vec{a}\right) + \sqrt{\rho_h}\left(\vec{v}_h\cdot\vec{d}\right)\left(\vec{v}_h\cdot\vec{a}\right)\right]^2, \\ G_2 &= \left[\sqrt{\rho_s}\left(\vec{v}_s\cdot\vec{d}\right) + \sqrt{\rho_h}\left(\vec{v}_h\cdot\vec{d}\right)\right]^2. \end{aligned} \tag{4.103}$$

Fig. (4.6) shows the amplitudes variations as function of time of the two oscillating terms the signal is made of. In order to derive (4.102-4.103) from (4.90), we used the relation

$$\begin{aligned} &A\cos\left(\omega t - \delta\right) - B\sin\left(\omega t - \delta\right) \\ &= \rho\cos\left(\omega t - \delta + \varphi\right), \end{aligned} \tag{4.104}$$

with

$$\rho = \sqrt{A^2 + B^2}, \qquad \varphi = atan2\left(B, A\right). \tag{4.105}$$

4.3.3 Search Strategy

Now that the signal has been cast in a more manageable form one can start discussing about its detection strategy. Although *a priori* the oscillation frequency of the signal is uniquely determined by the scalar field mass m_ϕ as in the case analyzed in [99], the dark matter virial velocity broadens the latter by a factor $\Delta f/f \sim |v_{DM}|^2 \simeq 10^{-6}$. As we are going to work with data sets whose time length will be of $T \sim 30$s, the resolution in the frequency domain will be of the order $1/T \simeq 10^{-2}$. In accordance to this, the signal can be considered to be monochromatic in the frequency band one is interested in. In their work, [99], A. Pierce et al. examine the gravitational antennas response to a near-monochromatic stochastic gravitational wave background and then translate such results to the case of dark photon dark matter taking into account all the peculiar features of the latter, e.g. the inherently long coherent time. In our case we decide to focus more on the dark matter signal,

whose form has been derived in great detail, and base our search strategy on it without using direct analogies with results provided by the gravitational wave sector. For this reason we adopt the approach suggested by B. Allen, M. A. Papa and B. F. Schutz [16] for an optimized search strategy whose detail will be discussed in the next lines.
Let us consider a data stream sampled at discrete times $t = t_j = j\Delta t$ for an observational time $T = 30s$. This will provide us with $N = T/\Delta t$ samples of the data here denoted as d_j for $j = 0, 1, ...N - 1$. For simplicity we will assume T to be an integer multiple of Δt. The question we would like to answer is whether or not the data set d_j contains the signal

$$h_j = h \cos\left(2\pi f_0 t_j - \vec{k}_{DM} \cdot \vec{x} - \delta + \varphi\right). \tag{4.106}$$

As one is considering an observational time of the order of tens of seconds, it make sense to average out the effects of the diurnal rotation of the Earth. Therefore we replace the quantities h and φ with

$$\bar{h} = \frac{1}{T_E}\int_0^{T_E} h dt, \qquad \bar{\varphi} = \frac{1}{T_E}\int_0^{T_E} \varphi dt, \tag{4.107}$$

and absorb the constants $\bar{\varphi}$ and $\vec{k}_{DM} \cdot \vec{x}$ into the random phase δ.
To continue, we consider the discrete Fourier Transform (DFT) of the dataset d_j defined as follows

$$x_k = \sum_{j=0}^{N-1} d_j e^{2\pi i t_j f_k}, \qquad \texttt{for}\, k = -N/2 + 1, ..., N/2, \tag{4.108}$$

where

$$f_k = \frac{k}{T} = \frac{k}{N\Delta t} \tag{4.109}$$

are the resolved frequencies, i.e. the frequencies that correspond to the k-th bin. Since the discrete Fourier transform is invertible, one can work in the frequency domain and then translate back any result in the time domain without any concerns. The other advantage offered by working in the frequency domain is that for stationary noise the different Fourier components are uncorrelated. As both the signal and the noise are made of real quantities it follows that $x_k = x^*_{-k}$. One can therefore restrict his or her attention to just the positive frequency without losing any information. Furthermore, x_0 and $x_{N/2}$ can be set to zero by removing from the data the direct current value and applying anti-aliasing filters. The data set we need to work with is then x_k for $k = 1, ..., N/2 - 1$. Each realization of the data set x will have a probability attached to it, here denoted by $p\left(x|h\right)$, where h is the amplitude of the signal. Let assume that both the real and imaginary part, $n_{k_{re}}$ and $n_{k_{im}}$, of the noise contribution to x_k to be independent and gaussian with average $\mu_{k_{re}} = \mu_{k_{im}} = 0$ and variance $\sigma_{k_{re}}^2 = \sigma_{k_{im}}^2 = \sigma_k^2$. The probability distributions of the noise realization of each bin are then described by

$$\begin{aligned} p\left(n_k\right) &= p\left(n_{k_{re}}\right) p\left(_{k_{im}}\right) \\ &= \frac{1}{\sqrt{2\pi}\sigma_k} e^{-\frac{n_{k_{re}}^2}{2\sigma_k^2}} \cdot \frac{1}{\sqrt{2\pi}\sigma_k} e^{-\frac{n_{k_{im}}^2}{2\sigma_k^2}} \\ &= \frac{1}{2\pi\sigma_k^2} e^{-\frac{n_k^2}{2\sigma_k^2}}. \end{aligned} \tag{4.110}$$

In absence of signal, i.e. $h = 0$, the probability distribution of our dataset x is given by

$$p\left(x|0\right) = \prod_{k=1}^{N/2-1} \frac{1}{2\pi\sigma_k^2} e^{-\frac{x_k^2}{2\sigma_k^2}}. \tag{4.111}$$

On the other hand, when the signal is present one has

$$p\left(x|h\right) = e^{-\frac{N^2}{4}\frac{h^2}{2\sigma_l^2}} I_0\left(\frac{Nh}{2\sigma_l}\frac{|x_l|}{\sigma_l}\right) p\left(x|0\right), \tag{4.112}$$

where I_0 is a modified Bessel function of the first kind described by

$$I_0\left(z\right) = \frac{1}{\pi}\int_0^{\pi} d\theta e^{z\cos\theta}. \tag{4.113}$$

In order to obtain the expression (4.112), one first assume the frequency f_0 of the signal to coincide with one of the resolved frequency, e.g. f_l. The probability distribution of the data is therefore equal to

$$p\left(x|h\right) = \frac{1}{2\pi\sigma_l^2}\int_0^{2\pi} d\delta \frac{1}{2\pi} e^{-\frac{|x_l - (N/2)he^{i\delta}|^2}{2\sigma_l^2}} \prod_{k=1,k\neq l}^{N/2-1} \frac{1}{2\pi\sigma_k^2} e^{-\frac{x_k^2}{2\sigma_k^2}}, \tag{4.114}$$

where we assumed the unknown phase δ to be uniformly distributed in the interval $[0, 2\pi)$. Let us write now the data sample x_l in terms of its modulus

$|x_l|$ and phase ϕ_l. Then

$$\begin{aligned}
-\frac{1}{2}|x_l-(N/2)\,he^{i\delta}|^2 &= -\frac{1}{2}|x_l|^2-\frac{1}{2}\frac{N^2}{4}h^2+\frac{N}{4}h|x_l|\left[e^{i(\phi_l-\delta)}+e^{-i(\phi_l-\delta)}\right]\\
&= -\frac{1}{2}|x_l|^2-\frac{1}{2}\frac{N^2}{4}h^2+\frac{N}{4}h|x_l|\cos\left(\phi_l-\delta\right).
\end{aligned} \tag{4.115}$$

The integration over δ gives therefore

$$\begin{aligned}
&\frac{1}{2\pi\sigma_l^2}\int_0^{2\pi}d\delta\frac{1}{2\pi}e^{-\frac{|x_l-(N/2)he^{i\delta}|^2}{2\sigma_l^2}}\\
&\quad=\frac{1}{2\pi\sigma_l^2}e^{-\frac{\left[|x_l|^2+\left(N^2/4\right)h^2\right]}{2\sigma_l^2}}\int_0^{2\pi}d\delta\frac{1}{2\pi}e^{\frac{|x_l|Nh}{2\sigma_l^2}\cos(\phi_l-\delta)}\\
&\quad=\frac{1}{2\pi\sigma_l^2}e^{-\frac{\left[|x_l|^2+\left(N^2/4\right)h^2\right]}{2\sigma_l^2}}I_0\left(\frac{Nh}{2\sigma_l}\frac{|x_l|}{\sigma_l}\right),
\end{aligned} \tag{4.116}$$

from which eq. (4.112) is easily recovered. Before proceed further let identify the quantities σ_k. In chapter 2 eq. (2.89) we have seen that

$$\begin{aligned}
&\left\langle n^*\left(f\right)n\left(f'\right)\right\rangle=\delta\left(f-f'\right)\frac{1}{2}S_n\left(f\right)\\
&\Longrightarrow\ \left\langle|n|^2\left(f\right)\right\rangle=\frac{1}{2}TS_n\left(f\right),
\end{aligned} \tag{4.117}$$

where $S_n\left(f\right)$ is the one-sided noise spectral density of the detector. Since $S_n\left(f\right)$ is a continuous quantity whereas the σ_k is a discrete one, the first thing to do is to re-write eq. (4.117) in terms of discrete quantities. It can be proved that, up to a factor Δt, the discrete Fourier transform of a finite set of discretely-sampled data is equivalent to the Fourier transform of the discretized data evaluated at the discrete frequency f_j. See appendix D in [106] fore more details. Therefore

$$\begin{aligned}
\left\langle|n|^2\right\rangle&=\left\langle n_{re}^2\right\rangle+\left\langle n_{im}^2\right\rangle\\
&=\Delta t^2\left\langle n_{k_{re}}^2\right\rangle+\Delta t^2\left\langle n_{k_{im}}^2\right\rangle\\
&=\frac{1}{2}N\Delta tS_n\left(f_k\right).
\end{aligned} \tag{4.118}$$

On the other side we know that

$$\left\langle n_{k_{re}}^2\right\rangle=\left\langle n_{k_{im}}^2\right\rangle=\sigma_k^2. \tag{4.119}$$

Adding all together one finally gets

$$\begin{aligned}\Delta t^2 \left\langle n_{k_{re}}^2 \right\rangle + \Delta t^2 \left\langle n_{k_{im}}^2 \right\rangle &= 2\Delta t^2 \sigma_k^2 \\ &= \frac{1}{2} N \Delta t S_n\left(f_k\right) \\ \rightarrow \sigma_k^2 &= \frac{1}{4}\frac{N}{\Delta t} S_n\left(f_k\right).\end{aligned} \tag{4.120}$$

In order to help simplifying the notation in some of the following results, let us define the parameter

$$\epsilon = \frac{\sqrt{T}h}{\sqrt{S_{n_k}}} = \frac{Nh}{2\sigma_k}. \tag{4.121}$$

Following the path described in chapter 2, one needs now to define a *statistic*, i.e. a function of the data set x. In order to do this, we first consider the likelihood ration statistic

$$\Gamma\left(x\right) = \frac{p\left(x|h\right)}{p\left(x|0\right)} = e^{-\frac{N^2}{4}\frac{h^2}{2\sigma_l^2}} I_0\left(\frac{Nh}{2\sigma_l}\frac{|x_l|}{\sigma_l}\right) = e^{-\frac{1}{2}\epsilon^2} I_0\left(\epsilon\frac{|x_l|}{\sigma_l}\right). \tag{4.122}$$

Such statistic plays in fact a key role because of the Neyman-Pearson criterion (or lemma). This criterion states that an optimal statistic $\Lambda\left(x\right)$, i.e. one that minimize the false dismissal probability for a given false alarm probability, is any function of the observed data which shares the same level surfaces of the likelihood ration function $\Gamma\left(x\right)$ [16]. In our case $\Gamma\left(x\right)$ depends only on the modulus of the l'th $|x_l|$. Since the likelihood function increases monotonically, any other monotonically increasing function of $|x_l|$ will share the same level surfaces with it. For these reason we choose as statistic the function

$$\Lambda = \frac{|x_l|^2}{\sigma_l^2}. \tag{4.123}$$

We need now to evaluate the false alarm probability α and the false dismissal probability β as function of the generic threshold Λ_*. According to eq. (2.91) one has

$$\begin{aligned}\alpha\left(\Lambda_*\right) &= \int_{\frac{|x_l|^2}{\sigma_l^2} > \Lambda_*} p\left(x|0\right) dx \\ &= e^{-\Lambda_*/2}\end{aligned} \tag{4.124}$$

where the integration measure is intended as follows

$$\int dx \equiv \prod_{k=1}^{N/2-1} \int_{-\infty}^{\infty} dx_{k_{re}} \int_{-\infty}^{\infty} dx_{k_{im}}. \tag{4.125}$$

In the same way, we can evaluate the false dismissal probability

$$\begin{aligned}\beta\left(\Lambda_*,h\right) &= \int_{\frac{|x_l|^2}{\sigma_l^2}\leq\Lambda_*} p\left(x|h\right)dx \\ &= e^{-\frac{N^2h^2}{8\sigma_l^2}}\int_0^{\sqrt{\Lambda_*}} u\,e^{-\frac{1}{2}u^2} I_0\left(\frac{Nh}{2\sigma_l}u\right)du \\ &= e^{-\frac{1}{2}\epsilon^2}\int_0^{\sqrt{\Lambda_*}} u\,e^{-\frac{1}{2}u^2} I_0\left(\epsilon u\right)du,\end{aligned} \tag{4.126}$$

with $u = |x_l|/\sigma_l$.
Unfortunately, as also remarked in [16], the last integral cannot be evaluated in closed form. However, for small signals, and therefore small values of ϵ, the modified Bessel function can be approximated with the first two terms of its power series representation

$$I_0\left(z\right) = 1 + \frac{z^2}{4}, \tag{4.127}$$

from which it follows

$$\beta\left(\Lambda_*,h\right) = 1 - e^{-\Lambda_*/2} - \frac{N^2h^2}{16\sigma_l^2}\Lambda_* e^{-\Lambda_*/2}, \tag{4.128}$$

or, equivalently

$$\beta\left(\Lambda_*,\epsilon\right) = 1 - e^{-\Lambda_*/2} - \frac{1}{4}\epsilon^2\Lambda_* e^{-\Lambda_*/2}. \tag{4.129}$$

In Fig. 4.8 (*top panel*) we show how the approximated form of β, eq. (4.128), compares with the corresponding exact expression, eq. (4.126). We see that even for ϵ of the order of unity, the error on beta is less than 5%. It is worth to remark here that, *a priori*, one cannot make any statements on the magnitude of ϵ as h, and thus ϵ itself, are proportional to the unknown parameter d_g^*. It is useful then to define the quantity

$$\delta_r\beta = \frac{|\beta - \tilde{\beta}|}{\beta}, \tag{4.130}$$

where $\tilde{\beta}$ is the approximated expression of the false dismissal probability given in eq. (4.128) whereas β is the exact value given by eq. (4.126). See Fig. 4.8 (*bottom panel*). In what follows our approximation will considered to be valid only in the region where $\delta_r\beta < 0.05$. Fig. 4.9 shows the repartition of the parameter space that follows from this assumption.

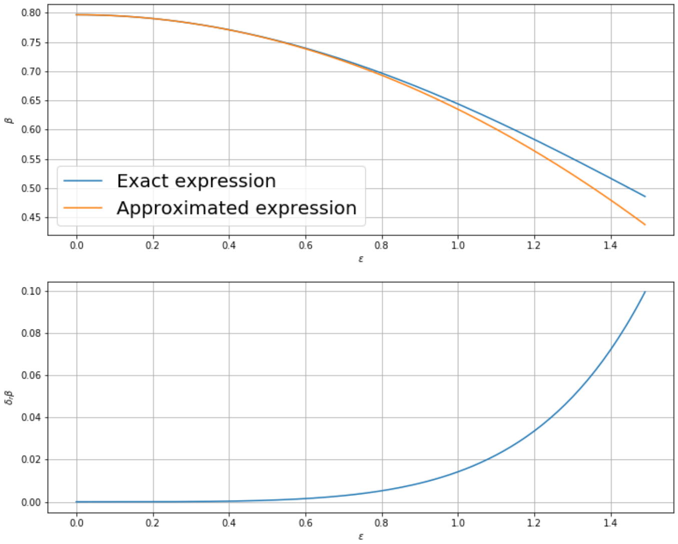

Figure 4.8: *Top panel:* the plot shows a confrontation between the exact expression of the false dismissal probability β and its approximated form as function of the magnitude of ϵ. *Bottom panel:* the plot show the relative error $\delta_r\beta$ as function of the magnitude of ϵ.

Fig. 4.10 shows the relationship between the false alarm probability $\alpha\left(\Lambda_*\right)$, the false dismissal probability $\beta\left(\Lambda_*, h\right)$ and the chosen threshold Λ_*. Because the statistic we used has been chosen through the Neyman-Pearson criteria we are assured that for any given signal magnitude h and false alarm probability, it will provide the minimum value for the false dismissal probability. We would like now to find the optimal choice for Λ_* to maximize our chances to detect the signal. To do this we assume a two years long observation campaign. Therefore, considering a single data stream time length of 30s, one ends up with $n \sim 10^6$ different data sets. For each of those data sets, in absence of signal, one has a probability $\alpha\left(\Lambda_*\right)$ to find a peak. Because the data sets are independent, the probability to find an overall number m of peaks follows the binomial distribution

$$p\left(m,\alpha\right) = \left(\begin{array}{c} n \\ m \end{array}\right) \alpha^m \left(1-\alpha\right)^{n-m} . \tag{4.131}$$

If no signal is present, one is expected to find on average αn peaks. On the other hand, if the signal is present, the average number of peaks is $\left(1-\beta\right) n$.

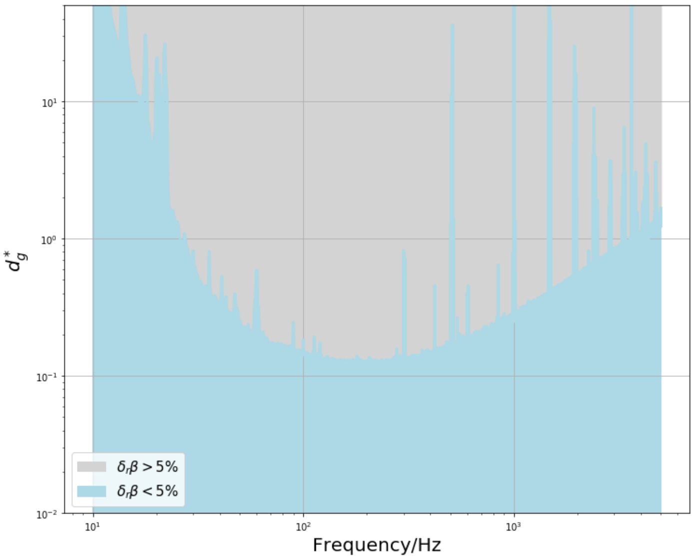

Figure 4.9: The plot shows how the constraint $\delta_r\beta < 0.05$ divides the d_g^* parameter space into two region. The region shaded in *lightblue* is therefore the parameter space region in which the approximation (4.128) can be used safely. We will further discuss on this subject later on, at the end of this subsection.

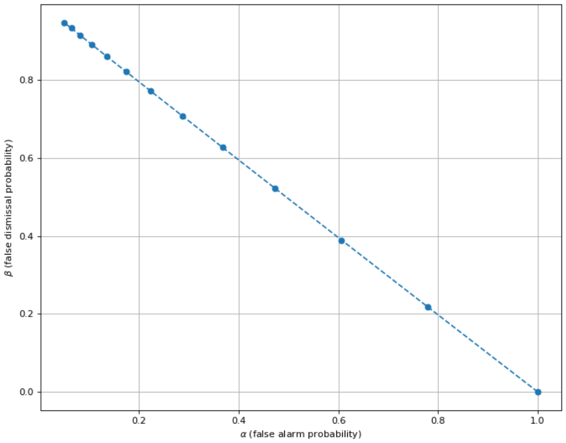

Figure 4.10: The false dismissal probability β as function of the false alarm probability α. We consider $d_g^* = 0.1$ and the frequency of the signal $f \simeq 30$Hz. The value of the threshold Λ_* is made to vary along the curve from 0 to 6. The marks correspond to the values $\Lambda_* = 0, 0.5, 1, 1.5, ..., 6$.

If one now defines the significance

$$\begin{aligned} s &= \frac{\langle m\rangle_{signal} - \langle m\rangle_{no\,signal}}{\sigma} \\ &= \frac{(1-\beta)\,n - \alpha n}{\sqrt{\alpha\,(1-\alpha)\,n}} \\ &= \frac{1}{4}\epsilon^2 \frac{\Lambda_*}{\sqrt{e^{\Lambda_*/2}-1}}\sqrt{n}, \end{aligned} \tag{4.132}$$

a good way to fix the threshold is to chose the value of Λ_* that maximizes s. In our case one obtains

$$\begin{aligned} 0 = \frac{ds}{d\Lambda_*} &\propto \left(e^{\Lambda_*/2}-1\right)^{-1/2} - \frac{1}{4}\Lambda_*\left(e^{\Lambda_*/2}-1\right)^{-3/2} e^{\Lambda_*/2} \\ &\implies 1 - \frac{1}{4}\Lambda_*\left(e^{\Lambda_*/2}-1\right)^{-1} e^{\Lambda_*/2} = 0 \\ &\implies (\Lambda_* - 4)\, e^{\Lambda_*/2} + 4 = 0 \\ &\implies \Lambda_* = 3.18721. \end{aligned} \tag{4.133}$$

One can check that for $\Lambda_* = 3.18721$ the second derivative $d^2 s/d\Lambda_*^2$ assume the negative value $\simeq -0.47$. This confirms that the value we found is indeed a maximum of the significance function s.
To conclude we would show the constraint that would arise in case of no detection. To do this we first define the value m_* such that

$$CDF\,[p\,(m,\alpha) < m_*] = \tilde{C}, \tag{4.134}$$

where $\tilde{C}$ is an adjusted threshold that takes in account the number of trials N_t performed during the search. Since we do not know a priori in which bin the signal should be present, i.e. we don't know the signal frequency, we scan over all the frequency range of the detector. The number of trials is therefore

$$N_t = \frac{(f_{max} - f_{min})}{\Delta f} + 1 = (f_{max} - f_{min})\,T + 1, \tag{4.135}$$

where f_{max} and f_{min} are the minimum and maximum frequency the detector is sensible to. For example let assume one wants to find the value m_* for which the probability to get $m > m_*$, when no signal is present, is less than 5% [3] then

$$\tilde{C} = \frac{0.95}{N_t}. \tag{4.136}$$

---

[3] Later on the considered confidence level will always be of 95%, when not otherwise specified.

Let us assume now the signal to be present. We could ask ourselves to find for which value of β the number m of peaks is at least equal to m_* 95% of the time. The value b_* that we are looking for is the one satisfying the relation

$$CDF\left[p\left(m, 1-\beta_*\right) < m_*\right] = 0.05. \tag{4.137}$$

As the threshold Λ_* have already be fixed, one can determine the minimum signal amplitude h_* needed in order to get $\beta = \beta_*$ by inverting eq. (4.128). Finally the constraint on the parameter d_g^* are obtained by isolating its contribution from the signal amplitude h_*

$$\begin{aligned}
\beta_* &= 1 - e^{-\Lambda_*/2} - \frac{N^2 h_*^2}{16\sigma_l^2}\Lambda_* e^{-\Lambda_*/2} \\
&= 1 - e^{-\Lambda_*/2} - \frac{T h_*^2}{4S_{n_l}}\Lambda_* e^{-\Lambda_*/2} \\
\rightarrow h_*^2 &= \frac{\left(e^{\Lambda_*/2} - 1 - \beta_* e^{\Lambda_*/2}\right)}{\Lambda_*}\frac{4S_{n_l}}{T} \\
\rightarrow d_g^* &= \frac{\left(e^{\Lambda_*/2} - 1 - \beta_* e^{\Lambda_*/2}\right)^{1/2}}{\Lambda_*^{1/2}}\sqrt{\frac{4}{T}}\sqrt{\frac{S_{n_l}}{\bar{h}^2}}.
\end{aligned} \tag{4.138}$$

Figure 4.11 shows the expected limit on d_g^* for a two years long observation campaign. The grey area defines the parameter region in which the approximated form used to evaluate the false dismissal probability β, eq. (4.128), leads to a relative error $\delta_r\beta$ greater than 5%. To extend the constraint also to the gray region would not be difficult. One just needs to invert eq. (4.126) numerically, something that can be easily done with Python (or other languages). The point is that, even if it is easy, its computational cost is also quite high. As one does not expect anyway a strong signal, we decided to not follow this route, but this is what the LVK collaboration should do if it decides to follow this type of analyses.

4.3.4 Comparison with Morisaki et al.

One can confront it with the result proposed by S. Morisaki and T. Suyama based on a very similar study [89]. This study appeared on arXiv while conducting the thesis work presented in the present manuscript (for which the results discussed in section 4.3 had already been obtained). Nevertheless, some key differences are present in the two works. In particular: *i*) we consider the effects of the dark matter stream S1, *ii*) we use a different windowing in order to take into account the glitches present in the data and

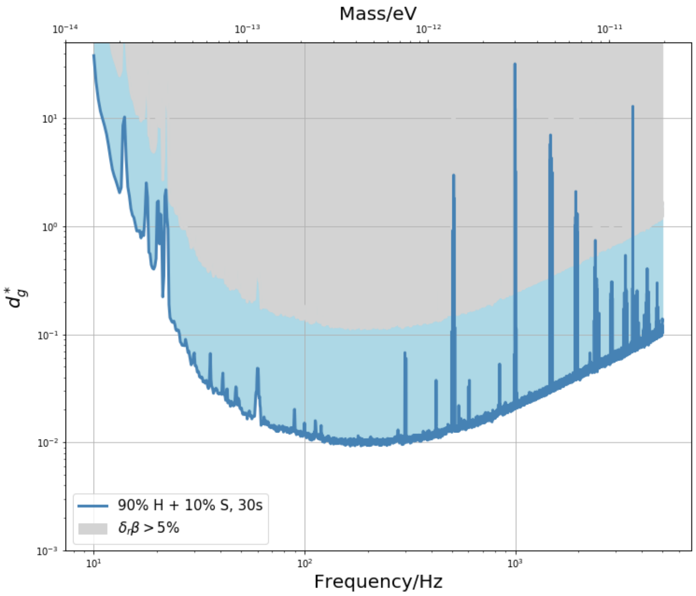

Figure 4.11: Constraints on d_g^* parameter at 95% confidence level. We considered a two-years long observation campaign and a single search time $T = 30$s. The dark matter local content is assumed to consist of 90% halo and the remaining 10% stream. The limit are derived considering the LIGO-Hanford interferometer sensitivity during O3. The code used to obtain this curve, as well as the following ones, has been posted in https://gitlab.com/FrancescoCipriano/phd-manuscript.git

iii) we use a more conservative statistical criterion to evaluate the possible constraint on the parameter d_g^*.

In order to confront these two works, we first show that the signal we derived in eq. (4.69) is exactly the same one described in equations (27) and (28) of their work. This is easily done once we re-write eq. (4.69) in natural units ($c = \hbar = 1$) and set $\kappa\phi_{\vec{k}} = \phi_0$. One gets in fact

$$\begin{aligned} &2d_g^*\kappa\phi_{\vec{k}}\frac{\sin^2\left(\frac{m_\phi L}{2}\right)}{m_\phi L}\frac{\left(\vec{k}\cdot\vec{n}-\vec{k}\cdot\vec{m}\right)}{m_\phi}\sin\left(\omega_k\left(t-L\right)-\vec{k}\cdot\vec{x}+\theta_{\vec{k}}\right)\\ =&+d_g^*\phi_0 2\frac{\sin^2\left(\frac{\omega L}{2}\right)}{\omega L}\left(\vec{v}\cdot\vec{n}-\vec{v}\cdot\vec{m}\right)\sin\left(\omega t-\vec{k}\cdot\vec{x}-\delta\right)\\ =&-d_g^*\phi_0\frac{\left[1-\cos\left(\omega L\right)\right]}{\omega L}\left(\vec{v}\cdot\vec{n}-\vec{v}\cdot\vec{m}\right)\sin\left(\vec{k}\cdot\vec{x}-\omega t+\delta\right), \end{aligned} \tag{4.139}$$

and

$$\begin{aligned} &-d_g^*\kappa\phi_{\vec{k}}\frac{\left(\vec{k}\cdot\vec{n}\right)^2-\left(\vec{k}\cdot\vec{m}\right)^2}{m_\phi^2}\cos\left(\omega_k\left(t-L\right)-\vec{k}\cdot\vec{x}+\theta_{\vec{k}}\right)\\ =&-d_g^*\phi_0\left[\left(\vec{v}\cdot\vec{n}\right)^2-\left(\vec{v}\cdot\vec{m}\right)^2\right]\cos\left(\vec{k}\cdot\vec{x}-\omega t+\delta\right). \end{aligned} \tag{4.140}$$

The overall minus sign is justified by the different definition of $h(t)$ as the one they use turns out to be the exact opposite of the one we use in our work (see eq. (26) in [89]).

Beside this, the models used to describe the dark matter content in the local system differ slightly: if in [89] the dark matter content is described by a superposition of non-relativistic waves and the result are given averaging the square of the signal obtained over all the possible direction of the wave vector $\vec{k}$, in our work instead (following the suggestions present in [94]) we consider the presence of both a dark matter halo and a dark matter stream each of which is modeled through a Maxwellian distribution boosted by some appropriate velocity. The presence of a dark matter stream in the vicinity of solar system seems to affect the magnitude of the constraint one is able to put on the coupling parameter d_g^* in a rather significant way. For this reason we think it would be of great interest to consider it in any kind of search whose goal is to detect dark matter presence in the local system.

As for the detection method, a difference is present in the observation time. In our work, in fact, the total time of the observational campaign is divided in smaller segment each of which is as long as 30s. Although such division has the side effect to smooth out the fine features of the dark matter signal, we think this choice is able to account for a more realistic scenario in which experimental limitations, e.g. the presence of transient noise (glitches), prevent the acquisition of a continuous data stream for long periods. The search strategy we propose is therefore slightly different as it account also for this experimental limit.

Finally a difference is also present in the way used to evaluate the signal amplitude threshold for detection, and thus the constraint on d_g^* one derives from it. In our case such amplitude is defined as the magnitude for which the signal, if present, will be detected 95% of the time. In [94] is instead defined as the magnitude for which the expected value of the detection statistic in presence of the signal exceeds the expected value of the detection statistic in absence of signal - pure noise - for a quantity greater of the square root of its variance. Despite our approach being more conservative the two final constraining curves do not differ a lot. To help this comparison we can consider a less conservative way to derive our limit on the parameter d_g^* that is more similar to the one used in [94]. To do this we look for the value h_{**} for which

$$s = \frac{\langle m \rangle_{h=h_{**}} - \langle m \rangle_{h=0}}{\sigma} \geq 1 \tag{4.141}$$

To further facilitate the confront we assume a total observational time of just one year and a local dark matter energy density $\rho_\phi = 3 \cdot 10^{14} eV m^{-3}$. The result obtained through the two method are compared in Fig. 4.12.

To conclude, we have seen how several differences distinguish our work from the one proposed in [89]. On one side there is the assumed dark matter galactic model. Although considering, or not considering, the presence of the dark matter S1 stream does not undermine the result obtained, in our work we have shown that its contribution does improve the boundaries one is able to set on the coupling parameter d_g^*. For this reason, as long as one can reasonably assume that this dark matter stream is present in our galaxy, we think it should be taken into account in this kind of experiments.

On the other side, for what concerns instead the detection method, one has two important difference. Respectively, they are the different approaches in determining the signal amplitude threshold and the different assumption the two studies make on the data flux. In the work discussed in [89], the authors seems to consider an uninterrupted flow of data over the entire observational campaign. In our study instead we take into consideration the fact that this is usually not the case. For this reason the method discussed in our work is meant to be applied to a set of short data samples (30s long) that could, or could not, be consecutive in time. This allows the method to be efficient even in situation in which, due to some detector downtime or spikes in the

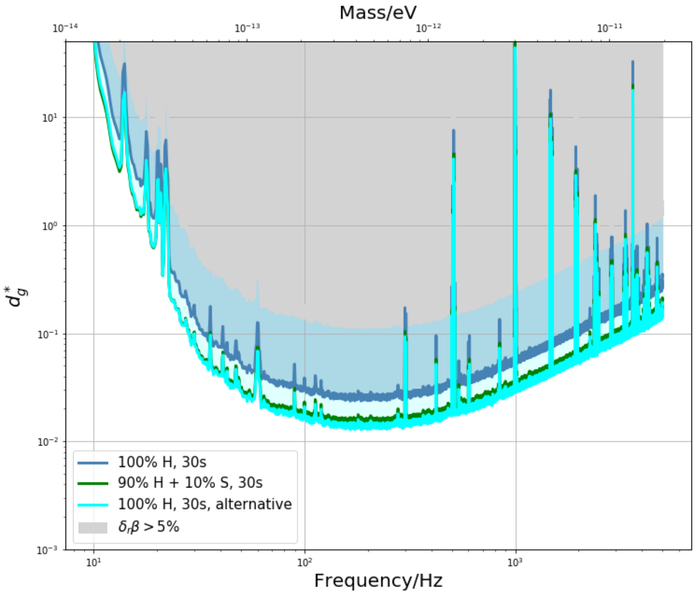

Figure 4.12: Comparison between the constraints obtained on d_g^* applying two different method to determine the signal amplitude threshold for detection. The curve in *blue* shows the limit obtained with the "standard" method proposed in our work (95% confidence) for an Halo-only dark matter model. The curve in *green* shows the constraint one gets with the same method but considering also the dark matter stream S1. Finally, the curve in *cyan* shows the limits obtained instead when one uses the "alternative" and less conservative method described by eq. (4.141). For all the curve we have assumed $\rho_\phi = 3 \cdot 10^{14} eVm^{-3}$ and a total observation time of one year.

background noise, one is obliged to reject part of the collected data. This unfortunately comes with a small drawback. As showed in Fig. 4.14, the greater is the duration of the single data samples, the better is the constraint one can set on d_g^*. However this is just a small price one has to pay to make the method work in scenarios that better represent a real world situation.

4.3.5 Impact of the window size

In Fig. 4.13 we show the constraints one gets for coupling parameter d_g^* for different choices of the single search time T. One can see how, as one increases the time T, the minimum of the constraint curve gets smaller and

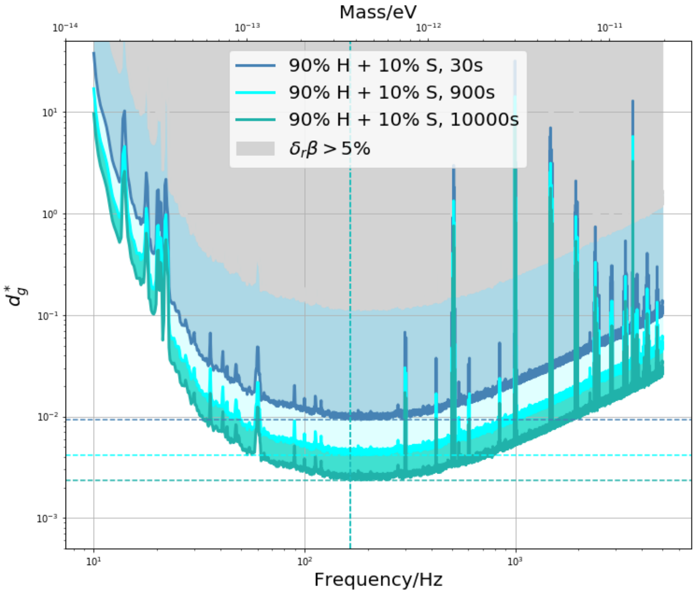

Figure 4.13: Different constraint curves on the parameter d_g^* for different choices of the single search time T.

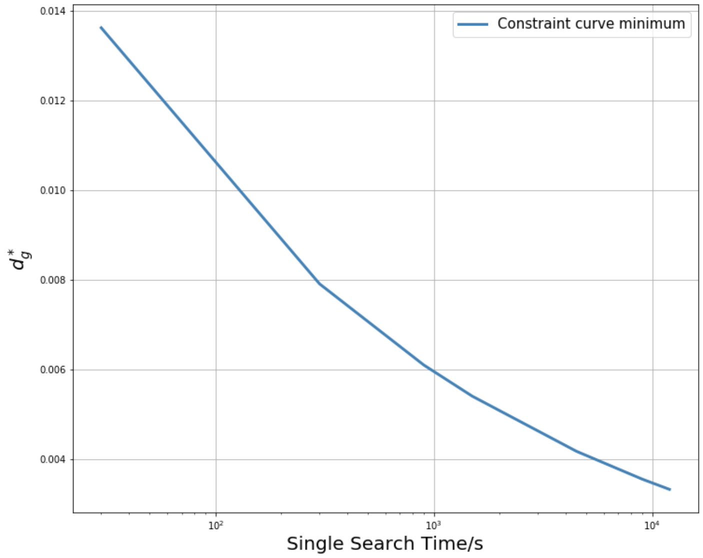

Figure 4.14: The minimum of the constraint curves as function of the single search time T for a two-year long observational campaign.

smaller. One can also notice that the frequency associated with the minimum of the curve doesn't seem to change for different values of the single search time. The first consideration is confirmed by the plot in Fig. 4.14 where we see that the minimum of the constrain curves is a monotonically decreasing function of T in the examined region. As for the second consideration, it is confirmed by the fact that the formula giving the constraint on d_g^* can be factorized into two terms. The first depending only on the search time T and the second depending only on the signal frequency f

$$d_g^* = F_1\left(T\right) \cdot F_2\left(f\right) \tag{4.142}$$

with

$$F_1\left(T\right) = \frac{\left(e^{\Lambda_*/2} - 1 - \beta_*\right)^{1/2}}{\Lambda_*^{1/2}} \sqrt{\frac{4}{T}}, \qquad F_2\left(f\right) = \sqrt{\frac{S_{n_l}}{\bar{h}^2}}. \tag{4.143}$$

Let see now more in detail why each of those terms depend only on the single search time T or, vice versa, on the frequency.

As for $F_1(T)$, the first thing one should notice is that Λ_* doesn't depend either on the frequency, nor on the single search time T. In fact, even if the significance function s is a function of the frequency and T, the value that maximize it doesn't depend on them. See eq. (4.132) and eq. (4.133) of this document.

The second and final thing one should notice is that β_* doesn't depend on the frequency while it does depend on T. The parameter β_* is in fact defined by eq. (4.137) that is based on the probability distribution

$$p\left(m, 1-\beta\right) = \left(\begin{array}{c} n \\ m \end{array}\right) \left(1-\beta\right)^{m} \left(\beta\right)^{n-m} . \tag{4.144}$$

For different values of T one gets different values of n as the number of data sets if defined by

$$n = \frac{2\, years}{T} . \tag{4.145}$$

This in turn will produce a different determination for β_*.

As for $F_2(f)$, we know that the one-sided noise spectral density S_n is by definition - see eq. (2.84) - a function of the frequency. On the other side $\tilde{h}$ is the signal amplitude divided by the coupling factor d_g^*. As such it depends on the signal frequency. See eq. (4.90). It is worth to notice that this factorization could be possible only because of the approximation expressed in eq. (4.127), although this should be checked rigorously.

In light of what we just said one would assume that choosing $T > 30s$ would be a better choice. This is indeed true, however one must account for limitation one has in deciding how big, or how small, the single searching time can be. For example, for obvious reasons, one cannot chose a single searching time smaller than the inverse of the sampling frequency of the instrumentation. At the same time an extremely small value of T would also be problematic for the frequency space resolution $\Delta f = 1/T$. For T much smaller than the unity, the resolution in frequency would be so poor to deprive the results of any interests. On the opposite side of the spectrum, because we are using a statistical approach to get our constraint on d_g^*, we need the number of search n to be big enough to have a statistical significance. However, the mean reason why we chose to not push the single search time T over the tens of second is because of the glitches that appear in the interferometers data-stream. The longer is T the higher is the probability for a glitch to occur and that is the reason behind our choice of $T = 30$s.

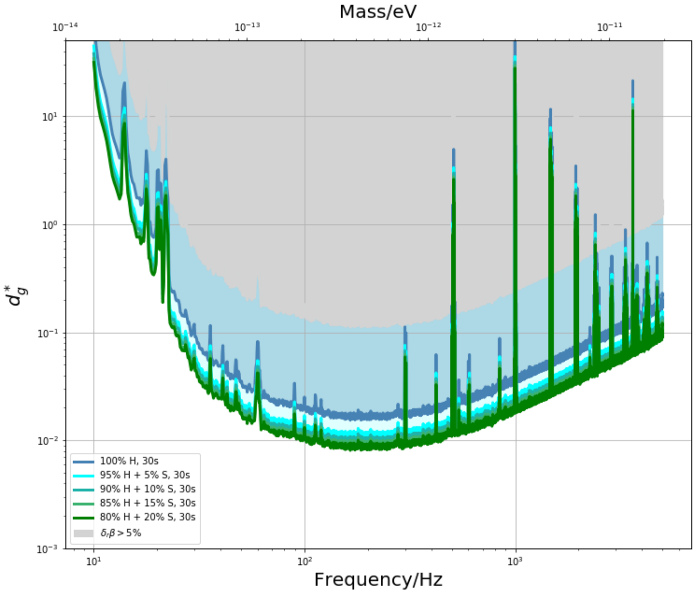

Figure 4.15: Different constraint curves on the parameter d_g^* for different local dark matter compositions.

4.3.6 Different constraints for different models

It is also interesting to see how the presence of the dark matter stream S1 affects the constraint on the parameter d_g^*. In Fig. 4.15 we show different limits curves for different rations between the dark matter present in the stream and the one present in the halo. One can see that not only the constraints become stronger the higher is the percentage of dark matter in the stream, but also that the presence of the stream itself even for low percentage improves remarkably the overall strength of the constraint. To get a better understanding of the effect of the stream on the final constraint curve, we plotted in Fig. 4.16 the contribution to the final curve due to the stream and the one due to the halo separately. We can immediately notice two things. The first is that they share the same magnitude, the second is that the stream seems to contribute more in the low-frequency band, whereas the halo the halo contribution is predominant in the high-frequency band. Our intuition suggests that this kind of behavior is due to the different strength of the signal components h_1 and h_2. We have a visual confirmation of such

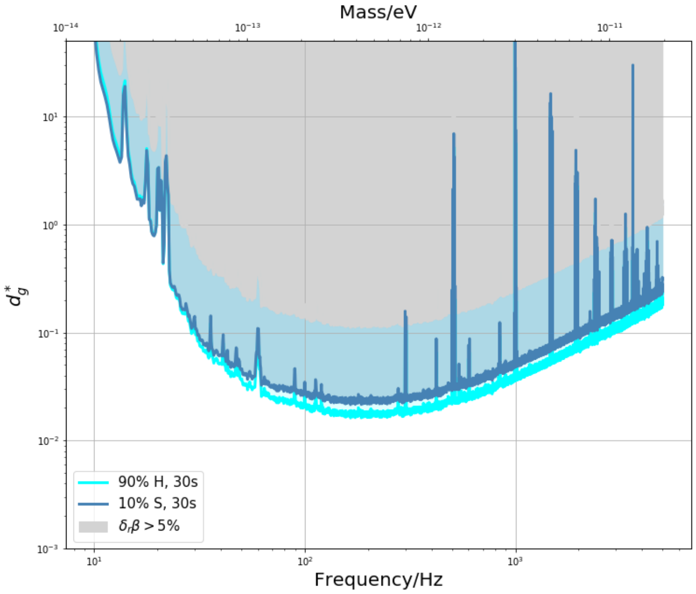

Figure 4.16: Constraint curves for the parameter d_g^* considering the halo and the stream contribution separately.

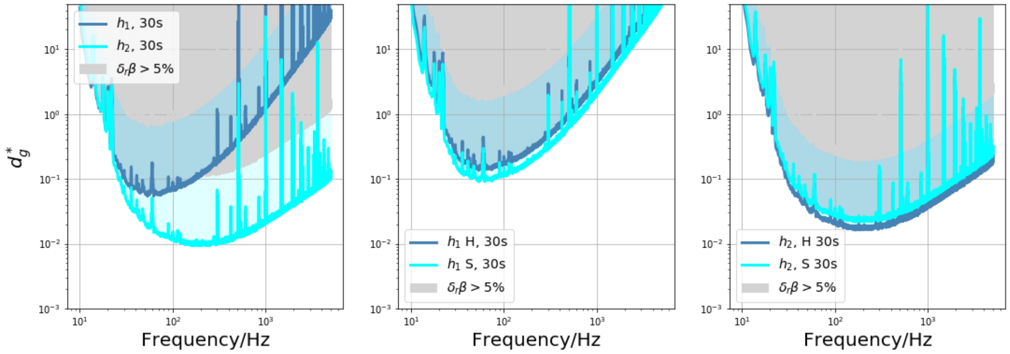

Figure 4.17: *Left-panel* contributions to the constraint curve on the parameter d_g^* due to h_1 and h_2, defined in (4.90). *Middle-panel* comparison between the contributions to the d_g^* constraint due to the stream and the halo component of h_1. *Right-panel* comparison between the contributions to the d_g^* constraint due to the stream and the halo component of h_2.

intuition in the panel 4.17 where one sees that the h_1 part of the signal generated by the stream S1 is stronger than the one that raises from the halo and vice versa for h_2. The reason why this is the case is because on one side $|v_s| \simeq 2|v_h|$ while on the other $\sqrt{\rho_h} = 3\sqrt{\rho_s}$. We know that h_2 is linear in $\sqrt{\rho}$ and $|v|$. Even if $|v_s|$ is higher than its halo counterpart, it is not high enough to compensate the discrepancy in energy density. On the other side, h_1 is linear in $\sqrt{\rho}$ but quadratic in $|v|$ and that is the reason why the stream contribution in this case becomes the stronger between the two. We would like to conclude this subsection underling that, although the presence of the S1 stream affects the result of our study enhancing the strength of the constraint we are able to set on the parameter d_g^*, it is by no means necessary. In Fig. 4.16 we show how the constraints one would obtain considering just the dark matter stream are almost as strong as the one that one gets from the halo itself, even if the former accounts only for the 10% of the total dark matter energy density. In Fig. 4.15 we show instead the constraint curves one obtains when the halo and the stream are combined together and how they change when one changes the model's parameters (in the specific case, the relative dark matter energy density percentage). On the other side, we focus particularly on the fraction of dark matter density accounted by the stream because it is, together with the dark matter mean velocity obtained from velocity distribution expressed in eq. (4.89), the feature that impacts the most the result of our work.

4.3.7 Comparison with other experiments

It proves interesting to confront the constraint curves obtained in this study with the one relative to different other works. The interaction between an ultra-light scalar field and the standard matter has been object of study of other experiments like MICROSCOPE [122], Eöt-Wash [111] and SYRTE [69].

However, an important difference between the latter and our study lies in the fact that the coupling constant d_g^* we are interested in does not depend on the composition of the test particles. It describes in fact an universal feature of the scalar-matter interaction. This translates in the fact that constraints obtained by those other experiments do not refer to d_g^* directly, but rather to some of its combinations with other coupling parameter. As a consequence, other experiments are only sensitive to terms that violate the universality of free fall but not to terms that do not; whereas gravitational waves detectors are sensitive to all terms, and in particular to terms that do not violate the universality of free fall. To phrase it differently, our goal is to test the universal part of the additional force that comes from this type of dark matter, whereas the other mentioned experiments are only sensitive to the parts that may violate the universality of free fall. One can see from Fig. 3 of [70] in fact that experiments like MICROSCOPE or Eöt-Wash do not give constraint directly on d_g^*. What do they give are constraints on the linear combinations

$$|d_{\hat{m}} - d_g|, \qquad and \qquad |d_{m_e} - d_g| \tag{4.146}$$

where d_g itself is a linear combination of d_g^* and other coupling constant as showed in eq. (4.22).

Despite the fact that those experiments are complementary in general, there is a subspace of the parameter space where one is able to compare the constraints obtained in all those experiments - that is, the region for which all the parameters but d_g are equal to 0. Indeed, in this case, the amplitude of both the universal and non-universal component of the dark matter induced force is only proportional to d_g. In accordance with that, we then re-plot the data in Fig. 3 of [70] considering all the coupling parameters (d_{m_e}, d_{m_u}, etc.) but d_g equal to zero and we scale the data through eq. (4.22) in order to get the corresponding limits on d_g^* and confront the with the one obtained in our work. See Fig. 4.18.

Therefore, under those assumptions the boundaries obtained from MICROSCOPE or Eöt-Wash do apply to d_g^* and, in the specific, are more competitive than the one obtained in this study. However, the latter is comple-

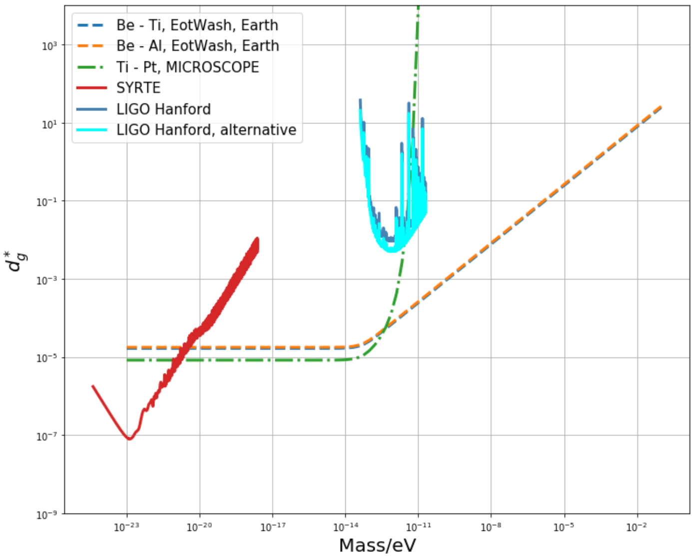

Figure 4.18: Confront of the upper limit on the coupling parameter d_g^* obtained considering the parameter region where all the coupling parameters but d_g are equal to zero. The limit are given with a 95% confidence level.

mentary to the results obtained by those other experiment because it allows to set constraints on the parameter d_g^* without having to make any sort of strong assumption on the other coupling parameters. Moreover, one can see that the region in the parameter space that correspond to a universal coupling (i.e. $d_g = d_m = d_{me}$) represents for the experiments mentioned above a blind-spot where they are unable to make any prediction, see eq. (4.146). On the other side the same region doesn't affect our experiment that would still be be able to constrain d_g, and therefore d_m and d_{me} at the same time. One can see why our proposed study is complementary to other studies that are probing this type of dark matter by other means - and in particular through the observations of signals related to a violation of the weak equivalence principle.

4.3.8 Data simulation and analysis

In order to test the effectiveness of the search strategy proposed in this work, a fake signal has been generated mimicking the interaction of the ultra-light scalar field with the interferometer optical apparatus. The latter has been then buried in Gaussian noise. The resulting stream of data has finally

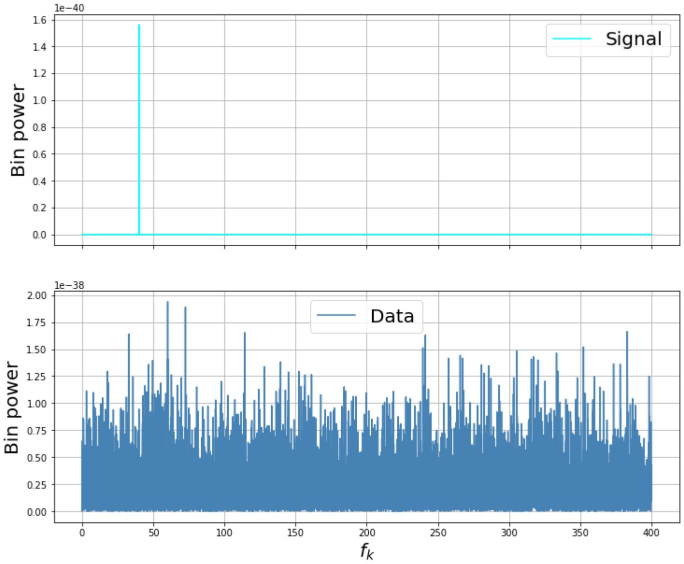

Figure 4.19: *Top* signal power spectrum as function of the frequency f_k. *Bottom* data power spectrum as function of the frequency. Note that the y-axis scale in the top panel is two order of magnitude smaller than the scale in the bottom one.

been analyzed following the method described in chapter 4[4]. A step-by-step discussion on our simulation is discussed in what follows.

Following eq. (4.106) we simulate a cosinusoidal signal

$$h_j = h \cos\left(2\pi f_0 t_j + \delta\right) , \tag{4.147}$$

where all the constant contribution to the signal phase have been incorporated in the term δ for simplicity. For our simulation we have chosen to work with a signal frequency of 20Hz whose corresponding amplitude is $h \simeq 1.04 \times 10^{-24}$. In the latter we have assumed $d_g^* = 0.1$.

We generated a total of 5000 sets of data each of which is 30 seconds long[5]. The time-step we used is $\Delta t = 0.00125$s. Because of glitches, maintenance and up-dates, the data generated by a gravitational antenna are not obtained in an uninterrupted flow. In order to take into account such features in our simulation, a delay is introduced between some of data set[6]. The effect of these delays is to reset any prior information on the signal phase.

---

[4] code posted in https://gitlab.com/FrancescoCipriano/phd-manuscript.git

[5] this adds up to less than two day of total observation time.

[6] for seek of simplicity we made so that the delay has a 50% chance to occur.

We then operate a discrete Fourier transform on the signal and add the Gaussian noise characterized by

$$\mu_k = 0, \tag{4.148}$$

and

$$\sigma_k^2 = \frac{N}{4\Delta t} S_n(f_k), \tag{4.149}$$

where $N = T/\Delta t$ is the number of point one has for each data set and $S_n(f_k)$ is the detector one-sided noise spectral density.

Finally the obtained data are analyzed following the search strategy proposed and discussed in the subsection (4.3.3). Although in this case - as we known the frequency of the signal we injected - we already know the exact frequency bin one should look at in order to find the signal, in order to make the simulation more realistic we decided to extend the search also to some of the adjacent bins. In particular for each run we chose to analyze a frequency range that goes from 39.83 Hz up to 40.17 Hz. The size of the analyzed frequency range is taken into account in the determination of the threshold needed to claim for a detection.

We initially tested the code performances with a "strong" injected signal ($d_g^* = 0.1 \implies h \simeq 1.04 \cdot 10^{-24}$). In 88 out of the 100 test runs we managed to detect the injected signal correctly. In 2 of the remaining runs the signal was correctly recovered but we also registered the presence of a false alarm. In other two a false alarm was present and the injected signal was not detected and, finally, in the remaining 8 no signal or false alarm was detected.

We have subsequently tested the code with a weaker signal ($d_g^* = 0.01 \implies h \simeq 1.04 \cdot 10^{-25}$). In this case we saw that, because of the weakness of the signal and the relatively small amount of simulated data[7], we where not able to detect the injected signal. In Fig. 4.20 we show the constraint we where able to put on the injected signal amplitude h and on the coupling parameter d_g^* as function of the length of the observational campaign. One can see how, even if because of our computational limits the obtained constraint are not as strong as the one inferred in chapter 4 (see Fig. 4.11 for example), they get better and better the longer is the time of the observational campaign we consider.

---

[7] for computational time limits we where able to simulate, at maximum, an amount of data equivalent to a 0.7 days of observational campaign.

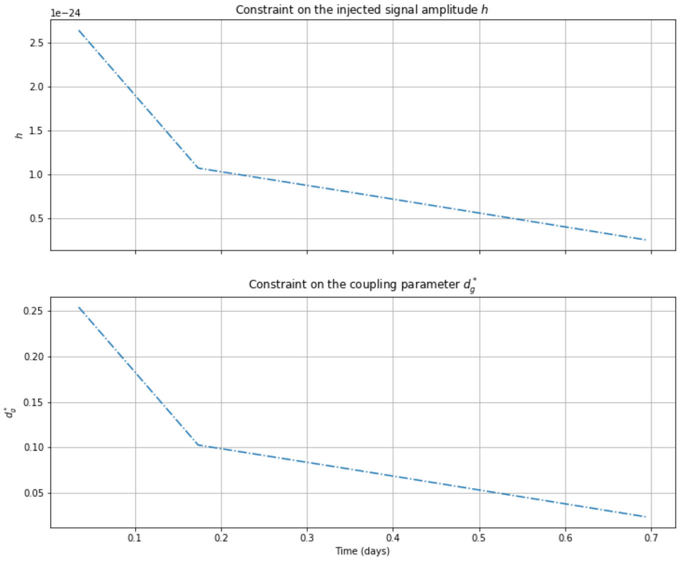

Figure 4.20: *Top panel:* 95% confidence level upper limit on the injected signal amplitude $h \simeq 1.04 \cdot 10^{-25}$. *Bottom panel:* 95% confidence level upper limit on the coupling parameter d_g^*.

4.3.9 Discussion

Looking forward, one major point would be of course to perform an analysis on real data provided by the already existing and operating ground-based interferometers such as LIGO and Virgo. A first step in this direction can be found in the subsection 4.3.8. There, we first generate a fake signal having the same characteristics of the one produced by the interaction between the ultra-light scalar field and the detectors optical apparatus, and we bury it with Gaussian noise consistent with the one generated in an interferometer. Then we analyze the data obtained in this way following the search method described in this chapter in order to detect the initial signal.

Beside this, an extensive study of the glitches occurrence frequency in the detectors would hallow for a more educated choice of single search time length T. We have seen how the constraints on the coupling parameter d_g^* benefit from the increase in the search time T. Therefore having at our disposal a precise statistical distribution of the glitches occurrence for each interferometer would allow us to determine how much the length of the search time can be pushed before having a negative impact on the final constraint as a consequence of the lost of data due to glitches.

Also, it would be interesting to study the other effects generated by the interaction between the ultra-light scalar field and the standard matter. In our work we have studied the effect that such interaction produces on the position of the key optical elements of the detectors. Other works however, like [67], suggest that other effects produced by the coupling between the dark matter field and the standard matter, e.g. the variation of the beam-splitter refractive index, could produce an interesting signature in the interferometer output. Also in [67], the authors show that introducing an asymmetry in the thickness of the mirrors located in the two different arms of the detector would produce a significant effect on the interferometer response to dark matter presence.

Finally, taken into account how well gravitational antenna seem to perform in this kind of dark matter search, it will be of great interest to extend this kind of dark matter search also to the other experiments currently dedicated to gravitational wave detection or those expected in the near future. A good example is the LISA experiment, whose sensibility to dark matter interaction has already been remarked by [99] and [89] among others. In this case one could extend their work by considering the effect of a different dark matter model as we have done by taking into account the presence of the dark matter stream S1.

4.4 Conclusion

To recap, we have seen how an ultra-light scalar field ϕ can be a valid candidate for dark matter. In particular, we have seen how a self-interacting massive scalar field defined by the potential (4.24) behaves as a pressureless fluid characterized only by its energy density ρ_ϕ and, as such, represents an optimal candidate for cold dark matter. We have seen how the field equation (4.2) admits an oscillating solution whose characteristic oscillating frequency depends directly on the value of the mass of the scalar field. The interaction between the scalar field and the optical apparatus of gravitational waves antenna, such as LIGO and Virgo, have been studied in detail. We have derived the effective signal produced by this interaction, first approximately, with the geodesic deviation, and then exactly, through a rigorous geometrical derivation. In particular we emphasized how the more rigorous approach allowed us to notice that, when the characteristic geometrical size and peculiar frequency working band of the aforementioned interferometers is took into consideration, the second-order term of the signal power series representation cannot be neglected. This second-order term in fact, which is usually considered to be negligible in the literature, must be taken into account and actually becomes the dominant one for frequencies greater than ∼10Hz. We also show how considering this additional term would be relevant in other experiments - such as the one proposed in [99] - that share the common goal to test dark matter model through the data collected by gravitational waves interferometers.

We proposed a two-step search strategy optimized to find sinusoidal-like signals. We discussed in detail the assumptions and approximations on which such detection method is based (e.g. weak signal approximation) and how one could adapt them if those assumptions would reveal to be unmet. We show that in case of no-detection, the sensitivities of the interferometers are high enough to allow us to constrain the coupling parameter d_g^* which accounts for the composition-independent part of the interaction between the scalar field and the standard matter present in the underling theoretical model. We analyze the effects that different choices of the single search time value T produce on the final constraint curves. In particular, we show how the equation that regulates the constraints magnitude can be factorized into two contributions. The first one, which depends only on the analyzed frequency, and the second which depends instead on single search time value. We also show how, for greater values of T, the minimum of the constraint curve gets smaller and smaller, thus suggesting that the optimal choice for the single search time is the highest value allowed by the glitches rate. We discuss how the constraint curves are affected by different assumptions on the underling dark matter distribution model, referring in particular to the presence of a dark matter stream in the solar system neighborhood. We see that the presence of the S1 stream, even if by no means necessary in order to establish the validity of the proposed experiment, enhances the strength of the constraint we are able to set on the parameter d_g^*. As proof of it, we show how the constraints one would obtain considering just the dark matter stream are almost as strong as the one that one gets from the halo itself, even if the former accounts only for the 10% of the total dark matter energy density (see Fig. 4.16).

The results of our work are finally confronted both with the ones obtained from the similar study proposed in [89] and the ones discussed in [70]. As for the former, we point out the main differences between the two studies: considering - or not - the presence of the dark matter stream S1, the different criterion used to evaluate the detection threshold for the signal amplitude and the different assumption made on the data flux. The method discussed in our work, in fact, is meant to be applied to a set of short data samples (30s long) that could, or could not, be consecutive in time. This allows the method to be efficient even in situation in which, due to some detector downtime or spikes in the background noise, one is forced to reject part of the collected data. We also confront the expected constraint curves obtained from the experiment proposed in this work with the ones one gets from other experiments, such as MICROSCOPE, Eöt-Wash and SYRTE. We show that, even if the overall sensitivity of the latter is overall greater, they present blind spots in some regions of the parameters space (e.g. where $d_g = d_m = d_{me}$). On the other side, the experiment we proposed doesn't have such issue and, in general, is able to constrain the parameter d_g^* without making any assumption on the other parameters of the theory. In other words, our proposal is aimed at testing the universal part of the additional force that comes from this type of dark matter, whereas the other mentioned experiments are only sensitive to the parts that may violate the universality of free fall. For this reason this experiment represents a test bench for the underling theory that is complementary to the ones already existing.

Finally we test the effectiveness of the search strategy proposed in this work by applying it to fake data. In particular, we buried in Gaussian noise a signal that reproduces the one that would be generated by the interaction of the ultra-light scalar field with the optical apparatus of the interferometers. The method has been tested both with a "strong" signal and a weak one. In the first scenario the signal has been correctly recovered in 90% of the simulations. In the second case, as expected, the signal was too weak to be detected. Nevertheless we show that the constraint obtained for the coupling parameter d_g^* improved as we increased the number of data sets simulated, that is to say the length of the observational campaign.

Appendix A

Geodesic deviation in presence of the scalar field ϕ

In this appendix we derive the geodesic deviation equation in presence of a ultra-light scalar field ϕ which interacts with the standard matter fields as described by equations (3.32-3.34).
Let us consider the field equations (4.2) that we rewrite here for simplicity

$$R_{\mu\nu} = k\left[T_{\mu\nu} - \frac{1}{2}g_{\mu\nu}T\right] + 2\partial_\mu\phi\partial_\nu\phi + \frac{1}{2}g_{\mu\nu}V\left(\phi\right), \tag{A.1}$$

$$\Box\phi = -\frac{k}{2}\sigma + \frac{V'\left(\phi\right)}{4}. \tag{A.2}$$

The first of them can be combined with its trace,

$$R = -kT + 2\partial_\gamma\phi\partial^\gamma\phi + 2V, \tag{A.3}$$

to obtain

$$R^{\mu\nu} - \frac{1}{2}g^{\mu\nu}R = kT^{\mu\nu} + 2\partial^\mu\phi\partial^\nu\phi - g^{\mu\nu}\partial_\gamma\phi\partial^\gamma\phi - \frac{1}{2}g^{\mu\nu}V. \tag{A.4}$$

Let us evaluate then the covariant derivatives of the latter. From the left-hand side one obtains

$$\nabla_\mu\left(R^{\mu\nu} - \frac{1}{2}g^{\mu\nu}R\right) = \nabla_\mu G^{\mu\nu} = 0, \tag{A.5}$$

where the last equality comes from the Bianchi identity. The covariant derivative of the right-hand side gives instead

$$\begin{aligned}
&k\nabla_\mu T^{\mu\nu} + 2\nabla_\mu\left(\nabla^\mu\phi\nabla^\nu\phi\right) - g^{\mu\nu}\nabla_\mu\left(\nabla_\gamma\phi\nabla^\gamma\phi\right) - \frac{1}{2}V'\nabla^\nu\phi \\
&= k\nabla_\mu T^{\mu\nu} + 2\nabla_\mu\left(\nabla^\mu\phi\nabla^\nu\phi\right) - g^{\mu\gamma}\nabla^\nu\left(\nabla_\mu\phi\nabla_\gamma\phi\right) - \frac{1}{2}V'\nabla^\nu\phi \\
&= k\nabla_\mu T^{\mu\nu} + 2\Box\phi\nabla^\nu - \frac{1}{2}V'\nabla^\nu\phi + 2\nabla^\mu\phi\nabla_\mu\nabla^\nu\phi - 2\nabla^\nu\nabla_\mu\phi\nabla^\mu \\
&= k\nabla_\mu T^{\mu\nu} - k\sigma\nabla^\nu\phi + \frac{1}{2}V'\nabla^\nu\phi - \frac{1}{2}V'\nabla^\nu\phi + 2\left(\nabla_\mu\nabla^\nu - \nabla^\nu\nabla_\mu\right)\phi\nabla^\mu\phi \\
&= k\nabla_\mu T^{\mu\nu} - k\sigma\nabla^\nu\phi.
\end{aligned} \tag{A.6}$$

Therefore, putting all together one finally gets

$$\nabla_\mu T^{\mu\nu} = \sigma\nabla^\nu\phi. \tag{A.7}$$

Let us consider now a test particles whose energy-momentum tensor $T^{\mu\nu}$ can be describes by

$$T^{\mu\nu} = \rho u^\mu u^\nu, \tag{A.8}$$

where ρ is the particle energy density and u^μ is its four-velocity. The quantity $\nabla_\mu T^{\mu\nu}$ is therefore equal to

$$\nabla_\mu T^{\mu\nu} = \nabla_\mu\left(\rho u^\mu u^\nu\right) = u^\nu\nabla_\mu\left(\rho u^\mu\right) + \rho u^\mu\nabla_\mu u^\nu. \tag{A.9}$$

One can combine now the latter with the continuity equation

$$\nabla_\mu\left(\rho u^\mu\right) = D. \tag{A.10}$$

It is worth to underline that a priori D is not equals to 0 because of the coupling between the matter and the scalar field. The correct value of D can be evaluated by multiplying eq. (A.7) and eq. (A.9) by u_ν and confronting the two results

$$D = -\sigma u^\mu\nabla_\mu\phi. \tag{A.11}$$

Finally one obtains the geodesic equation in presence of the ultra-light scalar field

$$\begin{aligned}
u^\mu\nabla_\mu u^\nu &= \frac{\sigma}{\rho}\left(g^{\mu\nu} + u^\mu u^\nu\right)\nabla_\mu\phi \\
&\simeq -d_g^*\left(g^{\mu\nu} + u^\mu u^\nu\right)\nabla_\mu\phi \\
&= -d_g^*\nabla^\nu\phi - d_g^* u^\mu u^\nu\nabla_\mu\phi
\end{aligned} \tag{A.12}$$

One can notice that, in absence of the scalar field ϕ, eq. (4.50) reduces to the standard geodesic equation

$$u^{\mu}\nabla_{\mu}u^{\nu}=0. \tag{A.13}$$

This also means that the presence of the scalar field and its interaction with the standard matter fields creates a violation of the Equivalence Principle. We have now all we need to calculate the geodesic deviation equation in presence of ϕ. To do so, let us consider the one parameter family of geodesic $\gamma_s\left(\tau\right)$. We define then the tangent to the family $u^{\mu}=\left(\partial_{\tau}\right)^{\mu}$ and the deviation vector $\xi^{\mu}=\left(\partial_{s}\right)^{\mu}$. The latter intuitively describes how far a geodesic is from its neighborhood, that is to say that it provides the notion of distance between two adjacent geodesic. The relative velocity between two adjacent geodesic can be therefore described by the vector field

$$v^{\mu}=u^{\nu}\nabla_{\nu}\xi^{\mu}, \tag{A.14}$$

while the relative acceleration is described by

$$a^{\mu}=u^{\rho}\nabla_{\rho}v^{\mu}=u^{\rho}\nabla_{\rho}\left(u^{\nu}\nabla_{\nu}\xi^{\mu}\right)=u^{\rho}\nabla_{\rho}\xi^{\nu}\nabla_{\nu}u^{\mu}+\xi^{\nu}u^{\rho}\nabla_{\rho}\nabla_{\nu}u^{\mu}. \tag{A.15}$$

The two terms on the right-hand side can be further developed obtaining

$$\begin{aligned}
&u^{\rho}\nabla_{\rho}\xi^{\nu}\nabla_{\nu}u^{\mu}+\xi^{\nu}u^{\rho}\nabla_{\rho}\nabla_{\nu}u^{\mu}\\
&=u^{\rho}\nabla_{\rho}\xi^{\nu}\nabla_{\nu}u^{\mu}+\xi^{\nu}u^{\rho}\nabla_{\nu}\nabla_{\rho}u^{\mu}-\xi^{\nu}u^{\rho}\nabla_{\nu}\nabla_{\rho}u^{\mu}+\xi^{\nu}u^{\rho}\nabla_{\rho}\nabla_{\nu}u^{\mu}\\
&=\xi^{\rho}\nabla_{\rho}u^{\nu}\nabla_{\nu}u^{\mu}+\xi^{\nu}u^{\rho}\nabla_{\nu}\nabla_{\rho}u^{\mu}-\xi^{\nu}u^{\rho}R^{\mu}_{\rho\nu\sigma}u^{\sigma}\\
&=\xi^{\rho}\nabla_{\rho}\left(u^{\nu}\nabla_{\nu}u^{\mu}\right)-u^{\nu}\xi^{\rho}\nabla_{\rho}\nabla_{\nu}u^{\mu}+\xi^{\nu}u^{\rho}\nabla_{\nu}\nabla_{\rho}u^{\mu}-\xi^{\nu}u^{\rho}R^{\mu}_{\rho\nu\sigma}u^{\sigma}\\
&=-\xi^{\nu}u^{\rho}R^{\mu}_{\rho\nu\sigma}u^{\sigma}-\xi^{\rho}\nabla_{\rho}\left(d^{*}_{g}\nabla^{\mu}\phi\right)-\xi^{\rho}\nabla_{\rho}\left(d^{*}_{g}u^{\nu}u^{\mu}\nabla_{\nu}\phi\right)\\
&=-\xi^{\nu}u^{\rho}R^{\mu}_{\rho\nu\sigma}u^{\sigma}-d^{*}_{g}\xi^{\nu}\nabla_{\nu}\nabla^{\mu}\phi-d^{*}_{g}\xi^{\nu}\nabla_{\nu}\left(u^{\nu}u^{\mu}\nabla_{\nu}\phi\right).
\end{aligned} \tag{A.16}$$

Therefore, combining the last two equations, one obtains

$$a^{\mu}+\xi^{\nu}u^{\rho}R^{\mu}_{\rho\nu\sigma}u^{\sigma}+d^{*}_{g}\xi^{\nu}\nabla_{\nu}\nabla^{\mu}\phi+d^{*}_{g}\xi^{\nu}\nabla_{\nu}\left(u^{\sigma}u^{\mu}\nabla_{\sigma}\phi\right)=0. \tag{A.17}$$

Appendix B

Second order term in the Dark Photon Dark Matter search

In this appendix we explicitly derive the signal produced by the interaction of the Dark Photon Dark Matter with the optical apparatus of a gravitational waves interferometer. In order to do this we will utilize the geometrical approach described in chapter 4 of this manuscript. This will allow us to put in evidence the presence of a not negligible second order term which is absent in [99].

As showed in [99], because of the interaction with the dark matter, each of the test masses undergoes the acceleration

$$\begin{aligned}\vec{a}_i\left(t,\vec{x}_i\right) = \frac{\vec{F}_i\left(t,\vec{x}_i\right)}{M_i} &\simeq \epsilon e \frac{q_{D,i}}{M_i}\partial_i \vec{A}\left(t,\vec{x}_i\right)\\ &= \epsilon e \frac{q_{D,i}}{M_i} m_A \vec{A}_0 \cos\left(m_A t - \vec{k}\cdot\vec{x}_i\right).\end{aligned} \tag{B.1}$$

Here ϵ gives the ratio of the dark photon coupling strength to the electromagnetic coupling strength, e is the electromagnetic coupling constant, M_i and $q_{D,i}$ are respectively the total mass and dark charge of the ith test object. The dark photon mass is described by m_a while $\vec{A}$ is the dark gauge field. In order to simplify the derivation that will follow, we introduce the quantity

$$\tilde{\epsilon} = -\epsilon e \frac{q_D}{M} m_A, \tag{B.2}$$

where one has taken in consideration that the test masses are composed of the same elements. The motion of the mirror and the beam-splitter are therefore described by

$$
\begin{aligned}
\vec{r}_M &= \frac{\tilde{\epsilon}}{m_A^2}\vec{A}_0 \cos\left(m_A t - \vec{k}\cdot\vec{r}_0^{M} + \delta\right) + \vec{r}_0^{M}, \\
\vec{r}_B &= \frac{\tilde{\epsilon}}{m_A^2}\vec{A}_0 \cos\left(m_A t - \vec{k}\cdot\vec{r}_0^{B} + \delta\right) + \vec{r}_0^{B}.
\end{aligned}
\tag{B.3}
$$

Let us consider a photon that starts at the beam-splitter at the time t_0, reaches the mirror at time t_1 moving along the positive x axis, and goes back to the beam-splitter at time t_2. The total length of its round trip is given by

$$
\Delta L_x = 2\vec{r}^{M}\left(t_1\right)\cdot\hat{x} - \vec{r}^{B}\left(t_0\right)\cdot\hat{x} - \vec{r}^{B}\left(t_2\right)\cdot\hat{x}. \tag{B.4}
$$

Let us now evaluate the terms on the right-hand side of the latter equation one by one.

$$
\begin{aligned}
&2\vec{r}^{M}\left(t_1\right)\cdot\hat{x} = 2\vec{r}_0^{M}\cdot\hat{x} + 2\frac{\tilde{\epsilon}\vec{A}_0\cdot\hat{x}}{m_A^2}\cos\left(m_A t_1 - \vec{k}\cdot\vec{r}_0^{M} + \delta\right) \\
&= 2\vec{r}_0^{B}\cdot\hat{x} + 2\left(\vec{r}_0^{M} - \vec{r}_0^{B}\right)\cdot\hat{x} + 2\frac{\tilde{\epsilon}\vec{A}_0\cdot\hat{x}}{m_A^2}\cos\left(m_A t_1 - \vec{k}\cdot\vec{r}_0^{B} - \vec{k}\cdot\left(\vec{r}_0^{M} - \vec{r}_0^{B}\right) + \delta\right) \\
&= 2\vec{r}_0^{B}\cdot\hat{x} + 2L + 2\frac{\tilde{\epsilon}\vec{A}_0\cdot\hat{x}}{m_A^2}\cos\left(m_A t_1 - \vec{k}\cdot\vec{r}_0^{B} - \vec{k}\cdot L + \delta\right),
\end{aligned}
\tag{B.5}
$$

$$
-\vec{r}^{B}\left(t_0\right)\cdot\hat{x} = -\vec{r}_0^{B}\cdot\hat{x} - \frac{\tilde{\epsilon}\vec{A}_0\cdot\hat{x}}{m_A^2}\cos\left(m_A t_1 - \vec{k}\cdot\vec{r}_0^{B} - m_A\frac{L}{c} + \delta\right), \tag{B.6}
$$

$$
-\vec{r}^{B}\left(t_2\right)\cdot\hat{x} = -\vec{r}_0^{B}\cdot\hat{x} - \frac{\tilde{\epsilon}\vec{A}_0\cdot\hat{x}}{m_A^2}\cos\left(m_A t_1 - \vec{k}\cdot\vec{r}_0^{B} + m_A\frac{L}{c} + \delta\right), \tag{B.7}
$$

where one has made use of the approximations

$$
t_0 \simeq t_1 - \frac{L}{c}, \qquad t_2 \simeq t_1 + \frac{L}{c}. \tag{B.8}
$$

One can now combine equations (B.5, B.6, B.7) to obtain, after some algebraic manipulation

$$
\begin{aligned}
\Delta L_x = 2L &+ 2\frac{\tilde{\epsilon}A_x}{m_A^2}\left[\cos\left(\vec{k}\cdot L\right) - \cos\left(\frac{m_A L}{c}\right)\right]\cos\left(m_A t - \vec{k}\cdot\vec{r}_0 + \delta\right) \\
&- 2\frac{\tilde{\epsilon}A_x}{m_A^2}\sin\left(\vec{k}\cdot L\right)\sin\left(m_A t - \vec{k}\cdot\vec{r}_0 + \delta\right),
\end{aligned}
\tag{B.9}
$$

where we have defined $A_x = \vec{A}_0 \cdot \hat{x}$ and set $t_1 = t$, $\vec{r}_0^B = \vec{r}_0$. Because $\vec{k} \cdot L \ll 1$ the previous equation can be approximated as follow

$$\begin{aligned}\Delta L_x = 2L + 2\frac{\tilde{\epsilon} A_x}{m_A^2}\left[1 - \cos\left(\frac{m_A L}{c}\right)\right]\cos\left(m_A t - \vec{k}\cdot\vec{r}_0 + \delta\right)\\ - 2\frac{\tilde{\epsilon} A_x}{m_A^2}\left(\vec{k}\cdot L\right)\sin\left(m_A t - \vec{k}\cdot\vec{r}_0 + \delta\right).\end{aligned} \tag{B.10}$$

The same process can be repeated for the y axis. We then obtain

$$\begin{aligned}\Delta L_y = 2L + 2\frac{\tilde{\epsilon} A_y}{m_A^2}\left[1 - \cos\left(\frac{m_A L}{c}\right)\right]\cos\left(m_A t - \vec{k}\cdot\vec{r}_0 + \delta\right)\\ - 2\frac{\tilde{\epsilon} A_y}{m_A^2}\left(\vec{k}\cdot L\right)\sin\left(m_A t - \vec{k}\cdot\vec{r}_0 + \delta\right).\end{aligned} \tag{B.11}$$

Therefore the relative change of the two arm lengths is

$$\begin{aligned}\Delta L &= \frac{\Delta L_x - \Delta L_y}{2}\\ &= \tilde{\epsilon}\frac{(A_x - A_y)}{m_A^2}\left[1 - \cos\left(\frac{m_A L}{c}\right)\right]\cos\left(m_A t - \vec{k}\cdot\vec{r}_0 + \delta\right)\\ &- \tilde{\epsilon}\frac{(A_x k_x - A_y k_y)\,L}{m_A^2}\sin\left(m_A t - \vec{k}\cdot\vec{r}_0 + \delta\right).\end{aligned} \tag{B.12}$$

The signal generated by the interaction of the dark photon with the interferometer is obtained via the equation

$$h\left(\vec{x}, t\right) = \frac{\Delta L_x - \Delta L_y}{2L}, \tag{B.13}$$

which leads to

$$\begin{aligned}h\left(\vec{x}, t\right) = \tilde{\epsilon}\frac{(A_x - A_y)}{m_A^2 L}\left[1 - \cos\left(\frac{m_A L}{c}\right)\right]\cos\left(m_A t - \vec{k}\cdot\vec{r}_0 + \delta\right)\\ - \tilde{\epsilon}\frac{(A_x k_x - A_y k_y)}{m_A^2}\sin\left(m_A t - \vec{k}\cdot\vec{r}_0 + \delta\right).\end{aligned} \tag{B.14}$$

Let us now confront our results with the one in [99]. In order to do this we rewrite eq. (B.12) defining

$$a_x = -\tilde{\epsilon} A_x, \qquad a_y = -\tilde{\epsilon} A_y. \tag{B.15}$$

Following [99] we also define α to be the angle between the wave vector $\vec{k}$ and the normal to the LIGO plane and θ to be the angle between the projected 2D wave vector and the x axis. We then obtain

$$\begin{aligned}\Delta L = & \left[a_x \cos\theta - a_y \sin\theta\right] \left(\frac{|k| L \sin\alpha}{m_A^2}\right) \sin\left(m_A t - \vec{k}\cdot\vec{r}_0 + \delta\right) \\ & - \frac{(a_x - a_y)}{m_A^2}\left[1 - \cos\left(\frac{m_A L}{c}\right)\right] \cos\left(m_A t - \vec{k}\cdot\vec{r}_0 + \delta\right).\end{aligned} \tag{B.16}$$

Applying eq. (4.104) one can see that ΔL oscillates with an amplitude equal to

$$|\Delta L| = \sqrt{\left[a_x \cos\theta - a_y \sin\theta\right]^2 \left(\frac{|k| L \sin\alpha}{m_A^2}\right)^2 + \frac{(a_x - a_y)^2}{m_A^4}\left[1 - \cos\left(\frac{m_A L}{c}\right)\right]^2}. \tag{B.17}$$

One can check that at the first order in $m_A L/c$ one recovers exactly eq. (A2) of [99]

$$|\Delta L| = |a_x \cos\theta - a_y \sin\theta| \left(\frac{|k| L \sin\alpha}{m_A^2}\right). \tag{B.18}$$

However, considering also the second order term, the amplitude becomes

$$|\Delta L| = \sqrt{\left[a_x \cos\theta - a_y \sin\theta\right]^2 \left(\frac{|k| L \sin\alpha}{m_A^2}\right)^2 + \frac{(a_x - a_y)^2 L^4}{4c^4}}. \tag{B.19}$$

To show that this additional term is not negligible let us assume, for simplicity, $\vec{a}$ and $\vec{k}$ to be both parallel to one of the interferometer arm. Because the geometrical factor we are getting rid off in this way are $\mathcal{O}(1)$ this will not affect our qualitative analysis. One therefore obtains

$$|\Delta L| = \sqrt{\left(\frac{\hbar^2 |a||k| L}{c^4 m_A^2}\right)^2 + \frac{|a|^2 L^4}{4c^4}}, \tag{B.20}$$

where all the physical constant have been restored. Let us consider the ratio of the square root of the two terms

$$\begin{aligned}\frac{\hbar^2 |a||k| L}{c^4 m_A^2} \cdot \frac{2c^2}{|a| L^2} &= \frac{2\hbar^2 |k|}{c^2 m_A^2 L} \\ &= \frac{2\hbar v_0}{c^2 m_A L} = \frac{2 v_0}{\omega_0 L} \\ &= \frac{v_0}{\pi f_0 L} \simeq 1,\end{aligned} \tag{B.21}$$

where one has considered $v_0 \simeq 10^5 m/s$, $f_0 \simeq 100 Hz$ and $L \simeq 10^3 m$.

Bibliography

[1] C. E. Aalseth, P. S. Barbeau, J. Colaresi, J. I. Collar, J. Diaz Leon, J. E. Fast, N. E. Fields, T. W. Hossbach, A. Knecht, M. S. Kos, M. G. Marino, H. S. Miley, M. L. Miller, J. L. Orrell, and K. M. Yocum. CoGeNT: A search for low-mass dark matter using p-type point contact germanium detectors. Phys. Rev. D, 88(1):012002, Jul 2013.

[2] C. E. Aalseth, P. S. Barbeau, J. Diaz Leon, J. E. Fast, T. W. Hossbach, A. Knecht, M. S. Kos, M. G. Marino, H. S. Miley, M. L. Miller, and J. L. Orrell. Maximum Likelihood Signal Extraction Method Applied to 3.4 years of CoGeNT Data. *arXiv e-prints*, page arXiv:1401.6234, Jan 2014.

[3] B. P. Abbott, R. Abbott, T. D. Abbott, M. R. Abernathy, F. Acernese, K. Ackley, C. Adams, T. Adams, P. Addesso, R. X. Adhikari, V. B. Adya, C. Affeldt, M. Agathos, K. Agatsuma, N. Aggarwal, O. D. Aguiar, L. Aiello, A. Ain, P. Ajith, B. Allen, A. Allocca, P. A. Altin, S. B. Anderson, W. G. Anderson, K. Arai, M. A. Arain, M. C. Araya, C. C. Arceneaux, J. S. Areeda, N. Arnaud, K. G. Arun, S. Ascenzi, G. Ashton, M. Ast, S. M. Aston, P. Astone, P. Aufmuth, C. Aulbert, S. Babak, P. Bacon, M. K. M. Bader, P. T. Baker, F. Baldaccini, G. Ballardin, S. W. Ballmer, J. C. Barayoga, S. E. Barclay, B. C. Barish, D. Barker, F. Barone, B. Barr, L. Barsotti, M. Barsuglia, D. Barta, J. Bartlett, M. A. Barton, I. Bartos, R. Bassiri, A. Basti, J. C. Batch, C. Baune, V. Bavigadda, M. Bazzan, B. Behnke, M. Bejger, C. Belczynski, A. S. Bell, C. J. Bell, B. K. Berger, J. Bergman, G. Bergmann, C. P. L. Berry, D. Bersanetti, A. Bertolini, J. Betzwieser, S. Bhagwat, R. Bhandare, I. A. Bilenko, G. Billingsley, J. Birch, R. Birney, O. Birnholtz, S. Biscans, A. Bisht, M. Bitossi, C. Biwer, M. A. Bizouard, J. K. Blackburn, C. D. Blair, D. G. Blair, R. M. Blair, S. Bloemen, O. Bock, T. P. Bodiya, M. Boer, G. Bogaert, C. Bogan,

A. Bohe, P. Bojtos, C. Bond, F. Bondu, R. Bonnand, B. A. Boom, R. Bork, V. Boschi, S. Bose, Y. Bouffanais, A. Bozzi, C. Bradaschia, P. R. Brady, V. B. Braginsky, M. Branchesi, J. E. Brau, T. Briant, A. Brillet, M. Brinkmann, V. Brisson, P. Brockill, A. F. Brooks, D. A. Brown, D. D. Brown, N. M. Brown, C. C. Buchanan, A. Buikema, T. Bulik, H. J. Bulten, A. Buonanno, D. Buskulic, C. Buy, R. L. Byer, M. Cabero, L. Cadonati, G. Cagnoli, C. Cahillane, J. Calderón Bustillo, T. Callister, E. Calloni, J. B. Camp, K. C. Cannon, J. Cao, C. D. Capano, E. Capocasa, F. Carbognani, S. Caride, J. Casanueva Diaz, C. Casentini, S. Caudill, M. Cavaglià, F. Cavalier, R. Cavalieri, G. Cella, C. B. Cepeda, L. Cerboni Baiardi, G. Cerretani, E. Cesarini, R. Chakraborty, T. Chalermsongsak, S. J. Chamberlin, M. Chan, S. Chao, P. Charlton, E. Chassande-Mottin, H. Y. Chen, Y. Chen, C. Cheng, A. Chincarini, A. Chiummo, H. S. Cho, M. Cho, J. H. Chow, N. Christensen, Q. Chu, S. Chua, S. Chung, G. Ciani, F. Clara, J. A. Clark, F. Cleva, E. Coccia, P.-F. Cohadon, A. Colla, C. G. Collette, L. Cominsky, M. Constancio, A. Conte, L. Conti, D. Cook, T. R. Corbitt, N. Cornish, A. Corsi, S. Cortese, C. A. Costa, M. W. Coughlin, S. B. Coughlin, J.-P. Coulon, S. T. Countryman, P. Couvares, E. E. Cowan, D. M. Coward, M. J. Cowart, D. C. Coyne, R. Coyne, K. Craig, J. D. E. Creighton, T. D. Creighton, J. Cripe, S. G. Crowder, A. M. Cruise, A. Cumming, L. Cunningham, E. Cuoco, T. Dal Canton, S. L. Danilishin, S. D'Antonio, K. Danzmann, N. S. Darman, C. F. Da Silva Costa, V. Dattilo, I. Dave, H. P. Daveloza, M. Davier, G. S. Davies, E. J. Daw, R. Day, S. De, D. DeBra, G. Debreczeni, J. Degallaix, M. De Laurentis, S. Deléglise, W. Del Pozzo, T. Denker, T. Dent, H. Dereli, V. Dergachev, R. T. DeRosa, R. De Rosa, R. DeSalvo, S. Dhurandhar, M. C. Díaz, L. Di Fiore, M. Di Giovanni, A. Di Lieto, S. Di Pace, I. Di Palma, A. Di Virgilio, G. Dojcinoski, V. Dolique, F. Donovan, K. L. Dooley, S. Doravari, R. Douglas, T. P. Downes, M. Drago, R. W. P. Drever, J. C. Driggers, Z. Du, M. Ducrot, S. E. Dwyer, T. B. Edo, M. C. Edwards, A. Effler, H.-B. Eggenstein, P. Ehrens, J. Eichholz, S. S. Eikenberry, W. Engels, R. C. Essick, T. Etzel, M. Evans, T. M. Evans, R. Everett, M. Factourovich, V. Fafone, H. Fair, S. Fairhurst, X. Fan, Q. Fang, S. Farinon, B. Farr, W. M. Farr, M. Favata, M. Fays, H. Fehrmann, M. M. Fejer, D. Feldbaum, I. Ferrante, E. C. Ferreira, F. Ferrini, F. Fidecaro, L. S. Finn, I. Fiori, D. Fiorucci, R. P. Fisher, R. Flaminio, M. Fletcher, H. Fong, J.-D. Fournier, S. Franco, S. Frasca, F. Frasconi, M. Frede, Z. Frei, A. Freise, R. Frey, V. Frey, T. T. Fricke,

P. Fritschel, V. V. Frolov, P. Fulda, M. Fyffe, H. A. G. Gabbard, J. R. Gair, L. Gammaitoni, S. G. Gaonkar, F. Garufi, A. Gatto, G. Gaur, N. Gehrels, G. Gemme, B. Gendre, E. Genin, A. Gennai, J. George, L. Gergely, V. Germain, Abhirup Ghosh, Archisman Ghosh, S. Ghosh, J. A. Giaime, K. D. Giardina, A. Giazotto, K. Gill, A. Glaefke, J. R. Gleason, E. Goetz, R. Goetz, L. Gondan, G. González, J. M. Gonzalez Castro, A. Gopakumar, N. A. Gordon, M. L. Gorodetsky, S. E. Gossan, M. Gosselin, R. Gouaty, C. Graef, P. B. Graff, M. Granata, A. Grant, S. Gras, C. Gray, G. Greco, A. C. Green, R. J. S. Greenhalgh, P. Groot, H. Grote, S. Grunewald, G. M. Guidi, X. Guo, A. Gupta, M. K. Gupta, K. E. Gushwa, E. K. Gustafson, R. Gustafson, J. J. Hacker, B. R. Hall, E. D. Hall, G. Hammond, M. Haney, M. M. Hanke, J. Hanks, C. Hanna, M. D. Hannam, J. Hanson, T. Hardwick, J. Harms, G. M. Harry, I. W. Harry, M. J. Hart, M. T. Hartman, C.-J. Haster, K. Haughian, J. Healy, J. Heefner, A. Heidmann, M. C. Heintze, G. Heinzel, H. Heitmann, P. Hello, G. Hemming, M. Hendry, I. S. Heng, J. Hennig, A. W. Heptonstall, M. Heurs, . Observation of gravitational waves from a binary black hole merger. *Phys. Rev. Lett.*, 116:061102, Feb 2016.

[4] B. P. Abbott, R. Abbott, T. D. Abbott, F. Acernese, K. Ackley, C. Adams, T. Adams, P. Addesso, R. X. Adhikari, V. B. Adya, C. Affeldt, M. Afrough, B. Agarwal, M. Agathos, K. Agatsuma, N. Aggarwal, O. D. Aguiar, L. Aiello, A. Ain, P. Ajith, B. Allen, G. Allen, A. Allocca, P. A. Altin, A. Amato, A. Ananyeva, S. B. Anderson, W. G. Anderson, S. V. Angelova, S. Antier, S. Appert, K. Arai, M. C. Araya, J. S. Areeda, N. Arnaud, K. G. Arun, S. Ascenzi, G. Ashton, M. Ast, S. M. Aston, P. Astone, D. V. Atallah, P. Aufmuth, C. Aulbert, K. AultONeal, C. Austin, A. Avila-Alvarez, S. Babak, P. Bacon, M. K. M. Bader, S. Bae, M. Bailes, P. T. Baker, F. Baldaccini, G. Ballardin, S. W. Ballmer, S. Banagiri, J. C. Barayoga, S. E. Barclay, B. C. Barish, D. Barker, K. Barkett, F. Barone, B. Barr, L. Barsotti, M. Barsuglia, D. Barta, S. D. Barthelmy, J. Bartlett, I. Bartos, R. Bassiri, A. Basti, J. C. Batch, M. Bawaj, J. C. Bayley, M. Bazzan, B. Bécsy, C. Beer, M. Bejger, I. Belahcene, A. S. Bell, B. K. Berger, G. Bergmann, S. Bernuzzi, J. J. Bero, C. P. L. Berry, D. Bersanetti, A. Bertolini, J. Betzwieser, S. Bhagwat, R. Bhandare, I. A. Bilenko, G. Billingsley, C. R. Billman, J. Birch, R. Birney, O. Birnholtz, S. Biscans, S. Biscoveanu, A. Bisht, M. Bitossi, C. Biwer, M. A. Bizouard, J. K. Blackburn, J. Blackman, C. D. Blair, D. G. Blair, R. M.

Blair, S. Bloemen, O. Bock, N. Bode, M. Boer, G. Bogaert, A. Bohe, F. Bondu, E. Bonilla, R. Bonnand, B. A. Boom, R. Bork, V. Boschi, S. Bose, K. Bossie, Y. Bouffanais, A. Bozzi, C. Bradaschia, P. R. Brady, M. Branchesi, J. E. Brau, T. Briant, A. Brillet, M. Brinkmann, V. Brisson, P. Brockill, J. E. Broida, A. F. Brooks, D. A. Brown, D. D. Brown, S. Brunett, C. C. Buchanan, A. Buikema, T. Bulik, H. J. Bulten, A. Buonanno, D. Buskulic, C. Buy, R. L. Byer, M. Cabero, L. Cadonati, G. Cagnoli, C. Cahillane, J. Calderón Bustillo, T. A. Callister, E. Calloni, J. B. Camp, M. Canepa, P. Canizares, K. C. Cannon, H. Cao, J. Cao, C. D. Capano, E. Capocasa, F. Carbognani, S. Caride, M. F. Carney, G. Carullo, J. Casanueva Diaz, C. Casentini, S. Caudill, M. Cavaglià, F. Cavalier, R. Cavalieri, G. Cella, C. B. Cepeda, P. Cerdá-Durán, G. Cerretani, E. Cesarini, S. J. Chamberlin, M. Chan, S. Chao, P. Charlton, E. Chase, E. Chassande-Mottin, D. Chatterjee, K. Chatziioannou, B. D. Cheeseboro, H. Y. Chen, X. Chen, Y. Chen, H.-P. Cheng, H. Chia, A. Chincarini, A. Chiummo, T. Chmiel, H. S. Cho, M. Cho, J. H. Chow, N. Christensen, Q. Chu, A. J. K. Chua, S. Chua, A. K. W. Chung, S. Chung, G. Ciani, R. Ciolfi, C. E. Cirelli, A. Cirone, F. Clara, J. A. Clark, P. Clearwater, F. Cleva, C. Cocchieri, E. Coccia, P.-F. Cohadon, D. Cohen, A. Colla, C. G. Collette, L. R. Cominsky, M. Constancio, L. Conti, S. J. Cooper, P. Corban, T. R. Corbitt, I. Cordero-Carrión, K. R. Corley, N. Cornish, A. Corsi, S. Cortese, C. A. Costa, M. W. Coughlin, S. B. Coughlin, J.-P. Coulon, S. T. Countryman, P. Couvares, P. B. Covas, E. E. Cowan, D. M. Coward, M. J. Cowart, D. C. Coyne, R. Coyne, J. D. E. Creighton, T. D. Creighton, J. Cripe, S. G. Crowder, T. J. Cullen, A. Cumming, L. Cunningham, E. Cuoco, T. Dal Canton, G. Dálya, S. L. Danilishin, S. D'Antonio, K. Danzmann, A. Dasgupta, C. F. Da Silva Costa, V. Dattilo, I. Dave, M. Davier, D. Davis, E. J. Daw, B. Day, S. De, D. DeBra, J. Degallaix, M. De Laurentis, S. Deléglise, W. Del Pozzo, N. Demos, T. Denker, T. Dent, R. De Pietri, V. Dergachev, R. De Rosa, R. T. DeRosa, C. De Rossi, R. DeSalvo, O. de Varona, J. Devenson, S. Dhurandhar, M. C. Díaz, T. Dietrich, L. Di Fiore, M. Di Giovanni, T. Di Girolamo, A. Di Lieto, S. Di Pace, I. Di Palma, F. Di Renzo, Z. Doctor, V. Dolique, F. Donovan, K. L. Dooley, S. Doravari, I. Dorrington, R. Douglas, M. Dovale Álvarez, T. P. Downes, M. Drago, C. Dreissigacker, J. C. Driggers, Z. Du, M. Ducrot, R. Dudi, P. Dupej, S. E. Dwyer, T. B. Edo, M. C. Edwards, A. Effler, H.-B. Eggenstein, P. Ehrens, J. Eichholz, S. S. Eikenberry, R. A. Eisenstein, R. C. Essick, D. Estevez,

Z. B. Etienne, T. Etzel, M. Evans, T. M. Evans, M. Factourovich, V. Fafone, H. Fair, S. Fairhurst, X. Fan, S. Farinon, B. Farr, W. M. Farr, E. J. Fauchon-Jones, M. Favata, M. Fays, C. Fee, H. Fehrmann, J. Feicht, M. M. Fejer, A. Fernandez-Galiana, I. Ferrante, E. C. Ferreira, F. Ferrini, F. Fidecaro, D. Finstad, I. Fiori, D. Fiorucci, M. Fishbach, R. P. Fisher, M. Fitz-Axen, R. Flaminio, M. Fletcher, H. Fong, J. A. Font, P. W. F. Forsyth, S. S. Forsyth, J.-D. Fournier, S. Frasca, F. Frasconi, Z. Frei, A. Freise, R. Frey, V. Frey, E. M. Fries, P. Fritschel, V. V. Frolov, P. Fulda, M. Fyffe, H. Gabbard, B. U. Gadre, S. M. Gaebel, J. R. Gair, L. Gammaitoni, M. R. Ganija, S. G. Gaonkar, C. Garcia-Quiros, F. Garufi, B. Gateley, S. Gaudio, G. Gaur, V. Gayathri, N. Gehrels, G. Gemme, E. Genin, A. Gennai, D. George, J. George, L. Gergely, V. Germain, S. Ghonge, Abhirup Ghosh, Archisman Ghosh, S. Ghosh, J. A. Giaime, K. D. Giardina, A. Giazotto, K. Gill, L. Glover, E. Goe. Gw170817: Observation of gravitational waves from a binary neutron star inspiral. *Phys. Rev. Lett.*, 119:161101, Oct 2017.

[5] R. Abbott, T. D. Abbott, S. Abraham, F. Acernese, K. Ackley, C. Adams, R. X. Adhikari, V. B. Adya, C. Affeldt, M. Agathos, K. Agatsuma, N. Aggarwal, O. D. Aguiar, A. Aich, L. Aiello, A. Ain, P. Ajith, S. Akcay, G. Allen, A. Allocca, P. A. Altin, A. Amato, S. Anand, A. Ananyeva, S. B. Anderson, W. G. Anderson, S. V. Angelova, S. Ansoldi, S. Antier, S. Appert, K. Arai, M. C. Araya, J. S. Areeda, M. Arène, N. Arnaud, S. M. Aronson, K. G. Arun, Y. Asali, S. Ascenzi, G. Ashton, S. M. Aston, P. Astone, F. Aubin, P. Aufmuth, K. AultONeal, C. Austin, V. Avendano, S. Babak, P. Bacon, F. Badaracco, M. K. M. Bader, S. Bae, A. M. Baer, J. Baird, F. Baldaccini, G. Ballardin, S. W. Ballmer, A. Bals, A. Balsamo, G. Baltus, S. Banagiri, D. Bankar, R. S. Bankar, J. C. Barayoga, C. Barbieri, B. C. Barish, D. Barker, K. Barkett, P. Barneo, F. Barone, B. Barr, L. Barsotti, M. Barsuglia, D. Barta, J. Bartlett, I. Bartos, R. Bassiri, A. Basti, M. Bawaj, J. C. Bayley, M. Bazzan, B. Bécsy, M. Bejger, I. Belahcene, A. S. Bell, D. Beniwal, M. G. Benjamin, J. D. Bentley, F. Bergamin, B. K. Berger, G. Bergmann, S. Bernuzzi, C. P. L. Berry, D. Bersanetti, A. Bertolini, J. Betzwieser, R. Bhandare, A. V. Bhandari, J. Bidler, E. Biggs, I. A. Bilenko, G. Billingsley, R. Birney, O. Birnholtz, S. Biscans, M. Bischi, S. Biscoveanu, A. Bisht, G. Bissenbayeva, M. Bitossi, M. A. Bizouard, J. K. Blackburn, J. Blackman, C. D. Blair, D. G. Blair, R. M. Blair, F. Bobba,

N. Bode, M. Boer, Y. Boetzel, G. Bogaert, F. Bondu, E. Bonilla, R. Bonnand, P. Booker, B. A. Boom, R. Bork, V. Boschi, S. Bose, V. Bossilkov, J. Bosveld, Y. Bouffanais, A. Bozzi, C. Bradaschia, P. R. Brady, A. Bramley, M. Branchesi, J. E. Brau, M. Breschi, T. Briant, J. H. Briggs, F. Brighenti, A. Brillet, M. Brinkmann, P. Brockill, A. F. Brooks, J. Brooks, D. D. Brown, S. Brunett, G. Bruno, R. Bruntz, A. Buikema, T. Bulik, H. J. Bulten, A. Buonanno, R. Buscicchio, D. Buskulic, R. L. Byer, M. Cabero, L. Cadonati, G. Cagnoli, C. Cahillane, J. Calderón Bustillo, J. D. Callaghan, T. A. Callister, E. Calloni, J. B. Camp, M. Canepa, K. C. Cannon, H. Cao, J. Cao, G. Carapella, F. Carbognani, S. Caride, M. F. Carney, G. Carullo, J. Casanueva Diaz, C. Casentini, J. Castañeda, S. Caudill, M. Cavaglià, F. Cavalier, R. Cavalieri, G. Cella, P. Cerdá-Durán, E. Cesarini, O. Chaibi, K. Chakravarti, C. Chan, M. Chan, K. Chandra, S. Chao, P. Charlton, E. A. Chase, E. Chassande-Mottin, D. Chatterjee, M. Chaturvedi, K. Chatziioannou, H. Y. Chen, X. Chen, Y. Chen, H.-P. Cheng, C. K. Cheong, H. Y. Chia, F. Chiadini, R. Chierici, A. Chincarini, A. Chiummo, G. Cho, H. S. Cho, M. Cho, N. Christensen, Q. Chu, S. Chua, K. W. Chung, S. Chung, G. Ciani, P. Ciecielag, M. Cieślar, A. A. Ciobanu, R. Ciolfi, F. Cipriano, A. Cirone, F. Clara, J. A. Clark, P. Clearwater, S. Clesse, F. Cleva, E. Coccia, P.-F. Cohadon, D. Cohen, M. Colleoni, C. G. Collette, C. Collins, M. Colpi, M. Constancio, L. Conti, S. J. Cooper, P. Corban, T. R. Corbitt, I. Cordero-Carrión, S. Corezzi, K. R. Corley, N. Cornish, D. Corre, A. Corsi, S. Cortese, C. A. Costa, R. Cotesta, M. W. Coughlin, S. B. Coughlin, J.-P. Coulon, S. T. Countryman, P. Couvares, P. B. Covas, D. M. Coward, M. J. Cowart, D. C. Coyne, R. Coyne, J. D. E. Creighton, T. D. Creighton, J. Cripe, M. Croquette, S. G. Crowder, J.-R. Cudell, T. J. Cullen, A. Cumming, R. Cummings, L. Cunningham, E. Cuoco, M. Curylo, T. Dal Canton, G. Dálya, A. Dana, L. M. Daneshgaran-Bajastani, B. D'Angelo, S. L. Danilishin, S. D'Antonio, K. Danzmann, C. Darsow-Fromm, A. Dasgupta, L. E. H. Datrier, V. Dattilo, I. Dave, M. Davier, G. S. Davies, D. Davis, E. J. Daw, D. DeBra, M. Deenadayalan, J. Degallaix, M. De Laurentis, S. Deléglise, M. Delfavero, N. De Lillo, W. Del Pozzo, L. M. DeMarchi, V. D'Emilio, N. Demos, T. Dent, R. De Pietri, R. De Rosa, C. De Rossi, R. DeSalvo, O. de Varona, S. Dhurandhar, M. C. Díaz, M. Diaz-Ortiz, T. Dietrich, L. Di Fiore, C. Di Fronzo, C. Di Giorgio, F. Di Giovanni, M. Di Giovanni, T. Di Girolamo, A. Di Lieto, B. Ding, S. Di Pace, I. Di Palma, F. Di Renzo, A. K. Divakarla,

A. Dmitriev, Z. Doctor, F. Donovan, K. L. Dooley, S. Doravari, I. Dorrington, T. P. Downes, M. Drago, J. C. Driggers, Z. Du, J.-G. Ducoin, P. Dupej, O. Durante, D. D'Urso, S. E. Dwyer, P. J. Easter, G. Eddolls, B. Edelman, T. B. Edo, O. Edy, A. Effler, P. Ehrens, J. Eichholz, S. S. Eikenberry, M. Eisenmann, R. A. Eisenstein, A. Ejlli, L. Errico, R. C. Essick, H. Estelles, D. Estevez, Z. B. Etienne, T. Etzel, M. Evans, T. M. Evans, B. E. Ewing, V. Fafone, S. Fairhurst, X. Fan, S. Farinon, B. Farr, W. M. Farr, E. J. Fauchon-Jones, M. Favata, M. Fays, M. Fazio, J. Feicht, M. M. Fejer, F. Feng, E. Fenyvesi, D. L. Ferguson, A. Fernandez-Galiana, I. Ferrante, E. C. Ferreira, T. A. Ferreira, F. Fidecaro, I. Fiori, D. Fiorucci, M. Fishbach, R. P. Fisher, R. Fittipaldi, M. Fitz-Axen, V. Fiumara, R. Flaminio, E. Floden, E. Flynn, H. Fong, J. A. Font,. Gw190521: A binary black hole merger with a total mass of 150 $M_{\odot}$. *Phys. Rev. Lett.*, 125:101102, Sep 2020.

[6] H. Abdallah, A. Abramowski, F. Aharonian, F. Ait Benkhali, A. G. Akhperjanian, E. Angüner, M. Arrieta, P. Aubert, M. Backes, A. Balzer, M. Barnard, Y. Becherini, J. Becker Tjus, D. Berge, S. Bernhard, K. Bernlöhr, E. Birsin, R. Blackwell, M. Böttcher, C. Boisson, J. Bolmont, P. Bordas, J. Bregeon, F. Brun, P. Brun, M. Bryan, T. Bulik, M. Capasso, J. Carr, S. Casanova, N. Chakraborty, R. Chalme-Calvet, R. C. G. Chaves, A. Chen, J. Chevalier, M. Chrétien, S. Colafrancesco, G. Cologna, B. Condon, J. Conrad, C. Couturier, Y. Cui, I. D. Davids, B. Degrange, C. Deil, P. deWilt, A. Djannati-Ataï, W. Domainko, A. Donath, L. O'C. Drury, G. Dubus, K. Dutson, J. Dyks, M. Dyrda, T. Edwards, K. Egberts, P. Eger, J. P. Ernenwein, S. Eschbach, C. Farnier, S. Fegan, M. V. Fernandes, A. Fiasson, G. Fontaine, A. Förster, S. Funk, M. Füßling, S. Gabici, M. Gajdus, Y. A. Gallant, T. Garrigoux, G. Giavitto, B. Giebels, J. F. Glicenstein, D. Gottschall, A. Goyal, M. H. Grondin, M. Grudzińska, D. Hadasch, J. Hahn, J. Hawkes, G. Heinzelmann, G. Henri, G. Hermann, O. Hervet, A. Hillert, J. A. Hinton, W. Hofmann, C. Hoischen, M. Holler, D. Horns, A. Ivascenko, A. Jacholkowska, M. Jamrozy, M. Janiak, D. Jankowsky, F. Jankowsky, M. Jingo, T. Jogler, L. Jouvin, I. Jung-Richardt, M. A. Kastendieck, K. Katarzyński, U. Katz, D. Kerszberg, B. Khélifi, M. Kieffer, J. King, S. Klepser, D. Klochkov, W. Kluźniak, D. Kolitzus, Nu. Komin, K. Kosack, S. Krakau, M. Kraus, F. Krayzel, P. P. Krüger, H. Laffon, G. Lamanna, J. Lau, J. P. Lees, J. Lefaucheur, V. Lefranc, A. Lemière, M. Lemoine-Goumard, J. P. Lenain, E. Leser, T. Lohse,

M. Lorentz, R. Lui, I. Lypova, V. Marandon, A. Marcowith, C. Mariaud, R. Marx, G. Maurin, N. Maxted, M. Mayer, P. J. Meintjes, U. Menzler, M. Meyer, A. M. W. Mitchell, R. Moderski, M. Mohamed, K. Morâ, E. Moulin, T. Murach, M. de Naurois, F. Niederwanger, J. Niemiec, L. Oakes, H. Odaka, S. Ohm, S. Öttl, M. Ostrowski, I. Oya, M. Padovani, M. Panter, R. D. Parsons, M. Paz Arribas, N. W. Pekeur, G. Pelletier, P. O. Petrucci, B. Peyaud, S. Pita, H. Poon, D. Prokhorov, H. Prokoph, G. Pühlhofer, M. Punch, A. Quirrenbach, S. Raab, A. Reimer, O. Reimer, M. Renaud, R. de los Reyes, F. Rieger, C. Romoli, S. Rosier-Lees, G. Rowell, B. Rudak, C. B. Rulten, V. Sahakian, D. Salek, D. A. Sanchez, A. Santangelo, M. Sasaki, R. Schlickeiser, F. Schüssler, A. Schulz, U. Schwanke, S. Schwemmer, A. S. Seyffert, N. Shafi, R. Simoni, H. Sol, F. Spanier, G. Spengler, F. Spieß, L. Stawarz, R. Steenkamp, C. Stegmann, F. Stinzing, K. Stycz, I. Sushch, J. P. Tavernet, T. Tavernier, A. M. Taylor, R. Terrier, M. Tluczykont, C. Trichard, R. Tuffs, J. van der Walt, C. van Eldik, B. van Soelen, G. Vasileiadis, J. Veh, C. Venter, A. Viana, P. Vincent, J. Vink, F. Voisin, H. J. Völk, T. Vuillaume, Z. Wadiasingh, S. J. Wagner, P. Wagner, R. M. Wagner, R. White, A. Wierzcholska, P. Willmann, A. Wörnlein, D. Wouters, R. Yang, V. Zabalza, D. Zaborov, M. Zacharias, A. A. Zdziarski, A. Zech, F. Zefi, A. Ziegler, N. Żywucka, and H. E. S. S. Collaboration. Search for Dark Matter Annihilations towards the Inner Galactic Halo from 10 Years of Observations with H.E.S.S. Phys. Rev. Lett., 117(11):111301, Sep 2016.

[7] M. Ackermann, M. Ajello, A. Albert, W. B. Atwood, L. Baldini, J. Ballet, G. Barbiellini, D. Bastieri, R. Bellazzini, E. Bissaldi, R. D. Bland ford, E. D. Bloom, R. Bonino, E. Bottacini, T. J. Brandt, J. Bregeon, P. Bruel, R. Buehler, T. H. Burnett, R. A. Cameron, R. Caputo, M. Caragiulo, P. A. Caraveo, E. Cavazzuti, C. Cecchi, E. Charles, A. Chekhtman, J. Chiang, A. Chiappo, G. Chiaro, S. Ciprini, J. Conrad, F. Costanza, A. Cuoco, S. Cutini, F. D'Ammando, F. de Palma, R. Desiante, S. W. Digel, N. Di Lalla, M. Di Mauro, L. Di Venere, P. S. Drell, C. Favuzzi, S. J. Fegan, E. C. Ferrara, W. B. Focke, A. Franckowiak, Y. Fukazawa, S. Funk, P. Fusco, F. Gargano, D. Gasparrini, N. Giglietto, F. Giordano, M. Giroletti, T. Glanzman, G. A. Gomez-Vargas, D. Green, I. A. Grenier, J. E. Grove, L. Guillemot, S. Guiriec, M. Gustafsson, A. K. Harding, E. Hays, J. W. Hewitt, D. Horan, T. Jogler, A. S. Johnson, T. Kamae, D. Kocevski, M. Kuss, G. La Mura, S. Larsson, L. Latronico, J. Li, F. Longo, F. Loparco,

M. N. Lovellette, P. Lubrano, J. D. Magill, S. Maldera, D. Malyshev, A. Manfreda, P. Martin, M. N. Mazziotta, P. F. Michelson, N. Mirabal, W. Mitthumsiri, T. Mizuno, A. A. Moiseev, M. E. Monzani, A. Morselli, M. Negro, E. Nuss, T. Ohsugi, M. Orienti, E. Orlando, J. F. Ormes, D. Paneque, J. S. Perkins, M. Persic, M. Pesce-Rollins, F. Piron, G. Principe, S. Rainò, R. Rando, M. Razzano, S. Razzaque, A. Reimer, O. Reimer, M. Sánchez-Conde, C. Sgrò, D. Simone, E. J. Siskind, F. Spada, G. Spandre, P. Spinelli, D. J. Suson, H. Tajima, K. Tanaka, J. B. Thayer, L. Tibaldo, D. F. Torres, E. Troja, Y. Uchiyama, G. Vianello, K. S. Wood, M. Wood, G. Zaharijas, S. Zimmer, and Fermi LAT Collaboration. The Fermi Galactic Center GeV Excess and Implications for Dark Matter. ApJ, 840(1):43, May 2017.

[8] R. Agnese, A. J. Anderson, M. Asai, D. Balakishiyeva, R. Basu Thakur, D. A. Bauer, J. Billard, A. Borgland, M. A. Bowles, D. Brandt, P. L. Brink, R. Bunker, B. Cabrera, D. O. Caldwell, D. G. Cerdeno, H. Chagani, J. Cooley, B. Cornell, C. H. Crewdson, P. Cushman, M. Daal, P. C. F. Di Stefano, T. Doughty, L. Esteban, S. Fallows, E. Figueroa-Feliciano, G. L. Godfrey, S. R. Golwala, J. Hall, H. R. Harris, S. A. Hertel, T. Hofer, D. Holmgren, L. Hsu, M. E. Huber, A. Jastram, O. Kamaev, B. Kara, M. H. Kelsey, A. Kennedy, M. Kiveni, K. Koch, B. Loer, E. Lopez Asamar, R. Mahapatra, V. Mandic, C. Martinez, K. A. McCarthy, N. Mirabolfathi, R. A. Moffatt, D. C. Moore, P. Nadeau, R. H. Nelson, K. Page, R. Partridge, M. Pepin, A. Phipps, K. Prasad, M. Pyle, H. Qiu, W. Rau, P. Redl, A. Reisetter, Y. Ricci, T. Saab, B. Sadoulet, J. Sander, K. Schneck, R. W. Schnee, S. Scorza, B. Serfass, B. Shank, D. Speller, A. N. Villano, B. Welliver, D. H. Wright, S. Yellin, J. J. Yen, B. A. Young, J. Zhang, and SuperCDMS Collaboration. Search for Low-Mass Weakly Interacting Massive Particles Using Voltage-Assisted Calorimetric Ionization Detection in the SuperCDMS Experiment. Phys. Rev. Lett., 112(4):041302, Jan 2014.

[9] R. Agnese, A. J. Anderson, D. Balakishiyeva, R. Basu Thakur, D. A. Bauer, J. Billard, A. Borgland , M. A. Bowles, D. Brandt, P. L. Brink, R. Bunker, B. Cabrera, D. O. Caldwell, D. G. Cerdeno, H. Chagani, Y. Chen, J. Cooley, B. Cornell, C. H. Crewdson, P. Cushman, M. Daal, P. C. F. Di Stefano, T. Doughty, L. Esteban, S. Fallows, E. Figueroa-Feliciano, M. Fritts, G. L. Godfrey, S. R. Golwala, M. Graham, J. Hall,

H. R. Harris, S. A. Hertel, T. Hofer, D. Holmgren, L. Hsu, M. E. Huber, A. Jastram, O. Kamaev, B. Kara, M. H. Kelsey, A. Kennedy, M. Kiveni, K. Koch, A. Leder, B. Loer, E. Lopez Asamar, R. Mahapatra, V. Mandic, C. Martinez, K. A. McCarthy, N. Mirabolfathi, R. A. Moffatt, D. C. Moore, R. H. Nelson, S. M. Oser, K. Page, W. A. Page, R. Partridge, M. Pepin, A. Phipps, K. Prasad, M. Pyle, H. Qiu, W. Rau, P. Redl, A. Reisetter, Y. Ricci, H. E. Rogers, T. Saab, B. Sadoulet, J. Sander, K. Schneck, R. W. Schnee, S. Scorza, B. Serfass, B. Shank, D. Speller, S. Upadhyayula, A. N. Villano, B. Welliver, D. H. Wright, S. Yellin, J. J. Yen, B. A. Young, J. Zhang, and SuperCDMS Collaboration. Maximum likelihood analysis of low energy CDMS II germanium data. Phys. Rev. D, 91(5):052021, Mar 2015.

[10] F. Aharonian, A. G. Akhperjanian, A. R. Bazer-Bachi, M. Beilicke, W. Benbow, D. Berge, K. Bernlöhr, C. Boisson, O. Bolz, V. Borrel, I. Braun, F. Breitling, A. M. Brown, R. Bühler, I. Büsching, S. Carrigan, P. M. Chadwick, L. M. Chounet, R. Cornils, L. Costamante, B. Degrange, H. J. Dickinson, A. Djannati-Ataï, L. O'C. Drury, G. Dubus, K. Egberts, D. Emmanoulopoulos, P. Espigat, F. Feinstein, E. Ferrero, A. Fiasson, G. Fontaine, Seb. Funk, S. Funk, Y. A. Gallant, B. Giebels, J. F. Glicenstein, P. Goret, C. Hadjichristidis, D. Hauser, M. Hauser, G. Heinzelmann, G. Henri, G. Hermann, J. A. Hinton, W. Hofmann, M. Holleran, D. Horns, A. Jacholkowska, O. C. de Jager, B. Khélifi, Nu. Komin, A. Konopelko, K. Kosack, I. J. Latham, R. Le Gallou, A. Lemière, M. Lemoine-Goumard, T. Lohse, J. M. Martin, O. Martineau-Huynh, A. Marcowith, C. Masterson, T. J. L. McComb, M. de Naurois, D. Nedbal, S. J. Nolan, A. Noutsos, K. J. Orford, J. L. Osborne, M. Ouchrif, M. Panter, G. Pelletier, S. Pita, G. Pühlhofer, M. Punch, B. C. Raubenheimer, M. Raue, S. M. Rayner, A. Reimer, O. Reimer, J. Ripken, L. Rob, L. Rolland , G. Rowell, V. Sahakian, L. Saugé, S. Schlenker, R. Schlickeiser, U. Schwanke, H. Sol, D. Spangler, F. Spanier, R. Steenkamp, C. Stegmann, G. Superina, J. P. Tavernet, R. Terrier, C. G. Théoret, M. Tluczykont, C. van Eldik, G. Vasileiadis, C. Venter, P. Vincent, H. J. Völk, S. J. Wagner, and M. Ward. Observations of the Crab nebula with HESS. A&A, 457(3):899–915, Oct 2006.

[11] M. Ajello, A. Albert, W. B. Atwood, G. Barbiellini, D. Bastieri, K. Bechtol, R. Bellazzini, E. Bissaldi, R. D. Blandford, E. D. Bloom, R. Bonino, E. Bottacini, T. J. Brandt, J. Bregeon, P. Bruel,

R. Buehler, S. Buson, G. A. Caliandro, R. A. Cameron, R. Caputo, M. Caragiulo, P. A. Caraveo, C. Cecchi, A. Chekhtman, J. Chiang, G. Chiaro, S. Ciprini, J. Cohen-Tanugi, L. R. Cominsky, J. Conrad, S. Cutini, F. D'Ammand o, A. de Angelis, F. de Palma, R. Desiante, L. Di Venere, P. S. Drell, C. Favuzzi, E. C. Ferrara, P. Fusco, F. Gargano, D. Gasparrini, N. Giglietto, P. Giommi, F. Giordano, M. Giroletti, T. Glanzman, G. Godfrey, G. A. Gomez-Vargas, I. A. Grenier, S. Guiriec, M. Gustafsson, A. K. Harding, J. W. Hewitt, A. B. Hill, D. Horan, T. Jogler, G. Jóhannesson, A. S. Johnson, T. Kamae, C. Karwin, J. Knödlseder, M. Kuss, S. Larsson, L. Latronico, J. Li, L. Li, F. Longo, F. Loparco, M. N. Lovellette, P. Lubrano, J. Magill, S. Maldera, D. Malyshev, A. Manfreda, M. Mayer, M. N. Mazziotta, P. F. Michelson, W. Mitthumsiri, T. Mizuno, A. A. Moiseev, M. E. Monzani, A. Morselli, I. V. Moskalenko, S. Murgia, E. Nuss, M. Ohno, T. Ohsugi, N. Omodei, E. Orlando, J. F. Ormes, D. Paneque, M. Pesce-Rollins, F. Piron, G. Pivato, T. A. Porter, S. Rainò, R. Rando, M. Razzano, A. Reimer, O. Reimer, S. Ritz, M. Sánchez-Conde, P. M. Saz Parkinson, C. Sgrò, E. J. Siskind, D. A. Smith, F. Spada, G. Spandre, P. Spinelli, D. J. Suson, H. Tajima, H. Takahashi, J. B. Thayer, D. F. Torres, G. Tosti, E. Troja, Y. Uchiyama, G. Vianello, B. L. Winer, K. S. Wood, G. Zaharijas, and S. Zimmer. Fermi-LAT Observations of High-Energy Gamma-Ray Emission toward the Galactic Center. ApJ, 819(1):44, Mar 2016.

[12] D. S. Akerib, S. Alsum, H. M. Araújo, X. Bai, A. J. Bailey, J. Balajthy, P. Beltrame, E. P. Bernard, A. Bernstein, T. P. Biesiadzinski, E. M. Boulton, R. Bramante, P. Brás, D. Byram, S. B. Cahn, M. C. Carmona-Benitez, C. Chan, A. A. Chiller, C. Chiller, A. Currie, J. E. Cutter, T. J. R. Davison, A. Dobi, J. E. Y. Dobson, E. Druszkiewicz, B. N. Edwards, C. H. Faham, S. Fiorucci, R. J. Gaitskell, V. M. Gehman, C. Ghag, K. R. Gibson, M. G. D. Gilchriese, C. R. Hall, M. Hanhardt, S. J. Haselschwardt, S. A. Hertel, D. P. Hogan, M. Horn, D. Q. Huang, C. M. Ignarra, M. Ihm, R. G. Jacobsen, W. Ji, K. Kamdin, K. Kazkaz, D. Khaitan, R. Knoche, N. A. Larsen, C. Lee, B. G. Lenardo, K. T. Lesko, A. Lindote, M. I. Lopes, A. Manalaysay, R. L. Mannino, M. F. Marzioni, D. N. McKinsey, D. M. Mei, J. Mock, M. Moongweluwan, J. A. Morad, A. St. J. Murphy, C. Nehrkorn, H. N. Nelson, F. Neves, K. O'Sullivan, K. C. Oliver-Mallory, K. J. Palladino, E. K. Pease, P. Phelps, L. Reichhart,

C. Rhyne, S. Shaw, T. A. Shutt, C. Silva, M. Solmaz, V. N. Solovov, P. Sorensen, S. Stephenson, T. J. Sumner, M. Szydagis, D. J. Taylor, W. C. Taylor, B. P. Tennyson, P. A. Terman, D. R. Tiedt, W. H. To, M. Tripathi, L. Tvrznikova, S. Uvarov, J. R. Verbus, R. C. Webb, J. T. White, T. J. Whitis, M. S. Witherell, F. L. H. Wolfs, J. Xu, K. Yazdani, S. K. Young, C. Zhang, and LUX Collaboration. Results from a Search for Dark Matter in the Complete LUX Exposure. Phys. Rev. Lett., 118(2):021303, Jan 2017.

[13] A. Albert, B. Anderson, K. Bechtol, A. Drlica-Wagner, M. Meyer, M. Sánchez-Conde, L. Strigari, M. Wood, T. M. C. Abbott, F. B. Abdalla, A. Benoit-Lévy, G. M. Bernstein, R. A. Bernstein, E. Bertin, D. Brooks, D. L. Burke, A. Carnero Rosell, M. Carrasco Kind, J. Carretero, M. Crocce, C. E. Cunha, C. B. D'Andrea, L. N. da Costa, S. Desai, H. T. Diehl, J. P. Dietrich, P. Doel, T. F. Eifler, A. E. Evrard, A. Fausti Neto, D. A. Finley, B. Flaugher, P. Fosalba, J. Frieman, D. W. Gerdes, D. A. Goldstein, D. Gruen, R. A. Gruendl, K. Honscheid, D. J. James, S. Kent, K. Kuehn, N. Kuropatkin, O. Lahav, T. S. Li, M. A. G. Maia, M. March, J. L. Marshall, P. Martini, C. J. Miller, R. Miquel, E. Neilsen, B. Nord, R. Ogando, A. A. Plazas, K. Reil, A. K. Romer, E. S. Rykoff, E. Sanchez, B. Santiago, M. Schubnell, I. Sevilla-Noarbe, R. C. Smith, M. Soares-Santos, F. Sobreira, E. Suchyta, M. E. C. Swanson, G. Tarle, V. Vikram, A. R. Walker, R. H. Wechsler, Fermi-LAT Collaboration, and DES Collaboration. Searching for Dark Matter Annihilation in Recently Discovered Milky Way Satellites with Fermi-Lat. ApJ, 834(2):110, Jan 2017.

[14] C. Alcock, R. A. Allsman, D. R. Alves, T. S. Axelrod, A. C. Becker, D. P. Bennett, K. H. Cook, N. Dalal, A. J. Drake, K. C. Freeman, M. Geha, K. Griest, M. J. Lehner, S. L. Marshall, D. Minniti, C. A. Nelson, B. A. Peterson, P. Popowski, M. R. Pratt, P. J. Quinn, C. W. Stubbs, W. Sutherland, A. B. Tomaney, T. Vand ehei, and D. Welch. The MACHO Project: Microlensing Results from 5.7 Years of Large Magellanic Cloud Observations. *The Astrophysical Journal*, 542(1):281–307, Oct 2000.

[15] J. Aleksić, E. A. Alvarez, L. A. Antonelli, P. Antoranz, M. Asensio, M. Backes, J. A. Barrio, D. Bastieri, J. Becerra González, W. Bednarek, A. Berdyugin, K. Berger, E. Bernardini, A. Biland, O. Blanch, R. K. Bock, A. Boller, G. Bonnoli, D. Borla Tridon, I. Braun, T. Bretz, A. Cañellas, E. Carmona, A. Carosi, P. Colin,

E. Colombo, J. L. Contreras, J. Cortina, L. Cossio, S. Covino, F. Dazzi, A. de Angelis, G. de Caneva, E. de Cea Del Pozo, B. de Lotto, C. Delgado Mendez, A. Diago Ortega, M. Doert, A. Domínguez, D. Dominis Prester, D. Dorner, M. Doro, D. Elsaesser, D. Ferenc, M. V. Fonseca, L. Font, C. Fruck, R. J. García López, M. Garczarczyk, D. Garrido, G. Giavitto, N. Godinović, D. Hadasch, D. Häfner, A. Herrero, D. Hildebrand, D. Höhne-Mönch, J. Hose, D. Hrupec, B. Huber, T. Jogler, H. Kellermann, S. Klepser, T. Krähenbühl, J. Krause, A. La Barbera, D. Lelas, E. Leonardo, E. Lindfors, S. Lombardi, M. López, A. López-Oramas, E. Lorenz, M. Makariev, G. Maneva, N. Mankuzhiyil, K. Mannheim, L. Maraschi, M. Mariotti, M. Martínez, D. Mazin, M. Meucci, J. M. Miranda, R. Mirzoyan, H. Miyamoto, J. Moldón, A. Moralejo, P. Munar-Adrover, D. Nieto, K. Nilsson, R. Orito, I. Oya, D. Paneque, R. Paoletti, S. Pardo, J. M. Paredes, S. Partini, M. Pasanen, F. Pauss, M. A. Perez-Torres, M. Persic, L. Peruzzo, M. Pilia, J. Pochon, F. Prada, P. G. Prada Moroni, E. Prandini, I. Puljak, I. Reichardt, R. Reinthal, W. Rhode, M. Ribó, J. Rico, S. Rügamer, A. Saggion, K. Saito, T. Y. Saito, M. Salvati, K. Satalecka, V. Scalzotto, V. Scapin, C. Schultz, T. Schweizer, M. Shayduk, S. N. Shore, A. Sillanpää, J. Sitarek, I. Snidaric, D. Sobczynska, F. Spanier, S. Spiro, V. Stamatescu, A. Stamerra, B. Steinke, J. Storz, N. Strah, T. Surić, L. Takalo, H. Takami, F. Tavecchio, P. Temnikov, T. Terzić, D. Tescaro, M. Teshima, O. Tibolla, D. F. Torres, A. Treves, M. Uellenbeck, H. Vankov, P. Vogler, R. M. Wagner, Q. Weitzel, V. Zabalza, F. Zandanel, and R. Zanin. Performance of the MAGIC stereo system obtained with Crab Nebula data. *Astroparticle Physics*, 35(7):435–448, Feb 2012.

[16] Bruce Allen, Maria Alessandra Papa, and Bernard F. Schutz. Optimal strategies for sinusoidal signal detection. Phys. Rev. D, 66(10):102003, Nov 2002.

[17] C. Amole, M. Ardid, I. J. Arnquist, D. M. Asner, D. Baxter, E. Behnke, P. Bhattacharjee, H. Borsodi, M. Bou-Cabo, S. J. Brice, D. Broemmelsiek, K. Clark, J. I. Collar, P. S. Cooper, M. Crisler, C. E. Dahl, M. Das, F. Debris, S. Fallows, J. Farine, I. Felis, R. Filgas, M. Fines-Neuschild, F. Girard, G. Giroux, J. Hall, O. Harris, E. W. Hoppe, C. M. Jackson, M. Jin, C. B. Krauss, M. Lafrenière, M. Laurin, I. Lawson, A. Leblanc, I. Levine, W. H. Lippincott, E. Mann, J. P. Martin, D. Maurya, P. Mitra, S. Olson, R. Neilson,

A. J. Noble, A. Plante, R. B. Podviianiuk, S. Priya, A. E. Robinson, M. Ruschman, O. Scallon, A. Sonnenschein, N. Starinski, I. Štekl, E. Vázquez-Jáuregui, J. Wells, U. Wichoski, V. Zacek, J. Zhang, and PICO Collaboration. Improved dark matter search results from PICO-2L Run 2. Phys. Rev. D, 93(6):061101, Mar 2016.

[18] C. Amole, M. Ardid, D. M. Asner, D. Baxter, E. Behnke, P. Bhattacharjee, H. Borsodi, M. Bou-Cabo, S. J. Brice, D. Broemmelsiek, K. Clark, J. I. Collar, P. S. Cooper, M. Crisler, C. E. Dahl, S. Daley, M. Das, F. Debris, N. Dhungana, S. Fallows, J. Farine, I. Felis, R. Filgas, F. Girard, G. Giroux, A. Grandison, M. Hai, J. Hall, O. Harris, M. Jin, C. B. Krauss, M. Lafrenière, M. Laurin, I. Lawson, I. Levine, W. H. Lippincott, E. Mann, D. Maurya, P. Mitra, R. Neilson, A. J. Noble, A. Plante, R. B. Podviianiuk, S. Priya, E. Ramberg, A. E. Robinson, R. Rucinski, M. Ruschman, O. Scallon, S. Seth, P. Simon, A. Sonnenschein, I. Štekl, E. Vázquez-Jáuregui, J. Wells, U. Wichoski, V. Zacek, J. Zhang, I. A. Shkrob, and PICO Collaboration. Dark matter search results from the PICO-60 CF_3 I bubble chamber. Phys. Rev. D, 93(5):052014, Mar 2016.

[19] G. Angloher, A. Bento, C. Bucci, L. Canonica, A. Erb, F. von Feilitzsch, N. Ferreiro Iachellini, P. Gorla, A. Gütlein, D. Hauff, P. Huff, J. Jochum, M. Kiefer, C. Kister, H. Kluck, H. Kraus, J. C. Lanfranchi, J. Loebell, A. Münster, F. Petricca, W. Potzel, F. Pröbst, F. Reindl, S. Roth, K. Rottler, C. Sailer, K. Schäffner, J. Schieck, J. Schmaler, S. Scholl, S. Schönert, W. Seidel, M. von Sivers, L. Stodolsky, C. Strand hagen, R. Strauss, A. Tanzke, M. Uffinger, A. Ulrich, I. Usherov, S. Wawoczny, M. Willers, M. Wüstrich, and A. Zöller. Results on low mass WIMPs using an upgraded CRESST-II detector. *European Physical Journal C*, 74:3184, Dec 2014.

[20] D. Antypas, O. Tretiak, A. Garcon, R. Ozeri, G. Perez, and D. Budker. Scalar dark matter in the radio-frequency band: atomic-spectroscopy search results. *arXiv e-prints*, page arXiv:1905.02968, May 2019.

[21] E. Aprile, J. Aalbers, F. Agostini, M. Alfonsi, L. Althueser, F. D. Amaro, M. Anthony, F. Arneodo, L. Baudis, B. Bauermeister, M. L. Benabderrahmane, T. Berger, P. A. Breur, A. Brown, A. Brown, E. Brown, S. Bruenner, G. Bruno, R. Budnik, C. Capelli, J. M. R. Cardoso, D. Cichon, D. Coderre, A. P. Colijn, J. Conrad, J. P. Cussonneau, M. P. Decowski, P. de Perio, P. di Gangi, A. di Giovanni,

S. Diglio, A. Elykov, G. Eurin, J. Fei, A. D. Ferella, A. Fieguth, W. Fulgione, A. Gallo Rosso, M. Galloway, F. Gao, M. Garbini, C. Geis, L. Grandi, Z. Greene, H. Qiu, C. Hasterok, E. Hogenbirk, J. Howlett, R. Itay, F. Joerg, B. Kaminsky, S. Kazama, A. Kish, G. Koltman, H. Landsman, R. F. Lang, L. Levinson, Q. Lin, S. Lindemann, M. Lindner, F. Lombardi, J. A. M. Lopes, J. Mahlstedt, A. Manfredini, T. Marrodán Undagoitia, J. Masbou, D. Masson, M. Messina, K. Micheneau, K. Miller, A. Molinario, K. Morâ, M. Murra, J. Naganoma, K. Ni, U. Oberlack, B. Pelssers, F. Piastra, J. Pienaar, V. Pizzella, G. Plante, R. Podviianiuk, N. Priel, D. Ramírez García, L. Rauch, S. Reichard, C. Reuter, B. Riedel, A. Rizzo, A. Rocchetti, N. Rupp, J. M. F. Dos Santos, G. Sartorelli, M. Scheibelhut, S. Schindler, J. Schreiner, D. Schulte, M. Schumann, L. Scotto Lavina, M. Selvi, P. Shagin, E. Shockley, M. Silva, H. Simgen, D. Thers, F. Toschi, G. Trinchero, C. Tunnell, N. Upole, M. Vargas, O. Wack, H. Wang, Z. Wang, Y. Wei, C. Weinheimer, C. Wittweg, J. Wulf, J. Ye, Y. Zhang, T. Zhu, and Xenon Collaboration. Dark Matter Search Results from a One Ton-Year Exposure of XENON1T. Phys. Rev. Lett., 121(11):111302, Sep 2018.

[22] Giorgio Arcadi, Maíra Dutra, Pradipta Ghosh, Manfred Lindner, Yann Mambrini, Mathias Pierre, Stefano Profumo, and Farinaldo S. Queiroz. The waning of the WIMP? A review of models, searches, and constraints. *European Physical Journal C*, 78(3):203, Mar 2018.

[23] W. B. Atwood, A. A. Abdo, M. Ackermann, W. Althouse, B. Anderson, M. Axelsson, L. Baldini, J. Ballet, D. L. Band, G. Barbiellini, J. Bartelt, D. Bastieri, B. M. Baughman, K. Bechtol, D. Bédérède, F. Bellardi, R. Bellazzini, B. Berenji, G. F. Bignami, D. Bisello, E. Bissaldi, R. D. Blandford, E. D. Bloom, J. R. Bogart, E. Bonamente, J. Bonnell, A. W. Borgland , A. Bouvier, J. Bregeon, A. Brez, M. Brigida, P. Bruel, T. H. Burnett, G. Busetto, G. A. Caliandro, R. A. Cameron, P. A. Caraveo, S. Carius, P. Carlson, J. M. Casandjian, E. Cavazzuti, M. Ceccanti, C. Cecchi, E. Charles, A. Chekhtman, C. C. Cheung, J. Chiang, R. Chipaux, A. N. Cillis, S. Ciprini, R. Claus, J. Cohen-Tanugi, S. Condamoor, J. Conrad, R. Corbet, L. Corucci, L. Costamante, S. Cutini, D. S. Davis, D. Decotigny, M. DeKlotz, C. D. Dermer, A. de Angelis, S. W. Digel, E. do Couto e Silva, P. S. Drell, R. Dubois, D. Dumora, Y. Edmonds, D. Fabiani, C. Farnier, C. Favuzzi, D. L. Flath, P. Fleury, W. B. Focke,

S. Funk, P. Fusco, F. Gargano, D. Gasparrini, N. Gehrels, F. X. Gentit, S. Germani, B. Giebels, N. Giglietto, P. Giommi, F. Giordano, T. Glanzman, G. Godfrey, I. A. Grenier, M. H. Grondin, J. E. Grove, L. Guillemot, S. Guiriec, G. Haller, A. K. Harding, P. A. Hart, E. Hays, S. E. Healey, M. Hirayama, L. Hjalmarsdotter, R. Horn, R. E. Hughes, G. Jóhannesson, G. Johansson, A. S. Johnson, R. P. Johnson, T. J. Johnson, W. N. Johnson, T. Kamae, H. Katagiri, J. Kataoka, A. Kavelaars, N. Kawai, H. Kelly, M. Kerr, W. Klamra, J. Knödlseder, M. L. Kocian, N. Komin, F. Kuehn, M. Kuss, D. Landriu, L. Latronico, B. Lee, S. H. Lee, M. Lemoine-Goumard, A. M. Lionetto, F. Longo, F. Loparco, B. Lott, M. N. Lovellette, P. Lubrano, G. M. Madejski, A. Makeev, B. Marangelli, M. M. Massai, M. N. Mazziotta, J. E. McEnery, N. Menon, C. Meurer, P. F. Michelson, M. Minuti, N. Mirizzi, W. Mitthumsiri, T. Mizuno, A. A. Moiseev, C. Monte, M. E. Monzani, E. Moretti, A. Morselli, I. V. Moskalenko, S. Murgia, T. Nakamori, S. Nishino, P. L. Nolan, J. P. Norris, E. Nuss, M. Ohno, T. Ohsugi, N. Omodei, E. Orlando, J. F. Ormes, A. Paccagnella, D. Paneque, J. H. Panetta, D. Parent, M. Pearce, M. Pepe, A. Perazzo, M. Pesce-Rollins, P. Picozza, L. Pieri, M. Pinchera, F. Piron, T. A. Porter, L. Poupard, S. Rainò, R. Rando, E. Rapposelli, M. Razzano, A. Reimer, O. Reimer, T. Reposeur, L. C. Reyes, S. Ritz, L. S. Rochester, A. Y. Rodriguez, R. W. Romani, M. Roth, J. J. Russell, F. Ryde, S. Sabatini, H. F. W. Sadrozinski, D. Sanchez, A. Sand er, L. Sapozhnikov, P. M. Saz Parkinson, J. D. Scargle, T. L. Schalk, G. Scolieri, C. Sgrò, G. H. Share, M. Shaw, T. Shimokawabe, C. Shrader, A. Sierpowska-Bartosik, E. J. Siskind, D. A. Smith, P. D. Smith, G. Spandre, P. Spinelli, J. L. Starck, T. E. Stephens, M. S. Strickman, A. W. Strong, D. J. Suson, H. Tajima, H. Takahashi, T. Takahashi, T. Tanaka, A. Tenze, S. Tether, J. B. Thayer, J. G. Thayer, D. J. Thompson, L. Tibaldo, O. Tibolla, D. F. Torres, G. Tosti, A. Tramacere, M. Turri, T. L. Usher, N. Vilchez, V. Vitale, P. Wang, K. Watters, B. L. Winer, K. S. Wood, T. Ylinen, and M. Ziegler. The Large Area Telescope on the Fermi Gamma-Ray Space Telescope Mission. ApJ, 697(2):1071–1102, Jun 2009.

[24] H. W. Babcock. The rotation of the Andromeda Nebula. *Lick Observatory Bulletin*, 19:41–51, 1939.

[25] Howard Baer, Ki-Young Choi, Jihn E. Kim, and Leszek Roszkowski. Dark matter production in the early Universe: Beyond the thermal

WIMP paradigm. Phys. Rep., 555:1–60, Feb 2015.

[26] Christophe Balland and Alain Blanchard. On the Uncertainty in X-Ray Cluster Mass Estimates from the Equation of Hydrostatic Equilibrium. ApJ, 487(1):33–37, Sep 1997.

[27] C. L. Bennett, A. J. Banday, K. M. Gorski, G. Hinshaw, P. Jackson, P. Keegstra, A. Kogut, G. F. Smoot, D. T. Wilkinson, and E. L. Wright. Four-Year COBE DMR Cosmic Microwave Background Observations: Maps and Basic Results. ApJ, 464:L1, June 1996.

[28] R. Bernabei, P. Belli, A. Bussolotti, F. Cappella, R. Cerulli, C. J. Dai, A. D'Angelo, H. L. He, A. Incicchitti, H. H. Kuang, J. M. Ma, A. Mattei, F. Montecchia, F. Nozzoli, D. Prosperi, X. D. Sheng, and Z. P. Ye. The DAMA/LIBRA apparatus. *Nuclear Instruments and Methods in Physics Research A*, 592(3):297–315, Jul 2008.

[29] R. Bernabei, P. Belli, F. Cappella, V. Caracciolo, S. Castellano, R. Cerulli, C. J. Dai, A. d'Angelo, S. d'Angelo, A. Di Marco, H. L. He, A. Incicchitti, H. H. Kuang, X. H. Ma, F. Montecchia, D. Prosperi, X. D. Sheng, R. G. Wang, and Z. P. Ye. Final model independent result of DAMA/LIBRA-phase1. *European Physical Journal C*, 73:2648, Dec 2013.

[30] B. Bertotti, L. Iess, and P. Tortora. A test of general relativity using radio links with the Cassini spacecraft. Nature, 425(6956):374–376, September 2003.

[31] Michael Boylan-Kolchin, James S. Bullock, and Manoj Kaplinghat. Too big to fail? The puzzling darkness of massive Milky Way subhaloes. MNRAS, 415(1):L40–L44, Jul 2011.

[32] C. Brans and R. H. Dicke. Mach's principle and a relativistic theory of gravitation. *Phys. Rev.*, 124:925–935, Nov 1961.

[33] E. Margaret Burbidge, G. R. Burbidge, William A. Fowler, and F. Hoyle. Synthesis of the elements in stars. *Rev. Mod. Phys.*, 29:547–650, Oct 1957.

[34] Scott Burles, Kenneth M. Nollett, and Michael S. Turner. Big Bang Nucleosynthesis Predictions for Precision Cosmology. *The Astrophysical Journal*, 552(1):L1–L5, May 2001.

[35] B. Carr and J. Primack. Searching for MACHOs. Nature, 345:478–479, June 1990.

[36] J. Carr, C. Balazs, T. Bringmann, T. Buanes, M. Daniel, M. Doro, C. Farnier, M. Fornasa, J. Gaskins, G. Gomez-Vargas, M. Hayashida, K. Kohri, V. Lefranc, A. Morselli, E. Moulin, N. Mirabal, J. Rico, T. Saito, M. Sanchez-Conde, M. Wilkinson, M. Wood, G. Zaharijas, and H. Zechlin. Prospects for Indirect Dark Matter Searches with the Cherenkov Telescope Array (CTA). In *34th International Cosmic Ray Conference (ICRC2015)*, volume 34 of *International Cosmic Ray Conference*, page 1203, Jul 2015.

[37] CDMS Collaboration, R. Agnese, Z. Ahmed, A. J. Anderson, S. Arrenberg, D. Balakishiyeva, R. Basu Thakur, D. A. Bauer, J. Billard, A. Borgland , D. Brandt, P. L. Brink, T. Bruch, R. Bunker, B. Cabrera, D. O. Caldwell, D. G. Cerdeno, H. Chagani, J. Cooley, B. Cornell, C. H. Crewdson, P. Cushman, M. Daal, F. Dejongh, E. Do Couto E Silva, T. Doughty, L. Esteban, S. Fallows, E. Figueroa-Feliciano, J. Filippini, J. Fox, M. Fritts, G. L. Godfrey, S. R. Golwala, J. Hall, R. H. Harris, S. A. Hertel, T. Hofer, D. Holmgren, L. Hsu, M. E. Huber, A. Jastram, O. Kamaev, B. Kara, M. H. Kelsey, A. Kennedy, P. Kim, M. Kiveni, K. Koch, M. Kos, S. W. Leman, B. Loer, E. Lopez Asamar, R. Mahapatra, V. Mandic, C. Martinez, K. A. McCarthy, N. Mirabolfathi, R. A. Moffatt, D. C. Moore, P. Nadeau, R. H. Nelson, K. Page, R. Partridge, M. Pepin, A. Phipps, K. Prasad, M. Pyle, H. Qiu, W. Rau, P. Redl, A. Reisetter, Y. Ricci, T. Saab, B. Sadoulet, J. Sander, K. Schneck, R. W. Schnee, S. Scorza, B. Serfass, B. Shank, D. Speller, K. M. Sundqvist, A. N. Villano, B. Welliver, D. H. Wright, S. Yellin, J. J. Yen, J. Yoo, B. A. Young, and J. Zhang. Silicon Detector Dark Matter Results from the Final Exposure of CDMS II. *arXiv e-prints*, page arXiv:1304.4279, Apr 2013.

[38] E. Charles, M. Sánchez-Conde, B. Anderson, R. Caputo, A. Cuoco, M. Di Mauro, A. Drlica-Wagner, G. A. Gomez-Vargas, M. Meyer, L. Tibaldo, M. Wood, G. Zaharijas, S. Zimmer, M. Ajello, A. Albert, L. Baldini, K. Bechtol, E. D. Bloom, F. Ceraudo, J. Cohen-Tanugi, S. W. Digel, J. Gaskins, M. Gustafsson, N. Mirabal, and M. Razzano. Sensitivity projections for dark matter searches with the Fermi large area telescope. Phys. Rep., 636:1–46, Jun 2016.

[39] Ilias Cholis, Carmelo Evoli, Francesca Calore, Tim Linden, Christoph Weniger, and Dan Hooper. The Galactic Center GeV excess from a series of leptonic cosmic-ray outbursts. J. Cosmology Astropart. Phys., 2015(12):005, Dec 2015.

[40] Hamish A. Clark, Pat Scott, Roberto Trotta, and Geraint F. Lewis. Dark matter substructure cannot explain properties of the Fermi Galactic Centre excess. J. Cosmology Astropart. Phys., 2018(7):060, Jul 2018.

[41] J. Conrad, J. Cohen-Tanugi, and L. E. Strigari. Wimp searches with gamma rays in the Fermi era: Challenges, methods and results. *Soviet Journal of Experimental and Theoretical Physics*, 121(6):1104–1135, Dec 2015.

[42] Jan Conrad. Indirect Detection of WIMP Dark Matter: a compact review. *arXiv e-prints*, page arXiv:1411.1925, Nov 2014.

[43] T. Damour and A. M. Polyakov. The string dilation and a least coupling principle. *Nuclear Physics B*, 423(2-3):532–558, July 1994.

[44] Thibault Damour and John F. Donoghue. Equivalence principle violations and couplings of a light dilaton. Phys. Rev. D, 82(8):084033, Oct 2010.

[45] Thibault Damour and Kenneth Nordtvedt. General relativity as a cosmological attractor of tensor-scalar theories. Phys. Rev. Lett., 70(15):2217–2219, April 1993.

[46] Jonathan H. Davis, Christopher McCabe, and Céline Bœhm. Quantifying the evidence for dark matter in CoGeNT data. J. Cosmology Astropart. Phys., 2014(8):014, Aug 2014.

[47] Hooman Davoudiasl and Peter B. Denton. Ultralight Boson Dark Matter and Event Horizon Telescope Observations of M 87*. Phys. Rev. Lett., 123(2):021102, Jul 2019.

[48] W. J. G. de Blok. The Core-Cusp Problem. *Advances in Astronomy*, 2010:789293, Jan 2010.

[49] Antonio De Felice and Shinji Tsujikawa. f(r) theories. *Living Reviews in Relativity*, 13(1), Jun 2010.

[50] Eugenio Del Nobile, Graciela B. Gelmini, Andreea Georgescu, and Ji-Haeng Huh. Reevaluation of spin-dependent WIMP-proton interactions as an explanation of the DAMA data. J. Cosmology Astropart. Phys., 2015(8):046, Aug 2015.

[51] Andrei Derevianko. Detecting dark-matter waves with a network of precision-measurement tools. Phys. Rev. A, 97(4):042506, Apr 2018.

[52] P. A. M. Dirac. The Cosmological Constants. Nature, 139(3512):323, February 1937.

[53] August E. Evrard, Christopher A. Metzler, and Julio F. Navarro. Mass Estimates of X-Ray Clusters. ApJ, 469:494, Oct 1996.

[54] S. M. Faber and J. S. Gallagher. Masses and mass-to-light ratios of galaxies. ARA&A, 17:135–187, 1979.

[55] Jonathan L. Feng. Dark Matter Candidates from Particle Physics and Methods of Detection. ARA&A, 48:495–545, Sep 2010.

[56] K. C. Freeman. On the Disks of Spiral and S0 Galaxies. ApJ, 160:811, June 1970.

[57] C. S. Frenk and S. D. M. White. Dark matter and cosmic structure. *Annalen der Physik*, 524(9-10):507–534, Oct 2012.

[58] Yasunori Fujii and Kei-ichi Maeda. *The Scalar-Tensor Theory of Gravitation.* Cambridge Monographs on Mathematical Physics. Cambridge University Press, 2003.

[59] R. J. Gaitskell. Direct detection of dark matter. *Ann. Rev. Nucl. Part. Sci.*, 54:315–359, 2004.

[60] Jennifer M. Gaskins. A review of indirect searches for particle dark matter. *Contemporary Physics*, 57(4):496–525, Oct 2016.

[61] Andrew A. Geraci, Colin Bradley, Dongfeng Gao, Jonathan Weinstein, and Andrei Derevianko. Searching for Ultralight Dark Matter with Optical Cavities. Phys. Rev. Lett., 123(3):031304, Jul 2019.

[62] G. K. Giovanetti, N. Abgrall, E. Aguayo, F. T. Avignone, A. S. Barabash, F. E. Bertrand, M. Boswell, V. Brudanin, M. Busch, D. Byram, A. S. Caldwell, Y. D. Chan, C. D. Christofferson, D. C. Combs, C. Cuesta, J. A. Detwiler, P. J. Doe, Yu. Efremenko,

V. Egorov, H. Ejiri, S. R. Elliott, J. E. Fast, P. Finnerty, F. M. Fraenkle, A. Galindo-Uribarri, J. Goett, M. P. Green, J. Gruszko, V. E. Guiseppe, K. Gusev, A. L. Hallin, R. Hazama, A. Hegai, R. Henning, E. W. Hoppe, S. Howard, M. A. Howe, K. J. Keeter, M. F. Kidd, O. Kochetov, S. I. Konovalov, R. T. Kouzes, B. D. LaFerriere, J. Leon, L. E. Leviner, J. C. Loach, J. MacMullin, S. MacMullin, R. D. Martin, S. Meijer, S. Mertens, M. Nomachi, J. L. Orrell, C. O'Shaughnessy, N. R. Overman, D. G. Phillips, A. W. P. Poon, K. Pushkin, D. C. Radford, J. Rager, K. Rielage, R. G. H. Robertson, E. Romero-Romero, M. C. Ronquest, A. G. Schubert, B. Shanks, T. Shima, M. Shirchenko, K. J. Snavely, N. Snyder, A. M. Suriano, J. Thompson, V. Timkin, W. Tornow, J. E. Trimble, R. L. Varner, S. Vasilyev, K. Vetter, K. Vorren, B. R. White, J. F. Wilkerson, C. Wiseman, W. Xu, E. Yakushev, A. R. Young, C. H. Yu, and V. Yumatov. A Dark Matter Search with MALBEK. *Physics Procedia*, 61:77–84, Jan 2015.

[63] Germán A. Gómez-Vargas, Miguel A. Sánchez-Conde, Ji-Haeng Huh, Miguel Peiró, Francisco Prada, Aldo Morselli, Anatoly Klypin, David G. Cerdeño, Yann Mambrini, and Carlos Muñoz. Constraints on WIMP annihilation for contracted dark matter in the inner Galaxy with the Fermi-LAT. J. Cosmology Astropart. Phys., 2013(10):029, Oct 2013.

[64] P. Gondolo and G. Gelmini. Cosmic abundances of stable particles: improved analysis. *Nuclear Physics B*, 360:145–179, August 1991.

[65] Michael B. Green, John H. Schwarz, and Edward Witten. *Superstring Theory: 25th Anniversary Edition*, volume 1 of *Cambridge Monographs on Mathematical Physics*. Cambridge University Press, 2012.

[66] Sheridan B. Green, Michelle Ntampaka, Daisuke Nagai, Lorenzo Lovisari, Klaus Dolag, Dominique Eckert, and John A. ZuHone. Using X-Ray Morphological Parameters to Strengthen Galaxy Cluster Mass Estimates via Machine Learning. *arXiv e-prints*, page arXiv:1908.02765, Aug 2019.

[67] H. Grote and Y. V. Stadnik. Novel signatures of dark matter in laser-interferometric gravitational-wave detectors. *Physical Review Research*, 1(3):033187, December 2019.

[68] A. Hees, J. Guéna, M. Abgrall, S. Bize, and P. Wolf. Searching for an Oscillating Massive Scalar Field as a Dark Matter Candidate

Using Atomic Hyperfine Frequency Comparisons. Phys. Rev. Lett., 117(6):061301, Aug 2016.

[69] A. Hees, J. Guéna, M. Abgrall, S. Bize, and P. Wolf. Searching for an oscillating massive scalar field as a dark matter candidate using atomic hyperfine frequency comparisons. *Physical Review Letters*, 117(6), Aug 2016.

[70] Aurélien Hees, Olivier Minazzoli, Etienne Savalle, Yevgeny V. Stadnik, and Peter Wolf. Violation of the equivalence principle from light scalar dark matter. Phys. Rev. D, 98(6):064051, September 2018.

[71] Catherine Heymans, Ludovic Van Waerbeke, Lance Miller, Thomas Erben, Hendrik Hildebrandt, Henk Hoekstra, Thomas D. Kitching, Yannick Mellier, Patrick Simon, Christopher Bonnett, Jean Coupon, Liping Fu, Joachim Harnois Déraps, Michael J. Hudson, Martin Kilbinger, Koenraad Kuijken, Barnaby Rowe, Tim Schrabback, Elisabetta Semboloni, Edo van Uitert, Sanaz Vafaei, and Malin Velander. CFHTLenS: the Canada-France-Hawaii Telescope Lensing Survey. MNRAS, 427(1):146–166, Nov 2012.

[72] G. Hinshaw, D. Larson, E. Komatsu, D. N. Spergel, C. L. Bennett, J. Dunkley, M. R. Nolta, M. Halpern, R. S. Hill, N. Odegard, L. Page, K. M. Smith, J. L. Weiland, B. Gold, N. Jarosik, A. Kogut, M. Limon, S. S. Meyer, G. S. Tucker, E. Wollack, and E. L. Wright. Nine-year Wilkinson Microwave Anisotropy Probe (WMAP) Observations: Cosmological Parameter Results. *The Astrophysical Journal Supplement Series*, 208(2):19, Oct 2013.

[73] J. Holder, V. A. Acciari, E. Aliu, T. Arlen, M. Beilicke, W. Benbow, S. M. Bradbury, J. H. Buckley, V. Bugaev, Y. Butt, K. L. Byrum, A. Cannon, O. Celik, A. Cesarini, L. Ciupik, Y. C. K. Chow, P. Cogan, P. Colin, W. Cui, M. K. Daniel, T. Ergin, A. D. Falcone, S. J. Fegan, J. P. Finley, G. Finnegan, P. Fortin, L. F. Fortson, A. Furniss, G. H. Gillanders, J. Grube, R. Guenette, G. Gyuk, D. Hanna, E. Hays, D. Horan, C. M. Hui, T. B. Humensky, A. Imran, P. Kaaret, N. Karlsson, M. Kertzman, D. B. Kieda, J. Kildea, A. Konopelko, H. Krawczynski, F. Krennrich, M. J. Lang, S. Lebohec, G. Maier, A. McCann, M. McCutcheon, P. Moriarty, R. Mukherjee, T. Nagai, J. Niemiec, R. A. Ong, D. Pandel, J. S. Perkins, M. Pohl, J. Quinn, K. Ragan, L. C. Reyes, P. T. Reynolds, H. J. Rose, M. Schroedter, G. H. Sembroski, A. W. Smith, D. Steele, S. P. Swordy, J. A. Toner,

L. Valcarcel, V. V. Vassiliev, R. Wagner, S. P. Wakely, J. E. Ward, T. C. Weekes, A. Weinstein, R. J. White, D. A. Williams, S. A. Wissel, M. Wood, and B. Zitzer. Status of the VERITAS Observatory. In Felix A. Aharonian, Werner Hofmann, and Frank Rieger, editors, *American Institute of Physics Conference Series*, volume 1085 of *American Institute of Physics Conference Series*, pages 657–660, Dec 2008.

[74] Dan Hooper and Lisa Goodenough. Dark matter annihilation in the Galactic Center as seen by the Fermi Gamma Ray Space Telescope. *Physics Letters B*, 697(5):412–428, Mar 2011.

[75] Shunsaku Horiuchi, Manoj Kaplinghat, and Anna Kwa. Investigating the uniformity of the excess gamma rays towards the galactic center region. J. Cosmology Astropart. Phys., 2016(11):053, Nov 2016.

[76] E. Hubble and M. L. Humason. The Velocity-Distance Relation among Extra-Galactic Nebulae. ApJ, 74:43, July 1931.

[77] Lam Hui, Jeremiah P. Ostriker, Scott Tremaine, and Edward Witten. Ultralight scalars as cosmological dark matter. Phys. Rev. D, 95(4):043541, Feb 2017.

[78] Nick Kaiser and Gordon Squires. Mapping the Dark Matter with Weak Gravitational Lensing. ApJ, 404:441, Feb 1993.

[79] Stacy Y. Kim, Annika H. G. Peter, and Jonathan R. Hargis. Missing Satellites Problem: Completeness Corrections to the Number of Satellite Galaxies in the Milky Way are Consistent with Cold Dark Matter Predictions. Phys. Rev. Lett., 121(21):211302, Nov 2018.

[80] Anatoly Klypin, Andrey V. Kravtsov, Octavio Valenzuela, and Francisco Prada. Where Are the Missing Galactic Satellites? ApJ, 522(1):82–92, Sep 1999.

[81] A. M. Koekemoer, H. Aussel, D. Calzetti, P. Capak, M. Giavalisco, J. P. Kneib, A. Leauthaud, O. Le Fèvre, H. J. McCracken, R. Massey, B. Mobasher, J. Rhodes, N. Scoville, and P. L. Shopbell. The COSMOS Survey: Hubble Space Telescope Advanced Camera for Surveys Observations and Data Processing. ApJS, 172(1):196–202, Sep 2007.

[82] M. Kuźniak, M. G. Boulay, and T. Pollmann. Surface roughness interpretation of 730 kg days CRESST-II results. *Astroparticle Physics*, 36(1):77–82, Aug 2012.

[83] T. Lasserre, C. Afonso, J. N. Albert, J. Andersen, R. Ansari, É. Aubourg, P. Bareyre, F. Bauer, J. P. Beaulieu, G. Blanc, A. Bouquet, S. Char, X. Charlot, F. Couchot, C. Coutures, F. Derue, R. Ferlet, J. F. Glicenstein, B. Goldman, A. Gould, D. Graff, M. Gros, J. Haissinski, J. C. Hamilton, D. Hardin, J. de Kat, A. Kim, É. Lesquoy, C. Loup, C. Magneville, B. Mansoux, J. B. Marquette, É. Maurice, A. Milsztajn, M. Moniez, N. Palanque-Delabrouille, O. Perdereau, L. Prévot, N. Regnault, J. Rich, M. Spiro, A. Vidal-Madjar, L. Vigroux, S. Zylberajch, and EROS Collaboration. Not enough stellar mass Machos in the Galactic halo. *Astronomy and Astrophysics*, 355:L39–L42, Mar 2000.

[84] Oscar Macias, Chris Gordon, Roland M. Crocker, Brendan Coleman, Dylan Paterson, Shunsaku Horiuchi, and Martin Pohl. Galactic bulge preferred over dark matter for the Galactic centre gamma-ray excess. *Nature Astronomy*, 2:387–392, Mar 2018.

[85] Teresa Marrodán Undagoitia and Ludwig Rauch. Dark matter direct-detection experiments. *Journal of Physics G Nuclear Physics*, 43(1):013001, Jan 2016.

[86] David J. E. Marsh and Joseph Silk. A model for halo formation with axion mixed dark matter. MNRAS, 437(3):2652–2663, Jan 2014.

[87] John F. Meekins, Gilbert Fritz, Talbot A. Chubb, and H. Friedman. Physical Sciences: X-rays from the Coma Cluster of Galaxies. Nature, 231(5298):107–108, May 1971.

[88] Ben Moore, Sebastiano Ghigna, Fabio Governato, George Lake, Thomas Quinn, Joachim Stadel, and Paolo Tozzi. Dark Matter Substructure within Galactic Halos. ApJ, 524(1):L19–L22, Oct 1999.

[89] Soichiro Morisaki and Teruaki Suyama. Detectability of ultralight scalar field dark matter with gravitational-wave detectors. Phys. Rev. D, 100(12):123512, Dec 2019.

[90] G C Myeong, N W Evans, V Belokurov, N C Amorisco, and S E Koposov. Halo substructure in the SDSS–Gaia catalogue: streams and clumps. *Monthly Notices of the Royal Astronomical Society*, 475(2):1537–1548, 12 2017.

[91] G. C. Myeong, N. W. Evans, V. Belokurov, J. L. Sand ers, and S. E. Koposov. Discovery of new retrograde substructures: the shards of ω Centauri? MNRAS, 478(4):5449–5459, Aug 2018.

[92] Wei-Tou Ni and Mark Zimmermann. Inertial and gravitational effects in the proper reference frame of an accelerated, rotating observer. Phys. Rev. D, 17(6):1473–1476, March 1978.

[93] International School of Cosmology, Italy) Gravitation (1982 : Erice, Ernst Schmutzer, Venzo De Sabbata, Ettore Majorana International Centre for Scientific Culture, International School of Cosmology, and Gravitation. Unified field theories of more than 4 dimensions : including exact solutions, 1983. "Proceedings of the International School of Cosmology and Gravitation held in Erice, Trapani, Sicily, 20 May-1 June 1982.".

[94] Ciaran A. J. O'Hare, Christopher McCabe, N. Wyn Evans, GyuChul Myeong, and Vasily Belokurov. Dark matter hurricane: Measuring the S1 stream with dark matter detectors. Phys. Rev. D, 98(10):103006, Nov 2018.

[95] T. Page. Radial Velocities and Masses of Double Galaxies. ApJ, 116:63, July 1952.

[96] P. J. E. Peebles. Penzias & Wilson's Discovery of the Cosmic Microwave Background. ApJ, 525C:1067, Nov 1999.

[97] A. A. Penzias. Free Hydrogen in the Pegasus I Cluster of Galaxies. AJ, 66:293, March 1961.

[98] Annika H. G. Peter, Vera Gluscevic, Anne M. Green, Bradley J. Kavanagh, and Samuel K. Lee. WIMP physics with ensembles of direct-detection experiments. *Physics of the Dark Universe*, 5:45–74, Dec 2014.

[99] Aaron Pierce, Keith Riles, and Yue Zhao. Searching for Dark Photon Dark Matter with Gravitational-Wave Detectors. Phys. Rev. Lett., 121(6):061102, Aug 2018.

[100] Planck Collaboration, P. A. R. Ade, N. Aghanim, C. Armitage-Caplan, M. Arnaud, M. Ashdown, F. Atrio-Barand ela, J. Aumont, C. Baccigalupi, A. J. Banday, R. B. Barreiro, J. G. Bartlett, E. Battaner, K. Benabed, A. Benoît, A. Benoit-Lévy, J. P. Bernard, M. Bersanelli,

P. Bielewicz, J. Bobin, J. J. Bock, A. Bonaldi, J. R. Bond, J. Borrill, F. R. Bouchet, M. Bridges, M. Bucher, C. Burigana, R. C. Butler, E. Calabrese, B. Cappellini, J. F. Cardoso, A. Catalano, A. Challinor, A. Chamballu, R. R. Chary, X. Chen, H. C. Chiang, L. Y. Chiang, P. R. Christensen, S. Church, D. L. Clements, S. Colombi, L. P. L. Colombo, F. Couchot, A. Coulais, B. P. Crill, A. Curto, F. Cuttaia, L. Danese, R. D. Davies, R. J. Davis, P. de Bernardis, A. de Rosa, G. de Zotti, J. Delabrouille, J. M. Delouis, F. X. Désert, C. Dickinson, J. M. Diego, K. Dolag, H. Dole, S. Donzelli, O. Doré, M. Douspis, J. Dunkley, X. Dupac, G. Efstathiou, F. Elsner, T. A. Enßlin, H. K. Eriksen, F. Finelli, O. Forni, M. Frailis, A. A. Fraisse, E. Franceschi, T. C. Gaier, S. Galeotta, S. Galli, K. Ganga, M. Giard, G. Giardino, Y. Giraud-Héraud, E. Gjerløw, J. González-Nuevo, K. M. Górski, S. Gratton, A. Gregorio, A. Gruppuso, J. E. Gudmundsson, J. Haissinski, J. Hamann, F. K. Hansen, D. Hanson, D. Harrison, S. Henrot-Versillé, C. Hernández-Monteagudo, D. Herranz, S. R. Hildebrand t, E. Hivon, M. Hobson, W. A. Holmes, A. Hornstrup, Z. Hou, W. Hovest, K. M. Huffenberger, A. H. Jaffe, T. R. Jaffe, J. Jewell, W. C. Jones, M. Juvela, E. Keihänen, R. Keskitalo, T. S. Kisner, R. Kneissl, J. Knoche, L. Knox, M. Kunz, H. Kurki-Suonio, G. Lagache, A. Lähteenmäki, J. M. Lamarre, A. Lasenby, M. Lattanzi, R. J. Laureijs, C. R. Lawrence, S. Leach, J. P. Leahy, R. Leonardi, J. León-Tavares, J. Lesgourgues, A. Lewis, M. Liguori, P. B. Lilje, M. Linden-Vørnle, M. López-Caniego, P. M. Lubin, J. F. Macías-Pérez, B. Maffei, D. Maino, N. Mand olesi, M. Maris, D. J. Marshall, P. G. Martin, E. Martínez-González, S. Masi, M. Massardi, S. Matarrese, F. Matthai, P. Mazzotta, P. R. Meinhold, A. Melchiorri, J. B. Melin, L. Mendes, E. Menegoni, A. Mennella, M. Migliaccio, M. Millea, S. Mitra, M. A. Miville-Deschênes, A. Moneti, L. Montier, G. Morgante, D. Mortlock, A. Moss, D. Munshi, J. A. Murphy, P. Naselsky, F. Nati, P. Natoli, C. B. Netterfield, H. U. Nørgaard-Nielsen, F. Noviello, D. Novikov, I. Novikov, I. J. O'Dwyer, S. Osborne, C. A. Oxborrow, F. Paci, L. Pagano, F. Pajot, R. Paladini, D. Paoletti, B. Partridge, F. Pasian, G. Patanchon, D. Pearson, T. J. Pearson, H. V. Peiris, O. Perdereau, L. Perotto, F. Perrotta, V. Pettorino, F. Piacentini, M. Piat, E. Pierpaoli, D. Pietrobon, S. Plaszczynski, P. Platania, E. Pointecouteau, G. Polenta, N. Ponthieu, L. Popa, T. Poutanen, G. W. Pratt, G. Prézeau, S. Prunet, J. L. Puget, J. P. Rachen, W. T. Reach, R. Rebolo, M. Reinecke, M. Remazeilles, C. Renault, S. Ricciardi, T. Riller, I. Ristorcelli, G. Rocha, C. Rosset, G. Roudier,

M. Rowan-Robinson, J. A. Rubiño-Martín, B. Rusholme, M. Sandri, D. Santos, M. Savelainen, G. Savini, D. Scott, M. D. Seiffert, E. P. S. Shellard, L. D. Spencer, J. L. Starck, V. Stolyarov, R. Stompor, R. Sudiwala, R. Sunyaev, F. Sureau, D. Sutton, A. S. Suur-Uski, J. F. Sygnet, J. A. Tauber, D. Tavagnacco, L. Terenzi, L. Toffolatti, M. Tomasi, M. Tristram, M. Tucci, J. Tuovinen, M. Türler, G. Umana, L. Valenziano, J. Valiviita, B. Van Tent, P. Vielva, F. Villa, N. Vittorio, L. A. Wade, B. D. Wandelt, I. K. Wehus, M. White, S. D. M. White, A. Wilkinson, D. Yvon, A. Zacchei, and A. Zonca. Planck 2013 results. XVI. Cosmological parameters. A&A, 571:A16, Nov 2014.

[101] Planck Collaboration, P. A. R. Ade, N. Aghanim, M. Arnaud, M. Ashdown, J. Aumont, C. Baccigalupi, A. J. Banday, R. B. Barreiro, J. G. Bartlett, N. Bartolo, E. Battaner, R. Battye, K. Benabed, A. Benoît, A. Benoit-Lévy, J. P. Bernard, M. Bersanelli, P. Bielewicz, J. J. Bock, A. Bonaldi, L. Bonavera, J. R. Bond, J. Borrill, F. R. Bouchet, F. Boulanger, M. Bucher, C. Burigana, R. C. Butler, E. Calabrese, J. F. Cardoso, A. Catalano, A. Challinor, A. Chamballu, R. R. Chary, H. C. Chiang, J. Chluba, P. R. Christensen, S. Church, D. L. Clements, S. Colombi, L. P. L. Colombo, C. Combet, A. Coulais, B. P. Crill, A. Curto, F. Cuttaia, L. Danese, R. D. Davies, R. J. Davis, P. de Bernardis, A. de Rosa, G. de Zotti, J. Delabrouille, F. X. Désert, E. Di Valentino, C. Dickinson, J. M. Diego, K. Dolag, H. Dole, S. Donzelli, O. Doré, M. Douspis, A. Ducout, J. Dunkley, X. Dupac, G. Efstathiou, F. Elsner, T. A. Enßlin, H. K. Eriksen, M. Farhang, J. Fergusson, F. Finelli, O. Forni, M. Frailis, A. A. Fraisse, E. Franceschi, A. Frejsel, S. Galeotta, S. Galli, K. Ganga, C. Gauthier, M. Gerbino, T. Ghosh, M. Giard, Y. Giraud-Héraud, E. Giusarma, E. Gjerløw, J. González-Nuevo, K. M. Górski, S. Gratton, A. Gregorio, A. Gruppuso, J. E. Gudmundsson, J. Hamann, F. K. Hansen, D. Hanson, D. L. Harrison, G. Helou, S. Henrot-Versillé, C. Hernández-Monteagudo, D. Herranz, S. R. Hildebrand t, E. Hivon, M. Hobson, W. A. Holmes, A. Hornstrup, W. Hovest, Z. Huang, K. M. Huffenberger, G. Hurier, A. H. Jaffe, T. R. Jaffe, W. C. Jones, M. Juvela, E. Keihänen, R. Keskitalo, T. S. Kisner, R. Kneissl, J. Knoche, L. Knox, M. Kunz, H. Kurki-Suonio, G. Lagache, A. Lähteenmäki, J. M. Lamarre, A. Lasenby, M. Lattanzi, C. R. Lawrence, J. P. Leahy, R. Leonardi, J. Lesgourgues, F. Levrier, A. Lewis, M. Liguori, P. B. Lilje, M. Linden-Vørnle, M. López-Caniego, P. M. Lubin, J. F. Macías-Pérez, G. Maggio, D. Maino, N. Mandolesi, A. Mangilli, A. Marchini,

M. Maris, P. G. Martin, M. Martinelli, E. Martínez-González, S. Masi, S. Matarrese, P. McGehee, P. R. Meinhold, A. Melchiorri, J. B. Melin, L. Mendes, A. Mennella, M. Migliaccio, M. Millea, S. Mitra, M. A. Miville-Deschênes, A. Moneti, L. Montier, G. Morgante, D. Mortlock, A. Moss, D. Munshi, J. A. Murphy, P. Naselsky, F. Nati, P. Natoli, C. B. Netterfield, H. U. Nørgaard-Nielsen, F. Noviello, D. Novikov, I. Novikov, C. A. Oxborrow, F. Paci, L. Pagano, F. Pajot, R. Paladini, D. Paoletti, B. Partridge, F. Pasian, G. Patanchon, T. J. Pearson, O. Perdereau, L. Perotto, F. Perrotta, V. Pettorino, F. Piacentini, M. Piat, E. Pierpaoli, D. Pietrobon, S. Plaszczynski, E. Pointecouteau, G. Polenta, L. Popa, G. W. Pratt, G. Prézeau, S. Prunet, J. L. Puget, J. P. Rachen, W. T. Reach, R. Rebolo, M. Reinecke, M. Remazeilles, C. Renault, A. Renzi, I. Ristorcelli, G. Rocha, C. Rosset, M. Rossetti, G. Roudier, B. Rouillé d'Orfeuil, M. Rowan-Robinson, J. A. Rubiño-Martín, B. Rusholme, N. Said, V. Salvatelli, L. Salvati, M. Sandri, D. Santos, M. Savelainen, G. Savini, D. Scott, M. D. Seiffert, P. Serra, E. P. S. Shellard, L. D. Spencer, M. Spinelli, V. Stolyarov, R. Stompor, R. Sudiwala, R. Sunyaev, D. Sutton, A. S. Suur-Uski, J. F. Sygnet, J. A. Tauber, L. Terenzi, L. Toffolatti, M. Tomasi, M. Tristram, T. Trombetti, M. Tucci, J. Tuovinen, M. Türler, G. Umana, L. Valenziano, J. Valiviita, F. Van Tent, P. Vielva, F. Villa, L. A. Wade, B. D. Wandelt, I. K. Wehus, M. White, S. D. M. White, A. Wilkinson, D. Yvon, A. Zacchei, and A. Zonca. Planck 2015 results. XIII. Cosmological parameters. A&A, 594:A13, Sep 2016.

[102] E. Rasia, S. Ettori, L. Moscardini, P. Mazzotta, S. Borgani, K. Dolag, G. Tormen, L. M. Cheng, and A. Diaferio. Systematics in the X-ray cluster mass estimators. MNRAS, 369(4):2013–2024, Jul 2006.

[103] H. Reeves, J. Audouze, W. A. Fowler, and D. N. Schramm. On the Origin of Light Elements. ApJ, 179:909–930, February 1973.

[104] M. S. Roberts. A High-Resolution 21-CM Hydrogen-Line Survey of the Andromeda Nebula. ApJ, 144:639, May 1966.

[105] D. H. Rogstad and G. S. Shostak. Gross Properties of Five Scd Galaxies as Determined from 21-CENTIMETER Observations. ApJ, 176:315, September 1972.

[106] Joseph D. Romano and Neil. J. Cornish. Detection methods for stochastic gravitational-wave backgrounds: a unified treatment. *Living Reviews in Relativity*, 20(1):2, April 2017.

[107] Leszek Roszkowski, Enrico Maria Sessolo, and Sebastian Trojanowski. WIMP dark matter candidates and searches—current status and future prospects. *Reports on Progress in Physics*, 81(6):066201, Jun 2018.

[108] V. C. Rubin and W. K. Ford, Jr. Rotation of the Andromeda Nebula from a Spectroscopic Survey of Emission Regions. ApJ, 159:379, February 1970.

[109] V. C. Rubin, W. K. Ford, Jr., and N. Thonnard. Extended rotation curves of high-luminosity spiral galaxies. IV - Systematic dynamical properties, SA through SC. ApJ, 225:L107–L111, November 1978.

[110] Hsi-Yu Schive, Tzihong Chiueh, and Tom Broadhurst. Cosmic structure as the quantum interference of a coherent dark wave. *Nature Physics*, 10(7):496–499, Jul 2014.

[111] S. Schlamminger, K.-Y. Choi, T. A. Wagner, J. H. Gundlach, and E. G. Adelberger. Test of the equivalence principle using a rotating torsion balance. *Phys. Rev. Lett.*, 100:041101, Jan 2008.

[112] Peter Schneider and Carolin Seitz. Steps towards nonlinear cluster inversion through gravitational distortions. I. Basic considerations and circular clusters. A&A, 294:411–431, Feb 1995.

[113] M. Schwarzschild. Mass distribution and mass-luminosity ratio in galaxies. AJ, 59:273, September 1954.

[114] Melanie Simet. Galaxy Cluster Center Detection Methods with Weak Lensing. In *American Astronomical Society Meeting Abstracts #221*, volume 221 of *American Astronomical Society Meeting Abstracts*, page 226.07, Jan 2013.

[115] Sinclair Smith. The Mass of the Virgo Cluster. ApJ, 83:23, Jan 1936.

[116] A. A. Starobinsky. Amplification of waves reflected from a rotating "black hole". *Sov. Phys. JETP*, 37(1):28–32, 1973. [Zh. Eksp. Teor. Fiz.64,48(1973)].

[117] Andi Tan, Mengjiao Xiao, Xiangyi Cui, Xun Chen, Yunhua Chen, Deqing Fang, Changbo Fu, Karl Giboni, Franco Giuliani, Haowei Gong, Xuyuan Guo, Ke Han, Shouyang Hu, Xingtao Huang, Xiangdong Ji, Yonglin Ju, Siao Lei, Shaoli Li, Xiaomei Li, Xinglong Li, Hao Liang,

Qing Lin, Huaxuan Liu, Jianglai Liu, Wolfgang Lorenzon, Yugang Ma, Yajun Mao, Kaixuan Ni, Xiangxiang Ren, Michael Schubnell, Manbin Shen, Fang Shi, Hongwei Wang, Jimin Wang, Meng Wang, Qiuhong Wang, Siguang Wang, Xuming Wang, Zhou Wang, Shiyong Wu, Xiang Xiao, Pengwei Xie, Binbin Yan, Yong Yang, Jianfeng Yue, Xionghui Zeng, Hongguang Zhang, Hua Zhang, Huanqiao Zhang, Tao Zhang, Li Zhao, Jing Zhou, Ning Zhou, Xiaopeng Zhou, and Pand aX-II Collaboration. Dark Matter Results from First 98.7 Days of Data from the PandaX-II Experiment. Phys. Rev. Lett., 117(12):121303, Sep 2016.

[118] J. Tarter and J. Silk. Current Constraints on Hidden Mass in the Coma Cluster. QJRAS, 15:122, Jun 1974.

[119] Max Tegmark, Michael A. Strauss, Michael R. Blanton, Kevork Abazajian, Scott Dodelson, Havard Sandvik, Xiaomin Wang, David H. Weinberg, Idit Zehavi, Neta A. Bahcall, Fiona Hoyle, David Schlegel, Roman Scoccimarro, Michael S. Vogeley, Andreas Berlind, Tamás Budavari, Andrew Connolly, Daniel J. Eisenstein, Douglas Finkbeiner, Joshua A. Frieman, James E. Gunn, Lam Hui, Bhuvnesh Jain, David Johnston, Stephen Kent, Huan Lin, Reiko Nakajima, Robert C. Nichol, Jeremiah P. Ostriker, Adrian Pope, Ryan Scranton, Uroš Seljak, Ravi K. Sheth, Albert Stebbins, Alexander S. Szalay, István Szapudi, Yongzhong Xu, James Annis, J. Brinkmann, Scott Burles, Francisco J. Castand er, Istvan Csabai, Jon Loveday, Mamoru Doi, Masataka Fukugita, Bruce Gillespie, Greg Hennessy, David W. Hogg, Željko Ivezić, Gillian R. Knapp, Don Q. Lamb, Brian C. Lee, Robert H. Lupton, Timothy A. McKay, Peter Kunszt, Jeffrey A. Munn, Liam O'Connell, John Peoples, Jeffrey R. Pier, Michael Richmond, Constance Rockosi, Donald P. Schneider, Christopher Stoughton, Douglas L. Tucker, Daniel E. vanden Berk, Brian Yanny, and Donald G. York. Cosmological parameters from SDSS and WMAP. Phys. Rev. D, 69(10):103501, May 2004.

[120] P. Tisserand, L. Le Guillou, C. Afonso, J. N. Albert, J. Andersen, R. Ansari, É. Aubourg, P. Bareyre, J. P. Beaulieu, X. Charlot, C. Coutures, R. Ferlet, P. Fouqué, J. F. Glicenstein, B. Goldman, A. Gould, D. Graff, M. Gros, J. Haissinski, C. Hamadache, J. de Kat, T. Lasserre, É. Lesquoy, C. Loup, C. Magneville, J. B. Marquette, É. Maurice, A. Maury, A. Milsztajn, M. Moniez, N. Palanque-Delabrouille, O. Perdereau, Y. R. Rahal, J. Rich, M. Spiro, A. Vidal-Madjar, L. Vigroux, S. Zylberajch, and EROS-2 Collaboration. Limits

on the Macho content of the Galactic Halo from the EROS-2 Survey of the Magellanic Clouds. *Astronomy and Astrophysics*, 469(2):387–404, Jul 2007.

[121] David Tong. Lectures on String Theory. *arXiv e-prints*, page arXiv:0908.0333, August 2009.

[122] Pierre Touboul, Gilles Métris, Manuel Rodrigues, Yves André, Quentin Baghi, Joël Bergé, Damien Boulanger, Stefanie Bremer, Patrice Carle, Ratana Chhun, Bruno Christophe, Valerio Cipolla, Thibault Damour, Pascale Danto, Hansjoerg Dittus, Pierre Fayet, Bernard Foulon, Claude Gageant, Pierre-Yves Guidotti, Daniel Hagedorn, Emilie Hardy, Phuong-Anh Huynh, Henri Inchauspe, Patrick Kayser, Stéphanie Lala, Claus Lämmerzahl, Vincent Lebat, Pierre Leseur, Fran çoise Liorzou, Meike List, Frank Löffler, Isabelle Panet, Benjamin Pouilloux, Pascal Prieur, Alexandre Rebray, Serge Reynaud, Benny Rievers, Alain Robert, Hanns Selig, Laura Serron, Timothy Sumner, Nicolas Tanguy, and Pieter Visser. Microscope mission: First results of a space test of the equivalence principle. *Phys. Rev. Lett.*, 119:231101, Dec 2017.

[123] J. A. Tyson, F. Valdes, and R. A. Wenk. Detection of Systematic Gravitational Lens Galaxy Image Alignments: Mapping Dark Matter in Galaxy Clusters. ApJ, 349:L1, Jan 1990.

[124] H. C. van de Hulst, E. Raimond, and H. van Woerden. Rotation and density distribution of the Andromeda nebula derived from observations of the 21-cm line. Bull. Astron. Inst. Netherlands, 14:1, November 1957.

[125] Ken Van Tilburg, Nathan Leefer, Lykourgos Bougas, and Dmitry Budker. Search for Ultralight Scalar Dark Matter with Atomic Spectroscopy. Phys. Rev. Lett., 115(1):011802, July 2015.

[126] Matteo Viel, George D. Becker, James S. Bolton, and Martin G. Haehnelt. Warm dark matter as a solution to the small scale crisis: New constraints from high redshift Lyman-α forest data. Phys. Rev. D, 88(4):043502, Aug 2013.

[127] Joachim Wambsganss. Gravitational lensing in astronomy. *Living Reviews in Relativity*, 1(1), Nov 1998.

[128] David H. Weinberg, James S. Bullock, Fabio Governato, Rachel Kuzio de Naray, and Annika H. G. Peter. Cold dark matter: Controversies on small scales. *Proceedings of the National Academy of Science*, 112(40):12249–12255, Oct 2015.

[129] S. D. M. White, C. S. Frenk, and M. Davis. Clustering in a neutrino-dominated universe. ApJ, 274:L1–L5, November 1983.

[130] Clifford M. Will. The confrontation between general relativity and experiment. *Living Reviews in Relativity*, 17(1), Jun 2014.

[131] Clifford M. Will. The Confrontation between General Relativity and Experiment. *Living Reviews in Relativity*, 17(1):4, December 2014.

[132] Gillian Wilson, Shaun Cole, and Carlos S. Frenk. Cluster mass reconstruction from weak gravitational lensing. MNRAS, 280(1):199–218, May 1996.

[133] XMASS Collaboration, K. Abe, K. Hiraide, K. Ichimura, Y. Kishimoto, K. Kobayashi, M. Kobayashi, S. Moriyama, M. Nakahata, T. Norita, H. Ogawa, H. Sekiya, O. Takachio, A. Takeda, M. Yamashita, B. S. Yang, N. Y. Kim, Y. D. Kim, S. Tasaka, K. Fushimi, J. Liu, K. Martens, Y. Suzuki, B. D. Xu, R. Fujita, K. Hosokawa, K. Miuchi, Y. Onishi, N. Oka, Y. Takeuchi, Y. H. Kim, J. S. Lee, K. B. Lee, M. K. Lee, Y. Fukuda, Y. Itow, R. Kegasa, K. Kobayashi, K. Masada, H. Takiya, K. Nishijima, and S. Nakamura. Direct dark matter search by annual modulation in XMASS-I. *arXiv e-prints*, page arXiv:1511.04807, Nov 2015.

[134] Rui Xu, Yong Gao, and Lijing Shao. Strong-field effects in massive scalar-tensor gravity for slowly spinning neutron stars and application to x-ray pulsar pulse profiles. *Physical Review D*, 102(6), Sep 2020.

[135] York et al. The Sloan Digital Sky Survey: Technical Summary. AJ, 120(3):1579–1587, Sep 2000.

[136] Q. Yue, W. Zhao, K. J. Kang, J. P. Cheng, Y. J. Li, S. T. Lin, J. P. Chang, N. Chen, Q. H. Chen, Y. H. Chen, Y. C. Chuang, Z. Deng, Q. Du, H. Gong, X. Q. Hao, H. J. He, Q. J. He, H. X. Huang, T. R. Huang, H. Jiang, H. B. Li, J. M. Li, J. Li, J. Li, X. Li, X. Y. Li, Y. L. Li, H. Y. Liao, F. K. Lin, S. K. Liu, L. C. Lü, H. Ma, S. J. Mao, J. Q. Qin, J. Ren, J. Ren, X. C. Ruan, M. B. Shen, L. Singh, M. K. Singh, A. K. Soma, J. Su, C. J. Tang, C. H. Tseng, J. M. Wang,

L. Wang, Q. Wang, H. T. Wong, S. Y. Wu, Y. C. Wu, Y. C. Wu, Z. Z. Xianyu, R. Q. Xiao, H. Y. Xing, F. Z. Xu, Y. Xu, X. J. Xu, T. Xue, L. T. Yang, S. W. Yang, N. Yi, C. X. Yu, H. Yu, X. Z. Yu, X. H. Zeng, Z. Zeng, L. Zhang, Y. H. Zhang, M. G. Zhao, Z. Y. Zhou, J. J. Zhu, W. B. Zhu, X. Z. Zhu, Z. H. Zhu, and CDEX Collaboration. Limits on light weakly interacting massive particles from the CDEX-1 experiment with a p -type point-contact germanium detector at the China Jinping Underground Laboratory. Phys. Rev. D, 90(9):091701, Nov 2014.

[137] F. Zwicky. Die Rotverschiebung von extragalaktischen Nebeln. *Helvetica Physica Acta*, 6:110–127, 1933.

[138] F. Zwicky. On the Masses of Nebulae and of Clusters of Nebulae. ApJ, 86:217, October 1937.